DISS. ETH NO. 30346

Hidden order, magnetoelectricity, and complex magnetism in corundum structure transition metal oxides

A thesis submitted to attain the degree of

DOCTOR OF SCIENCES
(Dr. sc. ETH Zurich)

presented by

XANTHE HENDERIKE VERBEEK

MSc Physics and Astronomy (Joint Degree)
University of Amsterdam & Vrije Universiteit Amsterdam

born on 12.08.1995

accepted on the recommendation of
Prof. Nicola A. Spaldin
Prof. Pietro Gambardella
Prof. Ulrich Zülicke

2024

"I am not young enough to know everything"

Oscar Wilde

Abstract

In this thesis, I investigate corundum-structured transition metal oxides, specifically Cr_2O_3, α-Fe_2O_3, and their heterostructures. By examining their similarities and differences, I explore the influence of local symmetry and magnetic ordering on their properties. Using the presence of hidden magnetic multipoles as a guide, we find as of yet unknown (anti-)magnetoelectric effects in both Cr_2O_3 and α-Fe_2O_3 and provide a route for manipulating the non-relativistic spin splitting in α-Fe_2O_3, showing that the presence of higher-order magnetic multipoles gives rise to several magnetic effects. We also resolve a long-standing debate regarding the correlation between the sign of the magnetoelectric effect in Cr_2O_3 and its antiferromagnetic domains and discover complex magnetic ground states in heterostructures of the two materials. This research elucidates the relationship between symmetry, magnetic multipoles, and phenomena such as magnetoelectric effects, non-relativistic spin splitting, and interface-dependent magnetic ordering. The distinct behaviors of Cr_2O_3 and α-Fe_2O_3 result from a difference in global symmetries, caused by their different antiferromagnetic orderings. I investigate these compounds and their properties with a combination of symmetry analysis, density functional theory (DFT) simulations and spin dynamics techniques, using effective Hamiltonian models with parameters determined by DFT for the latter. The magnetic multipoles, which form a hidden order, are extracted from DFT calculations of the charge density, and we associate them with different magnetoelectric effects and spin splitting of the electronic bands. First, employing symmetry arguments and DFT calculations, I investigate different magnetoelectric behaviors of the prototypical magnetoelectric Cr_2O_3 and centrosymmetric α-Fe_2O_3, and the connection with a hidden order of magnetic multipoles. We discuss the relation between a ferroic ordering of magnetic quadrupoles and the net linear magnetoelectric effect. Subsequently, we determine the symmetry allowed quadrupoles on the ionic sites in these compounds, and calculate them using DFT. We show the presence of antiferroically ordered magnetic quadrupoles in both Cr_2O_3 and α-Fe_2O_3. As a consequence, we predict antimagnetoelectric effects, in which local magnetic dipole moments are induced in opposite directions under the application of a uniform external electric field, thus creating an additional antiferromagnetic ordering. We confirm the predicted induced moments using first-principles calculations and show that there are second-order magnetoelectric effects as well, which we associate with the ordering of magnetic octupoles in both materials. Our results demonstrate the presence of hidden magnetic multipoles leads to local linear magnetoelectric responses, even in centrosymmetric magnetic materials, where a net bulk linear magnetoelectric effect is forbidden by symmetry. We outline the symmetry requirements for such local magnetoelectric responses, demonstrating the applicability to other materials. This expansion broadens the class of materials exhibiting magnetoelectric-type couplings and

highlights the utility of magnetic multipoles in predicting various magnetoelectric responses. Additionally, in a collaborative work on Cr_2O_3, we perform DFT calculations of the net magnetoelectric effect and a comprehensive reevaluation of experimental and computational literature to resolve the longstanding debate regarding the sign of the linear magnetoelectric effect and its relation to the antiferromagnetic domains. We find agreement between computations performed across a range of DFT codes and parameters, as well as with four earlier experimental investigations, and provide the community with a reference work. Further exploration of the magnetic multipoles establishes a connection with non-relativistic spin splitting in α-Fe_2O_3. We show that, below its Morin transition, there is a ferroic ordering of rank-5 magnetic triakontadipoles on the Fe ions in α-Fe_2O_3. This is the lowest-order magnetic multipole to be ordered ferroically in the absence of spin-orbit coupling. By altering the sign, arrangement, and magnitude of these magnetic triakontadipoles, we demonstrate that their ferroic ordering is the origin of the g-wave non-relativistic spin splitting in α-Fe_2O_3. Additionally, we discover that the ferroically ordered magnetic triakontadipoles arise from the concurrent antiferroic ordering of charge hexadecapoles and magnetic dipoles, offering a method to control the magnitude and sign of the magnetic triakontadipoles and the spin splitting. Furthermore, we find that both the ferroic ordering of the magnetic triakontadipoles and many spin-split features continue to exist in the weak ferromagnetic phase above the Morin transition temperature. Thus, we enhance the theoretical understanding of spin splitting, contribute to the efforts aimed at harnessing the g-wave spin splitting, and demonstrate that the relevance of the hidden order of the magnetic multipoles goes beyond the magnetoelectric effect. Finally, I calculate magnetism as a function of temperature in heterostructures of Cr_2O_3 and α-Fe_2O_3, using a combination of DFT and spin dynamics techniques. We explore magnetic models of different complexity, both for the individual compounds and the heterostructures. We demonstrate the importance of the dipole-dipole interactions for lowering the effective anisotropy and enabling the Morin transition in α-Fe_2O_3. For the heterostructures, our results reveal ground states that are strongly interface chemistry dependent. In summary, this research advances the understanding of corundum transition-metal magnetism in oxides Cr_2O_3 and α-Fe_2O_3 and their heterostructures, explores the utility of higher-order magnetic multipoles in describing magnetoelectric effects and non-relativistic spin splitting, and paves the way for future investigations into these phenomena.

Zusammenfassung

In dieser Arbeit untersuche ich Übergangsmetalloxide mit Korund-Struktur, insbesondere Cr_2O_3, α-Fe_2O_3 und ihre Heterostrukturen. Indem ich ihre Ähnlichkeiten und Unterschiede untersuche, erforsche ich den Einfluss der lokalen Symmetrie und der magnetischen Ordnung auf ihre Eigenschaften. Dank verborgener magnetischer Multipole finden wir bisher unbekannte (anti-)magnetoelektrische Effekte sowohl in Cr_2O_3 als auch in α-Fe_2O_3 und bieten einen Weg zur Manipulation der nichtrelativistischen Spinaufspaltung in α-Fe_2O_3. So zeigen wir dass das Vorhandensein von magnetischen Multipolen höherer Ordnung zu verschiedenen magnetischen Effekten führt. Wir lösen auch eine seit langem bestehende Debatte über die Korrelation zwischen dem Vorzeichen des magnetoelektrischen Effekten in Cr_2O_3 und seinen antiferromagnetischen Domänen und entdecken komplexe magnetische Grundzustände in Heterostrukturen der beiden Materialien. Diese Forschungsarbeiten erhellen die Beziehung zwischen Symmetrie, magnetischen Multipolen und Phänomenen wie magnetoelektrischen Effekten, nichtrelativistischer Spinaufspaltung und grenzflächenabhängiger magnetischer Ordnung. Die unterschiedlichen antiferromagnetischen Ordnungen in Cr_2O_3 und α-Fe_2O_3 führen zu unterschiedlichen globalen Symmetrien und damit auch zum unterschiedlichen Verhalten der beiden Kristalle. Ich untersuche diese Verbindungen und ihre Eigenschaften mit einer Kombination aus Symmetrieanalyse, Dichtefunktionaltheorie (DFT)-Simulationen und Spindynamik-Techniken, wobei ich für letztere effektive Hamilton-Modelle mit Parametern aus DFT-Berechnungen verwende. Die magnetischen Multipole, welche eine versteckte Ordnung bilden, werden aus DFT-Berechnungen der Ladungsdichte extrahiert, und mit verschiedenen magnetoelektrische Effekten und der Spin-Aufspaltung der elektronischen Bänder assoziiert. Zunächst untersuche ich mit Hilfe von Symmetrieargumenten und DFT-Berechnungen das unterschiedliche magnetoelektrische Verhalten des prototypischen magnetoelektrischen Cr_2O_3 und des zentrosymmetrischen α-Fe_2O_3 sowie dessen Zusammenhang mit einer verborgenen Ordnung magnetischer Multipole. Wir erörtern den Zusammenhang zwischen einer ferroischen Ordnung magnetischer Quadrupole und dem linearen gesamten magnetoelektrischen Effekt. Anschließend bestimmen wir die symmetrisch zulässigen Quadrupole auf der Ionen in diesen Verbindungen und berechnen sie mit DFT. Wir zeigen dass antiferroisch geordneten magnetischen Quadrupolen sowohl in Cr_2O_3 als auch in α-Fe_2O_3 vorhanden sind. Somit sagen wir antimagnetoelektrische Effekte voraus, bei denen lokale magnetische Dipolmomente beim Anlegen eines gleichmäßigen, von außen angelegten elektrischen Feldes in einander entgegengesetzten Richtungen induziert werden und die somit eine zusätzliche antiferromagnetische Ordnung kreieren. Wir bestätigen die vorhergesagten induzierten Momente durch *ab initio* Berechnungen und zeigen, dass es auch magnetoelektrische Effekte zweiter Ordnung gibt, die wir mit der Anordnung der magnetischen Oktupole in beiden

Materialien in Verbindung bringen. Unsere Ergebnisse zeigen, dass das Vorhandensein versteckter magnetischer Multipole zu lokalen linearen magnetoelektrischen Reaktionen führt. Diese linearen magnetoelektrischen Reaktionen sind sogar in zentrosymmetrischen magnetischen Materialien, in denen ein linearer gesamter magnetoelektrischer Effekt durch Symmetrie verboten ist, vorhanden. Wir beschreiben die Symmetrieanforderungen für solche lokalen magnetoelektrischen Reaktionen und zeigen die Anwendbarkeit auf andere Materialien. Dadurch erweitern wir die Klasse der Materialien, die magnetoelektrische Kopplungen aufweisen und unterstreichen zusätzlich den Nutzen von magnetischen Multipolen bei der Vorhersage verschiedener magnetoelektrischer Reaktionen. Darüber hinaus führen wir in einer kollaborativen Arbeit an Cr_2O_3 DFT-Berechnungen des gesamtes magnetoelektrisches Effekts und eine umfassende Neubewertung der experimentellen und rechnergestützten Literatur durch, um die langjährige Debatte über das Vorzeichen des linearen magnetoelektrische Effekts und seine Beziehung zu den antiferromagnetischen Domänen zu klären. Wir finden eine Übereinstimmung zwischen den Berechnungen, die mit einer Reihe von DFT-Codes und Parametern durchgeführt wurden, sowie mit vier früheren experimentellen Untersuchungen und stellen der Gemeinschaft ein Referenzwerk zur Verfügung. Eine weitere Untersuchung der magnetischen Multipole stellt einen Zusammenhang mit der nichtrelativistischen Spin-Spaltung in α-Fe_2O_3 her. Wir zeigen, dass es unterhalb des Morin-Übergangs eine ferroische Ordnung der magnetischen Triakontadipole fünfter Stufe bei den Fe-Ionen in α-Fe_2O_3 gibt. Dies ist der magnetische Multipol niedrigster Ordnung, der in Abwesenheit von Spin-Bahn-Kopplung ferroisch geordnet ist. Indem wir das Vorzeichen, die Anordnung und die Größe dieser magnetischen Triakontadipole verändern, zeigen wir, dass ihre ferroische Ordnung zu der nichtrelativistischen g-Wellen-Spinaufspaltung in α-Fe_2O_3 führt. Darüber hinaus entdecken wir, dass die ferroisch geordneten magnetischen Triakontadipole aus der gleichzeitigen antiferroischen Ordnung der Ladungshexadekapole und der magnetischen Dipole entstehen, und so eine Methode zur Kontrolle der Größe und des Vorzeichens der magnetischen Triakontadipole und der Spin-Aufspaltung bietet. Darüber hinaus stellen wir fest, dass sowohl die ferroische Ordnung der magnetischen Triakontadipole als auch viele Spinaufspaltungsmerkmale in der schwachen ferromagnetischen Phase oberhalb der Morin-Übergangstemperatur fortbestehen. Auf diese Weise verbessern wir das theoretische Verständnis der Spinaufspaltung, tragen zu den Bemühungen bei, die g-Wellen-Spinaufspaltung nutzbar zu machen, und zeigen, dass die Bedeutung der verborgenen Ordnung der magnetischen Multipole über den magnetoelektrischen Effekt hinausgeht. Schließlich berechne ich den Magnetismus in Abhängigkeit von der Temperatur in Heterostrukturen aus Cr_2O_3 und α-Fe_2O_3 unter Verwendung einer Kombination aus DFT- und Spindynamik-Methoden. Wir untersuchen magnetische Modelle unterschiedlicher Komplexität, sowohl für die einzelnen Verbindungen als auch für die Heterostrukturen. Wir zeigen die Bedeutung der Dipol-Dipol-Wechselwirkungen für die Verringerung der

effektiven Anisotropie und die Ermöglichung des Morin-Übergangs in α-Fe_2O_3. Für die Heterostrukturen zeigen unsere Ergebnisse eine starke Abhängigkeit der magnetischen Grundzustandsordnung von der Grenzflächenchemie. Zusammenfassend lässt sich sagen, dass diese Forschungsarbeit das Verständnis des Korund-Übergangsmetall-Magnetismus in den Oxiden Cr_2O_3 und α-Fe_2O_3 und ihren Heterostrukturen verbessert, den Nutzen von magnetischen Multipolen höherer Ordnung bei der Beschreibung von ME-Effekten und nichtrelativistischer Spin-Aufspaltung untersucht und den Weg für künftige Untersuchungen dieser Phänomene ebnet.

Acknowledgements

These past 4.5 years I have worked towards my PhD have been very challenging, but luckily I was never alone on this journey. This thesis would not be here without the help and support of many people, and I want to thank all of them sincerely. First of all, I would extend thanks to my PhD Supervisor Nicola, for giving me the opportunity to do a PhD and for all the scientific advice, which I have learned so much from. I greatly admire your ability to communicate the complex topics we work on to audiences of different backgrounds, as I have seen you do in talks and lectures. It is something I aspire to. I also want to thank my second advisor, Pietro, whom I always enjoyed talking with, and whose advice I am grateful for, including teaching me that the restaurant car is a great place to work on an SBB train. Many thanks to Uli for the fun discussions, and for coming all the way from New Zealand to be on the defense panel. Thank you also to Manfred for kindly agreeing to chair the defense. Further thanks go to Claude, for always being happy to advise me when I wandered into his office, and for the interesting conversations on the theory of DFT. Also, I want to thank Susanne very much for taking care of so many of the administrative tasks of the PhD and helping with everything from issues with the health insurance to moving flights, when changes in the conference schedule occurred. Many warm thanks to all my current and former colleagues in the Materials Theory group: Alex, Sophie, Quintin, Viktor, Jaime, Kane, Chiara, Fabrice, Bastien, Ankit, Aria, Marek, Andrea, Tobias, Sayantika, Tara, Alberto, Sophie, Carl, Peter, Luca, Edith, Jonathan and Nora. It has been such a joy working with all of you. Thank you for the advice, chats at the coffee machine, fun dinners, hikes, bike rides, game nights, cake breaks, and so much more! So many of you have become my friends and I hope to continue hanging out in the future. A special thanks to Bastien, Aria, Jonathan and Edith, for being the best office mates, for all the help and fun discussions, and for politely ignoring my awful habit of talking to myself. To Kane, for helping me get to know Cr_2O_3 and teaching me how to do convergence tests. I want to thank you and Yasmin also for the fun dinners, lovely chats and for donating me your tea when you left Switzerland. I can happily report it lasted me until (almost) the end of thesis writing. Tara, my conference roommate, thank you for putting up with me, and even lending me your sleeping bag when I decided to sleep on the floor. It will be weird going to conferences without you. Thank you, Luca and Alberto, for feeding me excellent Italian (and other) food, and continuing to invite the silly Dutch people that fall asleep before dessert. Max and Aria, thank you so much for all the fun trips, laughs, and checking up on me while I was writing this thesis. A big thank you to Edith, for helping me translate the abstract of this thesis into German. Andrea, Sophie, and Sayantika, thank you for the fruitful collaborations and support. I have learned so much from each of you, and you have always made me feel so safe in asking

questions. I also want to thank the excellent students I had the luck of supervising: Mayan, Stefan, Yannick, and David. It was great working with you! Many thanks to my collaborators outside ETH as well: Jian-Rui at EPFL in Lausanne, Eric at the University of Liège, and Eddy and Navid at Institut Laue Langevin in Grenoble. Also a thank you to Michael Fechner at Max-Planck-Institut für Struktur und Dynamik der Materie, for spending quite some time educating me on the finer details of running ELK. I am also very grateful to all the friends I made at ETH outside of the group, of whom I want to specifically name Steven, Julia, Andrea, Yvonne, Ipek, and Yenia. Thank you for all the good times, dinners, and hikes alike. I want to thank all my friends in the Netherlands, starting with all of Kløbβes for welcoming me back with open arms every time I return to Amsterdam, and so many of you for making the trip to visit us in our mountain home. I am happy that my moving 900 km away did not make us lose sight of each other. Special thanks to Els, Rien, Tamar, and Ellen, for calling/writing so many times, and listening to me rant about my calculations not converging. You are good people and probably should not have to put up with that, but I am so grateful that you do. Thank you so much to my family. My parents, possessing Dr. titles yourselves, understand the struggles of doing a PhD, and have been so supportive throughout the whole process. And to Opa, thank you for believing in me, till the end. Finally, Zazo, my heart, thank you for joining me on this mad Swiss adventure and supporting me through lockdowns, illness, and many a night of doubts, when I was not sure I was going to pull this off. Whatever I did to deserve you, it wasn't enough.

Contents

Abstract v

Zusammenfassung vii

Acknowledgements xi

1 Introduction 1
- 1.1 Motivation . . . 1
- 1.2 Overview of the thesis . . . 3
- 1.3 The magnetoelectric effect . . . 5
  - 1.3.1 Phenomenological picture . . . 5
  - 1.3.2 Microscopic origin . . . 7
- 1.4 Multipoles and hidden order . . . 9
  - 1.4.1 Hidden order . . . 9
  - 1.4.2 Multipoles . . . 10

2 Materials and methods 15
- 2.1 Cr_2O_3 and α-Fe_2O_3 . . . 15
  - 2.1.1 General properties . . . 15
  - 2.1.2 Unit cells . . . 16
  - 2.1.3 Magnetic structure and domains . . . 17
- 2.2 Density functional theory . . . 18
  - 2.2.1 Principles of DFT . . . 18
  - 2.2.2 Numerical process . . . 21
  - 2.2.3 DFT+U . . . 24
- 2.3 DFT extensions . . . 25
  - 2.3.1 Magnetoelectric response . . . 25
  - 2.3.2 Multipole calculations . . . 26
- 2.4 Effective Hamiltonian modeling . . . 31
  - 2.4.1 Monte Carlo . . . 32
  - 2.4.2 Atomistic spin dynamics . . . 33

3 Magnetic multipoles and (anti-)magnetoelectric effects 35
- 3.1 Cr_2O_3 and Fe_2O_3 in DFT . . . 36
  - 3.1.1 Exchange-correlation functional and Hubbard U . . . 36
  - 3.1.2 Convergence parameters . . . 37

3.2 Symmetry analysis of Cr_2O_3 and Fe_2O_3 . . . 40
3.2.1 Crystal symmetry group . . . 40
3.2.2 Wyckoff positions . . . 42
3.2.3 Symmetry operations on the positions . . . 45
3.2.4 Symmetry operations on the magnetic dipole moments . . . 46
3.2.5 Symmetry operations on components of the magnetoelectric multipole tensor . . . 49
3.2.5.1 Cr_2O_3 . . . 51
3.2.5.2 Fe_2O_3 . . . 54
3.2.6 Allowed magnetoelectric multipoles . . . 56
3.2.7 Conclusion from the symmetry analysis . . . 58
3.3 Hidden orders and (anti-)magnetoelectric effects in Cr_2O_3 and α-Fe_2O_3 . . . 58
3.3.1 Preface . . . 58
3.3.2 Abstract . . . 61
3.3.3 Paper body . . . 61
3.3.4 Acknowledgments . . . 69
3.3.5 Supplemental material . . . 69
3.3.5.1 Symmetry analysis . . . 69
3.3.5.2 Details of the method to calculate the magnetoelectric response . . . 70
3.3.5.3 Fitting the magnetic response . . . 75
3.3.5.4 DFT parameters details . . . 76
3.3.5.5 Magnetic response of the phonon modes . . . 76
3.3.5.6 Convergence tests . . . 77
3.4 Additional work . . . 82
3.5 Comments . . . 85

4 The sign of the magnetoelectric effect in Cr_2O_3 89
4.1 Spherical neutron polarimetry . . . 89
4.2 Magnetoelectric annealing . . . 91
4.3 On the sign of the linear magnetoelectric coefficient in Cr_2O_3 . . . 91
4.3.1 Preface . . . 91
4.3.2 Abstract . . . 93
4.3.3 Introduction . . . 93
4.3.4 Computational studies . . . 97
4.3.5 Experimental studies . . . 100
4.3.5.1 Spin vs magnetic moment . . . 102
4.3.6 Orientation of the crystal b axis . . . 103
4.3.6.1 Sign of γ . . . 106
4.3.7 Conclusion . . . 107
4.3.8 Acknowledgements . . . 108
4.3.9 Data availability statement . . . 109
4.3.10 Author Contributions . . . 109
4.3.11 Conflict of interest . . . 109
4.3.12 Appendix . . . 109
4.3.12.1 Computational details ELK . . . 109
4.3.12.2 Computational details VASP . . . 110

4.3.12.3 Computational details Quantum Espresso . . . 111
4.3.12.4 Computational details Abinit . . . 111
4.4 Comments and Outlook . . . 112

5 Magnetic multipoles and spin splitting in Fe_2O_3 115
5.1 Spin splitting and magnetic multipoles . . . 116
5.2 Non-relativistic ferromagnetotriakontadipolar order and spin splitting in hematite . . . 118
5.2.1 Preface . . . 118
5.2.2 Abstract . . . 120
5.2.3 Introduction . . . 120
5.2.4 Crystal and magnetic structure of α-Fe_2O_3 and computational methods . . . 121
5.2.5 Results and discussion . . . 123
5.2.5.1 Multipole analysis . . . 123
5.2.5.2 Spin splitting in the band structure of hematite . . . 124
5.2.5.3 Manipulation of magnetic triakontadipole and the resulting spin splitting . . . 126
5.2.5.4 Weakly ferromagnetic phase of α-Fe_2O_3 . . . 130
5.2.6 Summary and Outlook . . . 131
5.2.7 Acknowledgements . . . 132
5.3 Additional work . . . 133
5.3.1 Triakontadipoles and non-relativistic spin splitting with smaller U 133
5.3.2 The Brillouin zone of Fe_2O_3 . . . 134
5.3.3 The k-space representation of the triakontadipoles . . . 134
5.3.4 Multipole components in the high symmetry structure . . . 135
5.4 Comments . . . 136

6 Heterostructures 137
6.1 Oxide interfaces . . . 137
6.2 Cr_2O_3/Fe_2O_3 interfaces . . . 139
6.3 Magnetic interactions . . . 140
6.4 Determining the magnetic parameters . . . 142
6.4.1 Determining the symmetric exchange . . . 142
6.4.2 Determining the single-ion anisotropy . . . 145
6.4.3 Finding the Dzyaloshinskii-Moriya interactions and the two-site anisotropy . . . 147
6.5 Simulating the bulk materials . . . 148
6.5.1 Cr_2O_3 . . . 149
6.5.2 Fe_2O_3 . . . 150
6.5.3 Dipole-dipole interactions . . . 152
6.6 Simulating the heterostructures . . . 154
6.6.1 Electronic properties of the interface . . . 154
6.6.2 Simple model . . . 155
6.6.3 Full set of magnetic interactions . . . 160
6.7 Convergence . . . 164
6.8 Conclusion . . . 165

6.9 Outlook 167

7 Conclusion and Outlook **169**

A Overview of acronyms used in this thesis **173**

B List of publications **175**

C Curriculum Vitae **177**

Bibliography **179**

Chapter 1

Introduction

Owing to their rich chemistry and wide range of properties, transition metal oxides are among the most studied compounds. The intricate interplay between the localized d orbitals of transition metal ions and oxygen ligands gives rise to complex electronic behaviors. Specifically, the arrangement of oxygen ligands surrounding a transition metal ion induces a symmetry reduction, thereby disrupting the degeneracy of the d orbitals—a phenomenon known as crystal field splitting, the nature of which depends on the oxygen coordination. Moreover, the presence of d orbitals contributes to the manifestation of magnetism, introducing an additional layer of complexity. Although the combinations of complex interactions are often not completely understood, they yield a plethora of intriguing phenomena such as magnetoelectricity, phase transitions, and intricate forms of order.

1.1 Motivation

In materials research, simulations play a vital role in unraveling the properties of materials and furthering our understanding of them. Simulations help to decipher the underlying physics behind observed phenomena, forecast novel properties, and indicate methods to manipulate said properties. Unlike in experimental settings, simulations offer the advantage of easily adjusting or disabling interactions or contributions, allowing for a detailed exploration of their impact on a phenomenon. Moreover, simulations can direct experimental endeavors by identifying promising materials for synthesis, based on predicted properties. Conversely, experimental data serve as valuable guides for simulations. The synergy between experimentation and simulation is indispensable for a comprehensive understanding of materials. They complement each other, forming a symbiotic relationship essential for advancing our knowledge of materials.

In this thesis, I employ density functional theory (DFT) simulations to model insulating antiferromagnetic (AFM) transition-metal oxides, namely Cr_2O_3 and α-Fe_2O_3. DFT, falling under the category of *ab initio* or first-principles methods, is directly derived from quantum mechanics, making it theoretically parameter-free. However, practically handling these materials computationally involves some complexity, particularly due to the treatment of d orbitals of the transition metal ions, which necessitates careful consideration of local electron-electron interactions. To address this, I use the DFT+U extension [1]. Furthermore, controlling the convergence of the computational results requires additional convergence parameters.

Moreover, DFT operates under zero-temperature conditions and is limited in its ability to describe large systems and temperature effects. To explore larger systems and temperature-dependent phenomena, I supplement my DFT calculations by incorporating Monte Carlo simulations and atomistic spin dynamics simulations. Here I make use of effective magnetic Hamiltonians, with the parameters extracted from DFT.

The materials under study, Cr_2O_3 and α-Fe_2O_3, are well-established transition-metal oxides, whose properties have been explored both computationally and experimentally. These materials (and their heterostructures) hold promise for various applications, such as catalysts and detectors, owing to their magnetic, catalytic and/or insulating properties [2–4]. Furthermore, both materials exhibit AFM properties and have garnered interest for spintronics [5, 6]. The thesis aims to explore the properties of Cr_2O_3 and α-Fe_2O_3 further, both by searching for novel properties, and by enhancing understanding of known properties.

Despite their similarities, such as sharing the hexagonal corundum crystal structure, consisting of only two elements, with the same conformal charges on the ions (Cr^{3+}, Fe^{3+} and O^{2-}), and having comparable band gaps ($\sim$ 3 and $\sim$2 eV) [7–11], the transition-metal ions in Cr_2O_3 and α-Fe_2O_3 differ in orbital fillings (d^3 versus d^5), resulting in distinct AFM orderings [12]. The symmetry of the crystal structure is important, as it places relatively few restrictions on the local environment of the transition-metal ions. The difference in the AFM ordering is also important, as it results in distinct global symmetries in the two compounds. This difference in global symmetry and similarity in local symmetries influence various aspects, including magnetoelectric (ME) responses, magnetic band structures, and magnetism at interfaces.

Specifically, the inversion symmetry breaking magnetic ordering in Cr_2O_3 permits a net linear ME effect [13, 14], which is associated with ME multipoles and which is indicative of local coupling between electric and magnetic degrees of freedom [15]. Conversely, the preserved inversion symmetry in α-Fe_2O_3 results in non-relativistic spin splitting (NRSS), a phenomenon that was recently termed altermagnetism [16, 17].

In this work, we aim to clarify the interplay between magnetism and electric charge in both materials, understand the role of local and global symmetry and explore the presence of ME multipoles and associated (local) ME effects. We also seek to understand the NRSS in α-Fe_2O_3, both from a symmetry perspective, as well as by associating it with a ferroic ordering of higher-order multipoles. Finally, we seek to understand the effects of the difference in AFM ordering when we combine the materials. Oxide interfaces have attracted attention due to the occurrence of new phenomena, which are absent in the bulk compounds [18]. As our materials have different AFM ordering, we may expect interesting effects to occur when we make interfaces of the two.

1.2 Overview of the thesis

The results of this thesis can be divided into four topics; the ME multipoles and the local ME effects in Cr_2O_3 and α-Fe_2O_3 [19], the sign of the linear ME effect in Cr_2O_3 [20], the NRSS in α-Fe_2O_3, and the magnetism of the Cr_2O_3/α-Fe_2O_3 interface.

The thesis is structured as follows. First, in the remainder of this chapter, I discuss the background of the ME effect and higher-order magnetic multipoles. This includes a historical overview, the phenomenology of the ME effect, its relationship with symmetry, and the underlying microscopic mechanisms. Additionally, I explore how these higher-order magnetic multipoles are derived and explain their connection to different orders of the ME effect.

Moving on to Chapter 2, I provide a detailed introduction to the two materials, Cr_2O_3 and α-Fe_2O_3, along with a discussion on the computational methods employed. In Section 2.1, I cover some fundamental properties of both compounds, their unit cells, and their symmetries. Next, I give a conceptual overview of DFT and the DFT+U method. I also outline our approach to calculating electric and magnetic multipoles using DFT. Finally, I discuss effective Hamiltonian modeling as well as the use of Monte Carlo and atomistic spin dynamics.

I begin Chapter 3 by explaining our description of Cr_2O_3 and α-Fe_2O_3 within DFT, detailing our choices for various DFT parameters. I then analyze the symmetry of both materials and demonstrate how it restricts the shape of (local) ME tensor, and local ME multipole tensor. Subsequently, I present our calculations of these ME multipole components and corresponding responses with DFT, including magnetic octupoles and second-order ME effects. Additionally, I discuss our extensive convergence calculations and give additional details on the method for calculating the ME response, specifically the extension to include the second-order effect. I expand upon this work in Section 3.4,

by providing a complete overview of the ordering of the non-zero magnetic multipoles up to fifth order and discussing the calculation of a net third-order ME effect in Cr_2O_3. Finally, I address several open questions and consider some future research directions.

Chapter 4 focuses on determining the sign of the ME effect in Cr_2O_3. Starting from the multipole calculations, I introduce the connection between the sign of the net linear ME response in Cr_2O_3 and the AFM domain state. I also shortly discuss spherical neutron polarimetry as an experimental technique for distinguishing AFM domains. Afterward, I present our attempt at clarifying this relationship between the sign of the net linear ME effect in Cr_2O_3 and its AFM domains. We review previous DFT studies, present our calculations, and reanalyze spherical neutron polarimetry experiments to seek consensus between theoretical and experimental results. Finally, I address the spread in magnitude of the calculated linear ME tensor.

In the subsequent chapter, I shift the focus to α-Fe_2O_3 in the absence of spin-orbit coupling (SOC). Beginning with an overview of NRSS and altermagnetism, I discuss symmetry considerations, why α-Fe_2O_3 is expected to show g-wave altermagnetism, and how spin splitting can be related to ferroic ordering of magnetic multipoles. I subsequently present our investigation of ferroically ordered magnetic triakontadipoles and their relation to spin splitting in α-Fe_2O_3. Additionally, I expand on the method used to manipulate the magnetic triakontadipoles, and the relation with the charge hexadecapole. I end Chapter 5 by addressing some open questions regarding g-wave symmetry and altermagnetism in α-Fe_2O_3.

Chapter 6 delves into the magnetism of the Cr_2O_3/α-Fe_2O_3 interface. I begin by motivating the study of interfaces and explain how we constructed the interfaces we examined. Next, I discuss the extraction of DFT parameters and compare them to literature values, from both computational and experimental sources. I present a simple Hamiltonian model, with only Heisenberg exchange and single-ion anisotropy, and a more complicated model, which includes tensorial exchange and dipole-dipole interactions. I evaluate the models' description of the individual compounds, looking at temperature evolution, the Néel temperature, the Morin transition, and the ground state magnetic ordering and orientation. Next, I present the results for the Cr_2O_3/α-Fe_2O_3 interface, while comparing the two models. Finally, I discuss the convergence parameters and present some future research directions.

In the concluding chapter, Chapter 7, I summarize the key findings and emphasize some of the previously outlined opportunities for future research.

1.3 The magnetoelectric effect

The ME effect, in its most general definition, indicates any coupling between the magnetic and electric properties of a material. The first reported discovery of such a coupling was the measurement of an induced magnetization in a dielectric material that was moving through an externally applied electric field. This was shown by W. C. Röntgen in 1888 for both glass and rubber disks between two capacitor plates [21]. Subsequently, P. Curie proposed in 1894 that there must be materials that show a magnetization upon the application of an electric field without the necessity to move them, they show this effect intrinsically [22]. The term 'magnetoelectric' was consequently proposed by P. Debye in 1926 [23]. In this thesis, I will use the general term 'magnetoelectric effect' specifically to mean an intrinsic ME effect. Thirty-three years after the term was coined, I. Dzyaloshinkii proposed the first material candidate for the intrinsic linear ME effect, based on symmetry arguments: Cr_2O_3 [13]. A year later, in 1960, D. N. Astrov confirmed this prediction by measuring the linear ME coefficient in this material [14].

In recent times, ME materials have garnered considerable attention, due to the coupling of electric and magnetic degrees of freedom mentioned above. This connection between electricity and magnetism is interesting both from a fundamental physics perspective as well as for practical uses [24, 25]. Various applications have been suggested, such as low-energy memory devices, sensors, and transistors [26, 27]. However, the broader implementation of these applications has been hampered by the relatively small magnitude of the observed effects [28]. To make better use of these materials, we need a clearer understanding of how ME phenomena work and their associated effects. In this Section, I will introduce the ME effect, its phenomenology, the role symmetry plays, and the microscopic mechanisms from which it originates.

1.3.1 Phenomenological picture

A material shows an ME effect, when upon the application of an electric field, a (change in) magnetization is induced, or vice-versa, the application of a magnetic field induces a (change in) polarization [13] (Figure 1.1).

Using Landau theory, we can understand some of the requirements for such an ME effect. Starting with the free energy (F) for a material with arbitrary symmetry, we can expand simultaneously in terms of both an electric ($\boldsymbol{\mathcal{E}}$) and a magnetic ($\boldsymbol{\mathcal{H}}$) field [29]:

FIGURE 1.1: Visualization of the magnetoelectric effect, where an electric field induces a magnetization (M) and a magnetic field induces a polarization (P).

$$F(\boldsymbol{\mathcal{E}},\boldsymbol{\mathcal{H}}) = F_0 - P_i^0\mathcal{E}_i - M_i^0\mathcal{H}_i - \frac{1}{2}\chi_{ij}^e\mathcal{E}_i\mathcal{E}_j - \frac{1}{2}\chi_{ij}^m\mathcal{H}_i\mathcal{H}_j - \alpha_{ij}\mathcal{E}_i\mathcal{H}_j - \frac{1}{2}\beta_{ijk}\mathcal{E}_i\mathcal{H}_j\mathcal{H}_k - \frac{1}{2}\gamma_{ijk}\mathcal{H}_i\mathcal{E}_j\mathcal{E}_k - \frac{1}{2}\chi_{ijk}^{e(2)}\mathcal{E}_i\mathcal{E}_j\mathcal{E}_k - \frac{1}{2}\chi_{ijk}^{m(2)}\mathcal{H}_i\mathcal{H}_j\mathcal{H}_k + \ldots \quad , \tag{1.1}$$

with P_i^0 and M_i^0 the spontaneous polarization and magnetization, $\chi_{ij}^e = \epsilon_0\epsilon_{ij}$ the electric susceptibility and $\chi_{ij}^m = \mu_0\mu_{ij}$ the magnetic susceptibility, where ϵ_0 and μ_0 are the vacuum permittivity and magnetic permeability, respectively, and ϵ_{ij} and μ_{ij} are the relative permittivity and permeability. α_{ij} represents the linear ME tensor, β_{ijk} and γ_{ijk} the second-order ME tensors, and $\chi_{ijk}^{e(2)}$ and $\chi_{ijk}^{m(2)}$ the quadratic electric and magnetic susceptibilities. Finally, the i, j, k indices each loop over the Cartesian directions, and repeated indices indicate summation.

We can differentiate this expression for the free energy to obtain the polarization and magnetization [26]:

$$\begin{aligned} P_i(\boldsymbol{\mathcal{E}},\boldsymbol{\mathcal{H}}) &= -\frac{\partial F}{\partial \mathcal{E}_i} \\ &= P_i^0 + \frac{1}{2}\chi_{ij}^e\mathcal{E}_j + \underbrace{\alpha_{ij}\mathcal{H}_j}_{\text{linear ME}} + \underbrace{\frac{1}{2}\beta_{ijk}\mathcal{H}_j\mathcal{H}_k + \frac{1}{2}\gamma_{kji}\mathcal{H}_k\mathcal{E}_j}_{\text{second-order ME}} + \frac{1}{2}\chi_{ijk}^{e(2)}\mathcal{E}_j\mathcal{E}_k + \ldots \quad , \end{aligned} \tag{1.2}$$

$$\begin{aligned} M_i(\boldsymbol{\mathcal{E}},\boldsymbol{\mathcal{H}}) &= -\frac{\partial F}{\partial \mathcal{H}_i} \\ &= M_i^0 + \frac{1}{2}\chi_{ij}^m\mathcal{H}_j + \underbrace{\alpha_{ji}\mathcal{E}_j}_{\text{linear ME}} + \underbrace{\frac{1}{2}\beta_{kji}\mathcal{E}_k\mathcal{H}_j + \frac{1}{2}\gamma_{ijk}\mathcal{E}_j\mathcal{E}_k}_{\text{second-order ME}} + \frac{1}{2}\chi_{ijk}^{m(2)}\mathcal{H}_j\mathcal{H}_k + \ldots \quad , \end{aligned} \tag{1.3}$$

where we have indicated the contributions that come from the linear and second-order ME effects.

Most research has focused on the linear ME effect, which tends to be larger than the second-order one, but has strict symmetry requirements. Going back to Eq. 1.1, looking at the term containing α we see that only materials with broken time-reversal *and* broken space-inversion symmetry can support a non-zero α. If time-reversal symmetry is preserved that means that $F(\boldsymbol{\mathcal{E}}, \boldsymbol{\mathcal{H}}) = F(\boldsymbol{\mathcal{E}}, -\boldsymbol{\mathcal{H}})$ and when space-inversion symmetry is preserved $F(\boldsymbol{\mathcal{E}}, \boldsymbol{\mathcal{H}}) = F(-\boldsymbol{\mathcal{E}}, \boldsymbol{\mathcal{H}})$. Both of these requirements lead to $\alpha = -\alpha = 0$. Only if both symmetries are broken, can α be non-zero. Using the same arguments, we see that for each of the two components of the second-order effect, only one of these symmetries has to be broken. To be specific, space-inversion symmetry needs to be broken to have a non-zero β, and time-reversal symmetry needs to be broken to have a non-zero γ.

When the materials in question have no spontaneous polarization or magnetization ($P_i^0 = M_i^0 = 0$), as is the case for the materials discussed in this thesis, we can simply Eqs. 1.2 and 1.3. Furthermore, when only an external electric field $\boldsymbol{\mathcal{E}}$ is applied and a magnetic field is absent, these equations reduce to:

$$P_i(\boldsymbol{\mathcal{E}}) = \frac{1}{2}\chi^{e}_{ij}\mathcal{E}_j + \frac{1}{2}\chi^{e(2)}_{ijk}\mathcal{E}_j\mathcal{E}_k + O(\mathcal{E}^3), \tag{1.4}$$

$$M_i(\boldsymbol{\mathcal{E}}) = \alpha_{ji}\mathcal{E}_j + \frac{1}{2}\gamma_{ijk}\mathcal{E}_j\mathcal{E}_k + O(\mathcal{E}^3). \tag{1.5}$$

The effect under an applied electric field is what we will mostly focus on in this thesis when discussing the ME effect; we will determine the induced magnetization as a response to an electric field, to determine the type of ME response.[1]

1.3.2 Microscopic origin

Although the phenomenological picture is useful for determining the simple symmetry requirements for each order of the ME effect, it does not tell us about the microscopic materials physics from which the observed macroscopic effects originate. These microscopic origins give us insight into the physics of each material and help determine properties like temperature dependence [30].

[1] rather than the reverse: determining an electric polarization as a response to an applied magnetic field.

Several different microscopic origins can give rise to ME effects. As we focus on the $\mathcal{E}$-field induced ME effect, i.e., the induced magnetization under the application of an electric field, we discuss here the microscopic changes in a material that can be $\mathcal{E}$ induced and can lead to a change in the magnetization [29].

When an electric field is applied, the positions of the ions shift with respect to one another, as the positively and negatively charged ions are pulled in different directions. Furthermore, the shape of the electronic wavefunctions is modified, as the electrons are pulled in the opposite direction of the positively charged atomic core. Both of these changes have consequences for the local magnetic environment [30].

To begin with, the single-ion anisotropy is sensitive to changes in the relative positions of the metal ions and their ligands, and the symmetry of the arrangement. Changes to the anisotropy cause changes to the magnetic easy axis and can lead to canting of the magnetic moments. Secondly, both the change in atomic positions and the modification of the shape of the electronic wavefunctions can alter the orbital overlap. Both the symmetric and antisymmetric parts of the exchange and the superexchange are sensitive to the orbital overlap, and can thus be changed, leading to reoriention of the magnetic moments. Furthermore, the Zeeman energy can be adjusted, either due to changes in the crystal field (symmetry) caused by the change in atomic positions, or due to changes in the electronic wavefunctions, both of which can change the g tensor. These changes can in turn result in changes in both the magnitude and the direction of the magnetic moment. Finally, the dipole-dipole interactions can be modified if the electric field induces a piezoelectric distortion, which gives is non-uniform displacements of the magnetic ions. As the dipole-dipole interactions influence the effective anisotropy, this can lead to canting of the magnetic moments as well.

Each component of the ME effect can originate from different (combinations of) induced microscopic changes. For example, in Cr_2O_3, one of the materials studied in this thesis, there are two independent components to the linear ME effect. The first component is the diagonal in-plane component, i.e., $\alpha_{xx} = \alpha_{yy}$. This component is also called $\alpha_\perp$, because the effect occurs perpendicular to the magnetic easy axis. $\alpha_\perp$ is believed to be caused mostly by a change in the single-ion anisotropy [31]. The second component is the out-of-plane component, α_{zz}. This component is also called $\alpha_\parallel$ because the effect occurs parallel to the magnetic easy axis, and has different causes depending on the temperature. At low temperatures, the change in the g factor is believed to be responsible, while at high temperatures the change in the exchange energy dominates [31, 32]. The important role of the exchange energy mechanism was further highlighted in a computational study by Mostovoy *et al.* [33], where the temperature dependence of $\alpha_\parallel$ in Cr_2O_3 was calculated based on the Heisenberg exchange mechanism. They find quantitative agreement with

the experimental measurements, confirming that the exchange mechanism plays a vital role in mediating this component of the ME response. They furthermore stress that $\alpha_{\parallel}$ peaks at higher temperatures because the spin fluctuations are largest there. Because they have different microscopic origins, the temperature dependence of $\alpha_{\perp}$ and $\alpha_{\parallel}$ is quite different [14]. We will discuss this in more detail in Chapter 4.

It is important to note that some of the microscopic origins mentioned above depend on SOC while others do not. For example, without SOC, the magnetic and spatial directions are not coupled, and there is no single-ion anisotropy or antisymmetric exchange. Components originating from these microscopic mechanisms will therefore be absent. However, the Heisenberg exchange is not SOC-dependent, so components mediated through this mechanism will be independent of SOC as well.

1.4 Multipoles and hidden order

In this thesis, we will relate hidden orders to two distinct measurable effects. In this section, I will explain what I mean by hidden order and go into detail about the specific orders that will be relevant: higher-order magnetic multipoles.

1.4.1 Hidden order

One of the most well-known examples of hidden order is antiferromagnetism. Coined by Néel in 1936, it describes the antiparallel alignment of magnetic moments, as opposed to the parallel alignment that occurs with ferromagnetism. Antiferromagnetism was proposed as an explanation for the peaks in the temperature dependence of the magnetic susceptibility and the specific heat in MnO [34]. Such peaks were known to coincide with paramagnetic to ferromagnetic transitions, yet the characteristic signs of a ferromagnetic phase, like a net magnetic moment, were absent in this compound. At the time, there was no way to experimentally confirm the proposed AFM ordering, which made it a hidden order.

Another instance of hidden order occurs when an order emerges from the coupling of lower orders, though those lower orders are absent or arranged antiferroically. This phenomenon is evident in Cr_2O_3. Examining the unit cell depicted in Figure 2.1a and b, no net polarization or magnetization is apparent. There is no polarization due to the crystal structure's inversion symmetry, and no net magnetization due to AFM ordering. However, the inner product of position and magnetic moment, $\langle \sum_i r_i \cdot m_i \rangle$, remains nonzero, representing a ferroic order concealed behind the absence of a net electric or magnetic dipole moment.

Various other forms of hidden orders exist, including those based on electric or magnetic multipoles. For instance, the 17.5 K phase transition in URu_2Si is not yet understood and has been associated with proposed hidden orders encompassing higher-order charge multipoles, from second order (charge quadrupoles) to fifth order (charge triakontadipoles), along with different spin-based orders like distinct spin density waves and a nematic spin state [35]. While recent experimental findings lean towards an electric rather than magnetic explanation for this transition, the puzzle remains unsolved [36]. On the other hand, in Mn_3Sn, the anomalous Hall effect suggests the presence of hidden order linked to magnetic octupoles. These octupoles have recently been observed using X-ray magnetic circular dichroism [37].

As mentioned, our focus here will be on exploring various orders of magnetic multipoles as hidden order phenomena.

1.4.2 Multipoles

Multipoles as a concept are applied in many different fields of physics, but perhaps most famously in electrodynamics. It is understood that a general charge distribution can be described by a sum over the multipolar contributions: 0th-order behavior is described by the monopolar contribution (total charge), up to linear order by including the dipolar contribution, etc. A similar expansion can be done for magnetization density (e.g., a distribution of magnetic dipoles), where there is, of course, no monopolar contribution.

It was shown that the linear ME effect can be linked to an ordering of 'so-called' ME multipoles [15, 38–41]. These multipoles are, in fact, magnetic quadrupoles with odd parity and the same symmetry as the ME effect, as they consist of terms that combine position r and magnetization μ. We can see them arise most easily from the interaction of an applied magnetic field ($\boldsymbol{\mathcal{H}}$) with a spatially varying magnetization density $\boldsymbol{\mu}(\boldsymbol{r})$. In this case, the interaction energy E_{int} takes the following form [15]:

$$E_{int} = -\int \boldsymbol{\mu}(\boldsymbol{r}) \cdot \boldsymbol{\mathcal{H}}(\boldsymbol{r}) d^3\boldsymbol{r} \tag{1.6}$$

$$= -\underbrace{\int \boldsymbol{\mu}(\boldsymbol{r}) \cdot \boldsymbol{\mathcal{H}}(0) d^3\boldsymbol{r}}_{\text{dipole contribution}} - \underbrace{\int r_i \mu_j(\boldsymbol{r}) \partial_i H_j(0) d^3\boldsymbol{r}}_{\text{quadrupole contribution}} - \underbrace{\int r_i r_j \mu_k(\boldsymbol{r}) \partial_i \partial_j H_k(0) d^3\boldsymbol{r}}_{\text{octupole contribution}} - \ldots \quad . \tag{1.7}$$

Here we see the regular magnetic dipole contribution ($\sim \boldsymbol{\mu}$), plus additional quadrupole ($\sim \boldsymbol{\mu r}$) and octupole terms ($\sim \boldsymbol{\mu r}^2$). Although not written here, there are even higher-order contributions, such as the magnetic hexadecapole ($\sim \boldsymbol{\mu r}^3$) and the magnetic triakontadipole ($\sim \boldsymbol{\mu r}^4$), etc. Each multipole term describes the interaction of these multipoles with the appropriate derivatives of the field. Focusing on the magnetic quadrupoles, we can now define the magnetic quadrupole tensor or ME multipole tensor as [15] :

$$\mathcal{M}_{ij} = \int r_i \mu_j(\boldsymbol{r}) d^3\boldsymbol{r}. \tag{1.8}$$

Each multipole term describes the interaction of these multipoles with the appropriate derivatives of the field. Focusing on the magnetic quadrupoles, we can now define the magnetic quadrupole tensor or ME multipole tensor as [15] : This ME multipole tensor $\mathcal{M}$ is a Cartesian tensor and can be directly related to the linear ME tensor α. We can identify which element of the multipole tensor corresponds to which component of the linear ME effect by where it appears in the tensor. We can also split the tensor into its spherically irreducible parts. This is useful for visualization and for understanding the behavior under rotation operations, as the different irreducible component span different irreducible invariant subspaces of SO(3). We will also use this decomposition when calculating the components using DFT. Following the usual decomposition of a 3×3 matrix, i.e., $\mathbf{3} \otimes \mathbf{3} = \mathbf{1} \oplus \mathbf{3} \oplus \mathbf{5}$) [42], the three irreducible components of the ME multipole tensor are [15] :

$$a = \frac{1}{3}\mathcal{M}_{ii} = \frac{1}{3}\int \boldsymbol{r} \cdot \boldsymbol{\mu}(\boldsymbol{r}) d^3\boldsymbol{r}, \tag{1.9}$$

$$t_i = \frac{1}{2}\epsilon_{ijk}\mathcal{M}_{ji} = \frac{1}{2}\int [\boldsymbol{r} \times \boldsymbol{\mu}(\boldsymbol{r})]_i \, d^3\boldsymbol{r}, \tag{1.10}$$

$$q_{ij} = \frac{1}{2}\left(\mathcal{M}_{ij} + \mathcal{M}_{ji} - \frac{2}{3}\delta_{ij}\mathcal{M}_{ii}\right) \tag{1.11}$$

$$= \frac{1}{2}\int \left[r_i \mu_j(\boldsymbol{r}) + r_j \mu_i(\boldsymbol{r}) - \frac{2}{3}\delta_{ij}\boldsymbol{r} \cdot \boldsymbol{\mu}(\boldsymbol{r})\right] d^3\boldsymbol{r}, \tag{1.12}$$

where a represents the trace of $\mathcal{M}$ and is a scalar. It has also been called the ME monopole. Yet, it is not a magnetic monopole, which would appear in the 0th-order contribution to the multipole expansion of Eq. 1.7, whereas the ME monopole comes from the second-order quadrupole term. $\boldsymbol{t}$ is called the toroidal moment, is a vector quantity, and constitutes the completely antisymmetric part of the tensor. Finally, q is the symmetric traceless part, and a tensor. This component is simply called the

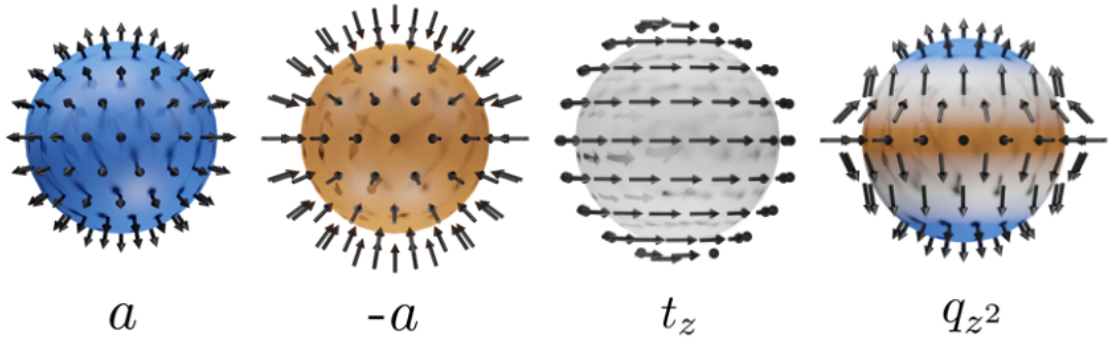

FIGURE 1.2: Visualization of several magnetoelectric multipoles. From left, to right: a positive monopole (a), a negative monopole (a), the z component of the toroidal moment (t_z) and the z^2 component of the quadrupole moment (q_{z^2}). The blue color corresponds to outward-pointing spins and the orange color to inward-pointing spins. White indicates spins parallel to the pictured surface.

quadrupoles (Figure 1.2). I will refer to this component as q, to not confuse it with the full set of magnetoelectric multipoles, as they are all technically magnetic quadrupoles. a, $\boldsymbol{t}$ and q are spherically irreducible tensors of rank 0, 1 and 2 respectively. Separating the Cartesian tensors that describe the multipoles into their spherically irreducible parts will become important in Section 2.3.2, where we discuss the calculation of these multipoles and specifically these spherically irreducible components in our material simulations.

We can also rewrite the tensor in its irreducible parts. As the monopoles a come from the trace of the ME multipole tensor $\mathcal{M}$, they appear on the diagonal only and are associated with a diagonal linear ME effect. The toroidal moments $\boldsymbol{t}$ form the antisymmetric part and thus appear only away from the diagonal. They are linked to off-diagonal linear ME effects [43, 44]. Finally, the quadrupoles are a traceless symmetric tensor with five independent components. q_{xy}, q_{xz}, q_{yz} appear away from the diagonal and contribute to the off-diagonal symmetric components of the linear ME effect. q_{z^2} and $q_{x^2-y^2}$ appear on the diagonal and contribute to the diagonal component of the ME effect. As the tensor is traceless, they have different contributions to each entry on the diagonal, such that the total contribution is traceless. These terms are thus associated with diagonal linear ME effects that are not equal in all directions.

We can further extend the concept of magnetic multipoles by considering the magnetic octupoles. Analogously to the quadrupole case, the magnetic octupole tensor can be defined as follows:

$$\mathcal{M}^{(2)}_{ijk} = \int r_i r_j \mu_k(\boldsymbol{r}) d^3\boldsymbol{r}. \tag{1.13}$$

The components of this tensor can be related to different components of the second-order ME effect, specifically the components described by γ_{ijk} in Eqs. 1.1, 1.2 and 1.3. This follows from a similar argument as before; the magnetic octupole tensor and the second-order ME effect described by γ_{ijk} have the same symmetry [45].

We note here that some of the discussed hidden orders have been observed and some have not, only the effects that they give rise to. The observation of toroidal moments has been reported [46], but no such experimental evidence exists for the ME monopoles, for example. As mentioned above, a ferroic ordering of magnetic octupoles has been observed [37], although not in the context of a second-order ME effect.

Chapter 2

Materials and methods

In this chapter, I will discuss the two materials of interest, Cr_2O_3 and α-Fe_2O_3, describe some general properties and examine their units cells, and symmetries. I will also outline the main computational methods used for the work in this thesis, starting with a short overview of density functional theory (DFT), DFT+U, and the different ways one can use DFT to calculate magnetoelectric (ME) responses. Next, I will discuss the way we determine the values of different charge and magnetic multipoles from the densities obtained from DFT. Finally, I examine extensions to DFT in the form of effective magnetic Hamiltonians, for which we can extract the parameters. We can then use these to model magnetic systems using atomistic spin-dynamics or Monte Carlo, which I also explain.

2.1 Cr_2O_3 and α-Fe_2O_3

This thesis focuses on the study of different aspects of two transition metal oxides, Cr_2O_3 and α-Fe_2O_3. In this section, we will introduce the two compounds.

2.1.1 General properties

Cr_2O_3 and α-Fe_2O_3 are both members of the corundum family. Cr_2O_3 is a chemically simple, binary compound, which crystallizes as a green solid. Despite its chemical simplicity, the physics of this material is quite rich, showing effects such as magnetoelectricity [14, 47] and voltage controllable spin currents [48]. It is an easy axis antiferromagnet below its Néel temperature of 307 K [49], with opposite spin orientation for every nearest neighbor along the magnetization axis [50, 51] (Figure 2.1a).

α-Fe_2O_3 is a similarly simple binary compound, although it is black in appearance. Unlike Cr_2O_3, Fe_2O_3 shows a wide range of crystal structures and magnetic orderings. We will focus on the alpha polymorph α-Fe_2O_3, which has the same crystal structure as Cr_2O_3 [52], and thus we will in the remainder of the text refer to α-Fe_2O_3 simply as Fe_2O_3. Fe_2O_3 is antiferromagnetic (AFM) below its Néel temperature of 960 K, and it has magnetic transition, called the Morin transition around 263 K. Between 263-960 K it is in a canted AFM or weakly ferromagnetic phase, where the spins lie in the plane perpendicular to the low-temperature easy axis. Below 263 K, Fe_2O_3 is in an easy axis AFM phase, with the spins oriented along this magnetic easy axis in a up-down-down-up pattern [53, 54] (Figure 2.1b). In the low-temperature phase, the similarities with Cr_2O_3 are the greatest, but some differences remain. Of course, the magnetic moments on the Fe in Fe_2O_3 are larger than those on the Cr in Cr_2O_3, due to the different filling of the d shell. Also, the unit cell of Fe_2O_3 is slightly larger, giving slightly different bond angles and different inter-atomic distances. Most importantly the AFM ordering is different in both compounds (Figure 2.1a and b). This has important consequences for the symmetry of the materials.

2.1.2 Unit cells

As stated before, both Cr_2O_3 and Fe_2O_3 adopt the corundum crystal structure. There are two common choices of unit cell for this crystal structure, the small 10-atom rhombohedral unit cell (Figure 2.1a and b), the primitive unit cell for this crystal structure, and the larger 30-atom hexagonal unit cell (Figure 2.1c), the conventional unit cell. The hexagonal unit cell is parameterized by the lengths a and c of lattice vectors $\boldsymbol{a}$ and $\boldsymbol{c}$, as the other lattice parameters are fixed by symmetry: $a = |\boldsymbol{a}| = |\boldsymbol{b}|$, $\boldsymbol{c} \perp \boldsymbol{a}$ (and $\boldsymbol{b}$), and the angle between $\boldsymbol{a}$ and $\boldsymbol{b}$ is 120°. The Cartesian axes are conventionally chosen such that $\boldsymbol{z} \parallel \boldsymbol{c}$ and $\boldsymbol{x} \parallel \boldsymbol{a}$.

The rhombohedral unit cell is parameterized by the length of the lattice vector $\boldsymbol{a'}$ and the angle between the lattice vectors α', with the symmetry fixing the other parameters as follows: $|\boldsymbol{a'}| = |\boldsymbol{b'}| = |\boldsymbol{c'}|$ and $\alpha' = \beta' = \gamma'$. The unit cells are related in the following way:

$$\boldsymbol{a'} = \begin{pmatrix} -\frac{a}{2} \\ \frac{a}{2\sqrt{3}} \\ \frac{c}{3} \end{pmatrix}, \ \boldsymbol{b'} = \begin{pmatrix} 0 \\ -\frac{a}{\sqrt{3}} \\ \frac{c}{3} \end{pmatrix}, \text{ and } \boldsymbol{c'} = \begin{pmatrix} \frac{a}{2} \\ \frac{a}{2\sqrt{3}} \\ \frac{c}{3} \end{pmatrix}, \tag{2.1}$$

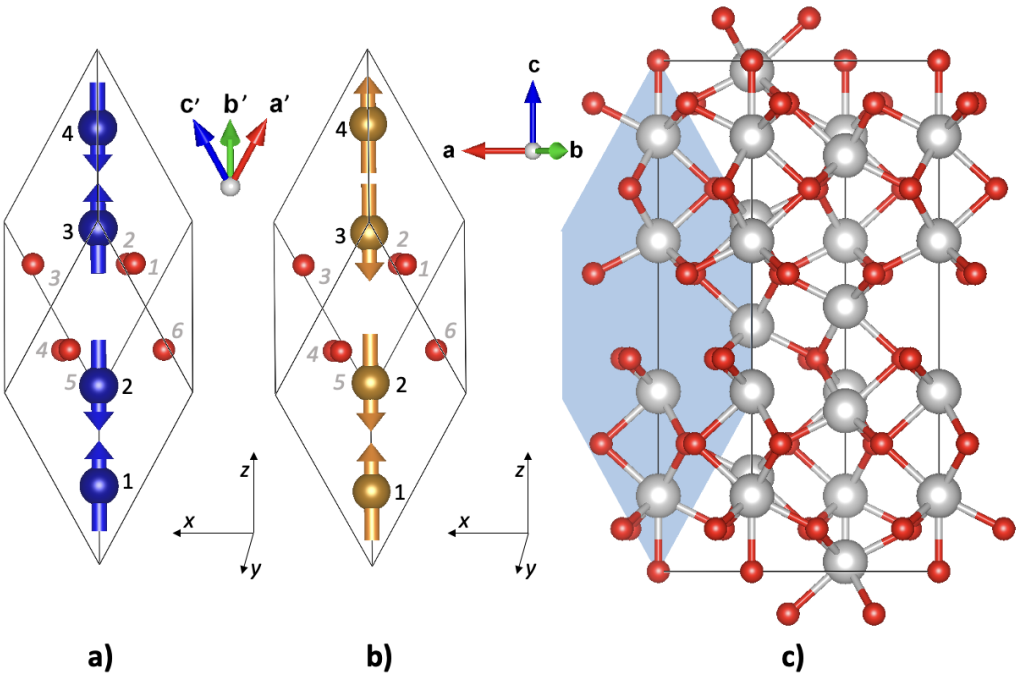

FIGURE 2.1: Unit cells of the corundum structure, with the magnetic order indicated in the primitive cells for Cr_2O_3 (a) and Fe_2O_3 (b) and the primitive cell shape indicated in the conventional cell (c). The chromium (Cr) ions are colored blue (a), the iron (Fe) ions gold (b), a general transition metal (TM) ion silver (c), and the oxygen (O) ions red (a,b,c). Magnetic moments on the Cr and Fe ions are indicated using arrows of the same color as the ion. Cr and Fe ions are numbered in black, and O atoms in gray (a,b). Rhombohedral lattice vectors $\boldsymbol{a'}$, $\boldsymbol{b'}$, and $\boldsymbol{c'}$ are indicated on the top between a) and b), hexagonal vectors $\boldsymbol{a}$, $\boldsymbol{b}$, and $\boldsymbol{c}$ on the top between b) and c) and Cartesian directions on the bottom between a) and b) and b) and c). All magnetic moments are aligned with the magnetic easy axis, which is $\parallel \hat{z}$.

in Cartesian coordinates, with $a = |\boldsymbol{a}|$ and $|\boldsymbol{c}|$. These relations ensure a consistent choice of the Cartesian axes, for example, in both unit cells the z axis is parallel with the AFM easy axis of Cr_2O_3 and Fe_2O_3. This means that in the rhombohedral cell, the Cartesian axes are chosen such that $\boldsymbol{z} \parallel$ rhombohedral [111] and $-\boldsymbol{y} \parallel$ to the projection of $\boldsymbol{b'}$ in the xy plane. We will stick to this choice of Cartesian coordinates throughout.

2.1.3 Magnetic structure and domains

As stated above, at low temperatures both Cr_2O_3 and Fe_2O_3 are easy axis antiferromagnets, albeit with a different pattern in the AFM ordering. Although they are different, both orderings break time-reversal symmetry. This means that both compounds have two distinct AFM domains, which can be transformed into each other by a time-reversal operation (Figure 2.2). These domains are also sometimes called 180° domains, as the magnetic moments in the two domains are equal and opposite, as if all the moments are rotated by 180° about an axis perpendicular to the z axis. We note that these domains

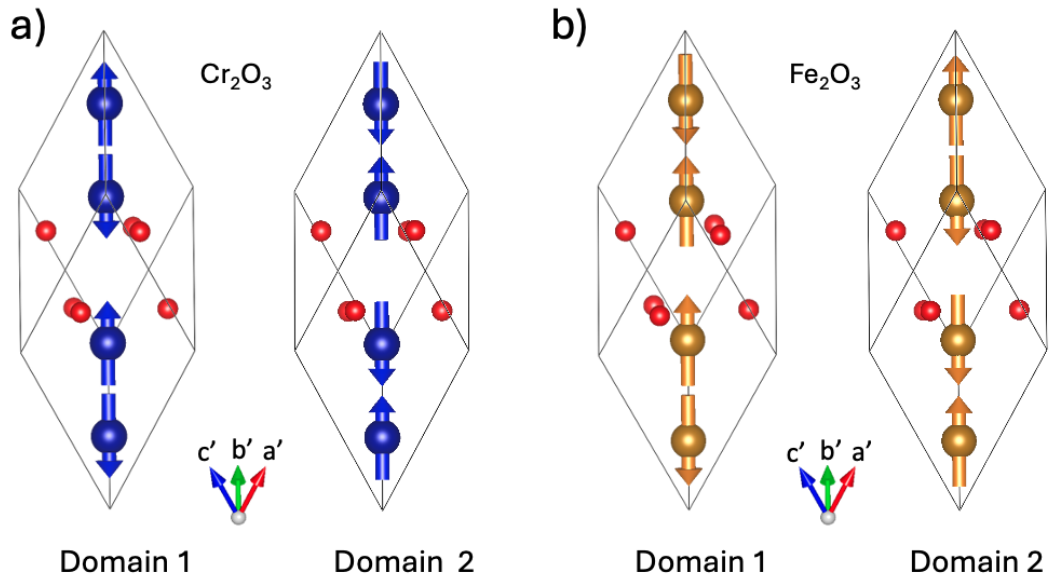

FIGURE 2.2: The two AFM domains for Cr_2O_3 (a) and Fe_2O_3 (b).

are different from 'so-called' configuration domains, where the magnetic ordering breaks a translation symmetry rather than the time-reversal symmetry.

In the bulk, without the application of external fields, these two domains are energy equivalent, although they do give rise to the formation of AFM domains and domain walls. When fields are applied, or when an interface is formed these domains can have different energies. We will see the lifting of this energy equivalence play a role with the sign of the linear ME effect in Cr_2O_3, as well as in the magnetic ordering of heterostructures of Cr_2O_3 and Fe_2O_3.

2.2 Density functional theory

The main method that will be used in this PhD work is density functional theory (DFT). This is a numerical technique used for finding the approximate electronic ground state in solids and molecules, where solving the Schrödinger equation exactly is not an option. There are many great reviews of DFT available, for example [55–60], so our goal here is to discuss the basic concepts which will be relevant for the research discussed in this thesis.

2.2.1 Principles of DFT

DFT is a well-established numerical technique for finding the ground state density of solids and molecules. It was developed in the 1960s as a way to reach an approximate

solution to said ground state when it became clear that finding an exact solution is not possible. It has become one of the most popular first-principles or *ab initio* methods, meaning that it allows the prediction of material properties without input parameters obtained from experiment (in principle).

Let us start with a Hamiltonian, which should, in principle, capture all the physics in a solid or molecule. For a set of N_n nuclei at positions $\boldsymbol{R} = \{\boldsymbol{R}_1, \boldsymbol{R}_2, \ldots, \boldsymbol{R}_{N_n}\}$, and N_e electrons at positions $\boldsymbol{r} = \{\boldsymbol{r}_1, \boldsymbol{r}_2, \ldots, \boldsymbol{r}_{N_e}\}$, the Hamiltonian takes the following form:[1]

$$\begin{aligned}\hat{H} = &\overbrace{-\sum_{\alpha}\frac{\hbar^2}{2M_\alpha}\nabla_\alpha^2}^{\hat{T}_n(\boldsymbol{R})} \overbrace{-\sum_{i}\frac{\hbar^2}{2m_e}\nabla_i^2}^{\hat{T}_e(\boldsymbol{r})} + \overbrace{\frac{e^2}{2}\sum_{\alpha\neq\beta}\frac{Z_\alpha Z_\beta}{|\boldsymbol{R}_\alpha - \boldsymbol{R}_\beta|}}^{\hat{V}_{nn}(\boldsymbol{R})} \\ &+ \underbrace{\frac{e^2}{2}\sum_{i\neq j}\frac{1}{|\boldsymbol{r}_i - \boldsymbol{r}_j|}}_{\hat{V}_{ee}(\boldsymbol{r})} \underbrace{- e^2\sum_{i,\alpha}\frac{Z_\alpha}{|\boldsymbol{R}_\alpha - \boldsymbol{r}_i|}}_{\hat{V}_{ne}(\boldsymbol{R},\boldsymbol{r})},\end{aligned} \tag{2.2}$$

where α and β label the nuclei and i and j label the electrons, m_e and e are the electron mass and charge, M is the mass of the nucleus and Z is the atomic number. The first two terms represent the kinetic energy of the nuclei ($\hat{T}_n(\boldsymbol{R})$) and the electrons ($\hat{T}_e(\boldsymbol{r})$), while the latter terms are the potential energy due to the Coulomb interaction between the nuclei ($\hat{V}_{nn}(\boldsymbol{R})$), the electrons ($\hat{V}_{ee}(\boldsymbol{r})$), and between the nuclei and the electrons ($\hat{V}_{ne}(\boldsymbol{R},\boldsymbol{r})$). With this Hamiltonian, we may attempt to solve the Schrödinger equation:

$$\hat{H}\Psi(\boldsymbol{R},\boldsymbol{r}) = E\Psi(\boldsymbol{R},\boldsymbol{r}), \tag{2.3}$$

with the E the energy corresponding to the wave function $\Psi(\boldsymbol{R},\boldsymbol{r})$. In principle, there should exist a many-body wave function $\Psi(\boldsymbol{R},\boldsymbol{r})$ such that this Schrödinger equation is solved. Yet, finding this solution becomes exponentially complicated with the number of particles, as the position (and hence its derivatives) of each nucleus and electron depends on the position of every other particle (Eq. 2.2). For a general piece of solid we would be dealing with a very large number of particles ($\sim 10^{23}$), making the exact solution completely inaccessible. Now, several steps can be taken to simplify the problem. First, we may apply the adiabatic or Born-Oppenheimer approximation [61]. Here, we decouple the motion of the much heavier, and hence slower, nuclei, from the much lighter, faster

[1] Here we have included only non-relativistic effects, i.e., the nuclei and electrons interact through the Coulomb interaction.

electrons. This leaves us with only the electrons, their interactions, and the potential they experience from the nuclei (i.e., we would lose the $\hat{T}_n(\boldsymbol{R})$ and $\hat{V}_{nn}(\boldsymbol{R})$ terms in Eq. 2.2, while keeping the others). For the amount of electrons in a general piece of solid, this remains an unsolvable problem.

The basis of DFT was lain with the realization by Hohenberg and Kohn, captured in their theorems [62], that the grounds state properties of an electronic system are determined completely by the electronic density $\rho(\boldsymbol{r})$ and that there is a one-to-one correspondence between this election density and the external potential $V_{ext}(\boldsymbol{r})$, i.e., the potential due to the nuclei (and any external fields). The ground state density of the system may be found by minimizing the total energy:

$$E_{tot}[\rho(\boldsymbol{r})] = \int V_{ext}(\boldsymbol{r})\rho(\boldsymbol{r})d^3r + F[\rho(\boldsymbol{r})], \tag{2.4}$$

where $F[\rho(\boldsymbol{r})]$ is some universal (meaning system-independent) functional of the density, and square brackets denote some complicated functional dependence. In this way, we have written our problem as a functional of the density, which is the origin of the name 'density functional theory'. Now, given an external potential $V_{ext}(\boldsymbol{r})$, we no longer need to find the complex many-electron wave function, which depends on the three dimensional position of each of the N_e electrons. Instead, we only have the much simpler electronic density, which only depends on the three-dimensional position.[2] Although the Hohennberg-Kohn theorems tell us this functional $F[\rho(\boldsymbol{r})]$ must exist, they do not tell us which shape it should take, or how to find it.

A way to tackle this issue was brought forward by Kohn and Sham [63], who showed that we can map the interacting many-body system to a hypothetical system of non-interacting electrons, with the same electronic density. The advantage of a non-interacting system is that the equations decouple, and we have, effectively, a set of single-particle problems. For the non-interacting system to have the same electronic density as the interacting system, of course the external potential of the non-interacting system must be different. The functional for the non-interacting Kohn-Sham system can now be written as:

$$F[\rho(\boldsymbol{r})] = \hat{T}_{KS}[\rho(\boldsymbol{r})] + E_H[\rho(\boldsymbol{r})] + E_{XC}[\rho(\boldsymbol{r})], \tag{2.5}$$

[2] In Eq. 2.4 we take $\boldsymbol{r}$ to mean a single position in space, rather than the positions of all the electrons as in Eqs. 2.2 and 2.3.

where the first term ($\hat{T}^{KS}[\rho(\boldsymbol{r})]$) describes the kinetic energy of the non-interacting Kohn-Sham system, the second term is the Hartree energy (classical Coulomb repulsion $E_H = \frac{1}{2}\int \frac{\rho(\boldsymbol{r})\rho(\boldsymbol{r'})}{|\boldsymbol{r}-\boldsymbol{r'}|} d^3r d^3r'$), and the last term is the exchange-correlation (XC) energy, which contains all the many-body effects of the real system.

We may now combine Eqs. 2.4 and 2.5 to rewrite the total energy as:

$$E_{tot}[\rho(\boldsymbol{r})] = \hat{T}_{KS}[\rho(\boldsymbol{r})] + \int V_{ext}(\boldsymbol{r})\rho(\boldsymbol{r})d^3r + E_H[\rho(\boldsymbol{r})] + E_{XC}[\rho(\boldsymbol{r})] \tag{2.6}$$

$$= \hat{T}_{KS}[\rho(\boldsymbol{r})] + \int \underbrace{\left(V_{ext}(\boldsymbol{r}) + V_H[\rho(\boldsymbol{r})] + V_{xc}[\rho(\boldsymbol{r})]\right)}_{V_{KS}[\boldsymbol{r},\rho(\boldsymbol{r})]} \rho(\boldsymbol{r})d^3r, \tag{2.7}$$

where we see that the first term ($\hat{T}^{KS}[\rho(\boldsymbol{r})]$) captures the kinetic energy of our auxiliary system, while the other terms together form the augmented Kohn-Sham potential, i.e., the potential that ensures our hypothetical non-interacting system has the same electronic density as the many-body system we started out with. This mapping is in principle exact if we would know the shape of the XC functional. The power of this approach lies in that all the unknown is hiding in this single term E_{xc}, which represents only a small (though important) contribution to the total energy, while all other terms may be computed. In practice, we make approximations for the shape of the XC functional. Several of such approximations have been made, and are available as options in most DFT codes. The most simple approximation is the local density approximation (LDA) [63, 64]. Here it is assumed that E_{XC} depends on $\rho(\boldsymbol{r})$ as it does in a uniform electron gas of the same density and that it depends on this density alone, and not any of its derivatives. In forms of the generalized gradient approximation (GGA), dependency on $\rho(\boldsymbol{r})$ and its gradient are taken into account. There are different forms of GGA available, including the Perdew-Burke-Ernzerhof (PBE) functional [65] and PBE optimized for solids (PBEsol) [66]. There are also hybrid functionals, which usually mix a GGA with exchange obtained from Hartree-Fock, and can give great improvement of the description of specific properties, but tend to increase the computational cost, as well as adding a parameter in the form or the degree of mixing. We explain our choice of XC functional for our description of Cr_2O_3 and Fe_2O_3 in the next chapter, in Section 3.1.1.

2.2.2 Numerical process

Using Eq. 2.7 and an approximation for the XC functional, we can find the ground state of our Kohn-Sham system using an iterative numerical process (Figure 2.3). Starting

from a guess of the electronic density, usually based on the atomic orbitals of the relevant elements and the structure of the crystal or molecule, we can construct the potential $V_{KS}[\boldsymbol{r}, \rho(\boldsymbol{r})]$ (see Eq. 2.5). From there we can solve the Kohn-Sham equations

$$\left[-\frac{\hbar^2}{2m_e}\nabla_i^2 + V_{KS}[\boldsymbol{r}, \rho(\boldsymbol{r})]\right]\phi_i(\boldsymbol{r}) = \epsilon_i\phi_i(\boldsymbol{r}), \tag{2.8}$$

which constitute the Schrödinger equations for the single-particle wavefunctions ϕ_i of our Kohn-Sham system. From the found wave functions a new density $\rho(\boldsymbol{r}) = \sum_i^{occ} |\phi_i(\boldsymbol{r})|^2$ can be constructed, where the sum runs over all occupied states. Subsequently, we can determine the new energy E_{KS}. Here we can restart the loop and calculate the new Kohn-Sham potential V_{KS}. This self-consistent process repeats itself until the desired degree of convergence is reached, usually when the energy difference between two iterations is less than a pre-set amount. We note that, although this process is iterative, and thus should give us an energy that is larger or equal to the ground state energy of our Kohn-Sham system, by the variational principle. However, due to the approximation of the XC functional, that does not mean that it cannot be lower than the ground state of the original many-body system. In general, E_{KS} is not considered to have any physical meaning, but we can track it to determine the convergence.

The Kohn-Sham energy of Eq. 2.7 can be expanded to include, for example spin, which we did not write explicitly as a variable, or spin-orbit coupling, which can be introduced as a correction to the kinetic energy. Also, to determine the minimal energy positions of the atoms, we may add a term that includes the ion-ion interactions at fixed positions. In general, DFT output will include the ground energy, the position of the atoms, the ground state electronic density and, when applicable, the magnetic moments.

In practice, the scheme is a bit more complicated that the sketch in Figure 2.3. First of all, solving the KS equations is usually bot done in real space, but in momentum space, where a set of points is chosen and then interpolated between [67]. Here, the degree of convergence is determined by the density of this grid of points. the 'so-called' k-point grid or mesh. This k-point grid is defined with respect to reciprocal lattice vectors, which depend on the chosen real space unit cell. This can be the primitive unit cell of the crystal structure or a larger repeating unit. So, if we want to simulate a solid, we choose a unit cell, which determines the amount of bands we have the include (i.e., the number of electrons). Also, periodic boundary conditions are applied, so that we simulate an infinite repetition of this unit.

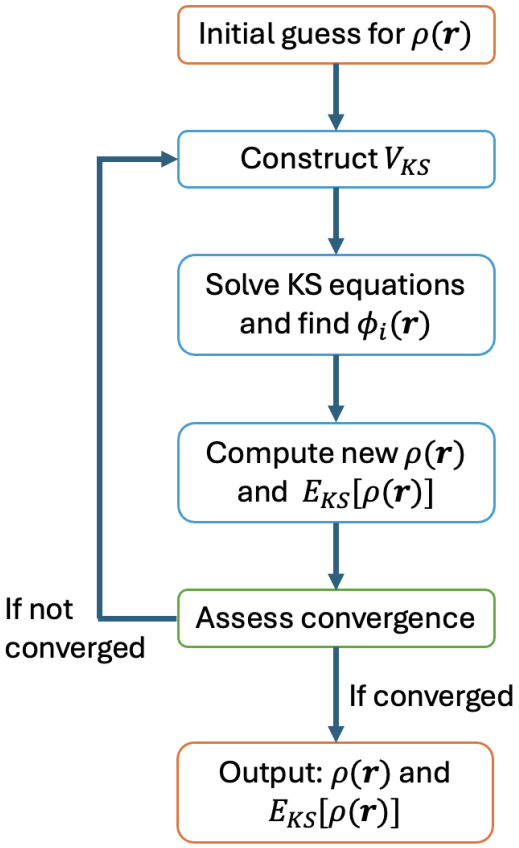

FIGURE 2.3: The typical iterative, self-consistent process performed in a DFT calculation.

Furthermore, as mentioned, our Kohn-Sham system is non-interacting which means we have a set of single-particle wavefunctions. We need to choose a basis to write said wavefunctions in. Plane waves are a common choice, although this basis, like any complete basis for writing all wavefunctions in three-dimensional space, is infinitely large, which is not practical. Instead, we must truncate or 'cut off' our basis somewhere, which limits our accuracy but makes the computation manageable. A plane-wave basis has the advantage that we can control the number of included plane waves and the degree of convergence of the calculation from the energy cutoff. Another possible choice of basis is the atomic orbitals, and different basis sets can even be used for different regions in the solids, e.g., close to the atoms or the spaces in between. Both the k-point grid and basis set cutoff are parameters we will set for our calculation of Cr_2O_3 and Fe_2O_3.

Most DFT calculations described in this thesis were performed in the Vienna *ab initio* simulation package (VASP) [68, 69] or in ELK [70]. VASP uses a plane-wave basis and the projector-augmented wave (PAW) method [71, 72]. Here PAW potentials are used to describe the core electrons, to save computational cost. As the core electrons are relatively localized, it would take a linear combination of a large number of plane waves

to describe them, which is computationally expensive. Furthermore, the core electrons do not contribute much to the physics of the system, other than shielding the charge of the nucleus. However, which atoms to include in the core and which to describe explicitly, is another parameter we must set. ELK [70] describes both the core and valence electrons explicitly, but uses different basis sets in different regions of space, where setting the border between the regions is another choice. So we see that, although in principle DFT is parameter-free, in practice there are quite a few choices that one must make when performing a calculation in practice.

2.2.3 DFT+U

Standard DFT works well to describe materials where the electron density varies slowly but fails when the electrons are more localized, for example in d or f orbitals. This can be traced back to a failure of the approximation to the XC functional, like LDA and GGA, to capture the local electron-electron interactions [73]. Instead, the electrons are more delocalized than they should be, and DFT predicts a large set of materials to be metallic, even when they are known to be semi-conducting or insulating. This is called the delocalization error, and one way to address it is by the so-called 'DFT+U' method [1, 74].

In this method, the XC functional is corrected by an additional term describing the local interactions. The shape of this correcting term is based on the physics of the Hubbard model. Late us take as an example a simple, single band, Hubbard model [75–80], which describes N particles occupying a lattice of sites and interacting with their nearest neighbors.[3] The Hamiltonian for such a system will look as follows:

$$\hat{H}_{Hubbard} = -t \sum_{\langle i,j\rangle,\sigma} (\hat{c}^{\dagger}_{i,\sigma}\hat{c}_{j,\sigma} + c.c.) + U \sum_{i} \hat{n}_{i,\uparrow}\hat{n}_{i,\downarrow}, \tag{2.9}$$

with $\langle i, j\rangle$ the nearest neighbor lattice sites, σ the spin of the particles and $\hat{c}^{\dagger}_{i,\sigma}\hat{c}_{j,\sigma}$ and $\hat{n}_{i,\sigma}$ the usual creation, annihilation and particle number operators. The first term describes the hopping of a particle between neighboring sites, i.e., annihilation on one site and creation on the other. Here t is the hopping parameter, which sets the energy gain (or cost if t is negative) from this hopping process. The second term in Eq. 2.9 captures the describes the Coulomb repulsion between two particles occupying the same site, where U determines the energy cost of having the two particles on the same site.

[3] 'Single band' means, in this case, that there is only one orbital or band, i.e., there are only two states to fill on each site: $\uparrow$ and $\downarrow$.

Let us consider two limits for the ratio of U and t. In the limit where $t \ll U$, the energy a particle gains by hopping is negligible compared to the energy cost of two particles occupying the same site, so hopping is strongly suppressed and the particles are effectively localized. On the other hand, in the limit where $t \gg U$, the Hamiltonian of Eq. 2.9 is dominated by the hopping term, and it is energy favorable to delocalize the particles as much as possible. The DFT+U uses a Hubbard-like term for describing the localization in certain bands, in our case the d bands of Cr and Fe, while using regular DFT to describe the other bands, where such a correction is not necessary [74]. For Cr_2O_3 and Fe_2O_3, several orbitals need a Hubbard U correction, as more than one d orbital is occupied. This means that we have the physics of a multiband Hubbard model, and we also need to consider the interactions of two electrons on the same site, but in different orbitals. Here we will use Hund's coupling J, which sets the energy gain for aligning the spins of two electrons in different orbitals on the same site.

2.3 DFT extensions

In this thesis, we will be computing several properties of materials, which are not standard outputs of DFT calculations, such as the ME response and the presence of higher-order magnetic multipoles. Here I discuss some of the methods we used to make these calculations.

2.3.1 Magnetoelectric response

In experiment, the ME effect is usually measured by applying a magnetic field and observing the resulting polarization, or by applying an electric field and determining the resulting magnetization. In DFT we usually use periodic boundary conditions, and applying a field would result in these conditions not being met, e.g., an applied electric field would result in a potential difference at the boundary. Several methods have been employed to study magnetoelctric responses in DFT [33, 81–83]. We will mostly focus on the method of Ref. [81] where the application of an electric field is simulated by the displacement of the ions such a field would cause. This only captures the change in the external potential V_{ext} caused by this displacement of the ions, and not the part caused by the field itself (and the fact that the electrons are of course charged). We expand this method to not just study the net linear response, but to also qualitatively determine *local* linear and second-order responses, as we explain in Section 3.3.5.2. Another method for calculating the ME effect is, for example, the application of a Zeeman-field, which is applied by adding a term to the Kohn-Sham Hamiltonian that favors one spin orientation

[20]. In Chapter 4 we will compare the results of different methods for calculating the net ME effect in Cr_2O_3.

2.3.2 Multipole calculations

As discussed in Chapter 1, we are interested in studying higher order multipoles. Thus we need to evaluate the values of the corresponding multipole tensors around each atom, for example, the ME multipole tensor:

$$\mathcal{M}_{ij} = \int r_i \mu_j(\boldsymbol{r}) d^3\boldsymbol{r}. \tag{2.10}$$

We should be able to perform this integration explicitly, as our DFT calculations output both the charge density and the magnetization. Writing the integration in spherical coordinates we obtain:

$$\mathcal{M}_{ij} = \int \left[r_i \mu_j(\boldsymbol{r}) r^2 \sin\phi\right] dr\, d\theta\, d\phi. \tag{2.11}$$

The integration over θ and ϕ can in principle be executed, but the integration over r requires us to set a boundary, which is difficult to define, i.e., what area do we mark as belonging to a specific atom? To circumvent this integration boundary problem, we make use of an alternative method, where we only access the spherical components of the multipole tensor [84–86]. This method is based on a similar multipole decomposition that is used in X-ray physics [87].

The key idea is to decompose the integral into radial and angular parts and to project the angular component of the local charge density around an atom onto the spherical harmonics. The formalism for this projection is complicated, and we will discuss first how it works for the charge multipoles, which are slightly simpler. We can see these charge multipoles arise when we consider the interaction energy of spatially varying applied electric potential $\Phi(\boldsymbol{r})$ with a charge density $\rho(\boldsymbol{r})$, a similar expression as the

interaction energy of an applied magnetic field and a magnetisation density of Eq. 1.7:

$$\mathcal{E}_{int,el} = -\int \rho(\boldsymbol{r})\Phi(\boldsymbol{r})\, d^3\boldsymbol{r} \tag{2.12}$$

$$- \underbrace{\left(\int \rho(\boldsymbol{r})\, d^3\boldsymbol{r}\right)}_{\text{charge monopole}} \Phi(0) - \underbrace{\left(\int \rho(\boldsymbol{r}) r_{\mathbf{i}}\, d\boldsymbol{r}\right)}_{\text{charge dipole}} \partial_i\Phi(0)$$

$$- \underbrace{\left(\int \rho(\boldsymbol{r}) r_i r_j\, d\boldsymbol{r}\right)}_{\text{charge quadrupole}} \partial_i\partial_j\Phi(0) - \underbrace{\left(\int \rho(\boldsymbol{r}) r_{\mathbf{i}} r_{\mathbf{j}} r_{\mathbf{k}}\, d\boldsymbol{r}\right)}_{\text{charge octupole}} \partial_i\partial_j\partial_k\Phi(0) - \dots . \tag{2.13}$$

Taking the charge quadrupole as an example:

$$\mathcal{C}_{ij} = \int \rho(\boldsymbol{r}) r_i r_j\, d\boldsymbol{r} = \int \left[\rho(r,\theta,\phi) r_i r_j r^2 \sin\phi\right] dr\, d\theta\, d\phi. \tag{2.14}$$

Again, the integral over r requires us to set an integration boundary. We can instead express the charge density $\rho(r,\theta,\phi)$ in terms of a density matrix $\rho_{\alpha,\beta}$, the latter being written in a complete basis of atomic-like orbitals $|\Psi_\alpha\rangle$:

$$\rho(r,\theta,\phi) = \langle r,\theta,\phi|\rho|r,\theta,\phi\rangle = \sum_{\alpha,\beta} \langle r,\theta,\phi|\Psi_\beta\rangle\langle\Psi_\beta|\rho|\Psi_\alpha\rangle\langle\Psi_\alpha|r,\theta,\phi\rangle \tag{2.15}$$

$$= \sum_{\alpha,\beta} \Psi_\beta(r,\theta,\phi)\rho_{\beta,\alpha}\Psi^*_\alpha(r,\theta,\phi). \tag{2.16}$$

Furthermore, we can use that $\Psi_\alpha(r,\theta,\phi) = R_{nl}(r)Y_{lm}(\theta,\phi)$, with n the principle quantum number, l and m the quantum number labelling the angular momentum, and Y_{lm} the spherical harmonics, to write:

$$\rho(r,\theta,\phi) = \sum_{n,n',l,l',m,m'} \langle r,\theta,\phi|n'l'm'\rangle\langle n'l'm'|\rho|nlm\rangle\langle nlm|r,\theta,\phi\rangle. \tag{2.17}$$

Because $\Psi_\alpha(r,\theta,\phi) = R_{nl}(r)Y_{lm}(\theta,\phi)$ also means the atomic-like orbitals decompose in a radial and spherical component, we can decompose the expression of Eq. 2.17 as well. Using that $\langle lm|\theta,\phi\rangle = Y_{lm}(\theta,\phi)$, we see that the spherically dependent part of the charge density can be expressed as:

$$\rho(\theta,\phi) \sim \sum_{ll'mm'} Y_{l'm'}(\theta,\phi)\langle l'm'|\rho|lm\rangle Y^*_{lm}(\theta,\phi) \tag{2.18}$$

$$\sim \sum_{ll'mm'} Y_{l'm'}(\theta,\phi)\rho_{l'm'lm}Y^*_{lm}(\theta,\phi). \tag{2.19}$$

Now we have an expression for the charge density, but in the expression of each multipole there is also a product of spatial components. For example, in the charge quadrupole of

Eq. 2.14, there is the product $r_i r_j$. Using the definition of the spherical coordinates

$$r_0 = x = r\cos\theta\cos\phi, r_1 = y = r\sin\theta\cos\phi, r_2 = z = r\sin\phi, \tag{2.20}$$

we see that the angular dependence of $r_i r_j$ can be expressed as a product of cosines and sines of θ and ϕ, which means that it can be expressed in terms of spherical harmonics as well. For example, $r_0 r_1 = r^2\cos\theta\sin\theta\cos^2\phi \sim r^2 Y_{2,-2}$. As discussed in Section 1.4.2, the Cartesian multipole tensors can be decomposed into spherically irreducible parts. Here it becomes useful to consider these spherically irreducible tensors, rather than the Cartesian tensors themselves. In general, the spherical dependence of the spatial coordinates in the integral of a spherically irreducible charge multipole component of order k, can be written as a single spherical harmonic, $Y_{kt}(\theta,\phi)$. Here k labels the degree of r dependence, e.g., $k = 0$ for the charge monopole, $k = 1$ for the charge dipole, etc. Furthermore, t labels the different independent components of the multipole, with $t \in \{-k, -k+1, ..., k\}$.

We can now write the angular parts of our spherically irreducible charge multipoles w_t^k:

$$w_t^k \sim \int Y_{kt}(\theta,\phi)\rho(\theta,\phi)\sin\phi\, d\theta\, d\phi \tag{2.21}$$

$$\sim \int \sum_{ll'mm'} Y_{kt}(\theta,\phi)Y_{l'm'}(\theta,\phi)\rho_{l'm'lm}Y^*_{lm}(\theta,\phi)\sin\phi\, d\theta\, d\phi \tag{2.22}$$

$$\sim \sum_{ll'mm'} \rho_{l'm'lm}\int Y_{kt}(\theta,\phi)Y_{l'm'}(\theta,\phi)Y^*_{lm}(\theta,\phi)\sin\phi\, d\theta\, d\phi \tag{2.23}$$

$$\sim \sum_{ll'mm'} \rho_{l'm'lm}\int Y_{kt}(\theta,\phi)Y_{l'm'}(\theta,\phi)(-1)^m Y_{l,-m}(\theta,\phi)\sin\phi\, d\theta\, d\phi \tag{2.24}$$

$$\sim \sum_{ll'mm'} (-1)^m\sqrt{\frac{(2k+1)(2l+1)(2l'+1)}{4\pi}}\rho_{l'm'lm}\begin{pmatrix} k & l' & l \\ 0 & 0 & 0\end{pmatrix}\begin{pmatrix} k & l' & l \\ t & m' & -m\end{pmatrix} \tag{2.25}$$

$$\sim \sum_{ll'mm'} (-1)^m\sqrt{\frac{(2l+1)(2k+1)(2l'+1)}{4\pi}}\rho_{l'm'lm}\begin{pmatrix} l & k & l' \\ 0 & 0 & 0\end{pmatrix}\begin{pmatrix} l & k & l' \\ -m & t & m'\end{pmatrix} \tag{2.26}$$

$$\sim \sum_{ll'mm'} (-1)^m\sqrt{\frac{(2l+1)(2k+1)(2l'+1)}{4\pi}}\langle l'm'|\rho|lm\rangle\begin{pmatrix} l & k & l' \\ 0 & 0 & 0\end{pmatrix}\begin{pmatrix} l & k & l' \\ -m & t & m'\end{pmatrix} \tag{2.27}$$

Where we used that $Y_{lm} = (-1)^m Y_{l,-m}$, the definition of the Wigner 3j-symbols in terms of an integral over the spherical harmonics [88]:

$$\int Y_{l_1,m_1}(\theta,\phi)Y_{l_2,m_2}(\theta,\phi)Y_{l_3,m_3}(\theta,\phi)\sin\phi\, d\theta\, d\phi = \tag{2.28}$$

$$\sqrt{\frac{(2l_1+1)(2l_2+1)(2l_3+1)}{4\pi}}\begin{pmatrix} l_1 & l_2 & l_3 \\ 0 & 0 & 0\end{pmatrix}\begin{pmatrix} l_1 & l_2 & l_3 \\ m_1 & m_2 & m_3\end{pmatrix}, \tag{2.29}$$

and that the Wigner 3j-symbols are equivalent under the cycling of the columns.

It is worth noting that the Wigner 3j-symbols are zero unless the following conditions are met [89]:

$$m_i \in \{-j_i, -j_i+1, \ldots, j_i\} \text{ with } i \in \{1,2,3\}, \tag{2.30}$$

$$m_1 + m_2 + m_3 = 0, \tag{2.31}$$

$$|j_1 - j_2| \leq j_3 \leq j_1 + j_2 \tag{2.32}$$

$$j_1 + j_2 + j_3 \in \mathbb{Z}, \tag{2.33}$$

$$\text{if } m_1 + m_2 + m_3 = 0,\ j_1 + j_2 + j_3 \in 2\mathbb{Z}. \tag{2.34}$$

Now, to find the exact expression for the spherically irreducible multipole components w_t^k we need to determine the normalization, where we use the explicit expression for the Wigner 3j-symbols and follow Ref. [84]. Assuming $l = l'$, the charge multipole component for each l can be written as:

$$w_{t,l}^k = \sum_{\substack{m\in\{-l,-l+1,\ldots,l\} \\ m'\in\{-l,-l+1,\ldots,l\}}} (-1)^{l-m} \frac{\sqrt{(2l-k)!(2l+k+1)!}}{(2l)!} \begin{pmatrix} l & k & l' \\ -m & t & m' \end{pmatrix} \langle m'|\rho|m\rangle \tag{2.35}$$

$$= \sum_{\substack{m\in\{-l,-l+1,\ldots,l\} \\ m'\in\{-l,-l+1,\ldots,l\}}} \langle m|v_t^k|m'\rangle\langle m'|\rho|m\rangle, \tag{2.36}$$

such that:

$$\langle m|v_t^k|m'\rangle = \frac{(-1)^{l-m}}{n_{lk}} \begin{pmatrix} l & k & l \\ -m & t & m' \end{pmatrix}, \text{ with } n_{lk} = \frac{(2l)!}{\sqrt{(2l-k)!(2l+k+1)!}} \tag{2.37}$$

This decomposition can be expanded to include the magnetic multipoles as well, but this is more complicated. First of all, to gain access to the magnetization, we need to consider the spin-dependent part of the density matrix as well: $\langle lmm_s|\rho|l'm'm_s'\rangle$, where $m_s \in \{-s, s\}$ and $s = 1/2$, with s, m_s the spin quantum numbers. Now, still using the normalization of Ref. [84], we can define the irreducible spherical tensors describing a specific multipole moment w_t^{kpr}, where k labels the spatial index ($k = 0, 1, 2$, etc), p the spin index ($p = 0$ for charge and $p = 1$ for magnetic multipoles) and r the rank of the tensor ($r \in \{|k-p|, |k-p|+1, \ldots, k+p\}$). Finally, t denotes the components of the tensor ($t \in \{-r, -r+1, \ldots, r\}$). Again taking $l = l'$, the w_t^{kpr} for each l can be defined from the density matrix ρ as follows [84] (dropping the subscript l):

$$w_t^{kpr} = \sum_{\substack{x\in\{-k,-k+1,\ldots,k\}\\ y\in\{-p,-p+1,\ldots,p\}}} \xi_{xyt}^{kpr} \sum_{\substack{m_s\in\{-s,s\}\\ m'_s\in\{-s,s\}}} \langle m_s|t_y^p|m'_s\rangle \sum_{\substack{m\in\{-l,-l+1\ldots,l\}\\ m'\in\{-l,-l+1\ldots,l\}}} \langle m|v_x^k|m'\rangle\langle m'm'_s|\rho|mm_s\rangle, \tag{2.38}$$

where using the Wigner 3j-symbols,

$$\xi_{xyt}^{kpr} = \frac{(-1)^{k-x+p-y}}{\underline{n}_{kpr}} \begin{pmatrix} k & r & p \\ -x & t & -y \end{pmatrix}, \tag{2.39}$$

$$\langle m_s|t_y^p|m'_s\rangle = \frac{(-1)^{s-m_s}}{n_{sp}} \begin{pmatrix} s & p & s \\ -m_s & y & m'_s \end{pmatrix}, \tag{2.40}$$

v_x^k and n_{lk} defined as before (Eq. 2.37), and

$$\underline{n}_{abc} = i^{a+b+c}\left[\frac{(-a+b+c)!(a-b+c)!(a+b-c)!}{(a+b+c+1)!}\right]^{1/2} \times \frac{(a+b+c)!!}{(-a+b+c)!!(a-b+c)!!(a+b-c)!!}. \tag{2.41}$$

As we see from Eq. 2.38, the tensor w_t^{kpr} can be computed directly from the electronic density ρ, and its components correspond to different multipoles. For example $w_{-1,0,1}^{011}$ correspond to the spin (i.e., the spin contribution to the magnetic dipoles) in the y, z, and x directions, and w_t^{11r} corresponds to the ME multipoles (for $r = 0$ we have the ME monopole, for $r = 1$ the toroidal moments and for $r = 2$ the quadrupoles). It is these w_t^{kpr} (for different l) that are output from the decomposition of the DFT charge density. Because of the Wigner 3j-selection rules, specifically Eq. 2.32, $|l - l'| \leq k \leq l + l'$, which means that we need higher l spherical harmonics to see multipoles of higher rank.

Not only is the expression Eq. 2.38 more complicated than when only the charge multipoles were included (Eq. 2.36), but due to the way angular momenta are summed, the rank r of the spherically irreducible parts can be smaller than $k + p$. We opt for the nomenclature where we call each multipole for the place where it arises in the expansion of Eq. 1.7, rather than after the 'spherical' rank r. For example, with our naming convention the magnetic quadrupole includes components w_0^{110} (rank = 0), $w_{-1,0,1}^{111}$ (rank = 1), and $w_{-2,-1,0,1,2}^{112}$ (rank = 2).

This decomposition method was originally developed for the ELK code [84, 85]. It was later implemented in the VASP code by Thöle [90], and in a Python pre-and post-processing code called MULTIPYLES by Merkel [91, 92]. We have used all three methods, and have confirmed that they are consistent.

2.4 Effective Hamiltonian modeling

As discussed in the sections above, DFT is a powerful way to model materials and their properties. However, there are limitations to DFT. For instance, when using plane-wave basis sets, the number of plane waves needed to describe a system at a given level of accuracy scales cubically with the system size [93]. This scalability issue is particularly pronounced for materials that already have heavy computational demands, such as magnetic materials.[4] Thus we are limited to relatively small unit cells, and cannot model long-range magnetic patterns. Furthermore, DFT describes the physics of systems at T=0 and lacks the capability to model temperature effects. Thus, to describe the physics of large magnetic systems at different temperatures, we must rely on another method.

Instead of trying to describe the electrons and the ways they interact with each other and the nuclei, we can instead focus on the effective physics of the magnetic moments. We know from atomic physics that the electrons in a less than half-filled d shell usually arrange with parallel spins, forming a 'high-spin' configuration. We can view this as a net magnetic moment localized on the atomic site. In materials like Cr_2O_3 and Fe_2O_3, where electrons tend to be localized, we can capture the effective behavior of the electrons by the interactions between these magnetic moments, localized on the Cr and Fe sites. An effective Hamiltonian describing the physics of these moments can take different shapes depending on the interactions we include. For example, we can make a simple Hamiltonian where we only include the symmetric exchanges (J) and the quadratic anisotropy (K):[5]

$$H = -\sum_{i \neq j} J_{ij}\, \hat{\boldsymbol{e}}_i \cdot \hat{\boldsymbol{e}}_j - K_i \sum_i e_{i,z}^2, \tag{2.42}$$

[4] The inclusion of spin adds complexity: without spin, we only have orbital degrees of freedom, i.e., each band contains two electrons and so the number of unique bands is half the number of electrons. When we include spin, the number of bands in equal to the number of electrons.

[5] Here we formulated the Hamiltonian in terms of the directions of magnitudes of the moments, and we absorbed the magnitudes of the moments into the interaction parameters. Even though spins and magnetic moments have opposite signs, the magnetic moments enter into this Hamiltonians only in even powers, such that a formulation in terms of the spins would be equivalent.

where i and j label the lattice sites and $\hat{\boldsymbol{e}}_i$ is the unit vector indicating the direction of the magnetic moment on-site i. If $J_{ij} > 0$ there is an energy gain when the moments on sites i and j align and an energy loss when they are anti-aligned. Instead, if $J_{ij} < 0$, there is an energy gain when the magnetic moments on sites i and j are anti-aligned, and a cost if they are aligned. The single ion anisotropy gives an energy gain (or cost when $K < 0$) when the magnetic moments are parallel to a specific axis, in this case the z axis. We will discuss other magnetic interactions and several different shapes these magnetic Hamiltonians can take in Chapter 6.

From Eq. 2.42, we see that the Hilbert space of this Hamiltonian is spanned by states which label the direction of the magnetic moment on each site, where we only take the magnetic ions into account, as there is no magnetic moments on the other sites in the crystal. This is much simpler than the set of single-electron wavefunctions that span the Hilbert space of our Kohn-Sham Hamiltonian, indicating that with this effective Hamiltonian, we could model much larger systems. Furthermore, one can model many different magnetic behaviors, e.g., paramagnetic, (anti-)ferromagnetic, et cetera [94]. Yet, as these are classical spin models, we cannot simulate quantum effects.

We can use DFT to determine the values of the parameters (e.g., J and K) in these Hamiltonians [95, 96]. We will describe how we perform these calculations in Chapter 6. In principle, we should be able to determine the ground state, once we have established a Hamiltonian and calculated the values of its parameters. Nevertheless, finding this ground state is not trivial, as we would have to test every possible state in the system. Instead, we can use different techniques to numerically solve this problem, while simultaneously also simulating temperature effects. We will make use of both Monte Carlo simulations and atomistic spin dynamics, as implemented in the UppASD code [97]. We will use both methods and compare the results.

2.4.1 Monte Carlo

Monte Carlo (MC) methods are well-established computational methods that use random sampling to solve deterministic problems and can be used to numerically find the minimal energy state at thermal equilibrium [98]. The basic idea for the modeling of a magnetic system is as follows [94]. Starting from some initial configuration of magnetic moments, a change in this configuration is randomly chosen. What this proposed change looks like depends on the algorithm, but let's take the reorientation of a single magnetic moment as an example. Using the provided classical magnetic moment Hamiltonian, it is determined if the proposed change would lower the energy. If it does, the change is accepted. If the change increases the energy, it is accepted with a chance that depends

on the change in energy and the given temperature, $p = e^{-\frac{\Delta E}{K_B T}}$. The smaller the energy change and the higher the temperature, the larger the chance the change gets accepted. In this way the randomness of thermal fluctuations is incorporated. Many different algorithms exist to perform such simulations [98], and UppaSD makes use of the Metropolis and Heat bath algorithms [99].

2.4.2 Atomistic spin dynamics

We can take an alternative route by considering the stochastic equation of motion for a classical spin coupled to a heat bath, the Landau-Lifshitz-Gilbert equation [100–103]:

$$\frac{\partial \boldsymbol{m}_i}{\partial t} = -\frac{\gamma}{1+\alpha^2}\, \boldsymbol{m}_i \times \boldsymbol{B}_i - \frac{\gamma}{|\boldsymbol{m}_i|}\frac{\alpha}{1+\alpha^2}[\boldsymbol{m}_i \times [\boldsymbol{m}_i \times \boldsymbol{B}_i]], \tag{2.43}$$

where $\boldsymbol{m}_i$ is the magnetic moment on site i, $\gamma = 1.76 * 10^{11}$ $(\mathrm{Ts})^{-1}$ is the gyromagnetic ratio. Thermal effects are included through $\boldsymbol{b}_i(t)$, a stochastic magnetic field with a Gaussian distribution, the size of which is connected to the temperature and α, the damping parameter. This is a microscopic damping parameter, which is not necessarily the same as the macroscopic damping parameter (citation), and in practice will chose a value for α to ensure proper convergence. Finally, $\boldsymbol{B}_i$ is the effective field experienced by the moment on site i ($\boldsymbol{m}_i$) and can be expressed as a partial derivative of the Hamiltonian with respect to $\boldsymbol{m}_i$:

$$\boldsymbol{B}_i = -\frac{\partial H}{\partial \boldsymbol{m}_i}. \tag{2.44}$$

Starting from some initial configuration, the stochastic differential equations of Eq. 2.43 can be solved numerically using Langevin dynamics [104]. We note that, at equilibrium, MC and spin dynamics should give the same results for a range of properties [97]. Specifically, we expect to find the same low-temperature ground state through both methods.

Chapter 3

Magnetic multipoles and (anti-)magnetoelectric effects

In this chapter, I discuss my work on calculating magnetic multipoles and associating these to local magnetoelectric (ME) effects in Cr_2O_3 and Fe_2O_3. On the one hand, this work was driven by the observed difference in ME response in Cr_2O_3 and Fe_2O_3, despite their similarities, and on the other by the association of these magnetic multipoles, specifically the 'so-called' ME multipoles, with the net linear ME effect [15]. The similarities between the compounds suggest that the ME effect's microscopic origin in Cr_2O_3 may also be present in Fe_2O_3, despite the lack of net effect, and the ME multipoles constitute an elegant way of probing that hypothesis. This chapter is structured as follows. First, I discuss how we described both Cr_2O_3 and Fe_2O_3 within our density functional theory (DFT) framework. Next, I explain how to use symmetry arguments to determine which multipole components are allowed to be non-zero, and which ordering they assume in each of the compounds. Subsequently, I will discuss how we calculated these multipole components and the associated local ME effects using DFT. To this end, I have incorporated the paper and its Supplemental Material which I co-wrote with Andrea Urru and Nicola Spaldin on this subject [19]. Here we discuss our findings of both linear and second-order local ME effects in Cr_2O_3 and Fe_2O_3, their relation to the specific multipole components, and the ubiquity of the local ME effect compared to the net one. Furthermore, I discuss some additional work regarding even higher-order multipoles, providing a full overview (up to fifth order) and discussing net third-order ME effects in Cr_2O_3. Finally, I give an overview of some of the open questions.

3.1 Cr_2O_3 and Fe_2O_3 in DFT

As mentioned in Chapter 2, the accuracy with which our DFT calculation can capture the physics of a specific compound depends on our choice of specific DFT parameters. In this section, I will discuss how we made these choices for Cr_2O_3 and Fe_2O_3.

3.1.1 Exchange-correlation functional and Hubbard U

The first important choice concerns the choice of exchange-correlation (XC) functional, as well as Hubbard U. Both Cr_2O_3 and Fe_2O_3 have been studied with DFT before, which gives us a starting point for our parameter search.

To begin with Cr_2O_3, a common choice in the literature for this compound is to use the local spin density approximation (LSDA), with a moderate U in the range 2-4 eV [105–107], although studies with the generalized gradient approximations (GGA), specifically using the Perdew-Burke-Ernzerhof (PBE) functional, have also been performed [83, 108]. We choose here to use the LSDA+U option, with a Hubbard U of 4.0 eV and a Hund's coupling J= 0.5 eV. We decided on these specific values by comparing the simulated band gap and the magnitude of the magnetic moments on the Cr atoms for different values for U and J. The band gap has experimentally been determined to be 3.1-3.31 eV [7–9], and the magnitude of the magnetic moment was measured to be 2.48-2.65 μ_B [51, 109]. With our chosen DFT parameters we find a band gap of 3.13 eV and a magnetic moment on the Cr of 2.60 μ_B.

For Fe_2O_3, it has been suggested that the best description of the structure would be given by hybrid functionals [110, 111]. However, the use of these functionals is computationally costly, and they are known to not always accurately capture magnetic properties correctly. Furthermore, we decided to stay with the same XC functional as we used for Cr_2O_3, to make a better comparison between the two compounds. We made a small exploration of the U to determine a good value, again by comparing with experimental values of the band gap, which is 2.14-2.2 eV [10, 11], and the magnitude of the magnetic moment on the Fe atoms, which is 4.1-4.2 μ_B [112, 113], although there is a completing value of 4.7-4.8 μ_B [114]. In Figure 3.1 we show the magnitude of the electronic band gap and the magnetic moment of the Fe atom as a function of U and J. We subsequently

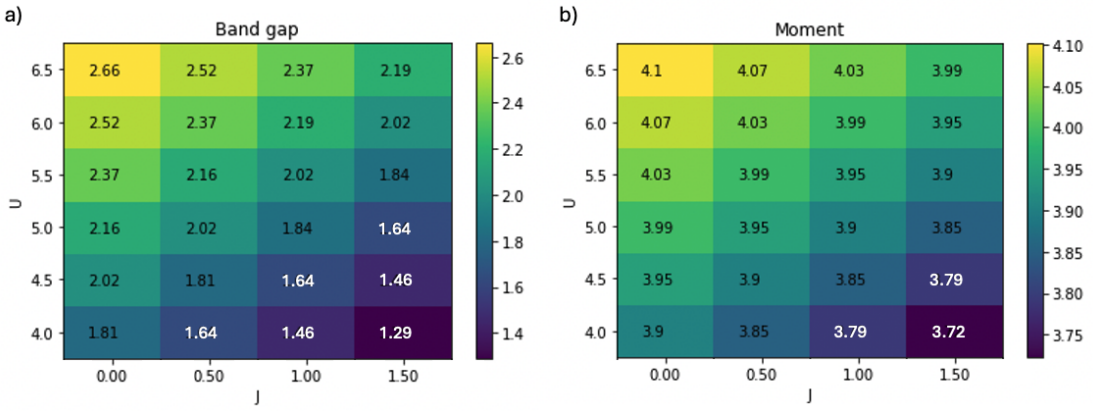

FIGURE 3.1: Band gap in eV (a) and magnetic moment in μ_B (b) for our DFT simulations of Fe_2O_3 at different values of U (4.0-6.5éV) and J (0.0-1.5éV).

chose a value of U = 5.5 eV and J = 0.5 eV.[1] With our chosen DFT parameters we find a band gap of 2.16 eV and a magnetic moment on the Fe of 4.01 μ_B.[2]

3.1.2 Convergence parameters

Next, we needed to determine what a valid choice was of k-point grid and energy cutoff. As explained before, these parameters determine the degree of convergence of the calculation. A finer k-point mesh and a higher energy cutoff will give a more converged result but will be more costly in terms of computational resources. Thus we must find a value for both where we can reach the desired accuracy, without wasting computational power. Below we show an exploration for Cr_2O_3 for different k-point grids and energy cutoff (Figure 3.2). We also compare the choice of projector-augmented wave (PAW) potential for the Cr atoms. As discussed in Section 2.2.2, the Vienna *ab initio* simulation package (VASP) uses an augmented potential to represent both the electric charge from the atomic core and the charge from the core electrons. The question is which electrons to include in the core. Here we compare on the one hand the `Cr_sv` dataset (Figure 3.2a,c, and e), which means that we take both the 3s and 3p electrons as valence electrons (Cr $3s^2 3p^6 3d^5 4s^1$, 14 valence electrons), and on the other hand the `Cr_pv` dataset (Figure 3.2b,d, and f), where we take the 3s electrons as part of the semi-core (Cr $3p^6 3d^5 4s^1$, 12 valence electrons).

[1] We also performed some calculations with GGA and found no qualitative difference between using LDSA+U and using GGA+U with the PBEsol parameterization, although for PBEsol the optimal U was lower than for LSDA. Using PBE however, even for a high value of J = 1.0 eV we find a low spin configuration for the Fe^{3+} ions in Fe_2O_3, giving a moment of 0.9 μ_B.

[2] This value for the magnetic moment is slightly larger than the one found in Figure 3.1 for U = 5.5 eV and J = 0.5 eV because of the final choice of convergence parameters, which we discuss in the next section.

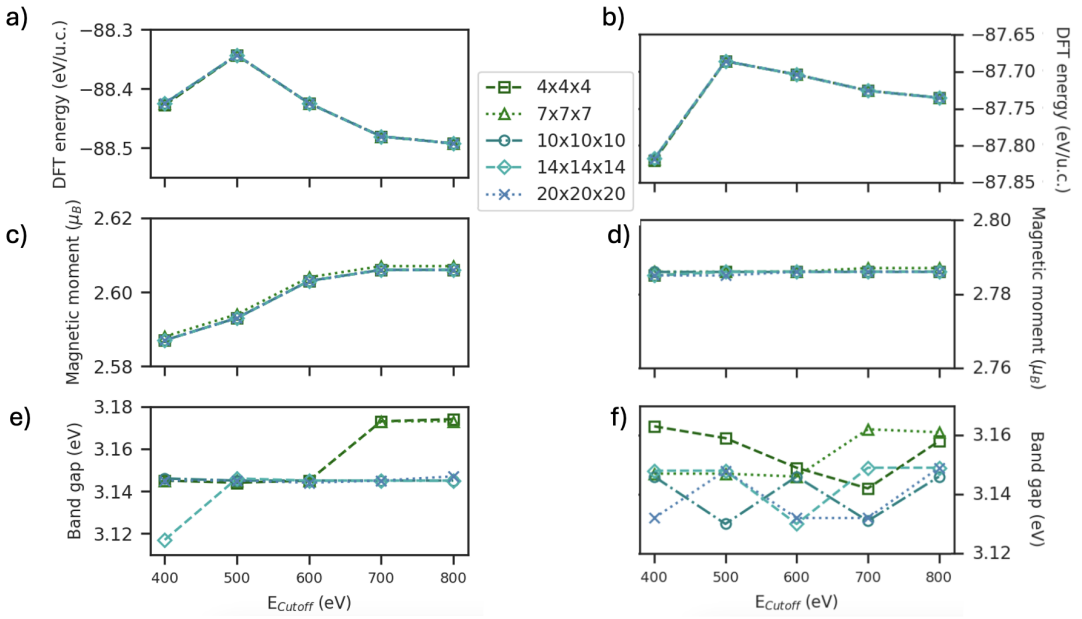

FIGURE 3.2: DFT energy per unit cell volume (a,b), band gap in eV (c,d) and magnetic moment in μ_B (e,f) as a function of the cutoff energy for the plane-wave basis (400-800 eV) for our DFT simulations of Cr_2O_3. Different colors and markers indicate different values for the k-point grid (4-14 points along each reciprocal lattice vector). Both the VASP PAW potential sets Cr_sv(a,c,e) and Cr_pv (b,d,f) were used. U = 4.0 eV and J = 0.5 eV for all these calculations.

Even though the DFT energy per unit cell does not tell us anything physical, we can use it to look at the convergence. Comparing Figures 3.2a and b we see that for the `Cr_sv` dataset, the trend is that the found energy decreases with increased energy cutoff for the plane-wave basis, as one would expect. Including more plane waves should lead to a more converged result. On the other hand, for the `Cr_pv` the trend is opposite. This indicated that this is not a good PAW potential set to use for this material, and we opt to use the `Cr_sv` dataset for all our VASP calculations. Similarly, for the Fe atoms we use the `Fe_sv` dataset (Fe $3s^2 3p^6 3d^7 4s^1$, 16 electrons). Furthermore, we see that for both datasets the magnitude of the magnetic moments depends mostly on the energy cutoff, and less on the density of the k-point grid. Finally, the band gap seems better converged for denser k-point grids. We choose to use $7 \times 7 \times 7$ k-point grid to relax the structure and an $11 \times 11 \times 11$ k-point grid for electronic relaxations in VASP. We furthermore use an energy cutoff of 800 eV.

With our found parameters, we then relaxed first the crystal structure. We found the following parameters for Cr_2O_3: $a' = |\boldsymbol{a'}| = 5.31$ Å, $\alpha' = 54.87°$, with α the angle between any two of the three rhombohedral lattice vectors. We can compare these with the values found at 2 K in neutron diffraction experiments: $a' = 5.35$ Å, $\alpha' = 55.01°$ [109], and see that the values we found are 0.78% and 0.26% smaller respectively. We note that the values measured were actually for the larger hexagonal unit cell, but they were

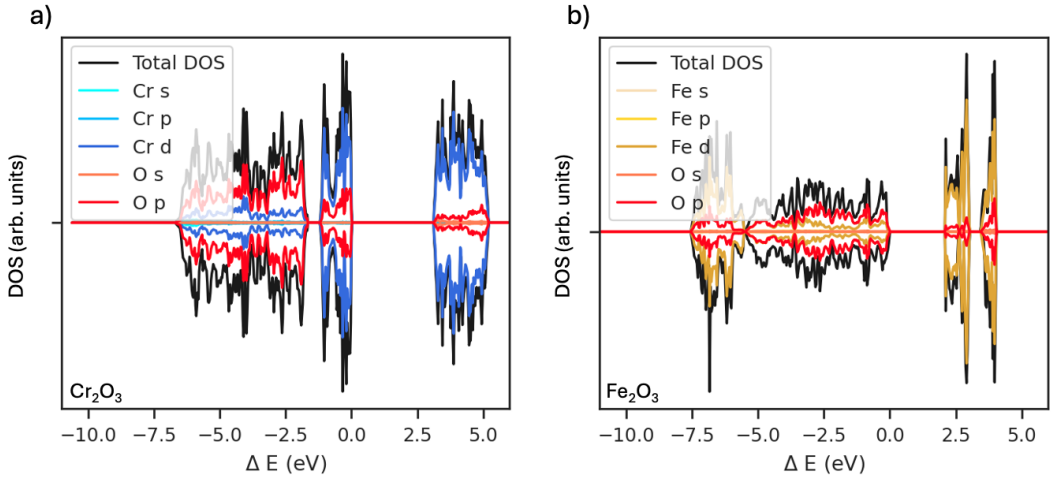

FIGURE 3.3: DFT density of states (DOS) for Cr_2O_3 (a) and Fe_2O_3 (b), with U = 4.0 (5.5) eV, J = 0.5 (0.5) eV for Cr_2O_3 (Fe_2O_3). The found band gaps are 3.13 eV and 2.16 eV for Cr_2O_3 and Fe_2O_3, respectively.

translated to values for the rhombohedral cell using the relations explained in Section 2.1.2.[3] For Fe_2O_3, we found $a' = 5.35\,\text{Å}$, $\alpha' = 55.25°$, which are 1.44% smaller and 0.03% larger, respectively, than the values found in experimentally at 2 K with neutron diffraction [113]. These values were $a' = 5.43\,\text{Å}$, $\alpha' = 55.22°$, which were again translated from the lattice parameters of the hexagonal unit cell.[4]

We note that all the calculations shown above were performed with the antiferromagnetic (AFM) collinear ordering we know each of the compounds to have, as determined in experiment (Figure 2.1). We tested for both compounds that these are indeed the lowest energy configurations. To be specific we tested the collinear magnetic configurations ++++ (FM), +−+−, ++−− and −++− (AFM) and +++−, ++−+ (ferrimagnetic), where + indicates a magnetic moment pointing upwards and − a magnetic moment pointing downwards. As expected, we find the lowest energy configuration to be +−+− (or equivalently −+−+) for Cr_2O_3, and −++− (or equivalently +−−+) for Fe_2O_3. We furthermore test that for non-collinear calculations, when we initialize the magnetic moments in these patterns there is no canting away from the collinear axis, when we relax the electronic structure.

Finally, with the DFT parameters as described above and the collinear AFM ordering, our relaxed electronic structure gives, for both compounds, a density of states (DOS) consistent with experimental results on these materials, including the AFM collinear nature and the size of the band gaps (Figure 3.3) [7–11].

Finally, we also perform some calculations in ELK. Here we used the same U and J values, but as ELK uses another way to describe the core electrons, we had to perform separate

[3] The hexagonal lattice parameters were $a = 4.94535(5)$ Å and $c = 13.58836(3)$ Å.
[4] The hexagonal lattice parameters were $a = 5.035476(16)$ Å and $c = 13.7676(4)$ Å.

convergence tests, which we describe later in this chapter in Sections 3.3.5.4 and 3.3.5.6. Let us just note here that we used a less dense k-point grid in ELK, both to reduce computational costs, which are in general higher due to the full-electron description and because we were able to achieve the desired accuracy with the less dense mesh in this code.

Now, having described Cr_2O_3 and Fe_2O_3 using DFT, we want to calculate additional properties regarding the magnetism, ME response, and magnetic multipoles, while comparing the two materials. Before we do that, we can determine what to expect from symmetry.

3.2 Symmetry analysis of Cr_2O_3 and Fe_2O_3

As mentioned in the introduction, symmetries give restrictions to what effects are allowed and in what form. It also restricts what components of different multipoles are allowed. In this section, I outline the steps necessary to determine the allowed ordering of the magnetic quadrupoles, also called ME multipoles, in Cr_2O_3 and Fe_2O_3.

3.2.1 Crystal symmetry group

As mentioned before, both Cr_2O_3 and Fe_2O_3 adopt the corundum crystal structure. This crystal structure corresponds to the space group $R\bar{3}c$. This is a non-symmorphic space group, with 12 operations that do not contain integer lattice translations. As integer lattice translations just change the choice of origin, we are not concerned with them here. The 12 operations without integer lattice translations can be split into two groups, the basic 6 operations and 6 operations that are multiplied with either just inversion I (Fe_2O_3) or with both inversion I and time reversal Θ (Cr_2O_3). The basic 6 operations are (with [abc] denoting the hexagonal unit cell directions):

$$\text{the identity operation: } E = \begin{pmatrix} 1 & 0 & 0 \\ 0 & 1 & 0 \\ 0 & 0 & 1 \end{pmatrix}, \tag{3.1}$$

$$\text{a counterclockwise rotation of } \frac{2\pi}{3} \text{ around the } z \text{ axis: } C_{3z^1} = \begin{pmatrix} -\frac{1}{2} & -\frac{\sqrt{3}}{2} & 0 \\ \frac{\sqrt{3}}{2} & -\frac{1}{2} & 0 \\ 0 & 0 & 1 \end{pmatrix}, \tag{3.2}$$

a counterclockwise rotation of $\frac{4\pi}{3}$ around the z axis: $C_{3z^2} = \begin{pmatrix} -\frac{1}{2} & \frac{\sqrt{3}}{2} & 0 \\ -\frac{\sqrt{3}}{2} & -\frac{1}{2} & 0 \\ 0 & 0 & 1 \end{pmatrix}$, (3.3)

a rotation of $\frac{\pi}{2}$ around the x axis (plus a translation):

$$C_{2x}(+f) = \begin{pmatrix} 1 & 0 & 0 \\ 0 & -1 & 0 \\ 0 & 0 & -1 \end{pmatrix} (+f), \tag{3.4}$$

a rotation of $\frac{\pi}{2}$ around the [010] axis (plus a translation):

$$C_{2[010]}(+f) = \begin{pmatrix} -\frac{1}{2} & -\frac{\sqrt{3}}{2} & 0 \\ -\frac{\sqrt{3}}{2} & \frac{1}{2} & 0 \\ 0 & 0 & -1 \end{pmatrix} (+f), \tag{3.5}$$

a rotation of $\frac{\pi}{2}$ around the [110] axis (plus a translation):

$$C_{2[110]}(+f) = \begin{pmatrix} -\frac{1}{2} & \frac{\sqrt{3}}{2} & 0 \\ \frac{\sqrt{3}}{2} & \frac{1}{2} & 0 \\ 0 & 0 & -1 \end{pmatrix} (+f), \tag{3.6}$$

$$\text{where } f = \begin{pmatrix} 0 \\ 0 \\ \frac{1}{2} \end{pmatrix}, \tag{3.7}$$

and the $\frac{1}{2}$ in the definition of f indicates a translation of half the unit cell length along the hexagonal c axis (Cartesian z axis). These symmetry operations are sketched in Figure 3.4a. We will apply these operations both in real and momentum space. Rotations act the same in real space and momentum space, translations do not alter momentum space, and inversion and time reversal take the following forms:

$$\text{the inversion operation: } I = \begin{pmatrix} -1 & 0 & 0 \\ 0 & -1 & 0 \\ 0 & 0 & -1 \end{pmatrix} \text{ (in real space),} \tag{3.8}$$

$$\text{the timer-reversal operation: } \Theta = \begin{pmatrix} -1 & 0 & 0 \\ 0 & -1 & 0 \\ 0 & 0 & -1 \end{pmatrix} \text{ (in momentum space).} \tag{3.9}$$

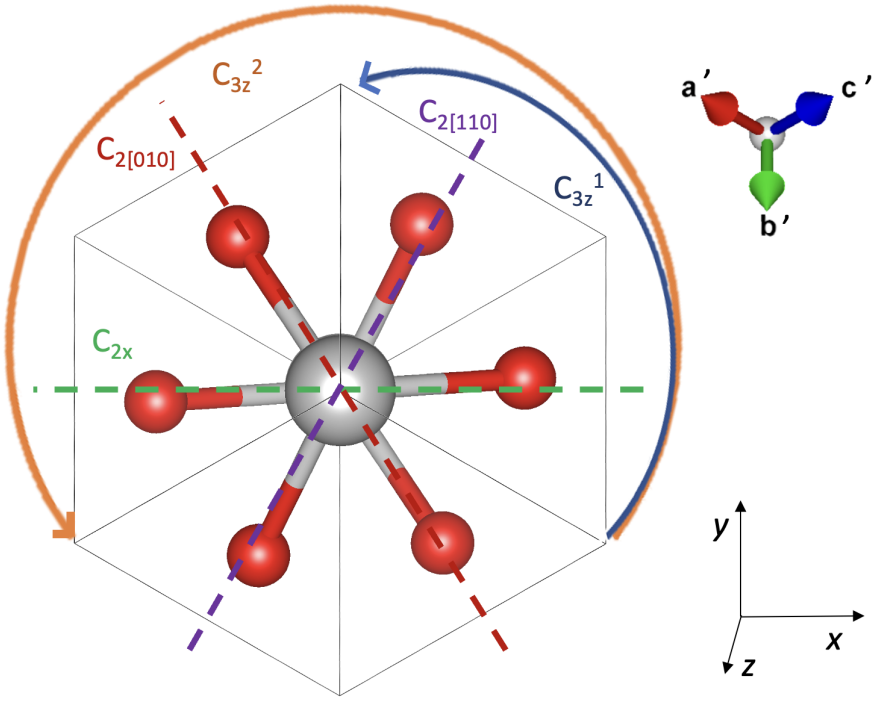

FIGURE 3.4: The symmetry operations in the primitive corundum unit cell, shown in a top view of the rhombohedral unit cell, with the actions of the symmetry operations (without inversion) sketched. Curved arrows indicate the rotations about the z axis and dashed lines indicate the axes for the $\frac{\pi}{2}$ rotations. Rhombohedral and Cartesian axes are indicated at the right of the figure.

3.2.2 Wyckoff positions

Next, we will consider the atoms' positions, making use of crystallographic symmetry positions called Wyckoff positions [115]. To understand what these positions are, we start with an ideal crystal, i.e., no defects and no surfaces. If we pick a position in this ideal crystal, we can consider how it transforms under the operations of the crystallographic space group, and see that each position has an infinite number of equivalent

positions. This whole set of equivalent positions is called a crystallographic orbit. Such a crystallographic orbit has eigensymmetries. These are the symmetries that leave the orbit invariant, i.e., symmetry operations that exchange the positions in the orbit. The group of eigensymmetries of an orbit is either the crystallographic space group itself, and such an orbit is called a characteristic orbit, or a supergroup containing the crystallographic space group, in which case the orbit is called a non-characteristic orbit. There are also symmetry operations that do not change one position in the orbit, for example, because this position lies on the axis of a rotation. The symmetries that leave a specific position unaltered together form the site symmetry group of that position. For a general position, the site symmetry group only contains the identity operation, but there are special points which have higher symmetry, i.e., their site symmetry group S is larger than the identity. The Wyckoff positions are those points whose site symmetry groups are conjugate subgroups of the space group [116]. Here conjugate means that we can write that relation between site symmetry groups S_1 and S_2 of two different positions as $S_1 = gS_2g^{-1}$, with g an operation of the space group. For example, S_1 and S_2 can both contain the identity and two rotations and g can be a translation, such that the rotations in S_1 and S_2 are about different axes. From this conjugation relation follows that the Wyckoff positions are classes of crystallographic orbits. The Wyckoff positions are labelled as follows; first comes a number, which indicated the number of positions in each orbit within one unit cell, meaning that this is the orbit without any integer translations. This is followed by a letter indicating the grade of symmetry, where 'a' labels points with the highest site symmetry, 'b' the points with the second highest symmetry, etc [117]. Extensive tables exist which list the Wyckoff positions for each crystallographic space group. In an ordered crystal, the atomic positions must transform into each other under the operations of the crystal space group, such that if we have an atom of type 1 in one unit cell, this atom must also exist in every other unit cell. This means that the atoms will sit on Wyckoff positions.

The Wyckoff positions are given in the coordinates of the conventional unit cell of the crystal structure. As discussed above, the conventional cell of the corundum structure, is the hexagonal, 30-atom unit cell. For the transition metal (TM) ions, i.e., Cr and Fe, the Wyckoff positions are (12c, local site symmetry 3.):

$$\left(0,\quad 0,\quad z\right),\ \left(0,\quad 0,\quad -z+\tfrac{1}{2}\right),\ \left(0,\quad 0,\quad z+\tfrac{1}{2}\right),\ \text{and}\ \left(0,\quad 0,\quad -z\right). \tag{3.10}$$

We call these TM_1-TM_4, where the numbering is the same as that in Figures 2.1a and 2.1b. As these only have non-zero z-coordinates and the Cartesian z axis lies along the hexagonal c axis, these coordinates directly translate to Cartesian coordinates, with $\frac{1}{2}$

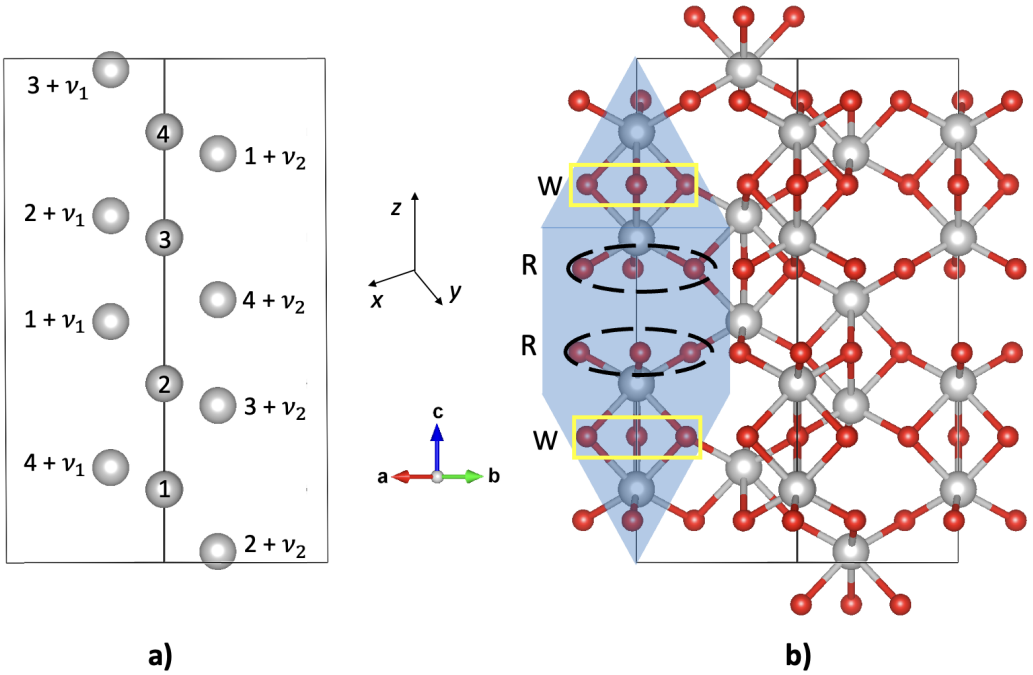

FIGURE 3.5: The conventional hexagonal 30-atom corundum unit cell of the corundum structure, with a) only the transition metal (TM) ions, and the Wyckoff positions (12c) where the 12 TM ions sit indicated, and b) with the TM ions, the oxygen (O) ions and the bonds, including ions beyond the boundary of the unit cell. The outline of the primitive, rhombohedral unit cell is indicated in blue, and the oxygens in the rhombohedral unit cell indicated with dashed black ellipses and a letter R, and the Wyckoff position oxygens indicated with solid yellow boxes and a W, indicating the relation between the O atoms in the primitive and conventional unit cells. Hexagonal and Cartesian axes are indicated in the center of the figure.

meaning $\frac{1}{2}$ of the unit cell length along the z axis. We note that the Wyckoff positions are 12c, indicating that there should be 12 atoms in the orbit of the unit cell. We can get the additional 8 TM position by performing the fractional translations $\nu_1 = \left(\frac{2}{3}, \frac{1}{3}, \frac{1}{3}\right)$ and $\nu_2 = \left(\frac{1}{3}, \frac{2}{3}, \frac{2}{3}\right)$, again in terms of the hexagonal unit cell vectors. We visualize all 12 TM sites in Figure 3.5a. We only need the first four positions for the symmetry analysis, as the other eight positions will obey the same symmetry relations, and none of the point group operations will exchange the first four positions with the other eight. We note that Eq. 3.10 shows how the Wyckoff positions are a class of crystallographic orbits. For these Wyckoff positions, there is one free variable, z. For every value of z the orbit is different, but it still belongs to Wyckoff position 12c. For the symmetry considerations, the specific value of z is not important, highlighting the power of the Wyckoff position classification. In our case for the corundum structure, the TM ions sit in positions with $0 < z < \frac{1}{4}$, but with a different z for Cr_2O_3 and Fe_2O_3.

For the oxygen (O) ions, the Wyckoff positions are (18e, local site symmetry .2):

$$\begin{gathered}\left(x,\ \ 0,\ \ \tfrac{1}{4}\right),\ \left(0,\ \ x,\ \ \tfrac{1}{4}\right),\ \left(-x,\ \ -x,\ \ \tfrac{1}{4}\right),\\ \left(-x,\ \ 0,\ \ \tfrac{3}{4}\right),\ \left(0,\ \ -x,\ \ \tfrac{3}{4}\right),\ \text{and}\ \left(x,\ \ x,\ \ \tfrac{3}{4}\right).\end{gathered} \tag{3.11}$$

We call these O_1-O_6, where the numbering is the same as that in Figures 2.1a and 2.1b.[5] Note that these coordinates are in hexagonal coordinates. As we chose the Cartesian coordinates such that $\boldsymbol{z} \parallel \boldsymbol{c}$ and $\boldsymbol{x} \parallel \boldsymbol{a}$, we have $\boldsymbol{b} \parallel -\frac{1}{2}\boldsymbol{x} + \frac{\sqrt{3}}{2}\boldsymbol{y}$. This means that in Cartesian coordinates the O ions are at:

$$\begin{gathered}\left(x,\ \ 0,\ \ \tfrac{1}{4}\right),\ \left(-\tfrac{1}{2}x,\ \ \tfrac{\sqrt{3}}{2}x,\ \ \tfrac{1}{4}\right),\ \left(-\tfrac{1}{2}x,\ \ -\tfrac{\sqrt{3}}{2}x,\ \ \tfrac{1}{4}\right),\\ \left(-x,\ \ 0,\ \ \tfrac{3}{4}\right),\ \left(\tfrac{1}{2}x,\ \ -\tfrac{\sqrt{3}}{2}x,\ \ \tfrac{3}{4}\right),\ \text{and}\ \left(\tfrac{1}{2}x,\ \ \tfrac{\sqrt{3}}{2}x,\ \ \tfrac{3}{4}\right).\end{gathered} \tag{3.12}$$

with $\frac{1}{4}$ and $\frac{3}{4}$, meaning $\frac{1}{4}$ and $\frac{3}{4}$ of the unit cell length along the z axis.

Finally, although we will be using the Wyckoff positions to analyze the symmetry restrictions on the TM and O ions, it is important to note that, for the O ions, the Wyckoff positions indicate oxygens that are different from the rhombohedral unit cell (Figure 3.5b). These two sets of O ions are of course related by translations, which is how the numbering in Figures 2.1a and 2.1b was obtained.

3.2.3 Symmetry operations on the positions

We can now perform the symmetry operations on the general coordinates (x, y, z) (Table 3.1). Note that, as the time-reversal operator leaves the real space coordinates invariant, the operations are the same in Cr_2O_3 and Fe_2O_3, and we denote them simply by inversion only. From the transformations of coordinates and the Wyckoff positions of the atoms, we can observe which atoms transform into each other under which symmetry operations (Table 3.2). We see that for each TM ion, 3 operations send the ion onto itself. For the O ions, there are two such operations.[6] We will use specifically these operations to constrain the allowed moments on these atoms. If operations send a specific atom to itself, then these operations must also leave the moment on this atom invariant. In general, this will restrict the shape this moment can take. Similarly, if an operation

[5] Similar as with the TM atoms, these are not all the positions in this orbit in the unit cell. The Wyckoff positions are 18e, indicating that there should be 18 atoms in the orbit of the unit cell. We can get the additional 12 O positions by performing the fractional translations ν_1 and ν_2, again in terms of the hexagonal unit cell vectors.

[6] These reflect the local site symmetry groups, 3. for the TM positions and .2 for the O positions.

sends atom 1 to atom 2, then the moment of atom 2 must take the shape of the moment on atom 1, transformed under this operation. In this manner, we can find the allowed ordering of the moments.

	E	C_{3z_1}	C_{3z_2}	$C_{2x}+f$	$C_{2[010]}+f$	$C_{2[110]}+f$
x	a	$-\frac{1}{2}(a+\sqrt{3}b)$	$\frac{1}{2}(-a+\sqrt{3}b)$	a	$-\frac{1}{2}(a+\sqrt{3}b)$	$\frac{1}{2}(-a+\sqrt{3}b)$
y	b	$\frac{1}{2}(\sqrt{3}a-b)$	$-\frac{1}{2}(\sqrt{3}a+b)$	$-b$	$\frac{1}{2}(-\sqrt{3}a+b)$	$\frac{1}{2}(\sqrt{3}a+b)$
z	c	c	c	$-c+\frac{1}{2}$	$-c+\frac{1}{2}$	$-c+\frac{1}{2}$
	I	IC_{3z_1}	IC_{3z_2}	$IC_{2x}+f$	$IC_{2[010]}+f$	$IC_{2[110]}+f$
x	$-a$	$\frac{1}{2}(a+\sqrt{3}b)$	$\frac{1}{2}(a-\sqrt{3}b)$	$-a$	$\frac{1}{2}(a+\sqrt{3}b)$	$\frac{1}{2}(a-\sqrt{3}b)$
y	$-b$	$\frac{1}{2}(-\sqrt{3}a+b)$	$\frac{1}{2}(\sqrt{3}a+b)$	b	$\frac{1}{2}(\sqrt{3}a-b)$	$-\frac{1}{2}(\sqrt{3}a+b)$
z	$-c$	$-c$	$-c$	$c+\frac{1}{2}$	$c+\frac{1}{2}$	$c+\frac{1}{2}$

TABLE 3.1: The transformation of the coordinates (a, b, c) under the 12 symmetry operations of the crystal symmetry point group.

	E	C_{3z_1}	C_{3z_2}	$C_{2x}+f$	$C_{2[010]}+f$	$C_{2[110]}+f$
Cr_i	Cr_1	Cr_1	Cr_1	Cr_2	Cr_2	Cr_2
Fe_i	Fe_1	Fe_1	Fe_1	Fe_2	Fe_2	Fe_2
O_i	O_1	O_2	O_3	O_1	O_3	O_2
	I	IC_{3z_1}	IC_{3z_2}	$IC_{2x}+f$	$IC_{2[010]}+f$	$IC_{2[110]}+f$
Cr_i	Cr_4	Cr_4	Cr_4	Cr_3	Cr_3	Cr_3
Fe_i	Fe_4	Fe_4	Fe_4	Fe_3	Fe_3	Fe_3
O_i	O_4	O_5	O_6	O_4	O_6	O_5

TABLE 3.2: The transformation of the different atoms into each other under the 12 symmetry operations of the crystal symmetry point group. The labeling and ordering of the atoms are based on the Wyckoff positions (Section 3.2.2), and follow the numbering in Figures 2.1a and 2.1b.

3.2.4 Symmetry operations on the magnetic dipole moments

We can now perform the same analysis for the transformation of a general magnetic dipole moment, but we should consider the symmetry carefully. As mentioned above, a real space translation leaves moment space, and thus the magnetic moments invariant, so we can remove the fractional translation indicated by f. Furthermore, we should be mindful of the difference in symmetry between Cr_2O_3 and Fe_2O_3.

In Cr_2O_3 inversion symmetry is broken by the magnetic ordering and is replaced by the product of time reversal Θ and inversion I. This product ΘI is preserved. As time reversal leaves the real space positions invariant, it was sufficient to just write inversion in the section above, even though for Cr_2O_3 this meant time reversal and

inversion. However, for the magnetic moments, the situation is reversed: inversion leaves the magnetic moments invariant, but time reversal causes a sign flip. Table 3.3 shows the transformation of a general magnetic moment $(m_\alpha, m_\beta, m_\gamma)$ under the symmetry operations, relevant for Cr_2O_3 and Fe_2O_3.

	E	C_{3z_1}	C_{3z_2}	C_{2x}	$C_{2[010]}$	$C_{2[110]}$
m_x	m_α	$-\frac{1}{2}(m_\alpha$ $+\sqrt{3}m_\beta)$	$\frac{1}{2}(-m_\alpha$ $+\sqrt{3}m_\beta)$	m_α	$-\frac{1}{2}(m_\alpha$ $+\sqrt{3}m_\beta)$	$\frac{1}{2}(-m_\alpha$ $+\sqrt{3}m_\beta)$
m_y	m_β	$\frac{1}{2}(\sqrt{3}m_\alpha$ $-m_\beta)$	$-\frac{1}{2}(\sqrt{3}m_\alpha$ $+m_\beta)$	$-m_\beta$	$\frac{1}{2}(-\sqrt{3}m_\alpha$ $+m_\beta)$	$\frac{1}{2}(\sqrt{3}m_\alpha$ $+m_\beta)$
m_z	m_γ	m_γ	m_γ	$-m_\gamma$	$-m_\gamma$	$-m_\gamma$
(Fe_2O_3)	I	IC_{3z_1}	IC_{3z_2}	IC_{2x}	$IC_{2[010]}$	$IC_{2[110]}$
m_x	m_α	$-\frac{1}{2}(m_\alpha$ $+\sqrt{3}m_\beta)$	$\frac{1}{2}(-m_\alpha$ $+\sqrt{3}m_\beta)$	m_α	$-\frac{1}{2}(m_\alpha$ $+\sqrt{3}m_\beta)$	$\frac{1}{2}(-m_\alpha$ $+\sqrt{3}m_\beta)$
m_y	m_β	$\frac{1}{2}(\sqrt{3}m_\alpha$ $-m_\beta)$	$-\frac{1}{2}(\sqrt{3}m_\alpha$ $+m_\beta)$	$-m_\beta$	$\frac{1}{2}(-\sqrt{3}m_\alpha$ $+m_\beta)$	$\frac{1}{2}(\sqrt{3}m_\alpha$ $+m_\beta)$
m_z	m_γ	m_γ	m_γ	$-m_\gamma$	$-m_\gamma$	$-m_\gamma$
(Cr_2O_3)	ΘI	ΘIC_{3z_1}	ΘIC_{3z_2}	ΘIC_{2x}	$\Theta IC_{2[010]}$	$\Theta IC_{2[110]}$
m_x	$-m_\alpha$	$\frac{1}{2}(m_\alpha$ $+\sqrt{3}m_\beta)$	$\frac{1}{2}(m_\alpha$ $-\sqrt{3}m_\beta)$	$-m_\alpha$	$\frac{1}{2}(m_\alpha$ $+\sqrt{3}m_\beta)$	$\frac{1}{2}(m_\alpha$ $-\sqrt{3}m_\beta)$
m_y	$-m_\beta$	$\frac{1}{2}(-\sqrt{3}m_\alpha$ $+m_\beta)$	$\frac{1}{2}(\sqrt{3}m_\alpha$ $+m_\beta)$	m_β	$\frac{1}{2}(\sqrt{3}m_\alpha$ $-m_\beta)$	$-\frac{1}{2}(\sqrt{3}m_\alpha$ $+m_\beta)$
m_z	$-m_\gamma$	$-m_\gamma$	$-m_\gamma$	m_γ	m_γ	m_γ

TABLE 3.3: The transformation of a general magnetic moment $(m_\alpha, m_\beta, m_\gamma)$ under the 12 symmetry operations of the crystal symmetry point group.

By combining the information from Tables 3.2 and 3.3 we can conclude which moments are allowed on which atoms. We see in Table 3.2 that there are three operations that transform Cr_1 to itself: The identity operator, E, the counterclockwise rotation of $\frac{2\pi}{3}$ around the z- xis, C_{3z^1}, and the counterclockwise rotation of $\frac{4\pi}{3}$ around the z axis, C_{3z^2}. This means that the moment that is allowed on Cr_1 must also be preserved by these operations. Now from Table 3.3 we see that under E, C_{3z^1} and C_{3z^2}, the x-component of the moment m_α transforms into m_α, $-\frac{1}{2}(m_\alpha+\sqrt{3}m_\beta)$ and $\frac{1}{2}(-m_\alpha+\sqrt{3}m_\beta)$, respectively. On our Cr atom, these must be the same, which means that both m_α and m_β (x- and y-components) must be zero. Only the z-component is allowed on Cr_1, as that one remains invariant under E, C_{3z^1} and C_{3z^2}. We can furthermore deduce the ordering of the allowed moments. For example, the three operations C_{2x}, $C_{2[010]}$ and $C_{2[110]}$ all transform Cr_1 into Cr_2. Furthermore, they transform a moment $(0, 0, m_\gamma)$ into $(0, , -m_\gamma)$. This means

that the moment on Cr_2 must be opposite to the one on Cr_1. The allowed moments and their ordering are summarized in Table 3.4.

(Cr_2O_3)	Cr_1	Cr_2	Cr_3	Cr_4		
m_z	$+m_\gamma$	$-m_\gamma$	$+m_\gamma$	$-m_\gamma$		
	O_1	O_2	O_3	O_4	O_5	O_6
m_x	m_α	$-\frac{1}{2}m_\alpha$	$-\frac{1}{2}m_\alpha$	$-m_\alpha$	$\frac{1}{2}m_\alpha$	$\frac{1}{2}m_\alpha$
m_y	0	$\frac{\sqrt{3}}{2}m_\alpha$	$-\frac{\sqrt{3}}{2}m_\alpha$	0	$-\frac{\sqrt{3}}{2}m_\alpha$	$\frac{\sqrt{3}}{2}m_\alpha$
(Fe_2O_3)	Fe_1	Fe_2	Fe_3	Fe_4		
m_z	$+m_\gamma$	$-m_\gamma$	$-m_\gamma$	$+m_\gamma$		
	O_1	O_2	O_3	O_4	O_5	O_6
mx	m_α	$-\frac{1}{2}m_\alpha$	$-\frac{1}{2}m_\alpha$	m_α	$-\frac{1}{2}m_\alpha$	$-\frac{1}{2}m_\alpha$
my	0	$\frac{\sqrt{3}}{2}m_\alpha$	$-\frac{\sqrt{3}}{2}m_\alpha$	0	$\frac{\sqrt{3}}{2}m_\alpha$	$-\frac{\sqrt{3}}{2}m_\alpha$

TABLE 3.4: The symmetry-allowed ordering of the magnetic dipole moments on the Cr, Fe, and O atoms in Cr_2O_3 and Fe_2O_3 transformation of the different atoms into each other under the 12 symmetry operations of the crystal symmetry point group. The labeling and ordering of the atoms are based on the Wyckoff positions (Section 3.2.2), and follow the numbering in Figures 2.1a and 2.1b.

We can see (Table 3.4) that the difference in symmetry leads to different allowed patterns for not just the magnetic moments on the Cr and Fe atoms, but also those on the O atoms. These patterns are displayed in Figure 3.6.

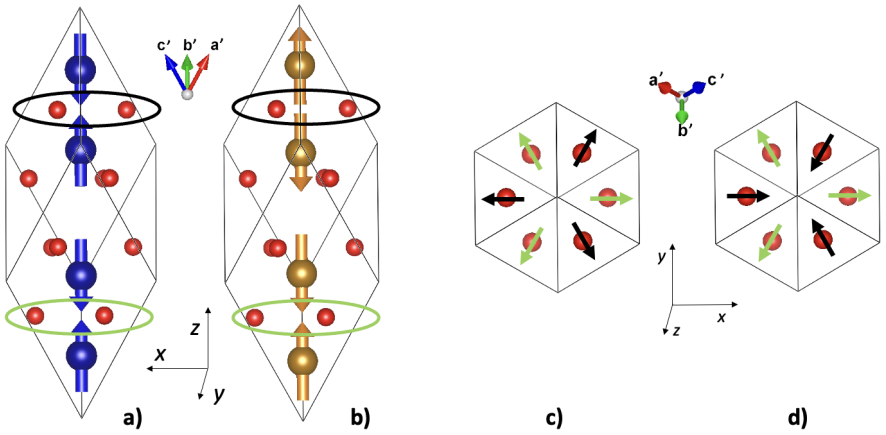

FIGURE 3.6: The allowed order of the magnetic moments in Cr_2O_3 (a,c) and Fe_2O_3 (b,d). Side views of the rhombohedral unit cells show the moments on the transition metal (TM) ions (a,b), with the Wyckoff position oxygens circled in green and black, and top views of the 6 Wyckoff position oxygens show the moment on the O ions (c,d). Cr atoms are indicated in blue, Fe atoms in gold, and O atoms in red. Moments on the oxygens are indicated with green and black, with the colors of the moments corresponding to the colors of the circled positions in panels a and b.

3.2.5 Symmetry operations on components of the magnetoelectric multipole tensor

Using the symmetry operations on the positions and the magnetic dipole moments, we can determine the symmetry-allowed magnetic dipole structure. Similarly, we can use the way the symmetry operations act on the different components of the ME multipole tensor (Eq. 1.8) to discover the symmetry constraints on the local components of this tensor.

	E	C_{3z_1}	C_{3z_2}
$\mathcal{M}_{11} \sim xm_x$	am_α	$\frac{1}{4}(a+\sqrt{3}b)(m_\alpha+\sqrt{3}m_\beta)$	$\frac{1}{4}(-a+\sqrt{3}b)(-m_\alpha+\sqrt{3}m_\beta)$
$\mathcal{M}_{12} \sim xm_y$	am_β	$-\frac{1}{4}(a+\sqrt{3}b)(\sqrt{3}m_\alpha-m_\beta)$	$-\frac{1}{4}(-a+\sqrt{3}b)(\sqrt{3}m_\alpha+m_\beta)$
$\mathcal{M}_{13} \sim xm_z$	am_γ	$-\frac{1}{2}(a+\sqrt{3}b)m_\gamma$	$\frac{1}{2}(-a+\sqrt{3}b)m_\gamma$
$\mathcal{M}_{21} \sim ym_x$	bm_α	$-\frac{1}{4}(\sqrt{3}a-b)(m_\alpha+\sqrt{3}m_\beta)$	$-\frac{1}{4}(\sqrt{3}a+b)(-m_\alpha+\sqrt{3}m_\beta)$
$\mathcal{M}_{22} \sim ym_y$	bm_β	$\frac{1}{4}(\sqrt{3}a-b)(\sqrt{3}m_\alpha-m_\beta)$	$\frac{1}{4}(\sqrt{3}a+b)(\sqrt{3}m_\alpha+m_\beta)$
$\mathcal{M}_{23} \sim ym_z$	bm_γ	$\frac{1}{2}(\sqrt{3}a-b)m_\gamma$	$-\frac{1}{2}(\sqrt{3}a+b)m_\gamma$
$\mathcal{M}_{31} \sim zm_x$	cm_α	$-\frac{1}{2}c(m_\alpha+\sqrt{3}m_\beta)$	$\frac{1}{2}c(-m_\alpha+\sqrt{3}m_\beta)$
$\mathcal{M}_{32} \sim zm_y$	cm_β	$\frac{1}{2}c(\sqrt{3}m_\alpha-m_\beta)$	$-\frac{1}{2}c(\sqrt{3}m_\alpha+m_\beta)$
$\mathcal{M}_{33} \sim zm_z$	cm_γ	cm_γ	cm_γ
	$C_{2x}(+f)$	$C_{2[010]}(+f)$	$C_{2[110]}(+f)$
$\mathcal{M}_{11} \sim xm_x$	am_α	$\frac{1}{4}(a+\sqrt{3}b)(m_\alpha+\sqrt{3}m_\beta)$	$\frac{1}{4}(-a+\sqrt{3}b)(-m_\alpha+\sqrt{3}m_\beta)$
$\mathcal{M}_{12} \sim xm_y$	$-am_\beta$	$\frac{1}{4}(a+\sqrt{3}b)(\sqrt{3}m_\alpha-m_\beta)$	$\frac{1}{4}(-a+\sqrt{3}b)(\sqrt{3}m_\alpha+m_\beta)$
$\mathcal{M}_{13} \sim xm_z$	$-am_\gamma$	$\frac{1}{2}(a+\sqrt{3}b)m_\gamma$	$\frac{1}{2}(a-\sqrt{3}b)m_\gamma$
$\mathcal{M}_{21} \sim ym_x$	$-bm_\alpha$	$\frac{1}{4}(\sqrt{3}a-b)(m_\alpha+\sqrt{3}m_\beta)$	$\frac{1}{4}(\sqrt{3}a+b)(-m_\alpha+\sqrt{3}m_\beta)$
$\mathcal{M}_{22} \sim ym_y$	bm_β	$\frac{1}{4}(-\sqrt{3}a+b)(-\sqrt{3}m_\alpha+m_\beta)$	$\frac{1}{4}(\sqrt{3}a+b)(\sqrt{3}m_\alpha+m_\beta)$
$\mathcal{M}_{23} \sim ym_z$	bm_γ	$\frac{1}{2}(\sqrt{3}a-b)m_\gamma$	$-\frac{1}{2}(\sqrt{3}a+b)m_\gamma$
$\mathcal{M}_{31} \sim zm_x$	$-cm_\alpha$	$\frac{1}{2}c(m_\alpha+\sqrt{3}m_\beta)$	$\frac{1}{2}c(m_\alpha-\sqrt{3}m_\beta)$
$\mathcal{M}_{32} \sim zm_y$	cm_β	$\frac{1}{2}c(\sqrt{3}m_\alpha-m_\beta)$	$-\frac{1}{2}c(\sqrt{3}m_\alpha+m_\beta)$
$\mathcal{M}_{33} \sim zm_z$	cm_γ	cm_γ	cm_γ

TABLE 3.5: The transformation of the nine components of the magnetoelectric multipole tensor $\mathcal{M}_{ij} \sim r_i M_j$ under the first 6 of the 12 symmetry operations of the crystal symmetry point group.

As the volume is invariant under all rotations and under both inversion and time reversal, for the symmetry, it is sufficient to consider the integrand: $r_i m_j$. The transformations of $r_i m_j$ under the first six symmetry operations are displayed in Table 3.5, under the second six operations, including time reversal in Table 3.6, and under the second six operation without time reversal in Table 3.7.

	ΘI	ΘIC_{3z_1}	ΘIC_{3z_2}
$\mathcal{M}_{11} \sim xm_x$	am_α	$\frac{1}{4}(a+\sqrt{3}b)(m_\alpha+\sqrt{3}m_\beta)$	$\frac{1}{4}(a-\sqrt{3}b)(m_\alpha-\sqrt{3}m_\beta)$
$\mathcal{M}_{12} \sim xm_y$	am_β	$\frac{1}{4}(a+\sqrt{3}b)(-\sqrt{3}m_\alpha+m_\beta)$	$\frac{1}{4}(a-\sqrt{3}b)(\sqrt{3}m_\alpha+m_\beta)$
$\mathcal{M}_{13} \sim xm_z$	am_γ	$-\frac{1}{2}(a+\sqrt{3}b)m_\gamma$	$-\frac{1}{2}(a-\sqrt{3}b)m_\gamma$
$\mathcal{M}_{21} \sim ym_x$	bm_α	$\frac{1}{4}(-\sqrt{3}a+b)(m_\alpha+\sqrt{3}m_\beta)$	$\frac{1}{4}(\sqrt{3}a+b)(m_\alpha-\sqrt{3}m_\beta)$
$\mathcal{M}_{22} \sim ym_y$	bm_β	$\frac{1}{4}(-\sqrt{3}a+b)(-\sqrt{3}m_\alpha+m_\beta)$	$\frac{1}{4}(\sqrt{3}a+b)(\sqrt{3}m_\alpha+m_\beta)$
$\mathcal{M}_{23} \sim ym_z$	bm_γ	$-\frac{1}{2}(-\sqrt{3}a+b)m_\gamma$	$-\frac{1}{2}(\sqrt{3}a+b)m_\gamma$
$\mathcal{M}_{31} \sim zm_x$	cm_α	$-\frac{1}{2}c(m_\alpha+\sqrt{3}m_\beta)$	$-\frac{1}{2}c(m_\alpha-\sqrt{3}m_\beta)$
$\mathcal{M}_{32} \sim zm_y$	cm_β	$\frac{1}{2}c(\sqrt{3}m_\alpha-m_\beta)$	$\frac{1}{2}c(\sqrt{3}m_\alpha+m_\beta)$
$\mathcal{M}_{33} \sim zm_z$	cm_γ	cm_γ	cm_γ
	$\Theta IC_{2x}(+f)$	$\Theta IC_{2[010]}(+f)$	$\Theta IC_{2[110]}(+f)$
$\mathcal{M}_{11} \sim xm_x$	am_α	$\frac{1}{4}(a+\sqrt{3}b)(m_\alpha+\sqrt{3}m_\beta)$	$\frac{1}{4}(a-\sqrt{3}b)(m_\alpha-\sqrt{3}m_\beta)$
$\mathcal{M}_{12} \sim xm_y$	$-am_\beta$	$\frac{1}{4}(a+\sqrt{3}b)(\sqrt{3}m_\alpha-m_\beta)$	$-\frac{1}{4}(a-\sqrt{3}b)(\sqrt{3}m_\alpha+m_\beta)$
$\mathcal{M}_{13} \sim xm_z$	$-am_\gamma$	$\frac{1}{2}(a+\sqrt{3}b)m_\gamma$	$\frac{1}{2}(a-\sqrt{3}b)m_\gamma$
$\mathcal{M}_{21} \sim ym_x$	$-bm_\alpha$	$\frac{1}{4}(\sqrt{3}a-b)(m_\alpha+\sqrt{3}m_\beta)$	$-\frac{1}{4}(\sqrt{3}a+b)(m_\alpha-\sqrt{3}m_\beta)$
$\mathcal{M}_{22} \sim ym_y$	bm_β	$\frac{1}{4}(\sqrt{3}a-b)(\sqrt{3}m_\alpha-m_\beta)$	$\frac{1}{4}(\sqrt{3}a+b)(\sqrt{3}m_\alpha+m_\beta)$
$\mathcal{M}_{23} \sim ym_z$	bm_γ	$\frac{1}{2}(\sqrt{3}a-b)m_\gamma$	$-\frac{1}{2}(\sqrt{3}a+b)m_\gamma$
$\mathcal{M}_{31} \sim zm_x$	$-cm_\alpha$	$\frac{1}{2}c(m_\alpha+\sqrt{3}m_\beta)$	$\frac{1}{2}c(m_\alpha-\sqrt{3}m_\beta)$
$\mathcal{M}_{32} \sim zm_y$	cm_β	$\frac{1}{2}c(\sqrt{3}m_\alpha-m_\beta)$	$-\frac{1}{2}c(\sqrt{3}m_\alpha+m_\beta)$
$\mathcal{M}_{33} \sim zm_z$	cm_γ	cm_γ	cm_γ

TABLE 3.6: The transformation of the nine components of the magnetoelectric multipole tensor $\mathcal{M}_{ij} \sim r_i m_j$ under the second 6 of the 12 symmetry operations of the crystal symmetry point group, including time-reversal symmetry, as in Cr_2O_3.

We can use the knowledge from Table 3.2, telling us how the atoms transform, to construct the symmetry restrictions on the components of the ME multipole tensor $\mathcal{M}_{ij}$.

	I	IC_{3z_1}	IC_{3z_2}
$\mathcal{M}_{11} \sim xm_x$	$-am_\alpha$	$-\frac{1}{4}(a+\sqrt{3}b)(m_\alpha+\sqrt{3}m_\beta)$	$\frac{1}{4}(a-\sqrt{3}b)(-m_\alpha+\sqrt{3}m_\beta)$
$\mathcal{M}_{12} \sim xm_y$	$-am_\beta$	$\frac{1}{4}(a+\sqrt{3}b)(\sqrt{3}m_\alpha-m_\beta)$	$\frac{1}{4}(-a+\sqrt{3}b)(\sqrt{3}m_\alpha+m_\beta)$
$\mathcal{M}_{13} \sim xm_z$	$-am_\gamma$	$\frac{1}{2}(a+\sqrt{3}b)m_\gamma$	$\frac{1}{2}(a-\sqrt{3}b)m_\gamma$
$\mathcal{M}_{21} \sim ym_x$	$-bm_\alpha$	$\frac{1}{4}(\sqrt{3}a-b)(m_\alpha+\sqrt{3}m_\beta)$	$\frac{1}{4}(\sqrt{3}a+b)(-m_\alpha+\sqrt{3}m_\beta)$
$\mathcal{M}_{22} \sim ym_y$	$-bm_\beta$	$\frac{1}{4}(-\sqrt{3}a+b)(\sqrt{3}m_\alpha-m_\beta)$	$-\frac{1}{4}(\sqrt{3}a+b)(\sqrt{3}m_\alpha+m_\beta)$
$\mathcal{M}_{23} \sim ym_z$	$-bm_\gamma$	$\frac{1}{2}(-\sqrt{3}a+b)m_\gamma$	$\frac{1}{2}(\sqrt{3}a+b)m_\gamma$
$\mathcal{M}_{31} \sim zm_x$	$-cm_\alpha$	$\frac{1}{2}c(m_\alpha+\sqrt{3}m_\beta)$	$\frac{1}{2}c(m_\alpha-\sqrt{3}m_\beta)$
$\mathcal{M}_{32} \sim zm_y$	$-cm_\beta$	$\frac{1}{2}c(-\sqrt{3}m_\alpha+m_\beta)$	$\frac{1}{2}c(\sqrt{3}m_\alpha+m_\beta)$
$\mathcal{M}_{33} \sim zm_z$	$-cm_\gamma$	$-cm_\gamma$	$-cm_\gamma$
	$IC_{2x}(+f)$	$IC_{2[010]}(+f)$	$IC_{2[110]}(+f)$
$\mathcal{M}_{11} \sim xm_x$	$-am_\alpha$	$-\frac{1}{4}(a+\sqrt{3}b)(m_\alpha+\sqrt{3}m_\beta)$	$\frac{1}{4}(a-\sqrt{3}b)(-m_\alpha+\sqrt{3}m_\beta)$
$\mathcal{M}_{12} \sim xm_y$	am_β	$\frac{1}{4}(a+\sqrt{3}b)(-\sqrt{3}m_\alpha+m_\beta)$	$\frac{1}{4}(a-\sqrt{3}b)(\sqrt{3}m_\alpha+m_\beta)$
$\mathcal{M}_{13} \sim xm_z$	am_γ	$-\frac{1}{2}(a+\sqrt{3}b)m_\gamma$	$\frac{1}{2}(-a+\sqrt{3}b)m_\gamma$
$\mathcal{M}_{21} \sim ym_x$	bm_α	$\frac{1}{4}(-\sqrt{3}a+b)(m_\alpha+\sqrt{3}m_\beta)$	$\frac{1}{4}(\sqrt{3}a+b)(m_\alpha-\sqrt{3}m_\beta)$
$\mathcal{M}_{22} \sim ym_y$	$-bm_\beta$	$\frac{1}{4}(\sqrt{3}a-b)(-\sqrt{3}m_\alpha+m_\beta)$	$-\frac{1}{4}(\sqrt{3}a+b)(\sqrt{3}m_\alpha+m_\beta)$
$\mathcal{M}_{23} \sim ym_z$	$-bm_\gamma$	$\frac{1}{2}(-\sqrt{3}a+b)m_\gamma$	$\frac{1}{2}(\sqrt{3}a+b)m_\gamma$
$\mathcal{M}_{31} \sim zm_x$	cm_α	$-\frac{1}{2}c(m_\alpha+\sqrt{3}m_\beta)$	$\frac{1}{2}c(-m_\alpha+\sqrt{3}m_\beta)$
$\mathcal{M}_{32} \sim zm_y$	$-cm_\beta$	$\frac{1}{2}c(-\sqrt{3}m_\alpha+m_\beta)$	$\frac{1}{2}c(\sqrt{3}m_\alpha+m_\beta)$
$\mathcal{M}_{33} \sim zm_z$	$-cm_\gamma$	$-cm_\gamma$	$-cm_\gamma$

TABLE 3.7: The transformation of the nine components of the magnetoelectric multipole tensor $\mathcal{M}_{ij} \sim r_i m_j$ under the second 6 of the 12 symmetry operations of the crystal symmetry point group, excluding time-reversal symmetry, as in Fe_2O_3.

3.2.5.1 Cr_2O_3

Let's take Cr_1 as an example again. We know from Table 3.2 that E, C_{3z^1} and C_{3z^2} transform this atoms onto itself. Simultaneously we see in Table 3.5 how these operations act on the nine components of the ME tensor. When we look at the first component M_{11}, on $Cr1$ it needs to stay the same under E, C_{3z^1} and C_{3z^2}, we see that this leads to the following relations:

$$am_\alpha = \frac{1}{4}(a+\sqrt{3}b)(m_\alpha+\sqrt{3}m_\beta) = \frac{1}{4}(-a+\sqrt{3}b)(-m_\alpha+\sqrt{3}m_\beta), \tag{3.13}$$

which we can expand to read

$$am_\alpha = \frac{1}{4}am_\alpha + \frac{\sqrt{3}}{4}bm_\alpha + \frac{\sqrt{3}}{4}am_\beta + \frac{3}{4}bm_\beta = \frac{1}{4}am_\alpha - \frac{\sqrt{3}}{4}bm_\alpha - \frac{\sqrt{3}}{4}am_\beta + \frac{3}{4}bm_\beta, \tag{3.14}$$

which means, in terms of $\mathcal{M}_{ij}$:

$$\mathcal{M}_{\alpha\alpha} = \frac{1}{4}\mathcal{M}_{\alpha\alpha} + \frac{\sqrt{3}}{4}\mathcal{M}_{\beta\alpha} + \frac{\sqrt{3}}{4}\mathcal{M}_{\alpha\beta} + \frac{3}{4}\mathcal{M}_{\beta\beta} = \frac{1}{4}\mathcal{M}_{\alpha\alpha} - \frac{\sqrt{3}}{4}\mathcal{M}_{\beta\alpha} - \frac{\sqrt{3}}{4}\mathcal{M}_{\alpha\beta} + \frac{3}{4}\mathcal{M}_{\beta\beta}, \tag{3.15}$$

from which we see that first of all:

$$\frac{\sqrt{3}}{4}\mathcal{M}_{\beta\alpha} + \frac{\sqrt{3}}{4}\mathcal{M}_{\alpha\beta} = -\frac{\sqrt{3}}{4}\mathcal{M}_{\beta\alpha} + -\frac{\sqrt{3}}{4}\mathcal{M}_{\alpha\beta} = 0 \;\rightarrow\; \mathcal{M}_{\beta\alpha} = -\mathcal{M}_{\alpha\beta}, \tag{3.16}$$

and secondly:

$$\mathcal{M}_{\alpha\alpha} = \frac{1}{4}\mathcal{M}_{\alpha\alpha} + \frac{3}{4}\mathcal{M}_{\beta\beta} \;\rightarrow\; \mathcal{M}_{\alpha\alpha} = \mathcal{M}_{\beta\beta}. \tag{3.17}$$

Similarly, we can explore how the operations work on the other components and extract relations from that. This will lead us to the following form for the local ME multipole tensor on Cr_1 in Cr_2O_3:

$$\mathcal{M}_{Cr_1} = \begin{pmatrix} \mathcal{M}_{\alpha\alpha} & \mathcal{M}_{\alpha\beta} & 0 \\ -\mathcal{M}_{\alpha\beta} & \mathcal{M}_{\alpha\alpha} & 0 \\ 0 & 0 & \mathcal{M}_{\gamma\gamma} \end{pmatrix}, \tag{3.18}$$

which is consistent with the local site symmetry of the Cr Wyckoff sites (3). For the other Cr atoms we can look at the restrictions placed on the symmetry operations by them (for example for Cr_2, the operations $C_{2x}, C_{2[010]}$ and $C_{2[110]}$ all transform Cr_1 to Cr_2, so their result should be the same), or we can transform the symmetry-allowed tensor of Cr_1 (Eq. 3.18) by one of the symmetries that send Cr_1 to another Cr.

We can do the same for the oxygen atoms. For O_1 this will give us:

$$\mathcal{M}_{O_1} = \begin{pmatrix} \mathcal{M}_{\alpha\alpha} & 0 & 0 \\ 0 & \mathcal{M}_{\beta\beta} & \mathcal{M}_{\beta\gamma} \\ 0 & \mathcal{M}_{\gamma\beta} & \mathcal{M}_{\gamma\gamma} \end{pmatrix}, \tag{3.19}$$

which has fewer symmetry restrictions than the tensor on the Cr atoms. Again the found tensor is consistent with the local site symmetry of the oxygen Wyckoff sites (2). Also, because of the 120-degree rotations, the allowed tensor on the other oxygen atoms becomes more complex, as the terms are mixed by these operations.

The results for the ME multipole tensor for the Cr and O atoms in Cr_2O_3 can be found in Table 3.8 and Table 3.9, respectively.

	Cr_1	Cr_2	Cr_3	Cr_4
$\mathcal{M}_{11}$	$\mathcal{M}_{\alpha\alpha}$	$\mathcal{M}_{\alpha\alpha}$	$\mathcal{M}_{\alpha\alpha}$	$\mathcal{M}_{\alpha\alpha}$
$\mathcal{M}_{12}$	$\mathcal{M}_{\alpha\beta}$	$-\mathcal{M}_{\alpha\beta}$	$-\mathcal{M}_{\alpha\beta}$	$\mathcal{M}_{\alpha\beta}$
$\mathcal{M}_{21}$	$-\mathcal{M}_{\alpha\beta}$	$\mathcal{M}_{\alpha\beta}$	$\mathcal{M}_{\alpha\beta}$	$-\mathcal{M}_{\alpha\beta}$
$\mathcal{M}_{22}$	$\mathcal{M}_{\alpha\alpha}$	$\mathcal{M}_{\alpha\alpha}$	$\mathcal{M}_{\alpha\alpha}$	$\mathcal{M}_{\alpha\alpha}$
$\mathcal{M}_{33}$	$\mathcal{M}_{\gamma\gamma}$	$\mathcal{M}_{\gamma\gamma}$	$\mathcal{M}_{\gamma\gamma}$	$\mathcal{M}_{\gamma\gamma}$

TABLE 3.8: The symmetry-allowed ordering of the magnetoelectric tensor on the Cr atoms in Cr_2O_3. The not-displayed elements are all zero.

	O_1	O_2	O_3	O_4	O_5	O_6
M_{11}	$\mathcal{M}_{\alpha\alpha}$	$\frac{1}{4}\mathcal{M}_{\alpha\alpha}$ $+\frac{3}{4}\mathcal{M}_{\beta\beta}$	$\frac{1}{4}\mathcal{M}_{\alpha\alpha}$ $+\frac{3}{4}\mathcal{M}_{\beta\beta}$	$\mathcal{M}_{\alpha\alpha}$	$\frac{1}{4}\mathcal{M}_{\alpha\alpha}$ $+\frac{3}{4}\mathcal{M}_{\beta\beta}$	$\frac{1}{4}\mathcal{M}_{\alpha\alpha}$ $+\frac{3}{4}\mathcal{M}_{\beta\beta}$
M_{12}	0	$-\frac{\sqrt{3}}{4}\mathcal{M}_{\alpha\alpha}$ $+\frac{\sqrt{3}}{4}\mathcal{M}_{\beta\beta}$	$\frac{\sqrt{3}}{4}\mathcal{M}_{\alpha\alpha}$ $-\frac{\sqrt{3}}{4}\mathcal{M}_{\beta\beta}$	0	$-\frac{\sqrt{3}}{4}\mathcal{M}_{\alpha\alpha}$ $+\frac{\sqrt{3}}{4}\mathcal{M}_{\beta\beta}$	$\frac{\sqrt{3}}{4}\mathcal{M}_{\alpha\alpha}$ $-\frac{\sqrt{3}}{4}\mathcal{M}_{\beta\beta}$
M_{13}	0	$-\frac{\sqrt{3}}{2}\mathcal{M}_{\beta\gamma}$	$\frac{\sqrt{3}}{2}\mathcal{M}_{\beta\gamma}$	0	$-\frac{\sqrt{3}}{2}\mathcal{M}_{\beta\gamma}$	$\frac{\sqrt{3}}{2}\mathcal{M}_{\beta\gamma}$
M_{21}	0	$-\frac{\sqrt{3}}{4}\mathcal{M}_{\alpha\alpha}$ $+\frac{\sqrt{3}}{4}\mathcal{M}_{\beta\beta}$	$\frac{\sqrt{3}}{4}\mathcal{M}_{\alpha\alpha}$ $-\frac{\sqrt{3}}{4}\mathcal{M}_{\beta\beta}$	0	$-\frac{\sqrt{3}}{4}\mathcal{M}_{\alpha\alpha}$ $+\frac{\sqrt{3}}{4}\mathcal{M}_{\beta\beta}$	$\frac{\sqrt{3}}{4}\mathcal{M}_{\alpha\alpha}$ $-\frac{\sqrt{3}}{4}\mathcal{M}_{\beta\beta}$
M_{22}	$\mathcal{M}_{\beta\beta}$	$\frac{3}{4}\mathcal{M}_{\alpha\alpha}$ $+\frac{1}{4}\mathcal{M}_{\beta\beta}$	$\frac{3}{4}\mathcal{M}_{\alpha\alpha}$ $+\frac{1}{4}\mathcal{M}_{\beta\beta}$	$\mathcal{M}_{\beta\beta}$	$\frac{3}{4}\mathcal{M}_{\alpha\alpha}$ $+\frac{1}{4}\mathcal{M}_{\beta\beta}$	$\frac{3}{4}\mathcal{M}_{\alpha\alpha}$ $+\frac{1}{4}\mathcal{M}_{\beta\beta}$
M_{23}	$\mathcal{M}_{\beta\gamma}$	$-\frac{1}{2}\mathcal{M}_{\beta\gamma}$	$-\frac{1}{2}\mathcal{M}_{\beta\gamma}$	$\mathcal{M}_{\beta\gamma}$	$-\frac{1}{2}\mathcal{M}_{\beta\gamma}$	$-\frac{1}{2}\mathcal{M}_{\beta\gamma}$
M_{31}	0	$-\frac{\sqrt{3}}{2}\mathcal{M}_{\gamma\beta}$	$\frac{\sqrt{3}}{2}\mathcal{M}_{\gamma\beta}$	0	$-\frac{\sqrt{3}}{2}\mathcal{M}_{\gamma\beta}$	$\frac{\sqrt{3}}{2}\mathcal{M}_{\gamma\beta}$
M_{32}	$\mathcal{M}_{\gamma\beta}$	$-\frac{1}{2}\mathcal{M}_{\gamma\beta}$	$-\frac{1}{2}\mathcal{M}_{\gamma\beta}$	$\mathcal{M}_{\gamma\beta}$	$-\frac{1}{2}\mathcal{M}_{\gamma\beta}$	$-\frac{1}{2}\mathcal{M}_{\gamma\beta}$
M_{33}	$\mathcal{M}_{\gamma\gamma}$	$\mathcal{M}_{\gamma\gamma}$	$\mathcal{M}_{\gamma\gamma}$	$\mathcal{M}_{\gamma\gamma}$	$\mathcal{M}_{\gamma\gamma}$	$\mathcal{M}_{\gamma\gamma}$

TABLE 3.9: The symmetry-allowed ordering of the magnetoelectric tensor on the O atoms in Cr_2O_3.

We see that for the Cr atoms, the ME multipole tensor keeps its shape, and only the sign of the off-diagonal elements changes. When we sum the contributions of the four different atoms, the off-diagonal contributions cancel. When we look at the O atoms, we see that the elements of the ME multipole tensor get mixed, due to the 120° ($\frac{2\pi}{3}$) rotation.

However, when we add up the contributions of all the oxygens, all the off-diagonal elements cancel out as well. Moreover, it turns out that $\mathcal{M}_{11}^{total} = \mathcal{M}_{22}^{total}$. Thus, we find that, adding the contributions of all the atoms, the total ME multipole tensor has the following shape:

$$\mathcal{M}_{Cr_2O_3} = \begin{pmatrix} \mathcal{M}_{11} & 0 & 0 \\ 0 & \mathcal{M}_{11} & 0 \\ 0 & 0 & \mathcal{M}_{33} \end{pmatrix}. \tag{3.20}$$

This is exactly the shape we know the ME tensor for Cr_2O_3 to have, i.e., $\alpha_{11} = \alpha_{22} \neq 0$ and $\alpha_{33} \neq 0$ indicating that our results for the local and global ME multipole tensor $\mathcal{M}_{ij}$ are consistent with the known results for the global ME tensor α_{ij}.

3.2.5.2 Fe_2O_3

Now we can do the same thing for Fe_2O_3, keeping in mind that for Fe_2O_3 we do not have broken inversion symmetry, and we do not need to replace the inversion operation with the product of time reversal and inversion. Thus, the effect of the second 6 operations is different, see Table 3.7. As the first 6 operations are the same, we find the same shapes for the ME tensor on Fe_1 and O_1 in Fe_2O_3 as we did for Cr_1 and O_1 in Cr_2O_3, i.e.:

$$\mathcal{M}_{Fe_1} = \begin{pmatrix} \mathcal{M}_{\alpha\alpha} & \mathcal{M}_{\alpha\beta} & 0 \\ -\mathcal{M}_{\alpha\beta} & \mathcal{M}_{\alpha\alpha} & 0 \\ 0 & 0 & \mathcal{M}_{\gamma\gamma} \end{pmatrix}, \tag{3.21}$$

and

$$\mathcal{M}_{O_1} = \begin{pmatrix} \mathcal{M}_{\alpha\alpha} & 0 & 0 \\ 0 & \mathcal{M}_{\beta\beta} & \mathcal{M}_{\beta\gamma} \\ 0 & \mathcal{M}_{\gamma\beta} & \mathcal{M}_{\gamma\gamma} \end{pmatrix}. \tag{3.22}$$

	Fe_1	Fe_2	Fe_3	Fe_4
$\mathcal{M}_{11}$	$\mathcal{M}_{\alpha\alpha}$	$\mathcal{M}_{\alpha\alpha}$	$-\mathcal{M}_{\alpha\alpha}$	$-\mathcal{M}_{\alpha\alpha}$
$\mathcal{M}_{12}$	$\mathcal{M}_{\alpha\beta}$	$-\mathcal{M}_{\alpha\beta}$	$\mathcal{M}_{\alpha\beta}$	$-\mathcal{M}_{\alpha\beta}$
$\mathcal{M}_{21}$	$-\mathcal{M}_{\alpha\beta}$	$\mathcal{M}_{\alpha\beta}$	$-\mathcal{M}_{\alpha\beta}$	$\mathcal{M}_{\alpha\beta}$
$\mathcal{M}_{22}$	$\mathcal{M}_{\alpha\alpha}$	$\mathcal{M}_{\alpha\alpha}$	$-\mathcal{M}_{\alpha\alpha}$	$-\mathcal{M}_{\alpha\alpha}$
$\mathcal{M}_{33}$	$\mathcal{M}_{\gamma\gamma}$	$\mathcal{M}_{\gamma\gamma}$	$-\mathcal{M}_{\gamma\gamma}$	$-\mathcal{M}_{\gamma\gamma}$

TABLE 3.10: The symmetry-allowed ordering of the magnetoelectric tensor on the Fe atoms in Fe_2O_3. The not-displayed elements are all zero.

	O_1	O_2	O_3	O_4	O_5	O_6
$\mathcal{M}_{11}$	$\mathcal{M}_{\alpha\alpha}$	$\frac{1}{4}\mathcal{M}_{\alpha\alpha}$ $+\frac{3}{4}\mathcal{M}_{\beta\beta}$	$\frac{1}{4}\mathcal{M}_{\alpha\alpha}$ $+\frac{3}{4}\mathcal{M}_{\beta\beta}$	$-\mathcal{M}_{\alpha\alpha}$	$-\frac{1}{4}\mathcal{M}_{\alpha\alpha}$ $-\frac{3}{4}\mathcal{M}_{\beta\beta}$	$-\frac{1}{4}\mathcal{M}_{\alpha\alpha}$ $-\frac{3}{4}\mathcal{M}_{\beta\beta}$
$\mathcal{M}_{12}$	0	$-\frac{\sqrt{3}}{4}\mathcal{M}_{\alpha\alpha}$ $+\frac{\sqrt{3}}{4}\mathcal{M}_{\beta\beta}$	$\frac{\sqrt{3}}{4}\mathcal{M}_{\alpha\alpha}$ $-\frac{\sqrt{3}}{4}\mathcal{M}_{\beta\beta}$	0	$\frac{\sqrt{3}}{4}\mathcal{M}_{\alpha\alpha}$ $-\frac{\sqrt{3}}{4}\mathcal{M}_{\beta\beta}$	$-\frac{\sqrt{3}}{4}\mathcal{M}_{\alpha\alpha}$ $+\frac{\sqrt{3}}{4}\mathcal{M}_{\beta\beta}$
$\mathcal{M}_{13}$	0	$-\frac{\sqrt{3}}{2}\mathcal{M}_{\beta\gamma}$	$\frac{\sqrt{3}}{2}\mathcal{M}_{\beta\gamma}$	0	$\frac{\sqrt{3}}{2}\mathcal{M}_{\beta\gamma}$	$-\frac{\sqrt{3}}{2}\mathcal{M}_{\beta\gamma}$
$\mathcal{M}_{21}$	0	$-\frac{\sqrt{3}}{4}\mathcal{M}_{\alpha\alpha}$ $+\frac{\sqrt{3}}{4}\mathcal{M}_{\beta\beta}$	$\frac{\sqrt{3}}{4}\mathcal{M}_{\alpha\alpha}$ $-\frac{\sqrt{3}}{4}\mathcal{M}_{\beta\beta}$	0	$\frac{\sqrt{3}}{4}\mathcal{M}_{\alpha\alpha}$ $-\frac{\sqrt{3}}{4}\mathcal{M}_{\beta\beta}$	$-\frac{\sqrt{3}}{4}\mathcal{M}_{\alpha\alpha}$ $+\frac{\sqrt{3}}{4}\mathcal{M}_{\beta\beta}$
$\mathcal{M}_{22}$	$\mathcal{M}_{\beta\beta}$	$\frac{3}{4}\mathcal{M}_{\alpha\alpha}$ $+\frac{1}{4}\mathcal{M}_{\beta\beta}$	$\frac{3}{4}\mathcal{M}_{\alpha\alpha}$ $+\frac{1}{4}\mathcal{M}_{\beta\beta}$	$-\mathcal{M}_{\beta\beta}$	$-\frac{3}{4}\mathcal{M}_{\alpha\alpha}$ $-\frac{1}{4}\mathcal{M}_{\beta\beta}$	$-\frac{3}{4}\mathcal{M}_{\alpha\alpha}$ $-\frac{1}{4}\mathcal{M}_{\beta\beta}$
$\mathcal{M}_{23}$	$\mathcal{M}_{\beta\gamma}$	$-\frac{1}{2}\mathcal{M}_{\beta\gamma}$	$-\frac{1}{2}\mathcal{M}_{\beta\gamma}$	$-\mathcal{M}_{\beta\gamma}$	$\frac{1}{2}\mathcal{M}_{\beta\gamma}$	$\frac{1}{2}\mathcal{M}_{\beta\gamma}$
$\mathcal{M}_{31}$	0	$-\frac{\sqrt{3}}{2}\mathcal{M}_{\gamma\beta}$	$\frac{\sqrt{3}}{2}\mathcal{M}_{\gamma\beta}$	0	$\frac{\sqrt{3}}{2}\mathcal{M}_{\gamma\beta}$	$-\frac{\sqrt{3}}{2}\mathcal{M}_{\gamma\beta}$
$\mathcal{M}_{32}$	$\mathcal{M}_{\gamma\beta}$	$-\frac{1}{2}\mathcal{M}_{\gamma\beta}$	$-\frac{1}{2}\mathcal{M}_{\gamma\beta}$	$-\mathcal{M}_{\gamma\beta}$	$\frac{1}{2}\mathcal{M}_{\gamma\beta}$	$\frac{1}{2}\mathcal{M}_{\gamma\beta}$
$\mathcal{M}_{33}$	$\mathcal{M}_{\gamma\gamma}$	$\mathcal{M}_{\gamma\gamma}$	$\mathcal{M}_{\gamma\gamma}$	$-\mathcal{M}_{\gamma\gamma}$	$-\mathcal{M}_{\gamma\gamma}$	$-\mathcal{M}_{\gamma\gamma}$

TABLE 3.11: The symmetry-allowed ordering of the magnetoelectric multipole tensor on the O atoms in Fe_2O_3.

Now using the symmetry operations again, we can find the ordering of the different components of the ME multipole tensor on the different atoms. This ordering for the Fe atoms is displayed in Table 3.10 and for the oxygen atoms in Table 3.11.

Also here we can add up the contributions of the different atoms. In contrast to Cr_2O_3 however, here the different contributions add up to a completely zero tensor, i.e.,

$$\mathcal{M}_{Fe_2O_3} = \begin{pmatrix} 0 & 0 & 0 \\ 0 & 0 & 0 \\ 0 & 0 & 0 \end{pmatrix}. \tag{3.23}$$

This is also in accordance with what is known about Fe_2O_3. As inversion symmetry is not broken in this material, it does not have to correct symmetry to support a ME effect. So here as well, our results for the local tensor are consistent with the known results for the global tensor.

3.2.6 Allowed magnetoelectric multipoles

Now we are ready to move on to the ME multipoles themselves, which can be extracted from the ME multipole tensor $\mathcal{M}_{ij}$ (Eq. 1.8). As discussed in Section 1.4, we can separate the tensor into its irreducible components (Eq. 1.12), where a represents the ME monopoles, t the toroidal moments and q the quadrupoles. We can write Eq. 1.12 explicitly as:

$$a = \frac{1}{3}\mathcal{M}_{ii} = \frac{1}{3}\big(\mathcal{M}_{11} + \mathcal{M}_{22} + \mathcal{M}_{33}\big), \tag{3.24}$$
$$t_x = \frac{1}{2}\epsilon_{ij1}\mathcal{M}_{ji} = \frac{1}{2}\big(\mathcal{M}_{32} - \mathcal{M}_{23}\big), \tag{3.25}$$
$$t_y = \frac{1}{2}\epsilon_{ij2}\mathcal{M}_{ji} = \frac{1}{2}\big(\mathcal{M}_{13} - \mathcal{M}_{31}\big), \tag{3.26}$$
$$t_z = \frac{1}{2}\epsilon_{ij3}\mathcal{M}_{ji} = \frac{1}{2}\big(\mathcal{M}_{21} - \mathcal{M}_{12}\big), \tag{3.27}$$
$$q_{xy} = \frac{1}{2}\big(\mathcal{M}_{12} + \mathcal{M}_{21}\big), \tag{3.28}$$
$$q_{xz} = \frac{1}{2}\big(\mathcal{M}_{13} + \mathcal{M}_{31}\big), \tag{3.29}$$
$$q_{yz} = \frac{1}{2}\big(\mathcal{M}_{23} + \mathcal{M}_{32}\big), \tag{3.30}$$

$$q_{x^2-y^2} = \frac{1}{2}(q_{xx} - q_{yy}) = \frac{1}{2}\big(\mathcal{M}_{11} - \mathcal{M}_{22}\big), \tag{3.31}$$
$$q_{z^2} = \frac{1}{2}(q_{xx} + q_{yy}) = -\frac{1}{2}q_{zz} = \frac{1}{6}\big(\mathcal{M}_{11} + \mathcal{M}_{22}\big) - \frac{1}{3}\mathcal{M}_{33}. \tag{3.32}$$

Using these relations, we can determine how the multipoles transform from the transformation of the local ME multipole tensor (Tables 3.8, 3.9, 3.10 and 3.11). The allowed ME multipoles on the TM ions in both compounds are displayed in Table 3.12, and on the O ions in Table 3.13 (Cr_2O_3) and Table 3.14 (Fe_2O_3).

	Cr_2O_3					Fe_2O_3			
	Cr_1	Cr_2	Cr_3	Cr_4		Fe_1	Fe_2	Fe_3	Fe_4
a	a	a	a	a		$-a$	$-a$	a	a
t_z	$-t_\gamma$	t_γ	t_γ	$-t_\gamma$		$-t_\gamma$	t_γ	$-t_\gamma$	t_γ
q_{z^2}	q_{γ^2}	q_{γ^2}	q_{γ^2}	q_{γ^2}		q_{γ^2}	q_{γ^2}	$-q_{\gamma^2}$	$-q_{\gamma^2}$

TABLE 3.12: The symmetry-allowed magnetoelectric multipoles on the transition metal ions in Cr_2O_3 and Fe_2O_3.

	O_1	O_2	O_3	O_4	O_5	O_6
a	a	a	a	a	a	a
t_x	t_α	$-\frac{1}{2}t_\alpha$	$-\frac{1}{2}t_\alpha$	t_α	$-\frac{1}{2}t_\alpha$	$-\frac{1}{2}t_\alpha$
t_y	0	$\frac{\sqrt{3}}{2}t_\alpha$	$-\frac{\sqrt{3}}{2}t_\alpha$	0	$\frac{\sqrt{3}}{2}t_\alpha$	$-\frac{\sqrt{3}}{2}t_\alpha$
q_{xy}	0	$-\frac{\sqrt{3}}{2}q_{\alpha^2-\beta^2}$	$\frac{\sqrt{3}}{2}q_{\alpha^2-\beta^2}$	0	$-\frac{\sqrt{3}}{2}q_{\alpha^2-\beta^2}$	$\frac{\sqrt{3}}{2}q_{\alpha^2-\beta^2}$
q_{xz}	0	$-\frac{\sqrt{3}}{2}q_{\beta\gamma}$	$\frac{\sqrt{3}}{2}q_{\beta\gamma}$	0	$-\frac{\sqrt{3}}{2}q_{\beta\gamma}$	$\frac{\sqrt{3}}{2}q_{\beta\gamma}$
q_{yz}	$q_{\beta\gamma}$	$-\frac{1}{2}q_{\beta\gamma}$	$-\frac{1}{2}q_{\beta\gamma}$	$q_{\beta\gamma}$	$-\frac{1}{2}q_{\beta\gamma}$	$-\frac{1}{2}q_{\beta\gamma}$
$q_{x^2-y^2}$	$q_{\alpha^2-\beta^2}$	$-\frac{1}{2}q_{\alpha^2-\beta^2}$	$-\frac{1}{2}q_{\alpha^2-\beta^2}$	$q_{\alpha^2-\beta^2}$	$-\frac{1}{2}q_{\alpha^2-\beta^2}$	$-\frac{1}{2}q_{\alpha^2-\beta^2}$
q_{z^2}	q_{γ^2}	q_{γ^2}	q_{γ^2}	q_{γ^2}	q_{γ^2}	q_{γ^2}

TABLE 3.13: The symmetry-allowed ordering of the magnetoelectric multipoles on the O atoms in Cr_2O_3. The not-displayed elements are zero.

	O_1	O_2	O_3	O_4	O_5	O_6
a	a	a	a	-a	-a	-a
t_x	t_α	$-\frac{1}{2}t_\alpha$	$-\frac{1}{2}t_\alpha$	$-t_\alpha$	$\frac{1}{2}t_\alpha$	$\frac{1}{2}t_\alpha$
t_y	0	$\frac{\sqrt{3}}{2}t_\alpha$	$-\frac{\sqrt{3}}{2}t_\alpha$	0	$-\frac{\sqrt{3}}{2}t_\alpha$	$\frac{\sqrt{3}}{2}t_\alpha$
q_{xy}	0	$-\frac{\sqrt{3}}{2}q_{\alpha^2-\beta^2}$	$\frac{\sqrt{3}}{2}q_{\alpha^2-\beta^2}$	0	$\frac{\sqrt{3}}{2}q_{\alpha^2-\beta^2}$	$-\frac{\sqrt{3}}{2}q_{\alpha^2-\beta^2}$
q_{xz}	0	$-\frac{\sqrt{3}}{2}q_{\beta\gamma}$	$\frac{\sqrt{3}}{2}q_{\beta\gamma}$	0	$\frac{\sqrt{3}}{2}q_{\beta\gamma}$	$-\frac{\sqrt{3}}{2}q_{\beta\gamma}$
q_{yz}	$q_{\beta\gamma}$	$-\frac{1}{2}q_{\beta\gamma}$	$-\frac{1}{2}q_{\beta\gamma}$	$-q_{\beta\gamma}$	$\frac{1}{2}q_{\beta\gamma}$	$\frac{1}{2}q_{\beta\gamma}$
$q_{x^2-y^2}$	$q_{\alpha^2-\beta^2}$	$-\frac{1}{2}q_{\alpha^2-\beta^2}$	$-\frac{1}{2}q_{\alpha^2-\beta^2}$	$-q_{\alpha^2-\beta^2}$	$\frac{1}{2}q_{\alpha^2-\beta^2}$	$\frac{1}{2}q_{\alpha^2-\beta^2}$
q_{z^2}	q_{γ^2}	q_{γ^2}	q_{γ^2}	$-q_{\gamma^2}$	$-q_{\gamma^2}$	$-q_{\gamma^2}$

TABLE 3.14: The symmetry-allowed ordering of the magnetoelectric multipoles on the O atoms in Fe_2O_3. The not-displayed elements are zero.

We see that, as expected, in Fe_2O_3 we always have an equal amount of positive and negative multipoles of the same type, consistent with its lack of net ME effect. In Cr_2O_3

we have ME monopoles a and q_{z^2} ME quadrupoles with the same sign on each atom. This is consistent with its diagonal ME effect.

3.2.7 Conclusion from the symmetry analysis

We performed symmetry analysis to figure out the allowed forms for the magnetic dipole moment, the local ME multipole tensor, and ME multipoles on each of the atoms in the corundum structure materials Cr_2O_3 and Fe_2O_3. We discovered local results consistent with the known global results. Moreover, locally more terms are allowed for the ME multipole tensor and ME multipoles, which allude to richer local effects. Furthermore, note that the symmetry analysis did not reveal to us the ratios or even relative signs, let alone size or signs, of the independent components of the dipole moments, ME multipole tensor, ME multipoles, or ME tensor and effect. We will now discuss how those things can be determined using DFT.

3.3 Hidden orders and (anti-)magnetoelectric effects in Cr_2O_3 and α-Fe_2O_3

3.3.1 Preface

In this publication I investigate how we can use hidden order to predict local effects, specifically looking at local magnetic multipoles, the way they are ordered and to which (local) ME effects they can be related. We focus on both magnetic quadrupoles, which are also called ME multipoles, and magnetic octupoles, and associate them to linear and second order local ME effects. As mentioned in Section 1.4.2, the relation between the *net* linear ME effect and the ME multipoles was pointed out previously [15, 38–41], but we expand it here to include also local effects. As mentioned in Section 1.3.1, Cr_2O_3 has both broken inversion and broken time-reversal symmetry, which allows for a net linear magnetoelectric effect. In contrast, the inversion symmetry is preserved in Fe_2O_3. However, locally the environment of each TM ion in both compounds looks very similar. Inspired by these similarities, we investigate if some of the special physics of Cr_2O_3 is preserved locally in Fe_2O_3, using the magnetic multipoles as a predictor.

The first goal of this work is to show that despite the global symmetry restrictions, there is still hidden order in Fe_2O_3. We use the symmetry tools explained in detail in the previous section to determine which components of the multipoles are allowed on each atomic site. We subsequently use DFT to calculate which multipole components are non-zero. The purpose of this is twofold. First, the presence of the same multipoles would indicate that the intuition that the local environments of Cr_2O_3 and Fe_2O_3 are very similar is grounded, after all these multipoles are present in Cr_2O_3. Second, by looking at where these multipoles occur in the multipole tensor, we can distinguish which part of the ME effect they are associated with and thus predict the type of effects we expect.

The second goal is to determine whether the predicted local effects are in fact present in the two materials. We choose to look at the response of the dipole moments under the application of an electric field.[7] To simulate the effect of such an electric field, we use a relatively simple lattice displacement technique [81], which we extend to capture part of the second-order effects as well. This technique, by definition, only captures the lattice-mediated response to an electric field, and misses the purely electronic contribution. Nevertheless, as we are interested in establishing the presence of these effects, but not their exact magnitude, this method should be sufficient. Moreover, the local effects will be quite small, and hence difficult to converge. We expect this to be an even larger issue with more complicated methods where one may capture both the lattice-mediated and purely electronic contributions [83]. By determining these local ME effects, we will show that they can be present despite global symmetry restrictions, thus expanding the definition of the term 'magnetoelectric'. We will furthermore extend the knowledge of ME responses in both Cr_2O_3 and Fe_2O_3. Finally, we show the predictive power of the magnetic multipoles, by showing how each multipole component is related to a specific part of the ME response.

The third goal is to establish symmetry principles for the occurrence of the local ME effect so that the concept can be extended to other materials. We find a basic set of rules based on the magnetic space group symmetry and the Wyckoff positions of the magnetic ions. We identify a large class of materials that has local linear ME effects, showing that these are much more ubiquitous than net linear ME effects.

The last goal is to inspire experimental investigation of these local effects and multipoles.

Explanatory remarks

Section 3.3.2 to 3.3.5 contain the publication:

[7] rather than the reverse: looking at local displacements (corresponding to local changes in electric dipole moment) as a function of applied magnetic field.

[19] X. H. Verbeek, A. Urru, and N. A. Spaldin. "Hidden orders and (anti-)magnetoelectric effects in Cr_2O_3 and α-Fe_2O_3". *Phys. Rev. Res.* 5 (2023), p. L042018. DOI: 10.1103/PhysRevResearch.5.L042018. URL: https://link.aps.org/doi/10.1103/PhysRevResearch.5.L042018

My contribution was to perform the symmetry analysis, perform the calculations in VASP and most of the calculations in ELK, and co-write the manuscript. Andrea Urru performed part of the calculations to determine the correct conversion parameters. I wrote the manuscript together with Andrea Urru and Nicola Spaldin. The version printed here is the author-accepted manuscript, with the formatting deviating from the published version to ensure a consistent style with the rest of the thesis.

3.3.2 Abstract

We present *ab initio* calculations of hidden magnetoelectric multipolar order in Cr_2O_3 and its iron-based analog, α-Fe_2O_3. First, we discuss the connection between the order of such hidden multipoles and the linear magnetoelectric effect. Next, we show the presence of hidden antiferroically ordered magnetoelectric multipoles in both the prototypical magnetoelectric material Cr_2O_3, and centrosymmetric α-Fe_2O_3, which has the same crystal structure as Cr_2O_3, but a different magnetic dipolar ordering. In turn, we predict antimagnetoelectric effects, in which local magnetic dipole moments are induced in opposite directions under the application of an uniform external electric field, to create an additional antiferromagnetic ordering. We confirm the predicted induced moments using first-principles calculations. Our results demonstrate the existence of hidden magnetoelectric multipoles leading to local linear magnetoelectric responses even in centrosymmetric magnetic materials, where a net bulk linear magnetoelectric effect is forbidden by symmetry, and broaden the definition of magnetoelectric materials by including those showing such local magnetoelectric responses.

3.3.3 Paper body

In 1936, Néel proposed a *hidden order* of antiparallel magnetic moments to explain the anomalous spike in the specific heat and magnetic susceptibility as a function of temperature in MnO [34]. Since then, many more hidden orders have been proposed, although they are usually either electric or magnetic in nature, among which we mention the antiferroic order of electric quadrupoles in UPd_3 [118] and the ferroic order of magnetic octupoles linked to the anomalous Hall effect in Mn_3Sn [37]. In this work, we show how magnetoelectric (ME) materials provide a platform for investigating a coupled magnetic-electric hidden order.

By definition, ME materials show a net change in magnetization M when an external electric field $\mathcal{E}$ is applied or, vice-versa, change their electric polarization P in the presence of a magnetic field $\mathcal{H}$ [13]. These materials have been a subject of active research [24, 28, 119] as the coupling of magnetic and electric degrees of freedom is potentially useful for applications including low-energy-consumption memory devices, sensors, and transistors [29, 120]. The lowest-order, *linear*, contribution to the ME response [121], which requires the simultaneous breaking of space- and time-inversion symmetries, is linked to the presence of ME multipoles [15, 38–41], which are odd-parity, second-order multipoles of the magnetization density $\boldsymbol{\mu}(\boldsymbol{r})$. In their irreducible spherical form, the ME multipoles are the scalar ME monopole (a), the ME toroidal moment vector ($\boldsymbol{t}$),

and the ME quadrupole tensor (q),

$$a = \frac{1}{3}\int \boldsymbol{r}\cdot\boldsymbol{\mu}(\boldsymbol{r})d^3\boldsymbol{r}, \tag{3.33}$$

$$t_i = \frac{1}{2}\int [\boldsymbol{r}\times\boldsymbol{\mu}(\boldsymbol{r})]_i\, d^3\boldsymbol{r}, \tag{3.34}$$

$$q_{ij} = \frac{1}{2}\int \left[r_i\mu_j(\boldsymbol{r}) + r_j\mu_i(\boldsymbol{r}) - \frac{2}{3}\delta_{ij}\boldsymbol{r}\cdot\boldsymbol{\mu}(\boldsymbol{r})\right] d^3\boldsymbol{r}, \tag{3.35}$$

which correspond respectively to the trace, the antisymmetric part, and the symmetric traceless part of the ME multipole tensor $\mathcal{M}_{ij} = \int r_i\mu_j(\boldsymbol{r})d^3\boldsymbol{r}$ [15]. ME multipoles provide a handle for understanding and predicting the linear ME effect starting from the microscopic environment since they have a one-to-one link to the linear ME tensor α_{ij}, defined as $\alpha_{ij} = \mu_0\partial M_j/\partial\mathcal{E}_i|_{\mathcal{H}}$, with μ_0 the vacuum permeability. Specifically, monopoles a and $q_{x^2-y^2}$, q_{z^2} quadrupoles account for the diagonal isotropic and anisotropic linear ME effect, whereas the toroidal moments t_i and the q_{xy}, q_{xz}, and q_{yz} quadrupoles are linked to the off-diagonal antisymmetric and symmetric linear ME effect, respectively. Analogously, the second-order ME effect can be captured by the next-higher order magnetic multipoles, the magnetic octupoles [45].

$\mathcal{M}_{ij}$ can be decomposed into a sum over products of the atomic positions and their magnetic dipole moments, capturing the asymmetry in the unit-cell magnetization due to the arrangement of the magnetic dipoles [15], and local atomic-site contributions, which describe asymmetries in the local spin densities around each ion [15]. Here we focus on the local atomic-site multipoles, which occur in both ME and non-ME materials whenever the local Wyckoff site symmetry lacks both time reversal and space inversion. In centrosymmetric magnetic materials, where a net ME effect is forbidden by global inversion symmetry, these local multipoles are antiferroically ordered, but can in principle provide a *local* ME response. Indeed, such local symmetries have recently been shown to be important in explaining hidden Rashba and Dresselhaus effects in centrosymmetric materials [122, 123].

In this work, we analyze the link between the local multipolar order and the local, atomic ME response in the isostructural materials Cr_2O_3 and α-Fe_2O_3 (from now on Fe_2O_3). Both materials adopt the corundum structure, with the centrosymmetric point group $\bar{3}m$ (space group R$\bar{3}c$), and are easy-axis antiferromagnets, below 307 K [49, 124] and 263 K [125, 126],[8] respectively. Importantly, however, they have different magnetic orderings, as shown in Figure 3.7. Specifically, the magnetic order in Cr_2O_3 breaks both inversion and time-reversal symmetries (magnetic space group (MSG) R$\bar{3}'c'$), whereas in Fe_2O_3 it breaks time-reversal symmetry only (MSG R$\bar{3}c$). As a result, Cr_2O_3 is a

[8] At 263 K Fe_2O_3 undergoes the Morin transition to the weakly ferromagnetic phase (until the Néel temperature of 960 K), with the moments lying in the plane perpendicular to the easy axis of the low-temperature phase.

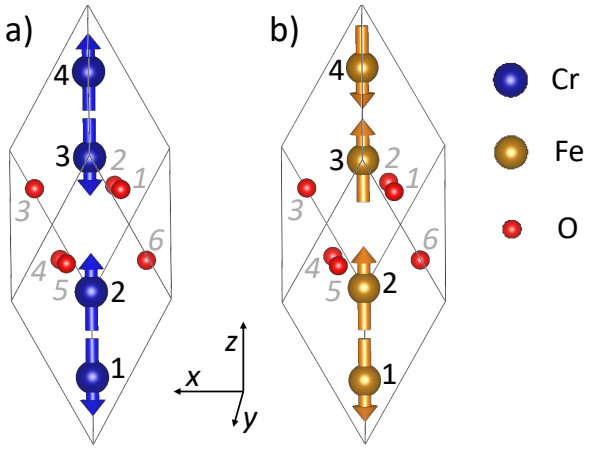

FIGURE 3.7: Crystal structure and magnetic order of a) Cr_2O_3, b) Fe_2O_3. Magnetic moments are indicated by arrows. The atoms are numbered following the conventional order of the Wyckoff positions. The magnetic easy axis is parallel to z.

well-known ME material [31, 32, 47, 108, 127], in which the linear ME effect was first identified [13, 14], whereas Fe_2O_3 does not show a net linear ME effect, and instead its symmetry allows a non-relativistic, altermagnetic spin splitting [17, 128]. Despite the difference in global symmetry, the local site symmetries are similar in Cr_2O_3 and Fe_2O_3. Local atomic ME multipoles and, in turn, a local ME response, are allowed in both compounds, since the *local* inversion symmetry is broken at the Cr, Fe, and O Wyckoff sites in both materials. Thus, we expect that locally some of the special physics seen in Cr_2O_3 may be preserved in Fe_2O_3. Indeed, our main finding is that Fe_2O_3 has a *hidden* antiferromultipolar order that leads to a local anti-ME response, with a strength that is comparable to that in ME Cr_2O_3.

We demonstrate the existence of the hidden ME multipoles and quantify the size of the ME responses using density-functional calculations.[9] We compute the spin contributions to the local diagonal and off-diagonal lattice-mediated ME response in the xy plane using the method described in Ref. [81], modified to extract the *local atomic* magnetic response. This approach does not require the application of an electric field. Instead, the local ME response is computed by freezing in the atomic displacement corresponding to the electric field strength, computed from a superposition of infrared-active phonon modes as explained in Ref. [81]. For details, see the Supplemental material [130]. Our density-functional calculations are performed within the non-collinear local spin density approximation (LSDA) [64], with spin-orbit interaction and Hubbard U correction [1] included, as implemented in the plane-wave code VASP [68, 69] and in the augmented-plane-wave (APW) code ELK [70]. We use VASP to compute the equilibrium structure and forces, and we interface it with phonopy [131, 132] to obtain the phonon

[9]The relevant input files and data of our *ab initio* calculations are openly available on the Materials Cloud Archive at [129].

	Cr_2O_3					Fe_2O_3			
	Cr_1	Cr_2	Cr_3	Cr_4		Fe_1	Fe_2	Fe_3	Fe_4
m_z	$-m_{Cr}$	m_{Cr}	$-m_{Cr}$	m_{Cr}		$-m_{Fe}$	m_{Fe}	m_{Fe}	$-m_{Fe}$
a	$-a_{Cr}$	$-a_{Cr}$	$-a_{Cr}$	$-a_{Cr}$		a_{Fe}	a_{Fe}	$-a_{Fe}$	$-a_{Fe}$
t_z	t_{Cr}	$-t_{Cr}$	$-t_{Cr}$	t_{Cr}		t_{Fe}	$-t_{Fe}$	t_{Fe}	$-t_{Fe}$
q_{z^2}	$-q_{Cr}$	$-q_{Cr}$	$-q_{Cr}$	$-q_{Cr}$		q_{Fe}	q_{Fe}	$-q_{Fe}$	$-q_{Fe}$

TABLE 3.15: Symmetry-allowed magnetic moments and ME multipoles, and their ordering on the TM ions in Cr_2O_3 and Fe_2O_3. Atoms are labeled as in Figure 3.7.

eigenvectors and frequencies. We use ELK to calculate the angular parts of the local magnetic multipoles, by decomposing the density matrix into its irreducible spherical tensors and extracting the relevant components [84], and to compute the ME responses. Since the resulting changes in the local magnetic moments are small at relevant phonon amplitudes, extensive convergence tests are performed (see Supplemental Material [130]).

As described above, the linear ME effect requires time-reversal and inversion symmetries to be broken. This is the case in Cr_2O_3, but in Fe_2O_3 the global inversion symmetry is preserved. We determine which multipoles are allowed and their subsequent arrangement by studying both how each multipole transforms and how the atoms permute under the 12 symmetry operations of the $R\bar{3}c$ space group (for more details see the Supplemental Material [130]). We find that on the transition metal (TM) ions in Cr_2O_3 and Fe_2O_3, which have the same Wyckoff site symmetry (3), ME monopoles a, t_z toroidal moments and q_{z^2} quadrupoles are allowed, but with different ordering. We support the results of our symmetry analysis with first-principles calculations of the multipole components in Cr_2O_3 and Fe_2O_3 at their respective equilibrium structures. These calculations confirm the multipolar ordering obtained from the symmetry analysis and provide the magnitude and absolute sign of each multipole (Table 3.15; the signs correspond to the antiferromagnetic domains shown in Figure 3.7.), whereas the symmetry analysis yields only the relative sign on the different sites. The sizes of our calculated angular parts of a, t_z, and q_{z^2} (3×10^{-3}, 2×10^{-5}, and $2 \times 10^{-3}\,\mu_B$ in Cr_2O_3 and 4×10^{-3}, 7×10^{-5}, and $4 \times 10^{-3}\,\mu_B$ in Fe_2O_3, respectively) are similar in both materials, approximately scaling with the size of the calculated dipole moments ($2.6\,\mu_B$ and $4.1\,\mu_B$ for Cr and Fe, respectively). The ferroic ordering of a and q_{z^2} ($----$ in both cases) in Cr_2O_3 is consistent with its established anisotropic linear diagonal ME effect. On the other hand, in Fe_2O_3 the antiferroic ordering of a and q_{z^2} ($++--$ in both cases) suggests an antiferroic linear diagonal ME response, in which an external electric field induces magnetic moments parallel to the field, but in opposite directions on Fe_1 and Fe_2 relative to Fe_3 and Fe_4, such that an antiferromagnetic order with no *net* magnetic moment is established

	O_1	O_2	O_3	O_4	O_5	O_6
m_x	m	$-\frac{1}{2}m$	$-\frac{1}{2}m$	$\mp m$	$\pm\frac{1}{2}m$	$\pm\frac{1}{2}m$
m_y	0	$\frac{\sqrt{3}}{2}m$	$-\frac{\sqrt{3}}{2}m$	0	$\mp\frac{\sqrt{3}}{2}m$	$\pm\frac{\sqrt{3}}{2}m$
a	$\mp a$	$\mp a$	$\mp a$	$-a$	$-a$	$-a$
t_x	$+t$	$-\frac{1}{2}t$	$-\frac{1}{2}t$	$\pm t$	$\mp\frac{1}{2}t$	$\mp\frac{1}{2}t$
t_y	0	$+\frac{\sqrt{3}}{2}t$	$-\frac{\sqrt{3}}{2}t$	0	$\pm\frac{\sqrt{3}}{2}t$	$\mp\frac{\sqrt{3}}{2}t$
q_{xy}	0	$\mp\frac{\sqrt{3}}{2}q_2$	$\pm\frac{\sqrt{3}}{2}q_2$	0	$-\frac{\sqrt{3}}{2}q_2$	$+\frac{\sqrt{3}}{2}q_2$
q_{xz}	0	$+\frac{\sqrt{3}}{2}q_1$	$-\frac{\sqrt{3}}{2}q_1$	0	$\pm\frac{\sqrt{3}}{2}q_1$	$\mp\frac{\sqrt{3}}{2}q_1$
q_{yz}	$-q_1$	$+\frac{1}{2}q_1$	$+\frac{1}{2}q_1$	$\mp q_1$	$\pm\frac{1}{2}q_1$	$\pm\frac{1}{2}q_1$
$q_{x^2-y^2}$	$\pm q_2$	$\mp\frac{1}{2}q_2$	$\mp\frac{1}{2}q_2$	$+q_2$	$-\frac{1}{2}q_2$	$-\frac{1}{2}q_2$
q_{z^2}	$\mp q_3$	$\mp q_3$	$\mp q_3$	$-q_3$	$-q_3$	$-q_3$

TABLE 3.16: Symmetry-allowed magnetic moments and ME multipoles, and their ordering on the O atoms in Cr_2O_3 and Fe_2O_3. When the sign is different in the two materials, two signs are given, with the top (bottom) sign corresponding to Cr_2O_3 (Fe_2O_3). The magnitudes (in μ_B) of m and the angular parts of a, t, q_1, q_2, q_3 are 7×10^{-5}, 1×10^{-2}, 1×10^{-2}, 2×10^{-2}, 4×10^{-5}, 1×10^{-2} in Cr_2O_3 and 2×10^{-3}, 3×10^{-2}, 2×10^{-2}, 2×10^{-2}, 3×10^{-4}, 4×10^{-2} in Fe_2O_3 respectively. Atoms are labeled as in Figure 3.7.

along the field direction. We refer to this response as an *anti*-ME effect. Furthermore, the antiferroically ordered t_z in both materials, two orders of magnitude smaller than a and q_{z^2}, indicate an additional off-diagonal anti-ME effect, with the induced magnetic moments ordered differently in Cr_2O_3 (Cr_1 and Cr_4 having opposite sign relative to Cr_2 and Cr_3) and Fe_2O_3 (Fe_1 and Fe_3 having opposite sign relative to Fe_2 and Fe_4).

We note that in both materials local ME multipoles are allowed on the oxygen sites as well (Table 3.16), where the absolute signs are obtained from our first-principles calculations. The Wyckoff site symmetry (2) of the O atoms does not include the three-fold axis, thus allows multipoles with non-zero in-plane components (t_x, t_y, q_{xz}, q_{yz}, q_{xy}, and $q_{x^2-y^2}$), in addition to the a and q_{z^2} also found on the TM ions, while it prohibits t_z. Out of all the multipole components on the O atoms, the only ones ordered ferroically are a and q_{z^2} in Cr_2O_3, indicating that the O atoms also contribute to the net ME effect in this material. All the other components sum up to zero, as dictated by the global symmetry, hence they do not contribute to a net ME effect, but rather to additional anti-ME responses.

In addition to the ME multipoles associated with the linear ME effect, magnetic octupoles are also symmetry-allowed. The relevant non-zero components on the TM ions are $\mathcal{O}_{-3}$ and $\mathcal{O}_3$, following the naming convention of Ref. [45] and, for an applied electric field along y, are associated with a local quadratic response in m_y and m_x, respectively

[45].[10] $\mathcal{O}_3$ and $\mathcal{O}_{-3}$ are ordered antiferroically ($--++$ and $-+-+$, respectively) in Cr_2O_3, and correspond to a second-order diagonal and off-diagonal anti-ME effect [45]. In Fe_2O_3, $\mathcal{O}_{-3}$ orders antiferroically ($-++-$) as well, but $\mathcal{O}_3$ orders ferroically ($++++$), which suggests that the lowest order *net* ME response is the second-order off-diagonal ME effect.

Now we use *ab initio* density-functional theory to calculate the anti-ME effects in Cr_2O_3 and Fe_2O_3 predicted by the symmetry arguments discussed above. Figure 3.8, which summarizes our results, shows the calculated lattice-mediated changes in the magnetic moments induced by an electric field pointing along the $+y$ direction, for both Cr_2O_3 (panels a and c) and Fe_2O_3 (panels b and d), for the antiferromagnetic domains shown in Figure 3.7. We separately consider the induced moments along y (panels a and b), associated with a diagonal ME response, and along x (panels c and d), associated with an in-plane off-diagonal response.[11] In Figure 3.8a, we see that the moments on all the four Cr atoms in Cr_2O_3 show an identical linear dependence on the strength of the applied electric field. This indicates an identical local diagonal linear ME response, adding up to a net diagonal linear ME effect over the unit cell. This is consistent with the ferroic ordering of a and q_{z^2} on the Cr ions. Furthermore, the sum of the induced local Cr magnetic moments (cyan circles) is close to the total induced magnetic moment per unit cell (black diagonal crosses), which includes contributions from the O atoms and the interstitial spaces, showing that the response is dominated by the Cr atoms.

We remark that the sign of the response matches that found in previous first-principles calculations [81, 83]. Although not visible in the plot, there is an additional small quadratic component to the induced magnetic moments as a function of electric field strength, but summed over the atoms this cancels out. This diagonal second-order anti-ME effect is consistent with the antiferroic ordering of the $\mathcal{O}_{-3}$ octupoles mentioned above.

The local induced magnetic moments parallel to the applied electric field on the four Fe atoms in Fe_2O_3 (Figure 3.8b) show linear dependence for small field strengths, with identical magnitude, but order pairwise, with opposite sign for the two pairs of Fe ions, resulting in no net induced magnetic moment in the unit cell. This linear anti-ME effect, consistent with the antiferroic ordering of a and q_{z^2} discussed before, is the lowest order ME response in Fe_2O_3 and, to the best of our knowledge, has not been previously discussed. In addition to the linear contribution, at high fields we note the presence of a non-negligible local quadratic response, consistent with the antiferroic ordering of the $\mathcal{O}_{-3}$ octupoles.

[10] Note the different choice of Cartesian axis with respect to Ref. [45].

[11] The linear out-of-plane response to an in-plane applied electric field is zero, so we do not consider it here.

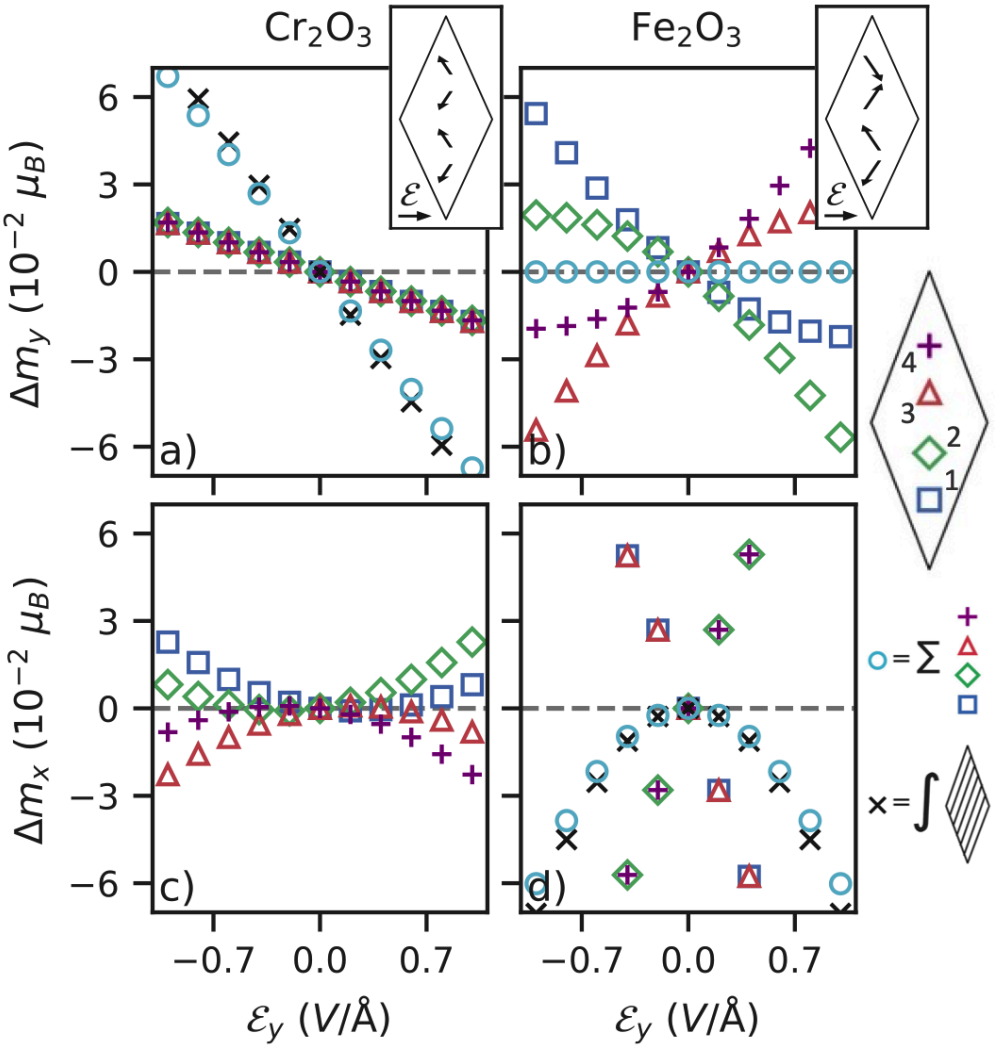

FIGURE 3.8: Local change in the in-plane magnetic moments (Δm_i) on the TM ions as a function of the applied electric field strength, with Δm_i parallel (a,b) and perpendicular (c,d) to the applied electric field direction, in Cr_2O_3 (a,c) and Fe_2O_3 (b,d). Blue squares, green diamonds, red triangles, and purple crosses represent Δm_i on TM ions 1-4, respectively. Cyan circles (a, b and d) depict the sum of Δm_i on the four TM ions, and black diagonal crosses (a,d) show the total induced magnetic moments in the unit cell. Insets in a and b sketch qualitatively the linear response parallel to the applied $\mathcal{E}$, by showing the induced magnetic moments on top of the equilibrium magnetic order.

Next, we consider the induced in-plane magnetic moments perpendicular to the applied electric field, corresponding to the off-diagonal in-plane ME response. In Cr_2O_3 (Figure 3.8c), these moments show a linear as well as a quadratic dependence on the strength of the applied electric field, but both contributions cancel out to make the net response zero. This indicates both a linear and quadratic off-diagonal anti-ME effect, which is expected from the antiferroic order of t_z $(+--+)$ and the $\mathcal{O}_3$ octupoles $(--++)$.

Finally, in Fe_2O_3 (Figure 3.8d), the induced in-plane magnetic moments perpendicular to the applied electric field have a large linear dependence, with opposite sign on different pairs of Fe atoms. The linear part of the induced moments sums to zero, leading to no

	Diagonal		Off-diagonal	
	L	Q	L	Q
Cr_2O_3	F	AF	AF	AF
Fe_2O_3	AF	AF	AF	F

TABLE 3.17: Summary of the in-plane linear (L) and quadratic (Q) ME effects found in Cr_2O_3 and Fe_2O_3, classified as ferroic (F) and antiferroic (AF) responses.

net induced moment in the unit cell. This corresponds to an off-diagonal anti-ME effect, following from the antiferroic ordering of t_z, similarly to Cr_2O_3. Interestingly, there is also a substantial quadratic dependence. As the summed (cyan circles) and total (black diagonal crosses) induced moments reveal, this contribution is ferroic and does not sum to zero, instead indicating a net bulk second-order ME response. This is thus the lowest order ferroic ME response in Fe_2O_3, and follows from the ferroic ordering $(++--)$ of the $\mathcal{O}_3$ octupoles.

Table 3.17 summarizes the ME responses discussed above. We note that the proposed anti-ME effect is more ubiquitous than the ferroic ME effect since it follows from less restrictive symmetry requirements. As a consequence, a substantial fraction of magnetic materials is expected to show a local antiferroically ordered ME response.

In this work, we studied the connection between the local ME multipolar order and the local atomic ME response. We discussed as case studies the prototypical ME material Cr_2O_3 and the centrosymmetric material Fe_2O_3. Beyond the well-established linear diagonal ME in Cr_2O_3, we predicted via symmetry and multipole analysis an off-diagonal anti-ME in Cr_2O_3 as well as both diagonal and off-diagonal anti-ME effects in Fe_2O_3, and confirmed our predictions using *ab initio* calculations. Additionally, we found in both materials a non-negligible local second-order ME response, which sums to a net response in Fe_2O_3, and which we rationalized with the presence of magnetic octupoles. In this way, we showed the strong connection between the orderings of the different ME effects and the underlying ME multipoles and magnetic octupoles. In particular, we identified an antiferroic order of ME multipoles that constitutes a new type of hidden order, adding another example to the growing list of hidden orders in condensed matter physics and highlighting their importance in determining material responses.
Furthermore, our findings allow us to broaden the concept of ME response in ordered materials: to have a local ME response, no global symmetry breaking is required, hence even materials that preserve both inversion and time reversal (the latter composed with a fractional translation), e.g., NiO, allow for a non-zero local ME tensor. The only strict requirement to have any local ME effect is the lack of time reversal among the Wyckoff site symmetries. This means that materials belonging to MSGs of type I (colorless), III or IV (black-white) allow local ME response; ordered materials of MSG II (grey),

instead, do not show any local ME response. If, besides local time-reversal breaking, at least one atomic species sits in a Wyckoff site that is not an inversion center, e.g., Mn_3O_4 [128], a local *linear* ME response is allowed, otherwise the lowest order response is quadratic.

Our calculations show that the local linear anti-ME response is of the same order of magnitude as the local ferro-ME response in similar non-centrosymmetric materials. Thus, the main challenge in measuring an anti-ME response is not the size of the response, but rather the anti-alignment of the induced magnetic moments, producing a vanishing net ME response.

In order to measure and possibly exploit such an anti-ME response, an external electric field varying at the length scale of the unit cell, would be desirable as it would induce a net magnetization. Such electric fields have recently been achieved with twisted bi-layer hexagonal boron nitride [133]. A net magnetization could alternatively be achieved by exciting a coherent phonon with the appropriate pattern of polar atomic displacements. Alternatively, the reversed effect, with a uniform magnetic field inducing an alternating polarization in the unit cell, could be detected using second harmonic generation. We hope that our findings motivate further experimental investigations to measure such anti-ME effects, as well as theoretical studies to identify promising candidates with effects of larger size.

3.3.4 Acknowledgments

The authors thank Dr. Michael Fechner, Dr. John Kay Dewhurst, Dr. Sayantika Bhowal, Dr. Sophie Weber and Max Merkel for useful discussions. NAS, XHV, and AU were supported by the ERC under the European Union's Horizon 2020 research and innovation programme grant No. 810451 and by the ETH Zürich. Computational resources were provided by ETH Zürich's Euler cluster.

3.3.5 Supplemental material

3.3.5.1 Symmetry analysis

In order to find the allowed components of the multipoles on each atom, we (i) identify the symmetry operations that send a given atom in the unit cell into itself, (ii) apply these operations to each component of the multipole moments. Since a multipole must not change if we apply a symmetry that sends the atom into itself, the symmetry-allowed components are those that are invariant under such symmetries.

To discuss Cr_2O_3 and Fe_2O_3, we start from the 12 symmetry operations of the R$\bar{3}$c space group. The six basic operations are:

1. E : the identity,
2. C_{3z}^1 : a counterclockwise rotation of $\frac{2\pi}{3}$ around the z axis,
3. C_{3z}^2 : a counterclockwise rotation of $\frac{4\pi}{3}$ around the z axis,
4. $C_{2x}(+\mathbf{f})$: a rotation of $\frac{\pi}{2}$ about the [100] axis, plus a fractional translation,
5. $C_{2[010]}(+\mathbf{f})$: a rotation of $\frac{\pi}{2}$ about the [010] axis, plus a fractional translation,
6. $C_{2[110]}(+\mathbf{f})$: a rotation of $\frac{\pi}{2}$ about the [110] axis, plus a fractional translation,

where the fractional translation $\mathbf{f} = (0, 0, 1/2)$. The other six operations are obtained by combining these basic six with inversion for Fe_2O_3, and with the product of inversion and time reversal for Cr_2O_3. As an example, we discuss how to determine the constraints on the components of the magnetic moments on the Cr atoms, sitting in the Wyckoff position $(0, 0, z)$. Among the symmetry operations listed above, E, C_{3z}^1 and C_{3z}^2 send each Cr atom into itself. Next, we take a general magnetic moment $\mathbf{m} = (m_\alpha, m_\beta, m_\gamma)$, and apply these operations; as a consequence, $\mathbf{m}$ transforms into $(m_\alpha, m_\beta, m_\gamma)$, $(-\frac{1}{2}(m_\alpha + \sqrt{3}m_\beta), \frac{1}{2}(\sqrt{3}m_\alpha - m_\beta), m_\gamma)$, and $(\frac{1}{2}(m_\alpha + \sqrt{3}m_\beta), -\frac{1}{2}(\sqrt{3}m_\alpha + m_\beta), m_\gamma)$ under E, C_{3z}^1, and C_{3z}^2, respectively. The invariant component of $\mathbf{m}$ is m_γ, hence the allowed magnetic moment on the first Cr atom is $(0, 0, m_z)$. Following the same procedure, we can construct the allowed components of all the magnetic moments and multipole moments, on both Cr, Fe, and O ions.

3.3.5.2 Details of the method to calculate the magnetoelectric response

A: Theoretical considerations

We consider the free energy of a general ME material and expand it in terms of the applied fields $\boldsymbol{\mathcal{E}}$ and $\boldsymbol{\mathcal{H}}$, with the sum over repeated indices implied:

$$F(\boldsymbol{\mathcal{E}}, \boldsymbol{\mathcal{H}}) = F_0 - P_i^0 \mathcal{E}_i - M_i^0 \mathcal{H}_i - \frac{1}{2}\chi_{ij}^e \mathcal{E}_i \mathcal{E}_j - \frac{1}{2}\chi_{ij}^m \mathcal{H}_i \mathcal{H}_j - \alpha_{ij}\mathcal{E}_i \mathcal{H}_j - \frac{1}{2}\beta_{ijk}\mathcal{E}_i \mathcal{H}_j \mathcal{H}_k$$
$$- \frac{1}{2}\gamma_{ijk}\mathcal{H}_i \mathcal{E}_j \mathcal{E}_k - \frac{1}{2}\chi_{ijk}^{e(2)}\mathcal{E}_i \mathcal{E}_j \mathcal{E}_k - \frac{1}{2}\chi_{ijk}^{m(2)}\mathcal{H}_i \mathcal{H}_j \mathcal{H}_k + ... \quad , \tag{3.36}$$

where P_i^0 and M_i^0 are the spontaneous polarization and magnetization that exist in the absence of any applied field. χ^e and χ^m are the linear electric and magnetic susceptibilities and $\chi^{e(2)}$ and $\chi^{m(2)}$ are the quadratic electric and magnetic susceptibilities. α_{ij} is the ME tensor, and β_{ijk} and γ_{ijk} are the second-order ME tensors. We can now compute the polarization and magnetization of the material in the following way:

$$\begin{aligned} P_i(\boldsymbol{\mathcal{E}}, \boldsymbol{\mathcal{H}}) &= -\frac{\partial F}{\partial \mathcal{E}_i} \\ &= P_i^0 + \frac{1}{2}\chi_{ij}^e \mathcal{E}_j + \alpha_{ij}\mathcal{H}_j + \frac{1}{2}\beta_{ijk}\mathcal{H}_j\mathcal{H}_k \\ &\quad + \frac{1}{2}\gamma_{kji}\mathcal{H}_k\mathcal{E}_j + \frac{1}{2}\chi_{ijk}^{e(2)}\mathcal{E}_j\mathcal{E}_k + \ldots \quad , \end{aligned} \tag{3.37}$$

$$\begin{aligned} M_i(\boldsymbol{\mathcal{E}}, \boldsymbol{\mathcal{H}}) &= -\frac{\partial F}{\partial \mathcal{H}_i} \\ &= M_i^0 + \frac{1}{2}\chi_{ij}^m \mathcal{H}_j + \alpha_{ji}\mathcal{E}_j + \frac{1}{2}\beta_{kji}\mathcal{E}_k\mathcal{H}_j \\ &\quad + \frac{1}{2}\gamma_{ijk}\mathcal{E}_j\mathcal{E}_k + \frac{1}{2}\chi_{ijk}^{m(2)}\mathcal{H}_j\mathcal{H}_k + \ldots \quad . \end{aligned} \tag{3.38}$$

The materials we study in this work have no spontaneous polarization or magnetization, i.e., $P_i^0 = M_i^0 = 0$. Thus, under the application of an external electric field $\boldsymbol{\mathcal{E}}$ and the absence of an applied magnetic field, the polarization and magnetization as a function of $\boldsymbol{\mathcal{E}}$ are:

$$P_i(\boldsymbol{\mathcal{E}}) = \frac{1}{2}\chi_{ij}^e \mathcal{E}_j + \frac{1}{2}\chi_{ijk}^{e(2)}\mathcal{E}_j\mathcal{E}_k + O(\mathcal{E}^3), \tag{3.39}$$

$$M_i(\boldsymbol{\mathcal{E}}) = \alpha_{ji}\mathcal{E}_j + \frac{1}{2}\gamma_{ijk}\mathcal{E}_j\mathcal{E}_k + O(\mathcal{E}^3). \tag{3.40}$$

In order to compute the full magnetization of Eq. (3.40) with *ab initio* techniques, a calculation under an applied electric field is necessary in principle. However, as shown in Ref. [81], such a delicate calculation can be avoided by splitting Eqs. (3.39) and (3.40) into 'lattice-mediated' and 'electronic' contributions. The lattice-mediated contribution, defined as the part of the response due to the lattice distortions produced by the electric field, can then be computed as the response to the atomic displacements caused by the electric field. In this way, only a calculation with displaced atoms but without explicitly applying an electric field is needed.

We now expand the arguments of Ref. [81] to deal with the second-order ME response. From here on we will write all sums explicitly, to avoid confusion. First, we write the atomic displacements caused by the applied electric field, indicated as $u_{\alpha i}$, where α labels the atom and i specifies the Cartesian component, in the complete basis of the

eigenvectors, $d_{\alpha,i}$, of the force constants matrix, as:

$$u_{\alpha,i} = \sum_{\eta} A^{(\eta)} d^{(\eta)}_{\alpha,i}, \tag{3.41}$$

where η labels the eigenvectors, henceforth modes, and $A^{(\eta)}$ is the amplitude of each mode contributing to the set of atomic displacements $u_{\alpha,i}$. These amplitudes can be expanded in powers of the applied electric field $\boldsymbol{\mathcal{E}}$. To second order in $\boldsymbol{\mathcal{E}}$, we have:

$$A^{(\eta)} = \sum_{j} a^{(\eta)}_{j} \mathcal{E}_j + \sum_{jk} b^{(\eta)}_{jk} \mathcal{E}_j \mathcal{E}_k. \tag{3.42}$$

In Ref. [81], the first-order amplitude was accounted for explicitly and was written as:

$$a^{(\eta)}_{j} = \frac{p^{e(\eta)}_{j}}{C^{(\eta)}}, \tag{3.43}$$

with $p^{e(\eta)}_{j}$ the mode polarity along j, i.e., the polarization along j induced by mode η with unitary amplitude, and $C^{(\eta)}$ the eigenvalue of the force constant matrix corresponding to mode η.

Next, we consider the net magnetization induced by the atomic displacements and we expand it to second order in the displacements:

$$M_{i,\mathrm{latt}} = \sum_{\alpha} \left[\sum_{j} \mathcal{Z}^{m}_{\alpha,ij} u_{\alpha,j} + \sum_{jk} \mathcal{Z}^{m(2)}_{\alpha,ijk} u_{\alpha,j} u_{\alpha,k} \right]. \tag{3.44}$$

Here $\mathcal{Z}^{m}_{\alpha,ij}$ is the so-called dynamical magnetic charge of atom α, i.e., the atomic magnetic moment of atom α along direction i induced by a displacement of atom α along j (see Ref. [108] for more details). $\mathcal{Z}^{m(2)}_{\alpha,ijk}$ in Eq. (3.44) is a generalization of the dynamical magnetic charge to second order. After substituting Eqs. (3.41), (3.42), and (3.43) into Eq. (3.44), the induced magnetization reads

$$\begin{aligned} M_{i,\mathrm{latt}} = \sum_{\alpha} \Bigg[& \sum_{\eta} \sum_{jj'} \frac{p^{e(\eta)}_{j'}}{C^{(\eta)}} \mathcal{Z}^{m}_{\alpha,ij} d^{(\eta)}_{\alpha,j} \mathcal{E}_{j'} + \sum_{\eta} \sum_{j} \sum_{j'k'} b^{(\eta)}_{j'k'} \mathcal{Z}^{m}_{\alpha,ij} d^{(\eta)}_{\alpha,j} \mathcal{E}_{j'} \mathcal{E}_{k'} \\ & + \sum_{\eta\eta'} \sum_{jk} \sum_{j'k'} \frac{p^{e(\eta)}_{j'} p^{e(\eta')}_{k'}}{C^{(\eta)} C^{(\eta')}} \mathcal{Z}^{m(2)}_{\alpha,ijk} d^{(\eta)}_{\alpha,j} d^{(\eta')}_{\alpha,k} \mathcal{E}_{j'} \mathcal{E}_{k'} \Bigg]. \end{aligned} \tag{3.45}$$

In our case, we are interested in the response to an electric field along a specific Cartesian direction, hence we take $j' = k' = \bar{\jmath}$ in Eq. (3.45). After further dropping $\bar{\jmath}$ for clarity,

Eq. (3.45) becomes:

$$M_{i,\mathrm{latt}} = \sum_{\alpha} \Bigg[\sum_{\eta} \sum_{j} \frac{p^{e(\eta)}}{C^{(\eta)}} \mathcal{Z}^{m}_{\alpha,ij} d^{(\eta)}_{\alpha,j} \mathcal{E} + \Bigg(\sum_{\eta} \sum_{j} b^{(\eta)} \mathcal{Z}^{m}_{\alpha,ij} d^{(\eta)}_{\alpha,j} + \sum_{\eta\eta'} \sum_{jk} \frac{p^{e(\eta)} p^{e(\eta')}}{C^{(\eta)} C^{(\eta')}} \mathcal{Z}^{m(2)}_{\alpha,ijk} d^{(\eta)}_{\alpha,j} d^{(\eta')}_{\alpha,k} \Bigg) \mathcal{E}^2 \Bigg] . \tag{3.46}$$

For the case of induced atomic magnetic moments that we address in the main paper, the induced magnetic moment of atom α, $\boldsymbol{\delta}\mathbf{m}_{\alpha}$ is:

$$\delta m_{\alpha,i} = \sum_{\eta} \sum_{j} \frac{p^{e(\eta)}}{C^{(\eta)}} \mathcal{Z}^{m}_{\alpha,ij} d^{(\eta)}_{\alpha,j} \mathcal{E} + \Bigg(\sum_{\eta} \sum_{j} b^{(\eta)} \mathcal{Z}^{m}_{\alpha,ij} d^{(\eta)}_{\alpha,j} + \sum_{\eta\eta'} \sum_{jk} \frac{p^{e(\eta)} p^{e(\eta')}}{C^{(\eta)} C^{(\eta')}} \mathcal{Z}^{m(2)}_{\alpha,ijk} d^{(\eta)}_{\alpha,j} d^{(\eta')}_{\alpha,k} \Bigg) \mathcal{E}^2 . \tag{3.47}$$

In our calculations, we adopt the following workflow: (i) we use Eqs. (3.41)-(3.43) to build, for selected values of the electric field, the corresponding atomic displacement. Note that in doing so, we neglect the contributions that are second-order in $\mathcal{E}$ in Eq. (3.42). (ii) We freeze in the atomic displacements obtained for different electric fields and compute the induced local magnetic moments; (iii) we fit the calculated curve with a second-order polynomial in the electric field. Note that this procedure allows us to extract the exact value for the first-order response, but it misses the contribution by $b^{(\eta)}$ (second line of Eq. (3.47)) to the second-order response, since only the first-order term in the electric field for the amplitude $A^{(\eta)}$ of Eq. (3.42) is considered. In order to obtain the complete second-order response, one would need to compute the response to atomic displacements obtained by relaxing the structure of the system under an applied electric field.

From a practical standpoint, the quantities needed to use Eq. (3.46) according to the workflow discussed above are (i) the force constant matrix, from which we can extract the eigenvectors $d^{(\eta)}_{\alpha i}$ and the eigenvalues $C^{(\eta)}$, and (ii) the mode polarizations $p^{e(\eta)}_{i}$ to construct the displacement of the lattice as a function of the electric field, up to linear order.

B: Computing the mode polarization

The polarization of each phonon mode $p_i^{e(\eta)}$ is computed as the product of the atomic displacements of the mode and the Born effective charge Z^e:

$$p_i^{e(\eta)} = \sum_\alpha \sum_j Z^e_{\alpha,ij} d^{(\eta)}_{\alpha j}. \tag{3.48}$$

To compute Z^e, we displace each atom in the unit cell along each Cartesian direction, and calculate the electronic and ionic polarizations using the LCALCPOL routine implemented in VASP, based on the modern theory of polarization. We perform a calculation for four different magnitudes of displacement, which allows us to assess the linear response regime. We then compute Z^e of each atom for each magnitude of displacement and take the average. This gives us the following Z^e for Cr_2O_3 and Fe_2O_3:

$$Z^e(\mathrm{Cr}) = \begin{pmatrix} 3.005 & -0.209 & 0 \\ 0.209 & 3.005 & 0 \\ 0 & 0 & 3.147 \end{pmatrix} |e|, \tag{3.49}$$

$$Z^e(\mathrm{O}) = \begin{pmatrix} -2.303 & 0 & 0 \\ 0 & -1.704 & -0.890 \\ 0 & -0.753 & -2.097 \end{pmatrix} |e|, \tag{3.50}$$

$$Z^e(\mathrm{Fe}) = \begin{pmatrix} 4.014 & -0.070 & 0 \\ 0.070 & 4.014 & 0 \\ 0 & 0 & 3.306 \end{pmatrix} |e|, \tag{3.51}$$

$$Z^e(\mathrm{O}) = \begin{pmatrix} -2.862 & 0 & 0 \\ 0 & -2.493 & -0.698 \\ 0 & -0.614 & -2.204 \end{pmatrix} |e|, \tag{3.52}$$

in excellent agreement with both the symmetry requirements and the numerical values reported in [108].

Note that the displacements $u_{\alpha,i}$ corresponding to the selected values of $\mathcal{E}$ when computing the response were sometimes considerably larger than those used to compute the Born effective charges. Thus, we calculated the polarization at large displacement explicitly, using the LCALCPOL routine. We found excellent agreement with the values obtained from multiplying the displacement with the Z^e, showing that the Born effective charges did not change significantly.

3.3.5.3 Fitting the magnetic response

When computing the response of the magnetic dipole moments, we initialize the system with the equilibrium collinear magnetic order and let the moments relax to find the magnetic order corresponding to the lowest energy in the distorted structure. We fit the induced local magnetic moments as a function of the electric field strength with a second-order polynomial, as we are interested in both the linear and second-order ME effects. We report the fit parameters in Table 3.18. To test the reliability of our calculations, we first compute the total energy and the forces on the transition metal ions as a function of the electric field strength. As an example, in Figure 3.9 we show the results for Cr_2O_3. The energy and the forces along the polarization direction as a function of the electric field strength show a quadratic and linear behavior, respectively, as expected in the linear response regime.

		linear	quadratic
Cr_2O_3	diagonal	0.01679(1)	0.0002(1)
	off-diagonal	0.00729(4)	0.0154(1)
Fe_2O_3	diagonal	0.038(1)	0.02(1)
	off-diagonal	0.137(2)	0.015(1)

TABLE 3.18: Absolute value of the linear and quadratic components of the magnetic response to the electric field, computed for the transition metal atoms in Cr_2O_3 and Fe_2O_3. Linear response in $10^{-2}\,\mu_B\,(Å/V)$, and quadratic response in $10^{-2}\,\mu_B\,(Å/V)^2$. The standard deviation errors on the parameters of the fit are given in brackets.

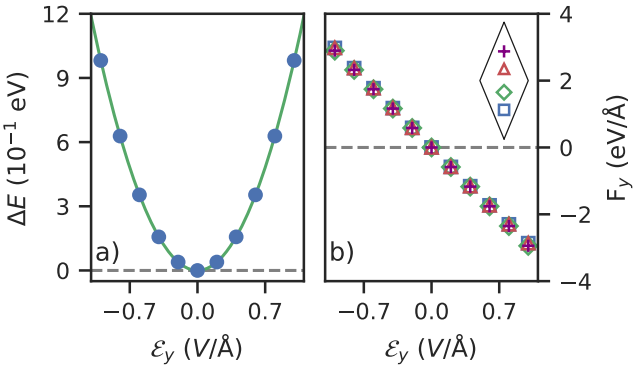

FIGURE 3.9: The a) change in energy, b) force along y on the Cr atoms in Cr_2O_3 as a function of electric field strength, with the field along the y axis. In a) data points are represented by blue dots and the second-order polynomial fit with a solid green line. In b) the force on Cr ions 1-4 is indicated with blue squares, green diamonds, red triangles, and purple crosses, respectively. The inset of Figure b) shows how the atoms are ordered in the unit cell, adopting the same order as Figure 3.7 in the main text.

3.3.5.4 DFT parameters details

Here we describe in more detail the DFT parameters and settings that were summarized in the main text. In both VASP and ELK correlation effects were dealt with by applying the rotationally invariant Hubbard U correction [1] on Fe (Cr) d states, with U = 5.5 (4.0) eV and J = 0.5 (0.5) eV. In VASP, projector-augmented wave pseudopotentials [71] (valence electrons: Cr $3p^6 3d^5 4s^1$, Fe $3d^7 4s^1$, O $2s^2 2p^4$, datasets Cr_sv, Fe_sv, O) were used, with a kinetic energy cut-off of 800 eV for the wavefunctions. Brillouin Zone (BZ) integrations were performed using a uniform Γ-centered $7 \times 7 \times 7$ k-point mesh [134]. With these parameters, we have accurately captured known experimental band gaps and magnetic moments. We found equilibrium lattice constants $a' = 5.31$ Å, $\alpha' = 54.87°$ for Cr_2O_3, 0.78% and 0.26% smaller than experiment, respectively [109]. For Fe_2O_3, we found $a' = 5.35$ Å, $\alpha' = 55.25°$, 1.44% smaller and 0.03% larger than experiment, respectively [113].[12] In ELK, the Cr, Fe, and O ion cores were described using muffin-tin spheres with radii 1.071 Å, 1.0400 Å and 0.80435 Å, respectively; the APW functions and the potential were expanded in a spherical harmonics basis, with cut-offs $l_{\max(\mathrm{apw})} = l_{\max(\mathrm{o})} = 12$. The BZ was sampled using a $6 \times 6 \times 6$ Γ-centered k-point mesh.

3.3.5.5 Magnetic response of the phonon modes

As stated above, we calculate the response of the magnetic dipole moments on the ions to the ionic displacements associated with the applied electric field, constructed from summing the ionic displacements of each phonon mode, with an appropriate amplitude, at each field strength. Note that freezing in each phonon mode separately and appropriately summing the separate magnetic responses gives exactly the same result for the linear response but misses part of the second-order response, i.e., the cross term in the third term of Eq. (3.47). Here, we discuss this method for completeness. Like before, we test the reliability of our calculations by computing the total energy and the forces on the transition metal ions as a function of the phonon amplitude. As an example, in Figure 3.10 we show the results for the highest frequency E_u phonon mode. The energy and the forces along the polarization direction as a function of the amplitude show a quadratic and linear behavior, respectively, as expected.

Next, we calculate the response of the magnetic dipole moments to the displacement of each phonon mode and fit it with a second-order polynomial. As an example, in Figure 3.11 we show the magnetic moments along y (diagonal response, Figure 3.11a) and x (off-diagonal response, Figure 3.11b) induced by the highest frequency E_u phonon mode

[12] Although our equilibrium lattice parameters are reduced with respect to the experimental ones, we are still able to capture the same physics. Fixing the lattice parameters to the experimental values did not qualitatively alter our results.

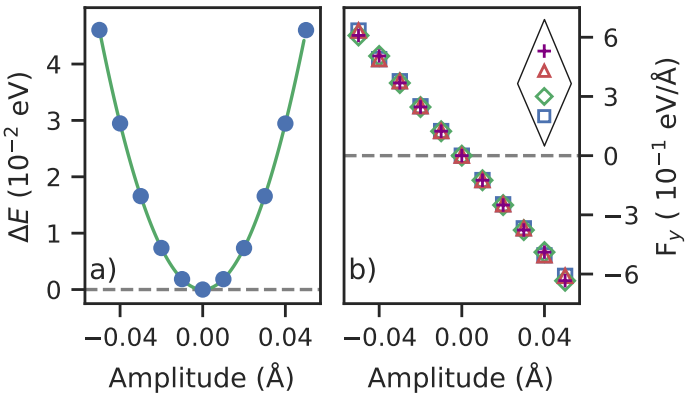

FIGURE 3.10: The a) change in energy, b) force along y on the Cr atoms in Cr_2O_3 as a function of amplitude for the highest energy E_u symmetry phonon mode, polarized along the y axis. In a) data points are represented by blue dots and the second-order polynomial fit with a solid green line. In b) the force on Cr ions 1-4 is indicated with blue squares, green diamonds, red triangles, and purple crosses, respectively. The inset of Figure b) shows how the atoms are ordered in the unit cell, adopting the same order as Figure 3.7 in the main text.

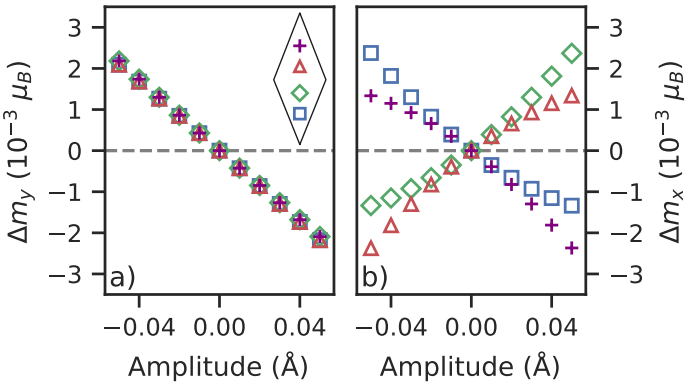

FIGURE 3.11: The a) parallel, b) perpendicular magnetic response on the Cr atoms in Cr_2O_3 as a function of phonon amplitude for the highest energy E_u symmetry phonon mode, polarized along the y axis. Blue squares, green diamonds, red triangles, and purple crosses represent the local response on Cr ions 1-4, respectively. The inset is the same as in Figure 3.10b.

in Cr_2O_3 polarized along the y direction. A summary of the resulting fit parameters for all the E_u modes is given in Table 3.19. We report the second-order fit parameters for completeness.

3.3.5.6 Convergence tests

A: Induced magnetic moments vs. number of self-consistent-field steps

Convergence of the induced magnetic moments on the individual atoms in a self-consistent field (SCF) calculation is non-trivial. Since the induced local magnetic moments Δm_x

		E_u 1 y		E_u 2 y	
		linear	quadratic	linear	quadratic
Cr_2O_3	diagonal	0.027(2)	0.437(5)	0.844(4)	0.69(5)
	off-diagonal	1.757(2)	1.74(3)	2.185(3)	3.09(5)
Fe_2O_3	diagonal	1.356(2)	2.0(5)	3.40(2)	0.61(8)
	off-diagonal	5.393(5)	0.60(8)	0.062(4)	0.66(2)
		E_u 3 y		Eu 4 y	
		linear	quadratic	linear	quadratic
Cr_2O_3	diagonal	6.70(4)	1.4(6)	4.27(1)	1.8(1)
	off-diagonal	0.201(5)	7.33(6)	3.71(1)	20.7(1)
Fe_2O_3	diagonal	6.95(7)	7(2)	1.498(8)	0.3(1)
	off-diagonal	12.59(5)	1.9(7)	19.30(1)	0.9(2)

TABLE 3.19: Absolute value of the linear and quadratic components of the magnetic response to each E_u phonon mode, computed for the transition metal atoms in Cr_2O_3 and Fe_2O_3. Linear response in $10^{-2}\,\mu_B/\text{Å}$ and quadratic response in $10^{-2}\,\mu_B/\text{Å}^2$. The standard deviation errors on the parameters of the fit are given in brackets.

and Δm_y are tiny, a standard convergence threshold on the total energy difference, ΔE, between two consecutive SCF steps, e.g., $\Delta E \approx 10^{-7}$ eV, or on the root mean square of the difference of Kohn-Sham potential, ΔV_{KS}, between two consecutive SCF steps, does not guarantee convergence of the induced moments. Figure 3.12 shows Δm_x, Δm_y, ΔE, and ΔV_{KS} as a function of the SCF step number, with the region between 50 and 150 SCF steps highlighted. Despite ΔE already being well-converged after ≈ 50 SCF steps, ΔV_{KS} is still decreasing and Δm_x, Δm_y are substantially varying. In order to have a small enough and stable ΔV_{KS}, and well converged induced moments, approximately 500 SCF steps are needed.

B: Convergence vs. angular momentum cut-off

We checked the convergence of the results with respect to the angular momentum cut-offs for both the APW wave functions and the KS potential inside the muffin-tin spheres. For the APW wave functions' cut-off, $l_{\text{max, apw}}$, our results are well converged for $l_{\text{max, apw}} \geq 8$. For the potential's cut-off, $l_{\text{max,o}}$, all our results are accurately converged for $l_{\text{max,o}} \geq 12$. The cut-off of the potential affects mostly the size of the induced moments; specifically, low values of $l_{\text{max,o}}$ result in a spurious shift of the induced magnetic moment curve vs. the mode amplitude, as shown in Figure 3.13a for the diagonal ME response of the highest frequency E_u mode. For $l_{\text{max,o}} \geq 12$ the shift disappears, see Figure 3.13b. Increasing $l_{\text{max,o}}$, however, has a negligible effect on the slope of the curve, which is the relevant physical quantity related to the size of the ME response. Figure

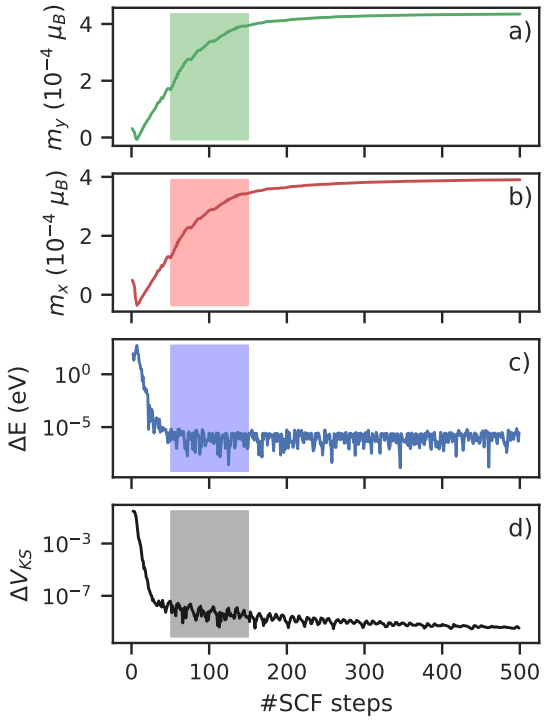

FIGURE 3.12: The magnetic moments along y (a), x (b) on one of the Cr atoms in Cr_2O_3, the change in total energy (c) and the root mean square of the Kohn-Sham potential (d) as a function of the number of SCF steps for the highest frequency E_u symmetry phonon mode, polarized along the y axis, at an amplitude of -0.01 Å.

3.14a shows that the slope does not depend significantly on $l_{\mathrm{max,o}}$, whereas the intercept of the curve with the y axis, Figure 3.14b, changes significantly until $l_{\mathrm{max,o}} \approx 12$. We see that a linear ME response converged within $2 \times 10^{-4}\,\mu_{\mathrm{B}}/\text{Å}$ can be obtained already with $l_{\mathrm{max,o}} = 6$, but the spurious shifts corresponding to the non-vanishing intercept need to be removed artificially.

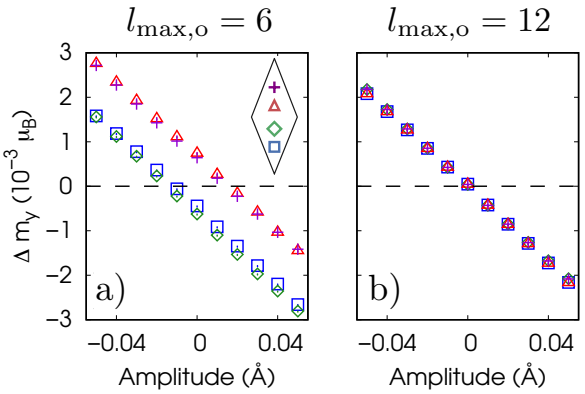

FIGURE 3.13: Change in magnetic moment of the 4 Cr ions in Cr_2O_3, Δm_y, induced by the highest energy E_u phonon mode polarized along y, obtained with (a) $l_{\mathrm{max,o}} = 6$ and (b) $l_{\mathrm{max,o}} = 12$. Blue squares, green diamonds, red triangles, and purple crosses represent the local response on Cr ions 1-4, respectively. The inset is the same as in Figure 3.11a.

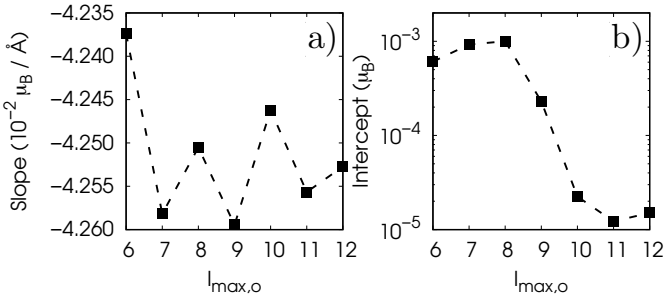

FIGURE 3.14: Slope (a) and intercept (b) of the induced magnetic moment Δm_y as a function of the angular momentum cut off, for the highest frequency E_u phonon mode of Cr_2O_3. The values reported are averaged over the four Cr ions.

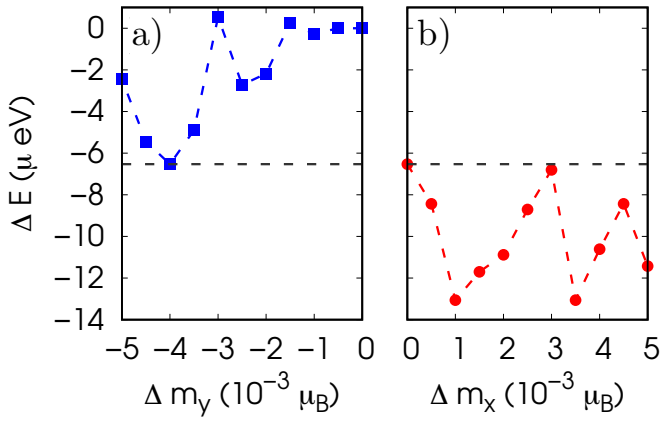

FIGURE 3.15: (a) Energy vs. induced (constrained) magnetic moment along y on the first Cr atom. (b) Energy vs. induced (constrained) magnetic moment along x on the first Cr atom, with $\Delta m_y = -4\times10^{-3}\,\mu_B$, the magnetic moment at the energy minimum in panel a. Calculation performed for the highest energy E_u phonon mode polarized along y, frozen in at an amplitude of 0.05 Å.

C: Constrained moment calculations

Non-collinear calculations with no constraints can sometimes result in a predicted magnetic state that is a metastable configuration, rather than the global minimum, of the total energy as a function of the direction and size of the atomic magnetic moments. To ascertain the reliability of the induced magnetic moments computed at the distorted geometries with unconstrained calculations, we perform additional unconstrained calculations with a different starting configuration than the collinear groundstate magnetic order of the equilibrium structure.

To get a reasonable starting configuration, we perform constrained non-collinear calculations imposing cantings of the magnetic moments, first along y, then additionally along x, arranged according to the predicted ordering for the local linear ME response in Cr_2O_3. To simplify the discussion, we consider the distorted structure obtained by freezing in the highest frequency E_u phonon mode, with amplitude 0.05 Å, and study the total energy as a function of the size of the constrained magnetic moments. Figure

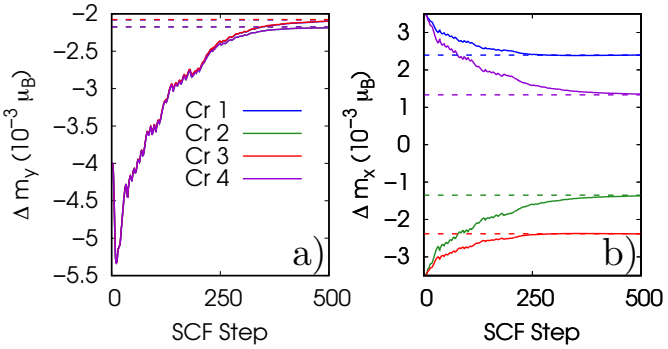

FIGURE 3.16: Δm_y (a) and Δm_x (b) vs. SCF step number for an unconstrained calculation starting from $\Delta m_y = -4\times10^{-3}\,\mu_B$ and $\Delta m_x = 3.5\times10^{-3}\,\mu_B$, corresponding to the minima of Figure 3.15. Dashed lines identify the relaxed values obtained with an unconstrained calculation starting from $|\Delta m_y| = |\Delta m_x| = 0\,\mu_B$.

3.15(a) shows the results obtained by constraining an induced moment ferroically ordered along y. The energy has a minimum for $|\Delta m_y| = 4\times10^{-3}\,\mu_B$, which we use as a starting point to further constrain induced antiferroically ordered moments along x. The total energy computed with constrained induced moments along both y and x is shown in Figure 3.15(b). The energy shows two comparable minima for $|\Delta m_x| = 10^{-3}\,\mu_B$ and $|\Delta m_x| = 3.5\times10^{-3}\,\mu_B$.

We pick the configuration with $|\Delta m_y| = 4\times10^{-3}\,\mu_B$ and $|\Delta m_x| = 3.5\times10^{-3}\,\mu_B$ as a starting configuration for an unconstrained non-collinear calculation. As shown in Figure 3.16, the induced magnetic moments eventually relax to the same values obtained with the starting configuration with $|\Delta m_y| = |\Delta m_x| = 0\,\mu_B$ (i.e., the collinear configuration of the equilibrium structure), thus the resulting configuration is reasonably not a metastable one.

3.4 Additional work

In this section, I will discuss some additional work, which was not published in the paper above. This will include a full overview of the multipoles found in both materials up to 5th order (triakontadipoles), and a relation between the hexadecapoles and the net third-order ME response in Cr_2O_3.

In Table 3.15 we show the ordering of the different quadrupole (ME multipole) components on the transition metal ions. In the paper body, we also discuss the ordering of two of the octupole components, $\mathcal{O}_3$ and $\mathcal{O}_{-3}$, which are relevant for the local ME effects we describe. Yet, there are more non-zero octupole components and even more non-zero components of higher-order multipoles. Here we include a table with the ordering of all non-zero multipole components on the TM atoms (up to 5th order) in both materials (Table 3.20). Here we used both the w_t^{kpr} notation introduced in Section 2.3.2, the naming convention for the ME multipoles (magnetic quadrupoles) introduced in Section 1.4.2, and the nomenclature for octupoles introduced by Urru and Spaldin [45].[13]

We see from this table that in Cr_2O_3 the ferroically ordered components are quadrupoles (ME multipoles) and hexadecapoles, i.e., multipoles that have an odd number of spatial components, consistent with the broken space inversion symmetry. On the other hand, in Fe_2O_3 we have ferroically ordered components that are octupoles and triakontadipoles, multipoles that have an even number of spatial components, consistent with the preserved space inversion symmetry.

We have already discussed the effects of the quadrupole components, as well the role of the $\mathcal{O}_3$ and $\mathcal{O}_{-3}$ components of the octupole. Specifically, we mentioned that for an applied electric field along y, $\mathcal{O}_{-3}$ is associated with a local quadratic response in m_y (in-plane diagonal response) and $\mathcal{O}_3$ with a local quadratic response in m_x (in-plane off-diagonal response). But there are more responses these multipoles are associated with. Furthermore, as seen from Tab. 3.20, there are more non-zero multipole components. Let us consider the octupole tensor $\mathcal{M}^{(2)}_{ijk}$, as defined in Eq. 1.13, where $\mathcal{M}^{(2)}_{ijj}$ is associated with γ_{ijj} as defined in Eq. 1.1, e.g., an induced change in m_i quadratic in the applied electric field along j. In principle $\mathcal{M}^{(2)}_{ijk}$ is a $3 \times 3 \times 3$ tensor with 27 entries, but due to the symmetry restrictions, the number of independent entries is much less than that. First, the two spatial directions are equivalent, so $\mathcal{M}^{(2)}_{ijk} = \mathcal{M}^{(2)}_{ikj}$. Below we list the independent entries, state the relations with the other entries (other than through the exchange of the spatial indices just mentioned), and declare explicitly which octupole component contributes to each:

[13] Note that, as mentioned before in Section 3.3.3, our choice of Cartesian axes differs from Ref. [45].

	multipole component		Ordering	
			Cr_2O_3	Fe_2O_3
dipoles	$-w_0^{011}$	m_z	− + −+	− + +−
quadrupoles	w_0^{110}	a	− − −−	+ + −−
	w_0^{111}	t_z	+ − −+	+ − +−
	w_0^{112}	q_{z^2}	− − −−	+ + −−
octupoles	w_0^{211}	$t_z^{(z)}$	+ − +−	− + +−
	w_0^{212}	$q_{z^2}^{(z)}$	+ + −−	− − −−
	w_0^{213}	$\mathcal{O}_0$	+ − +−	− + +−
	w_{-3}^{213}	$\mathcal{O}_{-3}$	− + −+	− + +−
	w_3^{213}	$\mathcal{O}_3$	− − ++	+ + ++
hexadecapoles	w_0^{312}		+ + ++	+ + −−
	w_0^{313}		− + +−	+ − +−
	w_{-3}^{313}		− + +−	− + −+
	w_3^{313}		− − −−	+ + −−
	w_0^{314}		+ + ++	+ + −−
	w_{-3}^{314}		+ + ++	+ + −−
	w_3^{314}		− + +−	− + −+
triakontadipoles	w_0^{413}		+ − +−	+ − −+
	w_{-3}^{413}		+ − +−	+ − −+
	w_3^{413}		− − ++	− − −−
	w_0^{414}		+ + −−	+ + ++
	w_{-3}^{414}		− − ++	− − −−
	w_3^{414}		− + −+	− + +−
	w_0^{415}		+ − +−	+ − −+
	w_{-3}^{415}		+ − +−	+ − −+
	w_3^{415}		− − ++	− − −−

TABLE 3.20: Symmetry-allowed magnetic dipoles, quadrupoles (ME multipoles), octupoles, hexadecapoles, triakontadipoles, and their ordering on the TM ions in Cr_2O_3 and Fe_2O_3. Atoms are labeled as in Figure 3.7.

$$\mathcal{M}^{(2)}_{111} = \frac{1}{4}\mathcal{O}_3 = -\mathcal{M}^{(2)}_{212} = -\mathcal{M}^{(2)}_{122}, \tag{3.53}$$

$$\mathcal{M}^{(2)}_{112} = \frac{1}{4}\mathcal{O}_{-3} = \mathcal{M}^{(2)}_{211} = -\mathcal{M}^{(2)}_{222}, \tag{3.54}$$

$$\mathcal{M}^{(2)}_{123} = -\frac{1}{2}q^z_{z^2} = -\mathcal{M}^{(2)}_{213}, \tag{3.55}$$

$$\mathcal{M}^{(2)}_{113} = -\frac{1}{10}\mathcal{O}_0 + \frac{1}{3}t_z^{(z)} = \mathcal{M}^{(2)}_{223}, \tag{3.56}$$

$$\mathcal{M}^{(2)}_{311} = -\frac{1}{10}\mathcal{O}_0 - \frac{2}{3}t_z^{(z)} = \mathcal{M}^{(2)}_{322}, \tag{3.57}$$

$$\mathcal{M}^{(2)}_{333} = \frac{1}{5}\mathcal{O}_0, \tag{3.58}$$

which is consistent with the local Wyckoff site symmetry (3). We note that our found $\mathcal{M}^{(2)}_{ijk}$ has slightly enhanced symmetry than expected from the local symmetry alone, which dictates these six independent components. In our found $\mathcal{M}_{ijk}$, the components $\mathcal{M}^{(2)}_{113}$, $\mathcal{M}^{(2)}_{311}$ and $\mathcal{M}^{(2)}_{333}$ are not independent, i.e., $\mathcal{M}_{333} = -\frac{2}{3}(2 * \mathcal{M}^{(2)}_{113} + \mathcal{M}^{(2)}_{311})$. Thus we have five independent components, as expected from the five non-zero octupole compounds we found.

In Cr_2O_3 $t^{(z)}_z$, $q^{(z)}_{z^2}$, $\mathcal{O}_0$, $\mathcal{O}_{-3}$ and $\mathcal{O}_3$ are ordered antiferroically, so there are only local second-order ME effects in Cr_2O_3. In Figure 3.8c (off-diagonal response) the quadratic part of the response is associated with $\mathcal{M}^{(2)}_{122} = -\frac{1}{4}\mathcal{O}_3$, as stated before. In Fe_2O_3 there are two components which are ordered ferroically; $q^{(z)}_{z^2}$ and $\mathcal{O}_3$. As $\frac{1}{4}\mathcal{O}_3 = \mathcal{M}^{(2)}_{111} = -\mathcal{M}^{(2)}_{212} = -\mathcal{M}^{(2)}_{221} = -\mathcal{M}^{(2)}_{122}$, we expect a net second-order response along x (induced m_x) for an electric field applied along x ($\mathcal{M}^{(2)}_{111}$, diagonal response) as well for an electric field applied along y ($\mathcal{M}^{(2)}_{122}$, off-diagonal response), the latter of which we showed in Figure 3.8d. We also expect a net second-order response along y for a field applied along both x and y ($\mathcal{M}^{(2)}_{212}$ and $\mathcal{M}^{(2)}_{221}$). It is clear that for the second-order ME response x and y are not equivalent, unlike for the linear response, where the diagonal response is the same regardless if the applied field is along x or along y. Finally, we also expect net second-order responses due to the ferroic ordering of $q^{(z)}_{z^2}$; a response along x for a field along y and z ($\mathcal{M}^{(2)}_{123}$) and a response along y for a field along x and z ($\mathcal{M}^{(2)}_{213}$).

We can also discuss the consequences of the hexadecapoles. In a similar way as the quadrupoles are associated with the linear ME effect, and the octupoles with the second-order ME effect, the hexadecapoles are associated with the third-order ME effect. However, with increasing order, the magnitude of the effect gets smaller. We found that the local third-order ME response was too small to be detected in our DFT calculations. Nevertheless, as Cr_2O_3 has ferroically ordered hexadecapole components, there should be a net third-order ME response, which may be large enough to be calculated. Indeed when we look at our calculations we see a net third-order response in Cr_2O_3 in different directions when we apply an electric field (Figure 3.17).

We found a third-order response along y for an applied electric field along y (diagonal response), which occurs on top of the linear diagonal response. We also found a third-order response along z for an applied electric field along y (off-diagonal response), which is the lowest-order response along z for a field applied along y.

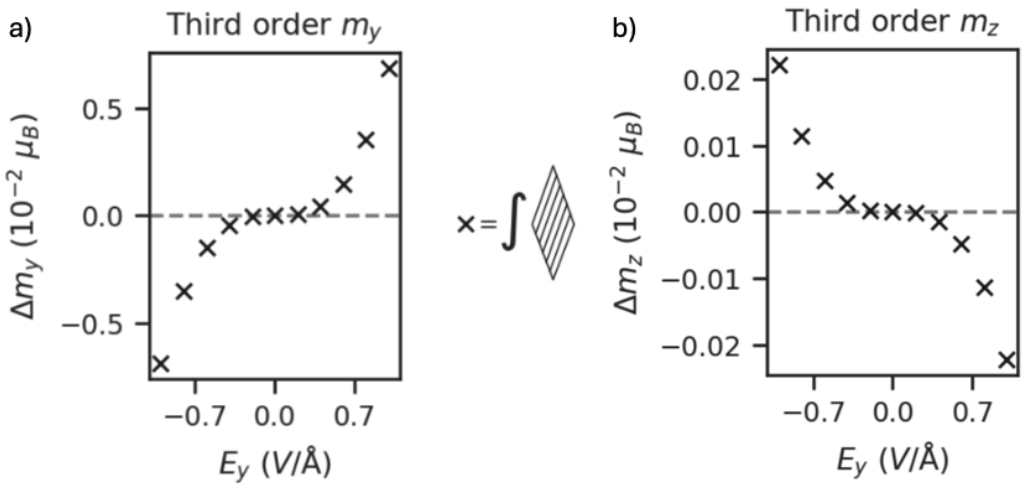

FIGURE 3.17: Third-order component to the induced magnetization along y (a) and z (c) in Cr_2O_3 under the application of an atomic displacement corresponding to an applied electric field along y. As in Figure 3.8 the black crosses indicated the total moment summed over the whole unit cell.

3.5 Comments

Finally, here we discuss some open questions from this work and make some suggestions for future research. The first open question concerns the specific relation between the dipole order and multipole order in the two compounds. In Table 3.20, we show the calculated dipoles and higher-order multipoles, and their signs relative to each other. As discussed above, there are two relative signs, which are relevant here. First, there is the sign of one multipole component, for example, a, on the different sites within one compound. This type of relative sign is set by the symmetry. Second, there is the relative sign of the multipoles on one site with respect to each other, for example, the sign of relative sign of a and t_z on Cr site 1. This is not set by symmetry and we calculated it from DFT. Now with this latter sign, something curious occurs. When we look at Cr_2O_3, we see that the dipole ordering (m_z) is $-+-+$, which means that we have two pairs of 'out-pointing' spins (Figure 3.7a). For both our pairs of 'out-pointing' spins, we have negative values of a and q_{z^2}. If we instead look at Fe_2O_3, we have a dipole ordering that is $-++-$, which means we have an 'out-pointing' bottom pair of Fe ions, and then an 'in-pointing' top pair (Figure 3.7b). Yet, when looking at the signs of the multipoles, we see that the 'out-pointing' pair has *positive* values of a and q_{z^2}, while the 'in-pointing' pair has negative values. This suggests a different coupling between the signs of dipoles and the ME multipoles. We investigated this further by forcing Cr_2O_3 to adopt the magnetic dipole ordering of Fe_2O_3, by initiating the moments in a $-++-$ pattern in ELK. We find that the magnetic dipole ordering stays as we initiated it, e.g., in a $-++-$ pattern. In this configuration, all the symmetries are

also the same as for Fe_2O_3. When we look at the ordering of the multipoles, we see that the 'out-pointing' pair has negative values of a and q_{z^2}, while the 'in-pointing' pair has positive values. In fact most of the multipole components have opposite sign, when we compare Cr_2O_3 with the Fe_2O_3 ordering and Fe_2O_3 itself, further supporting the idea that there is different coupling between the dipole order and higher multipole order in the compounds. We suspect that this is related to the d^3 respectively d^5 character of the d orbitals of the Cr^{3+} and Fe^{3+} ions. We note that this difference between the compounds persists for different DFT parameter choices, and even using different codes (ELK and VASP). However, the situation is complicated by the fact that not all multipole components have opposite signs when we compare Cr_2O_3 with the Fe_2O_3 ordering and Fe_2O_3 itself. For example the w_0^{212} ($q_{z^2}^{(z)}$) component does not have opposite sign, which is the lowest order multipole to not have opposite sign.

The second question concerns the relation between the sign of the multipoles and the sign of the effect. From previous work, it is clear that the multipoles' magnitude does not tell us the magnitude of the associated effect [135]. We see that in our work as well. For example, let's compare Figure 3.8b and d. We see that the off-diagonal linear response (associated with t_z) is larger than the diagonal ME response (associated with a and q_{z^2}). At the same time, the value of t_z is two orders of magnitude smaller. However, it seems that the sign of the multipoles does tell us something about the sign of the effect either. Take for example the linear diagonal effect in Cr_2O_3, which is negative in sign, i.e., the induced magnetization is antiparallel to the applied field and is associated with a and q_{z^2}, which are both negative in sign. We note that both the sign of the effect and the sign of the multipoles change if we go to the other AFM domain, something we will get into in more detail in the next chapter. The relation between the sign of the multipole, or more specifically the entry in the multipole tensor, and the sign of the effect seems to hold in this work, but we do not know that this relation is universal. We point out that the positive sign ferroic ordering of $\mathcal{O}_3$ in Fe_2O_3, associated with the negative second-order ME effect (Figure 3.8) appears to be a counter-example, but is not, as $\mathcal{O}_3$ appears with a minus sign in the relevant octupole tensor entry $\mathcal{M}_{122}^{(2)}$ (Eq. 3.53).

We can also examine the dependence on the spin-orbit coupling (SOC). All the multipoles calculations discussed so far were done in the presence of SOC. Instead, when SOC is turned off, some multipole components become zero, but not all. Specifically, the ferroically ordered octupoles in Fe_2O_3 become zero, suggesting that the net ME effect we found in this compound would disappear too. However, some of the antiferroically ordered octupole components remain. Take for example $\mathcal{O}_0$ (w_0^{213}), which is still present (with the same ordering) in the absence of SOC, although it is slightly reduced in magnitude. This may suggest that these effects have different microscopic origins, the

former depending on SOC and the latter not. The properties of Fe_2O_3 in the absence of SOC is something we get into in more detail in Chapter 5.

Finally, we discuss the macroscopic consequences of the ferroic orderings. In Cr_2O_3, the lowest ferroically ordered magnetic multipole is the ME multipole (quadrupole), to be precise both the a and q_{z^2} components. As a ferroic ordering of magnetic dipoles, if only one domain is present, leads to an external dipolar magnetic field, a ferroic ordering of quadrupoles should lead to an external quadrupolar magnetic field. For Cr_2O_3 Dzyaloshinskii argued based on symmetry, that the external field should be quadrupolar in nature, and thus should fall off obeying the corresponding power law, and this was subsequently confirmed experimentally by Astrov and collaborators, for single domain Cr_2O_3 [136, 137]. For Fe_2O_3, where the lowest order (in the presence of SOC) is the octupoles, one would thus expect an octupolar magnetic field, as long as only one domain is present. Yet, It may prove complicated to measure this, as a field falling off with the corresponding power law would decrease very quickly.

Chapter 4

The sign of the magnetoelectric effect in Cr_2O_3

As mentioned previously, time-reversal symmetry is broken in Cr_2O_3, resulting in two antiferromagnetic (AFM) domains (Figure 2.2), which are changed into each other by performing a time-reversal operation. In the previous chapter, we noted that we find opposite signs for the magnetoelectric (ME) multipoles in both domains and correspondingly opposite signs of the ME effects. That the sign of the linear ME effect is opposite in the two AFM domains had been noted before, but exactly which sign of the effect belonged to which domain remained unclear [14, 83]. In this chapter, I will first introduce spherical neutron polarimetry, an experimental technique that can be used to distinguish AFM domains. Next, I will explain the concept of ME annealing and the way it may be used to prepare a single-domain state in Cr_2O_3. In Section 4.3, I describe our work trying to clarify this relationship, by reviewing the computational literature, performing density functional theory (DFT) calculations in three different codes, and reanalyzing four sets of experimental measurements. Finally, I discuss some open questions.

4.1 Spherical neutron polarimetry

Spherical neutron polarimetry is a neutron scattering technique in which the polarization of the neutrons is set before they are scattered and determined after scattering. In this case, polarization means the orientation of the magnetic moment of the neutron. A detailed description of the technique can be found elsewhere, for example in Refs. [138, 139], so I will only introduce some of the main concepts in this section.

Spherical neutron polarimetry results are usually captured with a polarization matrix P_{ij}, which can be expressed as:

$$P_{ij} = \frac{I^{ij} - I^{-ij}}{I^{ij} + I^{-ij}}, \tag{4.1}$$

where I is a general scattering cross-section and i, j indicate orthogonal directions in real space. This formulation in terms of the polarization matrix is useful in experiment. Though it can be difficult to accurately determine the value of I_{ij}, P_{ij} can be captured with much more precision, as it depends on the sum and difference of two scattering cross-sections [139]. Moreover, I_{ij} and I_{-ij} can both be captured with the same rotation of the crystal, improving the accuracy of the determined P_{ij}.

The orientation of the magnetic moment of the neutrons changes when they interact with the sample, for example through dipole-dipole interactions with the magnetic moments. The amount of rotation depends on the magnetic structure. From the scattering and the reorientation of the polarization, conclusions regarding the magnetic structure can be drawn.

What is especially useful about spherical neutron polarimetry, is the ability to determine the presence of multiple AFM domains, determine how much of the volume of the sample is in which domain, and, if one domain is dominant, determine the orientation of that domain.

We can write the polarization of the neutron beam before the interaction with the materials as $\boldsymbol{P}$, and after the interaction as $\boldsymbol{P'}$. Due to the shape of the interaction, governed by the Blume-Maleev equations [140, 141], $|\boldsymbol{P'}| \geq |\boldsymbol{P}|$ if there is a single domain present. This means that if $|\boldsymbol{P'}| < |\boldsymbol{P}|$ there must be a mixture of multiple domains. Here it is important to distinguish between depolarization, i.e., different neutrons in the beam having different orientations of their magnetic moments, and a rotation of the polarization, i.e., all neutrons have the same polarization but the axis of this polarization has changed. This distinction can be made with spherical neutron polarimetry, where one can access the neutron polarization both parallel and perpendicular to the polarization of the incident neutron beam, while it cannot be made with conventional polarized neutron scattering, which only has access to the polarization component parallel to the polarization of the incident beam.

4.2 Magnetoelectric annealing

As discussed, Cr_2O_3 has two different AFM domains, and in general a piece of bulk material will show both domains. When performing experiments it is often useful to have only a single AFM domain. It was quickly realized that one can use the ME effect to prepare such a single domain state. Specifically, Shtrikman and Treves [142] showed that heating Cr_2O_3 above its Néel temperature and subsequently cooling it in simultaneous electric and magnetic fields parallel to magnetization axis, would result in the formation of a single AFM domain. Furthermore, they established that parallel electric and magnetic fields induced the opposite domain as antiparallel fields. Later, it was shown that an AFM domain state can also be flipped below the Néel temperature, by applying similarly oriented electric and magnetic fields, but of larger strength [143, 144]. This process of applying parallel or antiparallel fields to create a single or dominant domain state was then called ME annealing and has been successfully applied to other linear ME materials as well [145].

We can understand the process of ME annealing in the following way. If we apply an electric field to Cr_2O_3 we induce a magnetization parallel or antiparallel to the applied field, depending on the domain. If we simultaneously apply a parallel or antiparallel magnetic field, the magnetic moments prefer to align with the magnetic field. Hence the domain with the sign of the effect that matches the alignment of the fields is favored. To be specific, a parallel alignment of the fields favors the domain with a positive α (i.e., an electric field induces a magnetic moment parallel to the field) and an antiparallel alignment of the fields favors the domain with a negative α (i.e., an electric field induces a magnetic moment antiparallel to the field). The question is now, which of the the two AFM domains corresponds to which sign of α.

4.3 On the sign of the linear magnetoelectric coefficient in Cr_2O_3

4.3.1 Preface

In this work, we investigated the relation between the AFM domain state of Cr_2O_3 and the sign of linear magnetoelectric effect and its corresponding tensor α. Establishing which domain belongs with which sign of the effect is complicated by the existence of two independent components $\alpha_\perp$ and $\alpha_\parallel$. Moreover, the magnitude of these components is temperature dependent. $\alpha_\parallel$ even changes sign between room temperature, where

most experiments are performed, and absolute zero, the temperature described by DFT simulations.

In this work we aim to summarize the computational literature and supplement it with our own calculations. We seek to reveal if there is a consensus on the relation between AFM domain and sign of α among different DFT based-approaches. Specifically, consensus despite the use of different codes and parameter choice would indicate a robust, fundamental, relationship. The second goal was to reinterpret experimental results, such that they would all be consistent, thus establishing experimental consensus. Furthermore, we aim to compare the computational and experimental results. Finally, we aim to provide a clear overview of the work and the final established relation, taking into account the temperature effects.

Explanatory remarks

Sections 4.3.2-4.3.12 contain the publication:

[20] E. Bousquet, E. Lelièvre-Berna, N. Qureshi, J.-R. Soh, N. A. Spaldin, A. Urru, X. H. Verbeek, and S. F. Weber. "On the sign of the linear magnetoelectric coefficient in Cr_2O_3*". *J. Phys.: Condens. Matter* 36.15 (2024), p. 155701. DOI: 10.1088/1361-648X/ad1a59

My contribution here was to perform the calculations in VASP and ELK and to co-write the manuscript. The calculations in QUANTUM ESPRESSO were performed by Andrea Urru and those in ABINIT by Eric Bousquet. The reanalysis of the experimental data was performed by Jian-Rui Soh, Eddy Lelièvre-Berna and Navid Qureshi. The manuscript was written together by Eric Bousquet, Eddy Lelièvre-Berna, Navid Qureshi, Jian-Rui Soh, Nicola Spaldin, Andrea Urru, Sophie Weber and myself. The version printed here is author accepted manuscript, with the formatting deviating from the published version to ensure a consistent style with the rest of the thesis. This includes changing the spelling from British to American English and changes in punctuation and hyphenation.

4.3.2 Abstract

We establish the sign of the linear magnetoelectric coefficient, α, in chromium, Cr_2O_3. Cr_2O_3 is the prototypical linear magnetoelectric material, in which an electric (magnetic) field induces a linearly proportional magnetization (polarization), and a single magnetic domain can be selected by annealing in combined magnetic (**H**) and electric (**E**) fields. Opposite antiferromagnetic domains have opposite magnetoelectric responses, and which antiferromagnetic domain corresponds to which sign of response has previously been unclear. We use density functional theory (DFT) to calculate the magnetic response of a single antiferromagnetic domain of Cr_2O_3 to an applied in-plane electric field at zero kelvin. We find that the domain with nearest neighbor magnetic moments oriented away from (towards) each other has a negative (positive) in-plane magnetoelectric coefficient, $\alpha_\perp$, at zero kelvin. We show that this sign is consistent with all other DFT calculations in the literature that specified the domain orientation, independent of the choice of DFT code or functional, the method used to apply the field, and whether the direct (magnetic field) or inverse (electric field) magnetoelectric response was calculated. Next, we reanalyze our previously published spherical neutron polarimetry data to determine the antiferromagnetic domain produced by annealing in combined **E** and **H** fields oriented along the crystallographic symmetry axis at room temperature. We find that the antiferromagnetic domain with nearest-neighbor magnetic moments oriented away from (towards) each other is produced by annealing in (anti-)parallel **E** and **H** fields, corresponding to a positive (negative) axial magnetoelectric coefficient, $\alpha_\parallel$, at room temperature. Since $\alpha_\perp$ at zero kelvin and $\alpha_\parallel$ at room temperature are known to be of opposite sign, our computational and experimental results are consistent.

4.3.3 Introduction

Materials in which both time-reversal Θ and space-inversion $\mathcal{I}$ symmetries are broken, while the product $\mathcal{I}\Theta$ symmetry is preserved, have a term in their free energy of the form

$$F(\mathbf{E}, \mathbf{H}) = -\frac{1}{V}\alpha_{ij}E_iH_j, \tag{4.2}$$

where **E** / **H** are electric / magnetic fields, α is the nine-component *magnetoelectric* tensor (SI units s/m) and V is the unit cell volume. This term reveals two distinctive and related material properties. First, there is a preferred magnetic domain orientation, determined by the sign and form of α, in simultaneous magnetic and electric fields, so that annealing in such a combination of fields, called *magnetoelectric annealing*, can be used to select for a specific magnetic domain. Second, by differentiating Eq. 4.2 with respect to electric (magnetic) field to obtain the polarization (magnetization), we see

that

$$P_i(\mathbf{E},\mathbf{H}) = -\frac{\partial F}{\partial E_i} = \frac{1}{V}\alpha_{ij}H_j, \tag{4.3}$$

and

$$M_i(\mathbf{E},\mathbf{H}) = -\frac{1}{\mu_0}\frac{\partial F}{\partial H_i} = \frac{1}{\mu_0 V}\alpha_{ji}E_i, \tag{4.4}$$

where μ_0 is the vacuum permeability. Eqs. 4.3 and 4.4 reveal a linear proportionality between an applied electric (magnetic) field and an induced magnetization M_i (polarization P_i), with α the response tensor. Materials with non-zero α therefore show a linear magnetoelectric (ME) effect and are promising for spintronic applications since they enable voltage-control of magnetism [146].

Corundum-structure chromia, Cr_2O_3, is the prototypical linear magnetoelectric, and the first material in which the linear ME effect was predicted [13] and measured [14, 147]. In addition to its historical relevance, Cr_2O_3 has a high Néel temperature compared to other ME materials and continues to be the primary material of focus in theoretical, experimental, and technological studies of the ME effect. We show the primitive rhombohedral unit cell of Cr_2O_3 in Figure 4.1a. Below its Néel temperature T_N= 307 K [148], Cr_2O_3 adopts a superexchange-mediated easy-axis antiferromagnetic (AFM) "up-down-up-down" ordering of the magnetic dipole moments on the d^3 Cr^{3+} ions along the rhombohedral $\langle 111\rangle$ direction [149, 150]. The $R\bar{3}'c'$ magnetic space group breaks both $\mathcal{I}$ and Θ while preserving $\mathcal{I}\Theta$, thus allowing a linear ME response [107]. In Figure 4.1b

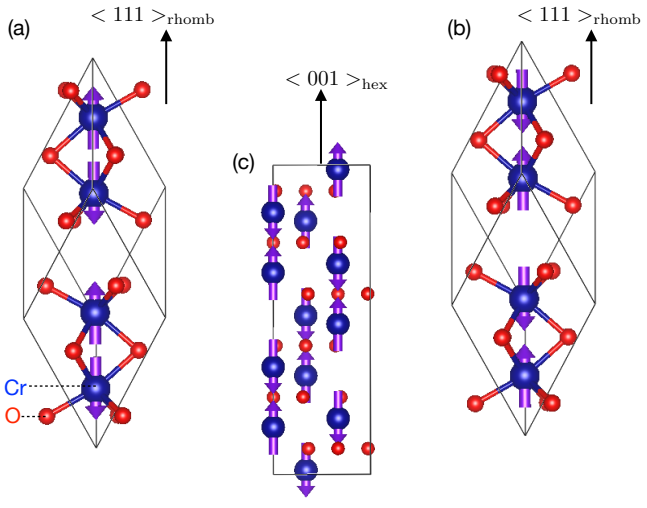

FIGURE 4.1: The crystal structure of Cr_2O_3 showing the primitive rhombohedral unit cell, with the two AFM domains, the 'out-pointing' domain (a) and the 'in-pointing' domain (b). The goal of this work is to determine the absolute signs of the components of α for the two individual domains." The hexagonal setting, which we use in our experimental discussion, is shown in (c) for the in-pointing magnetic domain. Note that $\langle 001\rangle_{\text{hex}} \parallel \langle 111\rangle_{\text{rhomb}}$.

we show the primitive unit cell of the opposite AFM domain, with "down-up-down-up" magnetic dipole ordering. While (a) and (b) are energetically degenerate in the absence of external fields, they correspond to opposite ME domains. As a result, the signs of their linear ME responses are opposite, and they are obtained by ME annealing in opposite combinations of **E** and **H** fields. In Figure 4.1c, we show the unit cell of Cr_2O_3 in the hexagonal setting conventionally used in neutron diffraction, in which the hexagonal $\langle 001 \rangle$ axis is parallel to the rhombohedral $\langle 111 \rangle$ axis.

The symmetry of the $R\bar{3}'c'$ magnetic space group allows for a diagonal response tensor α, described by two independent components which we denote as $\alpha_{\parallel}$ and $\alpha_{\perp}$[13]:

$$\begin{pmatrix} \alpha_{\perp} & 0 & 0 \\ 0 & \alpha_{\perp} & 0 \\ 0 & 0 & \alpha_{\parallel} \end{pmatrix}. \tag{4.5}$$

$\alpha_{\parallel}$ describes the magnetization (polarization) induced when **E** (**H**) is applied along the rhombohedral $\langle 111 \rangle$ axis, and $\alpha_{\perp}$ refers to the perpendicular ME response when the field and induced property lie in the basal plane. Figure 4.2 shows the measured temperature dependence of $\alpha_{\parallel}$ and $\alpha_{\perp}$, extracted from the original experimental report [14]. While $\alpha_{\perp}$, which results from the **E**-field induced canting of the magnetic dipole moments away from the easy axis [81, 83], follows the usual order-parameter onset below T_N, $\alpha_{\parallel}$ has a peak in magnitude just below T_N before decreasing and switching sign at low temperature. This is understood in terms of the response of spin fluctuations at high-temperature [33], with the orbital magnetization response [83] dominating at low temperature. Importantly, at T=0 K, relevant to first-principles calculations, $\alpha_{\perp}$ and $\alpha_{\parallel}$ have the same sign, whereas at room temperature, relevant to many experimental setups, $\alpha_{\perp}$ and $\alpha_{\parallel}$ have opposite signs.

While the *relative* signs of $\alpha_{\perp}$ and $\alpha_{\parallel}$ were established unambiguously in Ref. [147], it was not possible at the time to determine which set of α values correspond to the out-pointing or in-pointing magnetic domains of Figures 4.1a and b. Instead, Ref. [147] showed that reversal of the AFM domain reverses the signs of α as required by symmetry and that the measured magnitudes in multi-domain or poly-crystalline samples are substantially reduced due to cancellation effects. The experimental determination of the specific bulk AFM domain corresponding to a particular ME response is highly non-trivial and requires a generalized form of polarized neutron scattering called spherical neutron polarimetry; to our knowledge, only four such experiments have been performed for Cr_2O_3 [32, 51, 151]. While in principle first-principles calculations based on density

functional theory (DFT) yield this information directly, the AFM domain modeled is often not reported in the literature, and the sensitivity of the magnetic anisotropy to the details of the DFT parameters render an independent experimental determination desirable. To compound confusion, in both the theoretical and experimental literature the terms "magnetic moments" and "spins" have sometimes been used interchangeably, in spite of their being opposite in sign.

The purpose of this paper is to establish unambiguously the signs of the ME effect corresponding to each of the two opposite AFM domains in Cr_2O_3. We achieve this goal by reviewing and reanalyzing the relevant computational and experimental literature, as well as presenting the results of our own new DFT calculations. In Section 4.3.4, we begin by reviewing the DFT-based results for the zero-kelvin values of $\alpha_\perp$ and $\alpha_\parallel$, computed both by us and by others in earlier publications. We then perform a comprehensive cross-check of the domain-dependent sign of α using four different codes, three different methods for applying the external fields, and different choices of DFT parameters.

We find that the *ab initio* results give consistent signs for α across authors, DFT parameters, and codes used.
In Section 4.3.5, we reanalyze the seminal neutron polarimetry experiments which provided the first experimental indicator for the sign of α [32, 51, 151, 152]. While the stated conclusion of the original polarimetry papers contradicts the DFT findings, we show that this is actually due to the assumed sample orientation with respect to the instrument axes during analysis in Refs. [51, 151, 152]. When we account for and correct

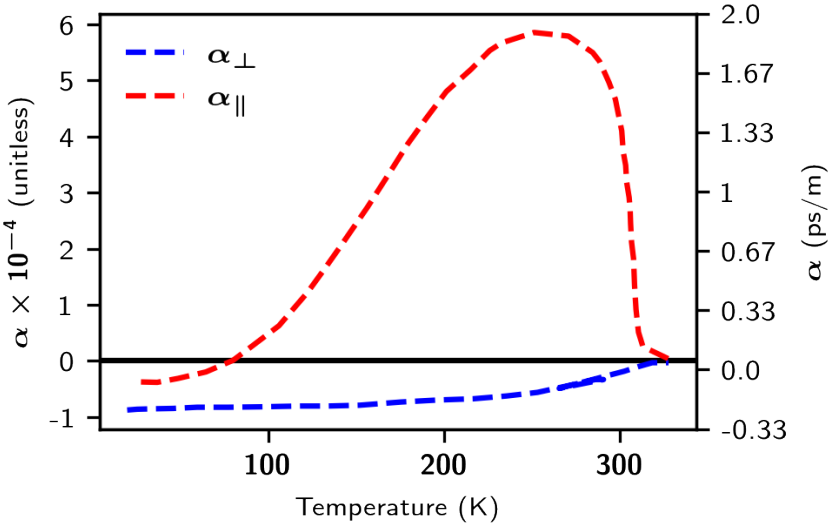

FIGURE 4.2: Temperature dependence of the parallel $\alpha_\parallel$ and perpendicular $\alpha_\perp$ ME responses in Cr_2O_3, extracted from Ref. [14]. α is given in dimensionless units (by multiplying by the speed of light) multiplied by 10^{-4} (left-hand y axis) and SI ps/m units (right-hand y axis).

these inconsistencies, the raw polarimetry data indicate a room-temperature sign of α for a given AFM domain consistent with all DFT calculations (taking into account the experimental temperature dependence of α found by Astrov in Figure 4.2). We hope that this paper clears up long-standing ambiguities and confusions in the literature, and facilitates future interpretations of theoretical and experimental data related to the ME effect in Cr_2O_3 and other ME materials.

4.3.4 Computational studies

Several *ab initio* studies of the magnitude and sign of the ME effect in Cr_2O_3 have been performed previously [33, 81–83, 108]. Three main techniques have been employed: Explicit inclusion of i) a static magnetic field or ii) a static electric field within the DFT Hamiltonian, and iii) the so-called "lattice-mediated" method, in which a polar displacement of the ions simulates the application of an electric field. Both spin and orbital contributions to the response have been calculated, and α has been resolved into so-called *clamped-ion* (the electronic response to an electric field with fixed ions) and *lattice-mediated* (in which the ions are displaced by the electric field) components. Since most DFT codes (in particular ABINIT [153, 154], ELK [70], QUANTUM ESPRESSO [155, 156] and VASP [68, 69]) output magnetic moments rather than spins, we adopt this convention here.

First, we summarize the results of the various literature studies that report both the AFM domain studied and the sign of the calculated α. The technical details for each calculation are summarized in Table 4.1. First, Malashevich *et al.* [83] found $\alpha_{\parallel}$ and $\alpha_{\perp}$ to have the same positive sign at 0 K for a domain with in-pointing moments (as in Figure 4.1b). They used the finite electric-field method so that both spin and orbital contributions and the full lattice-mediated and electronic responses were included. For the same domain, Íñiguez [81] used the 'lattice-mediated' method and obtained a positive 0 K lattice-mediated spin ME response $\alpha_{\perp}$; since Ref. [81] did not include orbital contributions, $\alpha_{\parallel}$ was zero. Also using the lattice-mediated approach but including the orbital contributions, Ye and Vanderbilt [108] found positive $\alpha_{\parallel}$ and $\alpha_{\perp}$ for the domain with in-pointing moments at 0 K. Bousquet *et al.* [82], using an explicitly applied magnetic Zeeman field, including both the lattice-mediated and clamped-ion spin contributions, find a positive 0 K $\alpha_{\perp}$ for the in-pointing domain as well [157]. Finally, Mostovoy *et al.* [33] considered the opposite domain (note that Figure 1 of Ref. [33] shows *spins*) and calculated the finite-temperature spin contribution to $\alpha_{\parallel}$, using Monte-Carlo simulations of a DFT-derived model Hamiltonian containing Heisenberg exchanges and a magnetic moment - polarization coupling. They found a positive $\alpha_{\parallel}$ in the temperature range of T = 60-400 K, consistent with a negative $\alpha_{\parallel}$ at T = 0 K (Figure 4.2). Since

									$\alpha_\perp$		$\alpha_\parallel$	
Source	Code	PP	XC	U (eV)	SOC	Unit cell	Contributions to α	Method	ps/m	g.u. ($\times 10^{-4}$)	ps/m	g.u. ($\times 10^{-4}$)
Ref. [83]	QE	NC	PBE	no U	yes	PBE	LM+CI, S+O	electric field	-1.04	-3.12	-0.02	-0.06
Ref. [81]	VASP	PAW	LDA	$U_{eff} = 2$	yes	expt.	LM, S	lattice-mediated	-0.43	-1.3	–	–
Ref. [108]	QE	NC	PBE	no U	yes	PBE	LM, S+O	lattice-mediated	-0.658	-1.97	-0.0221	-0.0663
Ref. [82]	VASP	PAW	LDA	$U_{eff} = 2$	yes	expt.	LM+CI,S	Zeeman field	-1.45	-4.35	–	–
Ref. [33]*	VASP	PAW	LDA	$U_{eff} = 2$	no	expt.	LM+CI, S	magnetic exchange	–	–	3.77	11.3
This work	ELK	AE	LDA	U = 4.0 J = 0.5	yes	LDA	LM, S	lattice-mediated	-0.921	-2.76	–	–
This work	VASP	PAW	LDA	U = 4.0 J = 0.5	yes	LDA	LM, S	lattice-mediated	-0.857	-2.57	–	–
This work	QE	US	PBE	no U	yes	PBE	LM, S	lattice-mediated	-0.773	-2.32	–	–
This work	Abinit	NC	LDA	no U	yes	expt.	LM+CI, S	Zeeman field	-1.48	-4.44	–	–
This work	Abinit	NC	LDA	no U	yes	expt.	LM+CI, S	electric field	-1.48	-4.44	–	–

TABLE 4.1: Overview of parameters used in different DFT calculations, performed with different codes (QE stands for QUANTUM ESPRESSO). The short-hand notations for pseudopotentials (PP) and exchange-correlation functionals (XC) are: projector-augmented wave (PAW) [71], norm-conserving (NC), ultra-soft (US), all-electron (AE), local-density approximation (LDA) and generalized-gradient approximation with the Perdew-Burke-Ernzerhof (PBE) parametrization. SOC denotes spin-orbit coupling and the different contributions to α are indicated with LM (lattice-mediated) and CI (clamped-ion), spin (S) and orbital (O).
* Results obtained at $T = 240\,\mathrm{K}$.

their calculations modeled the out-pointing domain, these results are consistent with the other computational studies discussed earlier.

To supplement the literature results, we perform a comprehensive cross-check of the domain-dependent sign of $\alpha_\perp$ using four different codes and three different methods.[1] First, we calculate the lattice-mediated spin contribution to $\alpha_\perp$ using the lattice-mediated method, as described in Ref. [81], using the ELK [70], VASP [68, 69], and QUANTUM ESPRESSO [155, 156] codes, with the parameters listed in Table 4.1. In all cases we find $\alpha_\perp < 0$ for the out-pointing domain at 0 K, consistent with the literature findings summarized above. In addition, we use the ABINIT code [153, 154] to calculate the spin contribution to the ME effect by both explicitly applying an electric field as in Ref. [83], and a magnetic Zeeman field method as in Ref. [82]. Both methods give the same positive value of $\alpha_\perp$ for the in-pointing domain at 0 K. Computational details for the calculations in ELK, VASP, QUANTUM ESPRESSO, and ABINIT can be found in Appendices 4.3.12.1-4.3.12.4. We list our calculated $\alpha_\perp$ values in Table 4.1, and in Figure 4.3, we plot the induced in-plane magnetizations as a function of in-plane electric fields calculated here and from the literature. Although there is complete agreement on the sign of α, it is clear that there is some spread in the magnitude of calculated values.

[1] The relevant input files and data of our *ab initio* calculations are openly available on the Materials Cloud Archive at [158].

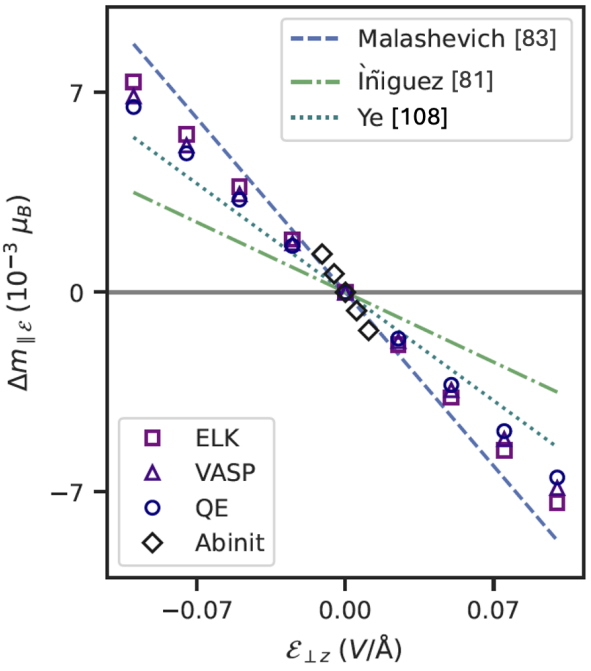

FIGURE 4.3: Induced net magnetic moment per rhombohedral unit cell parallel to an applied electric field oriented perpendicular to the easy axis, as a function of electric field strength for the out-pointing domain. The three lines show the response calculated from literature $\alpha_\perp$ values. Markers indicate our results using four different DFT codes.

		$\alpha_\parallel$	$\alpha_\perp$
0 K	out-pointing domain	–	**–**
	in-pointing domain	+	**+**
		$\alpha_\parallel$	$\alpha_\perp$
RT	out-pointing domain	**+**	–
	in-pointing domain	–	+

TABLE 4.2: The sign of alpha for the two domains, at 0 K and room temperature (RT) as determined by different *ab initio* calculations. Note that not always both domains were calculated explicitly, but we infer the sign of α in one domain from the sign of α in the other, as they have to be opposite. Thus, we infer the sign of $\alpha_\parallel$ for the out-pointing domain at 0K and for the in-pointing domain at RT. $\alpha_\perp$at RT was not calculated but is inferred from the 0 K results, as it is known not to change sign between 0 K and RT, from the temperature dependence measured by Astrov, see Figure 4.2. The inferred signs are displayed in grey, while the explicitly calculated ones are in black and bold.

This distribution cannot be explained only by the different contributions to α that were taken into account and is most likely also the result of the different choices in electronic structure code, electronic exchange parameters, and convergence criteria. Considering these differences, the agreement on the magnitude of α is remarkable.

In summary, the calculated signs of α are consistent across DFT codes and methodologies, with the 0 K $\alpha_\perp$ and $\alpha_\parallel$ positive for the in-pointing domain, the 0 K $\alpha_\perp$ negative for the out-pointing domain, and the room temperature $\alpha_\parallel$ positive for the out-pointing domain. We summarize this result in Table 4.2, where we also inferred the sign of $\alpha_\parallel$ for the in-pointing domain at room temperature from the knowledge that it must be opposite to the sign of $\alpha_\parallel$ for the out-pointing domain at room temperature. Similarly, we infer the sign of $\alpha_\parallel$ for the out-pointing domain at 0K. Finally, the signs of $\alpha_\perp$ at room temperature are inferred from the sign at 0K and the knowledge from experiment (Figure 4.2) that $\alpha_\perp$ maintains the same sign at 0K and room temperature.

4.3.5 Experimental studies

To our knowledge, there exist four sets of data in which the magnetic structure of Cr_2O_3 was measured using spherical neutron polarimetry (SNP), the generalized form of polarized neutron scattering [32, 51, 151, 152]. This technique allows for both the detection of the domain imbalance between the two different magnetic structures shown in Figure 4.1, and for the determination of the magnetic moment configuration of the predominant domain [32]. This is possible because with SNP, the polarization vectors

of both the incident and scattered neutron beams are determined; in comparison, in conventional (uniaxial) polarized neutron scattering, the scattered neutron polarization information is only analyzed along the direction of the incident beam polarization [138]. Therefore, SNP is an ideal method for elucidating which spin configuration shown in Figure 4.1 is stabilized by the parallel or antiparallel combination of electric and magnetic fields.

The SNP measurements reported in Refs. [32, 51, 151, 152] were performed at the IN20 and D3 beamlines at the Institut Laue Langevin (ILL, Grenoble), using the CRYOgenic Polarization Analysis Device (Cyopad). The Cryopad consists of a zero-magnetic field sample chamber surrounded by magnetic fields manipulating the incident ($\mathbf{P}_i$) and scattered ($\mathbf{P}_f$) beam polarizations [159, 160]. The field regions are decoupled with a pair of concentric superconducting Meissner shields combined with μ-metal yokes and screens. The incident neutron beam polarization was controlled using a combination of a nutator and precession coil, and was oriented along one of three orthogonal experimental coordinates which were defined as x, which is along the direction of the scattering vector $\mathbf{Q}$, z, which is perpendicular to the horizontal scattering plane, and y, which completes the right-handed coordinate set. The polarization of the scattered neutron beam was also analyzed along these three principal axes using another set of precession and nutator coils.

In each of the four studies, the Cr_2O_3 sample was aligned so that the crystal b axis was perpendicular to the horizontal scattering plane, which allowed access to the $(h\,0\,l)$ reflections (importantly, this introduces an ambiguity between $b\|+z$ and $b\|-z$, which we will discuss in more detail in the following section). Here, the Miller indices correspond to the hexagonal setting of the rhombohedral ($R\bar{3}c$) unit cell of Cr_2O_3 adopted in Refs. [32, 51, 151, 152]. In the three most recent studies, prior to installing the sample in the Cryopad for the SNP measurements, the Cr_2O_3 sample was cooled through the Néel temperature (T_N∼310 K) in a combination of electric and magnetic fields oriented along the crystallographic c axis to achieve an imbalance of 180° domain population [32, 51, 151]. Brown *et al.* reported that this annealing process stabilized a single AFM domain [32, 51, 151], and that the type of AFM domain (Figure 4.1) could be chosen based on the relative orientation of the external magnetic ($\mathbf{H}$) and electric fields ($\mathbf{E}$). The experimental determination of which magnetic domain is favored then boils down to the determination and interpretation of the sign of the polarization matrix element P_{zx}.

Experimentally, P_{zx} is determined by measuring two quantities, namely n_{zx} and $n_{z\bar{x}}$, which are the number of scattered neutrons with the polarization parallel and antiparallel to $+x$ for the incident neutron polarization along $+z$. The experimental P_{zx} matrix

element is in turn obtained by taking the ratio,

$$P_{zx} = \frac{n_{zx} - n_{z\bar{x}}}{n_{zx} + n_{z\bar{x}}}, \tag{4.6}$$

for a given Bragg reflection $\mathbf{Q} = (h\,k\,l)$. As such, the quantity P_{zx} is bounded between -1 and 1.

In order to determine which AFM domain is favored, the authors in Refs. [32, 51, 151, 152] expressed P_{zx} in terms of three dimensionless quantities,

$$P_{zx} = \eta \frac{-2q_y\gamma}{1+\gamma^2}. \tag{4.7}$$

The η term defines the population imbalance between the two magnetic domains and is given by $\eta = (v^+ - v^-)/(v^+ + v^-)$, where v^+ and v^- are the volumes of the two magnetic domains. Hence, the value of η is bounded between 1 and -1. If the two magnetic domains are equally populated, the factor η becomes 0. The term q_y is determined by the orientation of the crystal with respect to the experimental setup, with the sign of q_y depending on whether the crystallographic $+b$ axis is along the $+z$ or $-z$ direction of the experimental geometry; for example, q_y is +1 (-1) if the magnetic interaction vector $\mathbf{M}_\perp(\mathbf{Q})$ is parallel (antiparallel) to the $+y$ axis of the experimental geometry. Hence, it is crucial to determine whether $+b$ is along the $+z$ or $-z$ direction. Finally, the term γ is associated with the magnetic structure, with the sign of γ being positive (negative) for the out-pointing (in-pointing) magnetic domain.

Based on this discussion, we identify three inconsistencies across the four Refs. [32, 51, 151, 152], which we clarify here. (Note that the measurements in Refs. [32, 51, 151, 152] were made with the same crystal by the same group of coauthors so we expect the underlying physics to be consistent).

4.3.5.1 Spin vs magnetic moment

The first discrepancy is between Ref. [51] and Ref. [32], regarding the definition of spin $\mathbf{S}$ and magnetic moments $\boldsymbol{\mu}$. In Ref. [51], the authors propose that the antiparallel $\mathbf{E}$ and $\mathbf{H}$ fields favor the 'out-pointing' arrows (Figure 4.1a) and designate the arrows as spin directions. On the other hand in Ref. [32], the authors present 'in-pointing' arrows (Figure 4.1b), which they designate as magnetic moments, and state that this magnetic structure is stabilized by parallel $\mathbf{E}$ and $\mathbf{H}$ fields. These two statements are incompatible since the Cr spin direction and magnetic moment direction are antiparallel, i.e., $\boldsymbol{\mu}_s = -g_s\mu_B\mathbf{S}/\hbar$, where g_s is the electron g-factor.

In the neutron scattering community, however, the terms spin and magnetic moment are often used interchangeably to mean magnetic moment direction. We should therefore assume that the arrows in Ref. [51] actually indicate magnetic moments, rather than spins as stated. This resolves the apparent discrepancy between Ref. [32] and Ref. [51].

4.3.6 Orientation of the crystal *b* axis

Second, the labeling of the Miller indices $(h0l)$ across the four reports is inconsistent. In the first report [152], the two reported reflections, namely $(1\,0\,2)$ and $(\bar{1}\,0\,4)$, are in fact forbidden by the $R\bar{3}c$ space group in the hexagonal setting of Cr_2O_3. In the subsequent study, the two reported reflections, $(\bar{1}\,0\,2)$ and $(1\,0\,\bar{2})$ are both allowed by $R\bar{3}c$. In the following two reports [51, 151], where forty reflections were reported in total, thirty-two are in fact forbidden by the $R\bar{3}c$ space group of Cr_2O_3. The h and l Miller indices of the remaining eight reflections are both multiples of 3, e.g., $(3\,0\,6)$ and $(3\,0\,\bar{6})$, and are hence allowed.

Given that the magnetic propagation vector of Cr_2O_3 is $\mathbf{Q}_m$=(0 0 0), the magnetic scattering intensity occurs at the same reciprocal space location as the structural Bragg peaks of Cr_2O_3. As such, the Miller index of the magnetic/nuclear reflections should follow the general condition of the $R\bar{3}c$ space group, where $-h+k+l$=3n. Since the four reports were concerned with reflections in the $(h\,0\,l)$ plane, the observed reflections should obey the rule $-h+l$=3n, given that k=0. In Figure 4.4a we plot the calculated reciprocal space maps for Cr_2O_3 in the $(h\,0\,l)$ scattering plane, assuming that the $+b$ crystal axis is along the $+z$ direction as stated in the original papers. Here, the allowed reflections, such as $(\bar{1}\,0\,2)$ and $(1\,0\,4)$, are denoted by the black-filled circles, and the reciprocal space location of the forbidden reflections that do not obey $-h+l$=3n are shown by the crosses $(\times)$.

The observed reflections in Refs. [51, 151, 152] are denoted by the arrows in the reciprocal space map. Indeed, many of the observed reflections, including $(1\,0\,2)$ and $(1\,0\,\bar{4})$, are in fact forbidden by the $R\bar{3}c$ space group.

If instead, we assume that the $+b$ crystal axis was oriented along the $-z$ direction (rather than $+z$), then the reciprocal space location of all forty-two observed reflections reported in [51, 151, 152], is fully compatible with the $R\bar{3}c$ space group. This scenario is very plausible, due to a possible mix-up between the $+b$ and $-b$ crystal axes, which are inequivalent in Cr_2O_3. As shown in Figure 4.4b, where we plot the calculated reciprocal space maps for Cr_2O_3 in the $(h\,0\,l)$ scattering plane, assuming that the $+b$ crystal axis is

Parallel **H** and **E**

Crystal	$(h\,k\,l)$	Axis$\|\|z$	Axis$\|\|$**H**	Axis$\|\|$**E**	P_i			$P_f^{\text{obs.}}$			$P_f^{\text{calc.}}$ out pointing			$P_f^{\text{calc.}}$ in pointing		
					x	y	z	x	y	z	x	y	z	x	y	z
I	$\bar{1}\,0\,2$	$0\,1\,0$	$0\,0\,1$	$0\,0\,1$	0.00	0.00	0.88	0.83	0.06	0.08	0.88	0.00	0.00	-0.88	0.00	0.00
		$0\,\bar{1}\,0$	$0\,0\,\bar{1}$	$0\,0\,\bar{1}$	0.00	0.00	0.72	-0.69	0.06	-0.06	-0.72	0.00	0.00	0.72	0.00	0.00
		$0\,\bar{1}\,0$	$0\,0\,1$	$0\,0\,1$	0.00	0.00	0.72	-0.70	0.05	-0.05	-0.72	0.00	0.00	0.72	0.00	0.00
II	$1\,0\,\bar{2}$	$0\,\bar{1}\,0$	$0\,0\,\bar{1}$	$0\,0\,\bar{1}$	0.88	0.00	0.00	-0.10	0.00	0.86	0.00	0.00	0.88	0.00	0.00	-0.88
		$0\,\bar{1}\,0$	$0\,0\,\bar{1}$	$0\,0\,\bar{1}$	0.00	0.88	0.00	0.06	0.88	0.03	0.00	0.88	0.00	0.00	0.88	0.00
		$0\,\bar{1}\,0$	$0\,0\,\bar{1}$	$0\,0\,\bar{1}$	0.00	0.00	0.88	-0.87	0.03	0.02	-0.88	0.00	0.00	0.88	0.00	0.00

TABLE 4.3: Comparison between the measured ($P_f^{\text{obs.}}$) and calculated ($P_f^{\text{calc.}}$) polarization matrices with 'out-pointing' and 'in-pointing' magnetic domain for the data collected with **E** and **H** parallel. The data is consistent with the 'out-pointing' magnetic domain, as shown in Figure 4.1a.

Antiparallel **H** and **E**

Crystal	$(h\,k\,l)$	Axis$\|\|z$	Axis$\|\|$**H**	Axis$\|\|$**E**	P_i			$P_f^{\text{obs.}}$			$P_f^{\text{calc.}}$ out pointing			$P_f^{\text{calc.}}$ in pointing		
					x	y	z	x	y	z	x	y	z	x	y	z
I	$\bar{1}\,0\,2$	$0\,\bar{1}\,0$	$0\,0\,1$	$0\,0\,\bar{1}$	0.00	0.00	0.72	0.71	0.12	0.02	-0.72	0.00	0.00	0.72	0.00	0.00
		$0\,\bar{1}\,0$	$0\,0\,\bar{1}$	$0\,0\,1$	0.00	0.00	0.72	0.70	0.16	0.05	-0.72	0.00	0.00	0.72	0.00	0.00
II	$1\,0\,\bar{2}$	$0\,\bar{1}\,0$	$0\,0\,\bar{1}$	$0\,0\,1$	0.88	0.00	0.00	0.12	0.00	-0.85	0.00	0.00	0.88	0.00	0.00	-0.88
		$0\,\bar{1}\,0$	$0\,0\,\bar{1}$	$0\,0\,1$	0.00	0.88	0.00	0.00	0.88	-0.05	0.00	0.88	0.00	0.00	0.88	0.00
		$0\,\bar{1}\,0$	$0\,0\,\bar{1}$	$0\,0\,1$	0.00	0.00	0.88	0.86	0.12	0.14	-0.88	0.00	0.00	0.88	0.00	0.00
II	$\bar{1}\,0\,2$	$0\,\bar{1}\,0$	$0\,0\,\bar{1}$	$0\,0\,1$	0.88	0.00	0.00	0.10	0.06	-0.86	0.00	0.00	0.88	0.00	0.00	-0.88
		$0\,\bar{1}\,0$	$0\,0\,\bar{1}$	$0\,0\,1$	0.00	0.88	0.00	-0.09	0.88	0.02	0.00	0.88	0.00	0.00	0.88	0.00
		$0\,\bar{1}\,0$	$0\,0\,\bar{1}$	$0\,0\,1$	0.00	0.00	0.88	0.87	0.03	0.08	-0.88	0.00	0.00	0.88	0.00	0.00

TABLE 4.4: Comparison between the measured ($P_f^{\text{obs.}}$) and calculated ($P_f^{\text{calc.}}$) polarization matrices with 'out-pointing' and 'in-pointing' magnetic domain for the data collected with **E** and **H** antiparallel. The data is consistent with the 'in-pointing' magnetic domain, as shown in Figure 4.1b.

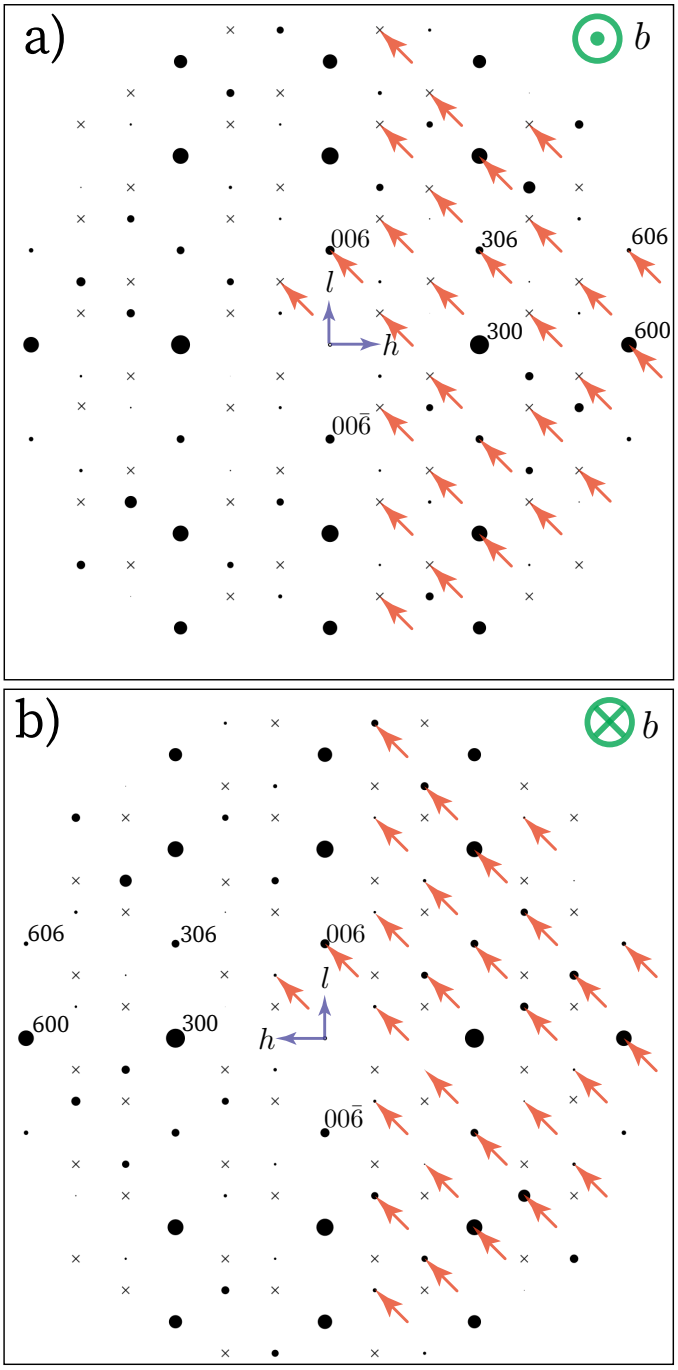

FIGURE 4.4: Plan view of the horizontal scattering plane of the reciprocal space map of Cr_2O_3, with the crystal b axis (a) along the $+z$ direction quoted in [51, 151, 152] and (b) -z directions, respectively. Here the filled circles indicate the allowed reflections, with the size of the circle proportional to the neutron scattering cross-section, whereas the cross ($\times$) denotes forbidden reflections. (a), The arrows indicate the reciprocal space location of the observed reflections in Refs. [51, 151, 152], of which many are forbidden by the $R\bar{3}c$ space group of Cr_2O_3. (b), Instead, if the crystal b axis were actually along the -z direction, then the observed reflections denoted by the arrows can be accounted for.

along the $-z$ direction, the reciprocal space location of the observed reflections denoted by all of the arrows can now be accounted for.

Changing the direction of the $+b$ axis has two main consequences for the interpretation of the results in Refs. [51, 151, 152]. First, it swaps the h Miller index of the reflections, such that the observed peaks which were designated as $(h\,0\,l)$ should be assigned as $(\bar{h}\,0\,l)$ instead. This would allow the thirty-four reflections which were originally forbidden now be compatible with $R\bar{3}c$, i.e., to obey the $-h + l{=}3n$ condition. The remaining eight reflections which have the h and l Miller indices both being multiples of 3, still obey this condition. The second is that in Ref. [32] the sign of q_y changes, which means that the interpretation of which magnetic domain is favored also changes.

Therefore, we conclude that the conjugate field with **E** and **H** parallel favors the 'out-pointing' domain, as shown in Figure 4.1a. By the same token, the antiparallel **E** and **H** field favor the 'in-pointing' domain. This is opposite to the interpretation in Ref. [51].

4.3.6.1 Sign of γ

Finally, the third inconsistency is between Refs. [151] and [51]. In these studies, the γ term was obtained by measuring the polarization P_{zx} component of various reflections. Ref. [151] reports, in Table 3, the γ values for twelve reflections obtained on the IN20 instrument with thermal neutrons ($\lambda{=}1.532\,$Å). On the other hand, Ref. [51] reports the measurements of γ for a further fifteen reflections acquired on the D3 instrument with hot neutrons. Table 2 of Ref. [51] lists the γ data acquired from the D3 instrument along with those measured on the IN20 instrument, which were reported in Ref. [151].

The discrepancy lies in the sign of γ of the data collected on the IN20 instrument, which are reported both in Table 2 of Ref. [51] and also in Table 3 of Ref. [151]. Although the Miller indices of the twelve reflections and their corresponding magnitude of γ are the same, the signs are different. Since the sign of γ is used to interpret whether the magnetic domain is 'out-pointing' or 'in-pointing', this discrepancy calls into question which sign of γ was measured.

To resolve the ambiguity, here we use the Mag2Pol software [161] to re-analyze the measured spherical neutron polarimetry data presented in Table 2 of Ref. [32]. We choose this data set because the Miller indices are allowed by the $R\bar{3}c$ space group, and the raw data are presented explicitly. Moreover, these measurements were performed on cooling the Cr_2O_3 sample with a conjugate field of parallel or antiparallel **E** and **H** fields through T_N to $T{=}290\,$K, where the measurements were performed. Tables 4.3 and 4.4 tabulate the measured polarization matrices for the case where **E** and **H** are parallel and antiparallel, respectively, along with the results of our new analysis for the two cases where the magnetic domain is 'out-pointing' or 'in-pointing'.

Our analysis assuming an 'out-pointing' domain is consistent with the measured scattered neutron polarization for the case where **E** and **H** are parallel, contrary to the conclusions in Refs. [32, 51, 151, 152]. Similarly, for the case where **E** and **H** are antiparallel, we find that the measured polarization matrices are consistent with an 'in-pointing' domain.

4.3.7 Conclusion

We have combined a literature review, new *ab initio* results, and a careful reanalysis of spherical neutron polarimetry data in an effort to resolve long-standing confusion regarding the domain-dependent sign of the ME coefficient in Cr_2O_3. We have shown that all *ab initio* results to date are in agreement in the assignments of negative and positive low-temperature α to the out-pointing and in-pointing domains depicted in Figure 4.1. These conclusions are remarkably consistent across multiple codes and methods. Gratifyingly, the room-temperature spherical neutron polarimetry *data* are consistent with the low-temperature *ab initio* findings given that the room-temperature sign of $\alpha_{\parallel}$ is opposite to its low-temperature sign. The opposite interpretation in some of our literature experimental papers stems from a sign error due to subtle inconsistencies in the analysis which we discussed in Section 4.3.5. The confusion and deceptive inconsistency have also been compounded in the past by ambiguous terminology from numerous authors related to the usage of "spin" versus "magnetic" moment. We summarize the relationship between the domains and the sign of α, as well as the necessary alignment of the **E** and **H** fields during magnetoelectric annealing, in Figure 4.5.

We mention here an important consequence of our work for a related feature of Cr_2O_3; the magnitude and sign of the uncompensated magnetization on the (001) surface for a given bulk domain [162, 163]. At the 0-K limit in the absence of thermal fluctuations, the direction of the (001) surface magnetization is unambiguously determined by the bulk domain which is selected in the ME annealing process. For example, with the in-pointing domain depicted for the hexagonal cell in Figure 4.1c, the surface magnetization from the dangling Cr at the (001) surface points outwards (positive). However, for any experimental characterizations performed at room temperature, the relation between the bulk domain and the sign of surface magnetization is much less clear. Indeed, recent DFT-Monte Carlo calculations performed by some of the authors [164] indicate that the (001) surface magnetic moments of Cr_2O_3 are essentially paramagnetic at room temperature due to weak coupling to the bulk order parameter. Thus, it is likely that for a fixed domain, the surface magnetization is substantially reduced, or even switches sign, with respect to its 0 K value. Now that we have definitively determined which domain is selected by a given ME annealing at room temperature, it will be very interesting to

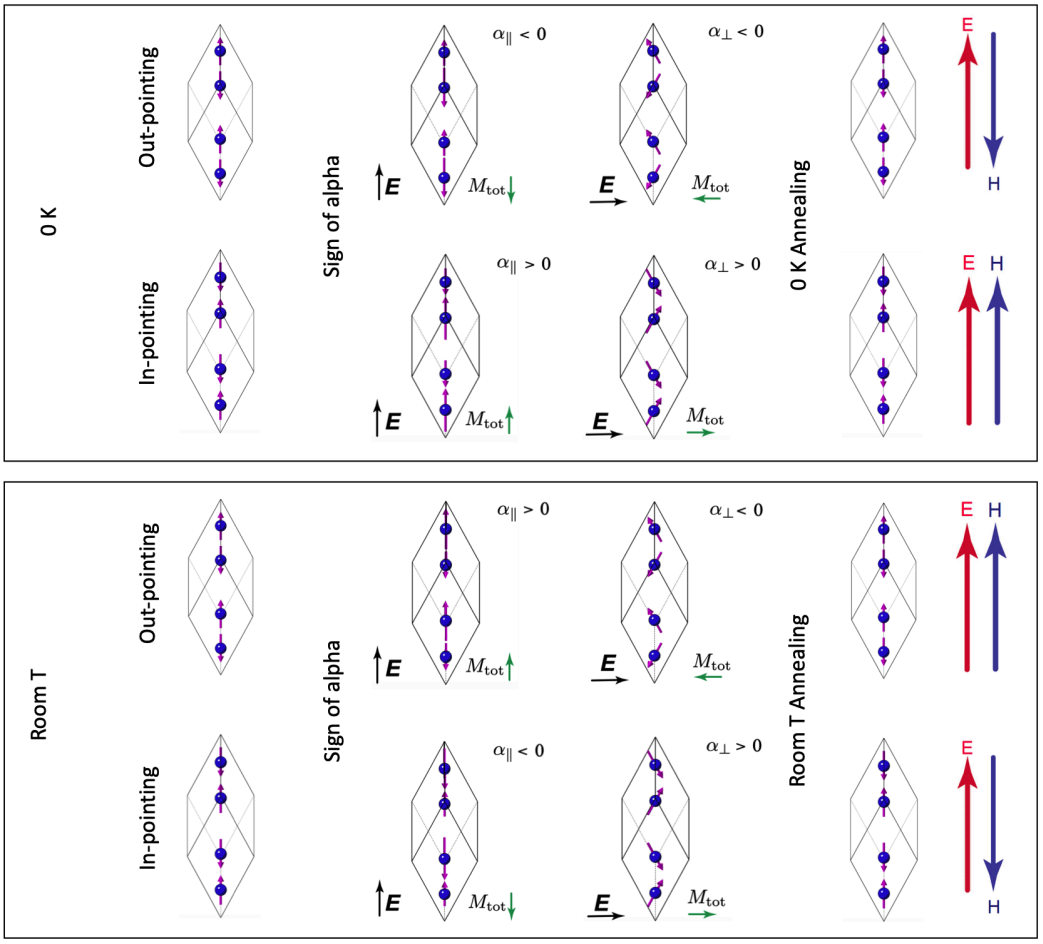

FIGURE 4.5: The in- and out-pointing domains of Cr_2O_3 with the sign of $\alpha_{\perp}$ and $\alpha_{\parallel}$ and alignment of the **E** and **H** fields during the ME annealing that favors each domain at 0 K and at room temperature.

re-examine and perform new, experimental measurements of surface magnetization to determine its sign for an unambiguous selection of bulk domain.

We hope that our work convincingly demonstrates the previously questioned consistency of computational and experimental findings on the sign of the ME coefficient in Cr_2O_3, and that it may motivate new, updated polarimetry measurements to test and confirm existing experimental and theoretical results. We also hope that this paper will assist in the correct interpretation of future studies of Cr_2O_3, as well as providing a cautionary tale for similar investigations of other ME materials.

4.3.8 Acknowledgements

JRS, NAS, AU, XHV, and SFW were supported by the ERC under the European Union's Horizon 2020 research and innovation programme grant No. 810451 and by the ETH Zürich. Computational resources for the ELK and VASP calculations were provided by

ETH Zürich's Euler cluster, and by SISSA through its Linux Cluster and ITCS for the QUANTUM ESPRESSO calculations. EB acknowledges the FNRS for support and the computational resources provided by the Consortium des Équipements de Calcul Intensif (CÉCI, FNRS grant No. 2.5020.11) and the Tier-1 supercomputer of the Fédération Wallonie-Bruxelles funded by the Walloon Region (Grant No. 1117545). The authors thank Kris Delaney for providing us with the original input files for Ref. [82] so that we could extract the magnetic domain used for the applied Zeeman field calculations. ELB and NQ would like to pay tribute to their friend F. Tasset, inventor of the Cryopad, who passed away earlier this year.

4.3.9 Data availability statement

All data that support the findings of this study are included within the article (and any supplementary files).

4.3.10 Author Contributions

XHV performed the calculations in ELK and VASP, AU performed those in QUANTUM ESPRESSO and EB those in ABINIT. JRS, NQ and ELB performed the re-analysis of the SNP data. NAS conceived of and coordinated the project. All authors co-wrote the manuscript.

4.3.11 Conflict of interest

The authors declare that there is no conflict of interest.

4.3.12 Appendix

4.3.12.1 Computational details ELK

Our DFT calculations in the augmented-plane wave (APW) code ELK were performed with spin-orbit interaction included, using the non-collinear local spin density approximation (LSDA) [64]. Correlation effects were taken into account by applying a rotationally invariant Hubbard U correction [1] on the Cr d states, with U = 4.0 eV and J = 0.5 eV, which well describe the physics of Cr_2O_3 [105–107]. Muffin-tin spheres were used to describe the Cr and O core states, with radii of 1.0716 Å and 0.80435 Å. These radii are reduced by 4% with respect to the standard setting to prevent overlap of the

muffin-tin spheres. The APW functions and the potential were expanded in a spherical harmonics basis, with cut-offs $l_{\max(\mathrm{apw})} = l_{\max(\mathrm{o})} = 12$. A $6 \times 6 \times 6$ Γ-centered k-point mesh was used to sample the Brillouin Zone (BZ) [134]. We obtained the spin contributions to the lattice-mediated ME response in the xy plane using the lattice-mediated method of Ref. [81], in which the response is constructed from a superposition of the magnetic moments induced by freezing in those eigenmodes of the force constant matrix that give a net polarization, in this case those with E_u symmetry. We used LSDA + U relaxed lattice parameters and atomic positions obtained from VASP calculations (see the description below). Force constant matrix eigenmodes and their energies were obtained from VASP interfaced with phonopy [131, 132]. Born effective charges, used to calculate the polarization, were taken from VASP calculations as well.

4.3.12.2 Computational details VASP

In the plane-wave code VASP, we performed density functional theory calculations with the LSDA+U method, spin-orbit coupling included, and a Hubbard U correction on the Cr d states, with U (J) = 4.0 (0.5) eV, as in the ELK calculations. The ionic cores of Cr and O were described with projector-augmented wave pseudopotentials [71]. We used the following settings for the valence electrons: Cr $3p^6 3d^5 4s^1$ and O $2s^2 2p^4$, corresponding to the datasets Cr_sv and O. We used a kinetic energy cut-off of 800 eV for the wavefunctions and performed the BZ integrations using a uniform Γ-centered $7 \times 7 \times 7$ k-point mesh. Structural and electronic relaxations performed with these parameters yielded a band gap and magnetic moment close to known experimental values and lattice parameters of $a' = 5.31$ Å, the length of the rhombohedral unit cell vectors and $\alpha' = 54.87°$, the angle between the unit cell vectors. These values are 0.78% and 0.26% smaller than experiment [109]. As for the ELK calculations, we used the method of Ref. [81] to construct the lattice-mediated spin response to an applied electric field, from the net spin magnetic moment induced by freezing in appropriate eigenmodes of the force constant matrix. The eigenmodes and corresponding energies were calculated by interfacing VASP with phonopy. The polarizations of each of the eigenmodes were obtained from the product of the atomic displacements of the mode and the Born effective charges Z^e. We computed the Z^e by displacing each atom in the unit cell along each Cartesian direction and determining the ionic polarization using the modern theory of polarization, as implemented in VASP in the LCALCPOL routine. These calculations were performed for four displacements of different magnitudes, allowing us to assess the linear response regime. The final Z^e were obtained from the average of the Z^e for different atoms of the same species and different displacements within the linear regime.

4.3.12.3 Computational details Quantum Espresso

First-principles calculations in QUANTUM ESPRESSO [155, 156] and `thermo_pw` [165] were performed in non-collinear DFT using the generalized gradient approximation, with the Perdew-Burke-Ernzerhof parametrization of the exchange-correlation energy [65]. Ions were described by fully relativistic ultrasoft pseudopotentials (PPs) [166], with $3s$, $3p$, $4s$, and $4d$ valence electrons for Cr (PP `Cr.rel-pbe-spn-rrkjus_psl.0.2.3.UPF` from pslibrary 1.0.0 [167, 168]) and with $2s$ and $2p$ valence electrons for O (PP `O.rel-pbe-n-rrkjus_psl.0.1.UPF` from pslibrary 0.1). The pseudo wavefunctions (charge density) were expanded in a plane-wave basis set with kinetic energy cut-off of 140 (560) Ry. BZ integrations were performed using a shifted k-point mesh of $6 \times 6 \times 6$ points. The lattice-mediated spin contribution to the ME response was computed following the approach of Ref. [81]: specifically, Born effective charges and phonon frequencies at Γ were computed using density functional perturbation theory [169].

4.3.12.4 Computational details Abinit

The ABINIT calculations (version 8.8) were done with the norm-conserving pseudopotentials coming from the PseudoDojo project [170] (v0.3) and within the LDA approximation for the exchange-correlation functional without Hubbard U correction. We used a kinetic energy cut-off of 40 Ha (1088 eV) for the plane-wave expansion and integrated the BZ using a Monkhorst-Pack k-point mesh of $3 \times 3 \times 3$ points, shifted by (0.5, 0.5, 0,5). Spin-orbit coupling was included in all the calculations for both applied Zeeman field and applied electric field calculations. The cell parameters and shape were fixed to the experimental ones ($a' = 5.37\,\text{Å}$ and $\alpha' = 55.13°$). The forces were relaxed up to a tolerance of $2.7 \times 10^{-8}\,\text{eV/Å}$ and the self-consistent field cycles to a tolerance of $2.7 \times 10^{-9}\,\text{eV/Å}$ on the force residual.

4.4 Comments and Outlook

Table 4.1 shows the values of $\alpha_\perp$ and $\alpha_\parallel$ as calculated in DFT, using different DFT codes and parameters. As discussed, there is perfect agreement on the sign, but somewhat of a spread in the magnitude of the calculated value of $\alpha_\perp$ at 0K. In fact, the smallest value is a factor of three smaller than the largest one. We discuss here some of the possible explanations for this spread. First, let's look at the calculations we performed in VASP, ELK, and QUANTUM ESPRESSO. These all used the same lattice-mediated method, and calculated the lattice-mediated spin contribution only. Despite the difference in code, exchange-correlation functional, pseudopotential, and value of Hubbard U, the calculated values from these three calculations are very similar, as can be seen in Table 4.1 and Figure 4.3. This indicates that these parameters play relatively minor roles in determining the magnitude of $\alpha_\perp$. An important, if obvious, source of this difference is the components that were taken into account. For example, Malashevich *et al.* [83], report each contribution separately. They find a magnitude of the lattice-mediated spin-contribution to $\alpha_\parallel$ of 0.77 ps/m, much closer to the values we calculated in VASP, ELK, and QUANTUM ESPRESSO. It also seems that the method may be significant, for example, the Zeeman field method seems to give larger values on average. On the other hand, our calculations in ABINIT give equal values for both the Zeeman field method and the electric field method. Finally, we point out the unusual sensitivity of the induced magnetic moments, and hence the magnitude of $\alpha_\perp$, to the convergence parameters. This might also explain some of the spread in the value of $\alpha_\perp$. As an example, in Figure 4.6a we show the convergence of the magnitude of the magnetic moment in VASP when using the lattice-mediated method. We see that it takes 200+ self-consistent field (SCF) steps for the magnitude of the small moment to converge. On the other hand, the DFT energy (Figure 4.6b) shows a minimum around $\sim$ 30 SCF steps. Hence, a usual calculation may stop here because the convergence criteria are met, resulting in a smaller magnitude of the induced magnetic moment and hence a smaller value of α.

We also see that the sign of the ME effect is robust with convergence. The induced magnetic moment in Figure 4.6a becomes larger if we converge further, but it never changes sign.

Thus we have established that which sign of the ME effect belongs with which AFM domain can be accurately calculated by DFT, where it is independent of the choices of DFT code and DFT parameters, and the level of convergence. *Why* the 'out-pointing' domain corresponds to negative $\alpha_\perp$ and $\alpha_\parallel$ at 0K and the 'in-pointing' domain corresponds to positive $\alpha_\perp$ and $\alpha_\parallel$ at 0 K (and not the other way around) is not clear. It seems this depends on the details of the microscopic coupling, which may very well change between materials. As we saw in Section 3.4, the relation between the ordering of

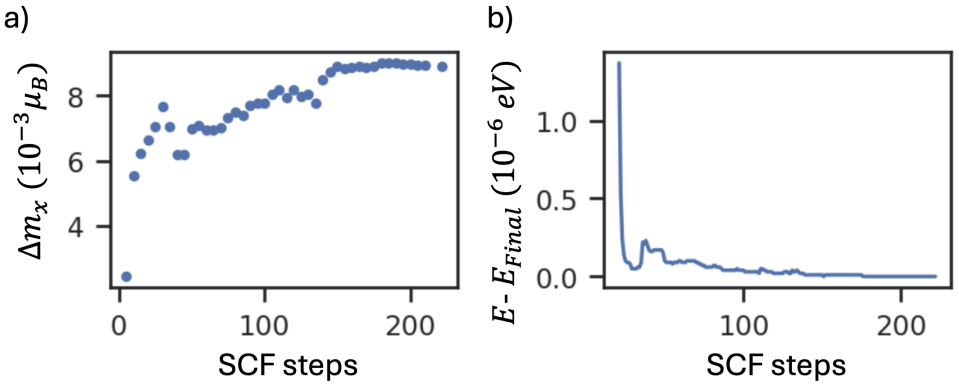

FIGURE 4.6: Induced net magnetic moment (a) and difference in DFT energy (b) per rhombohedral unit cell with respect to the converged energy as a function of the number of SCF steps. This is the convergence path for the highest energy E_u symmetry eigenmode of the force constant matrix, frozen in at an amplitude of 0.5 Å, as calculated in VASP. The energy plot starts at SCF step 20, to improve visibility.

the dipoles and the sign of the ME multipoles was different for Cr_2O_3 and Fe_2O_3, which we attribute to the difference in filling of the transition-metal d shell. As both AFM domains in Cr_2O_3 show opposite sign of both the ME multipoles and the ME effect, we can reasonably expect that an opposite sign of the ME multipoles means an opposite sign of the ME effect. This would mean that if one could force Fe_2O_3 to adopt the Cr_2O_3 magnetic ordering, the relation between the AFM domains and the effect would be opposite, i.e., the 'out-pointing' domain would correspond to negative $\alpha_\perp$ and $\alpha_\parallel$ at 0 K and the 'in-pointing' domain would correspond to positive $\alpha_\perp$ and $\alpha_\parallel$ at 0 K. Not only does it seem like the relation would be opposite for Fe_2O_3, it appears this relation is hard to predict. Even if another transition metal oxide with the same magnetic ordering as Cr_2O_3 would be found, the relation between the domain and the sign of the effect may not be the same.

Furthermore, we may discuss the usage of the sign of the ME multipoles (and thus the ME effect) to classify the AFM domains. Distinguishing the domains this way makes them dependent on the sign of one quantity, rather than the sign of the Néel vector, which has to be constructed from the ordering of the dipoles. It also seems tantalizing to suggest the ME multipoles as an order parameter. Both of these options are hindered by the fact that we do not actually know what happens to the multipoles at finite temperatures, and we cannot confirm, for example, an onset of a net ME multipole moment at the transition temperature, similar to the onset of a net dipole moment in a ferromagnetic transition. Interestingly, magnetic multipoles have been assigned as a secondary order parameter for non-relativistic spin splitting in AFM materials [171]. The next chapter will discuss such spin splitting in Fe_2O_3.

Finally, the presence of $\alpha_\perp$ suggests that ME annealing should also work for fields perpendicular to the magnetization axis. However, at room temperature, where the annealing is usually performed, $\alpha_\parallel$ is much larger than $\alpha_\perp$. This probably means that one would need much stronger fields to achieve the same selection of an AFM single domain.

Chapter 5

Magnetic multipoles and spin splitting in Fe_2O_3

As discussed in Chapter 3, magnetic multipoles of many different orders are present in both Cr_2O_3 and Fe_2O_3, which can be associated with different magnetoelectric (ME) effects. In this chapter, I discuss the magnetic multipoles of rank 5 in Fe_2O_3 and the non-relativistic spin splitting (NRSS) they give rise to. This research was motivated both by the interest in finding other effects that the magnetic multipoles give rise to, and by the search for a better understanding of the NRSS in antiferromagnets, which has recently gathered so much attention.

This chapter is structured as follows. First I discuss recent developments in the theory of NRSS in antiferromagnets, also called 'altermagnetism', the symmetry requirements, and the connections between such spin splitting and the ordering of magnetic multipoles. Next, I explain how we calculated the spin splitting in Fe_2O_3 and established its relation to the rank-5 magnetic multipole (triakontadipole) in Fe_2O_3. To this end, I have incorporated the paper that I co-wrote with David Voderholzer, Stefan Schären, Yannick Gachnang, Nicola Spaldin, and Sayantika Bhowal on this subject [172]. In this work, we discuss the different ways we altered the ordering, sign, or magnitude of the magnetic triakontadipoles and the according changes in the NRSS in the low-temperature magnetic phase in Fe_2O_3. Subsequently, I present some additional work and open questions on the spin-splitting landscape of Fe_2O_3 and the k-space representation of the triakontadipole.

5.1 Spin splitting and magnetic multipoles

Magnetically ordered materials are usually divided into two groups, the ferromagnets and the antiferromagnets. In ferromagnets, the ferroic ordering of the dipoles breaks the time-reversal symmetry. It allows for spin splitting of the electronic bands, i.e., the bands are not spin degenerate (Figure 5.1a). On other the hand, in antiferromagnets, the dipole moments are compensated, and these materials do not conventionally show spin splitting anywhere in k-space (Figure 5.1b). This lack of spin splitting is called Kramer's spin degeneracy [173, 174], and occurs when $\Theta\mathcal{I}$, the product of time reversal and space inversion, is a symmetry of the system. We can see how this symmetry prevents spin splitting by considering how these operations act in momentum space: Θ causes a sign-reversal of both the spin and the wave vector, while $\mathcal{I}$ reverses only the wave vector. Thus, $\Theta\mathcal{I}$ preserves the wave vector and while reversing the spin. Hence, when $\Theta\mathcal{I}$ is a symmetry, all the bands are spin-degenerate. We will call materials with this symmetry conventional antiferromagnets. We note that $\Theta\mathcal{I}$ symmetry does not require Θ and $\mathcal{I}$ to be preserved separately. For example, in Cr_2O_3 both Θ and $\mathcal{I}$ are broken, but the $\Theta\mathcal{I}$ symmetry is preserved. Kramer's spin degeneracy can be lifted by spin-orbit coupling (SOC), causing the Rashba effect [175–177].

It was realized recently, that spin splitting can also occur in antiferromagnets in the absence of SOC, as a non-relativistic effect [16, 128, 178–188]. In these antiferromagnets, the Θ and $\Theta\mathcal{I}$ symmetries are broken by a combination of the dipole order and the local crystallographic symmetries. These materials, unconventional antiferromagnets or altermagnets, do show spin splitting. We remark that while in ferromagnets there is uniform spin splitting across k-space, the spin splitting in these unconventional antiferromagnets is compensated; For every direction in k-space that shows spin splitting, there is a corresponding direction that shows the opposite spin splitting (Figure 5.1c). How these directions of opposite NRSS are oriented with respect to each other depends on the symmetry of the system. The different patterns of NRSS are called d-wave, g-wave, and i-wave, similar to the nomenclature for unconventional superconductivity, with the symmetry of each spin-splitting type matching that of the corresponding orbitals [16].

The NRSS in unconventional antiferromagnets can be fairly large, much larger than Rashba effect, and has attracted a lot of interest, both from a theory perspective as for possible applications, for example in spintronics [16, 17, 181, 189–198].

To describe the NRSS, a non-relativistic framework is used, which involves spin Laue groups, rather than magnetic space groups. We note that real materials do show relativistic effects, but these are usually small, such that the non-relativistic effects dominate. In spin Laue groups, the symmetry operations have two parts $[R_{spin} \parallel R_{real}]$, one acting

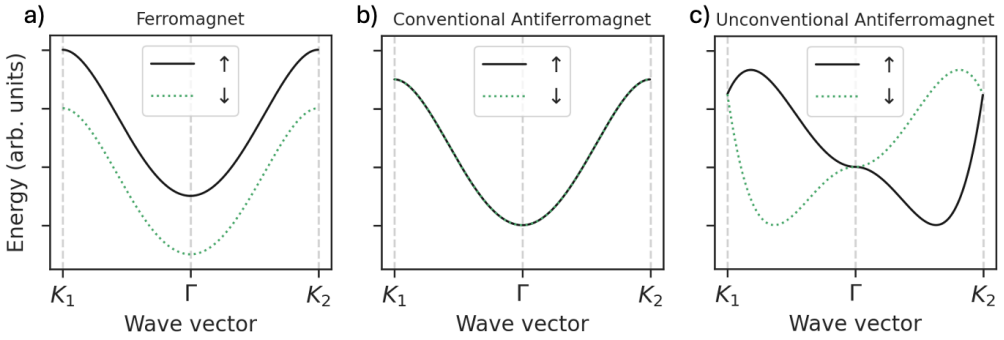

FIGURE 5.1: Sketches of spin splitting or lack thereof in the band structure of ferromagnets (a), conventional antiferromagnets, which preserve $\Theta\mathcal{I}$ symmetry (b), and unconventional antiferromagnets that break $\Theta\mathcal{I}$ symmetry (c). K_1 and K_2 represent different directions in k-space. Image adapted from Ref. [16].

in spin space and one acting in real space, which are decoupled in the non-relativistic limit. Focusing on collinear magnets, we can define the spin space transformation group $\boldsymbol{S} = \{E, C_2\}$, where E is the identity and C_2 is a rotation of π about an axis perpendicular to the collinear spin axis. Following Ref. [16], we can divide the non-trivial spin Laue groups into three types:

The first type is $R_s^I = [E \parallel \boldsymbol{G}]$, where $\boldsymbol{G}$ is the crystallographic Laue group, containing the real-space symmetry operations. This group describes the conventional collinear ferromagnets, which show spin splitting throughout k-space. The second type $R_s^{II} = [E \parallel \boldsymbol{G}] + [C_2 \parallel \boldsymbol{G}]$ describes the conventional collinear antiferromagnets, which show spin-degenerate bands across k-space in the absence of SOC. Cr_2O_3 is part of this group, and as a consequence, there is no NRSS in Cr_2O_3. Finally, the last type is $R_s^{III} = [E \parallel \boldsymbol{H}] + [C_2 \parallel \boldsymbol{G} - \boldsymbol{H}]$, where $\boldsymbol{H}$ is halving subgroup (a subgroup containing half the elements) of $\boldsymbol{G}$. $\boldsymbol{H}$ contains those real space operations that send each spin sublattice to itself. $\boldsymbol{G} - \boldsymbol{H}$ is a coset containing the remaining elements of $\boldsymbol{G}$, i.e., those operations that map one spin sublattice to the other. This last group describes the unconventional antiferromagnets that show NRSS. The elements in the coset $\boldsymbol{G} - \boldsymbol{H}$ determine planes, generated by mirrors, and lines, generated by rotations, where the spin splitting is zero. These planes of zero splitting are called nodal planes, and, together with the symmetry operations in $\boldsymbol{H}$ determine the type of spin splitting, i.e., d-wave, g-wave, or i-wave. The symmetries of Fe_2O_3, in the non-relativistic limit, can be described by a Laue spin group of type III, and, due to the three-fold rotational symmetry of the corundum structure, it is a g-wave spin-splitting candidate.

As mentioned before, the NRSS requires the broken time-reversal symmetry Θ. Usually, this symmetry breaking is formulated in terms of the pattern of antiferroic arrangement of the magnetic dipoles. However, spin splitting also occurs in ferromagnets, where Θ is

broken due to the ferroic ordering of the magnetic *dipoles*, which suggests that the time-reversal symmetry breaking in antiferromagnets may also be captured by some ferroic ordering, but of higher-order magnetic multipoles. In fact, a relation between magnetic octuples and d-wave spin splitting has been established previously [199]. Magnetic multipoles have also been proposed as a secondary order parameter for altermagnetism [171]. Furthermore, we saw in Chapter 3 that Fe_2O_3 does show ferroic ordering of several higher-order multipoles, although that was in the presence of SOC. This leaves the question if g-wave spin splitting in general, and the predicted g-wave NRSS in Fe_2O_3 in particular, may also be captured by a ferroic ordering of magnetic multipoles.

5.2 Non-relativistic ferromagnetotriakontadipolar order and spin splitting in hematite

5.2.1 Preface

In this work, we investigate the ferroic ordering of magnetic multipoles in the absence of SOC in Fe_2O_3, which differ from those in the presence of SOC we discussed in Chapter 3. As mentioned in Section 5.1, the relation between the ferroic ordering of magnetic octupoles and d-wave spin splitting in the absence of SOC was pointed out previously [199]. We explore a similar relation between magnetic triakontadipoles and the g-wave NRSS in Fe_2O_3.

The first goal of this work is to establish the lowest order magnetic multipole in Fe_2O_3 that is ordered ferroically in the absence of SOC, and show it has the same symmetry as the NRSS. We calculate both the magnetic multipole components and the spin splitting using density functional theory (DFT), without the inclusion of SOC, allowing us to assess the symmetry of both. The second goal is to confirm that the found magnetic multipole, the rank-5 magnetic triakontadipole, is indeed responsible for the NRSS. To this end, we manipulate the triakontadipole sign and ordering by changing the magnetic ordering and the crystal structure, and by varying the magnitude of the magnetic multipole itself, to show that the NRSS changes accordingly. This immediately connects to the third goal, which is to demonstrate a path for manipulating the magnitude of the ferroically ordered triakontadipole components and, as a consequence the spin splitting. This is achieved by exploiting the relationship between the magnetic triakontadipole and the rank-4 charge multipole, the charge hexadecapole. The fourth goal is to determine the shape of the NRSS in the high-temperature phase of Fe_2O_3.

Explanatory remarks

Sections 5.2.2 to 5.2.7 contain the publication:

[172] X. H. Verbeek, D. Voderholzer, S. Schären, Y. Gachnang, N. A. Spaldin, and S. Bhowal. "Non-relativistic ferromagnetotriakontadipolar order and spin splitting in hematite" (2024). https://arxiv.org/abs/2405.10675

My contribution was to perform the symmetry analysis, part of the post-processing of the data and co-supervising the MSc and BSc students. The preliminary calculations, exploring the spin-splitting landscape of Fe_2O_3, were performed by Stefan Schären and Yannick Gachnang in the context of a MSc project and BSc thesis, respectively. The multipole calculations, the spin splitting in the modified crystal structure, and the constrained multipole calculations were performed by David Voderholzer, in the context of his MSc project. Sayantika Bhowal and I co-supervised David, Stefan, and Yannick. The manuscript was written by Sayantika Bhowal, David Voderholzer, Nicola Spaldin and myself, with feedback from Stefan Schären and Yannick Gachnang. The version printed here is the last submitted version, with a deviating format to ensure a consistent style with the rest of the thesis.

5.2.2 Abstract

We show that hematite, α-Fe_2O_3, below its Morin transition, has a ferroic ordering of rank-5 magnetic triakontadipoles on the Fe ions. In the absence of spin-orbit coupling, these are the lowest-order ferroically aligned magnetic multipoles, and they give rise to the g-wave non-relativistic spin splitting in hematite. We find that the ferroically ordered magnetic triakontadipoles result from the simultaneous antiferroic ordering of the charge hexadecapoles and the magnetic dipoles, providing a route to manipulating the magnitude and the sign of the magnetic triakontadipoles as well as the spin splitting. Furthermore, we find that both the ferroic ordering of the magnetic triakontadipoles and many of the spin-split features persist in the weak ferromagnetic phase above the Morin transition temperature.

5.2.3 Introduction

Recently, there has been a surge of interest in an unconventional spin splitting observed in the band structure of collinear compensated antiferromagnetic (AFM) materials. The key feature of this class of AFM materials, often referred to as 'altermagnets', is the large spin splitting they exhibit, surpassing typical Rashba splitting magnitudes without requiring spin-orbit coupling (SOC) [175–177]. The interest in this class of antiferromagnets originates from the intriguing symmetries underlying the deviation from typical degenerate spin-polarized bands in conventional antiferromagnets [16, 128, 178–182, 187, 188], and the potential for offering exotic physics that results from it, including AFM spintronics [16, 17, 181, 189–198], giant magnetoresistance [200], chiral magnons [198], and superconductivity [201–203].

The non-relativistic spin splitting (NRSS) in collinear compensated antiferromagnets requires broken *global* time-reversal symmetry, as well as a specific correlation between the structural symmetry of the magnetic sub-lattices, dictated by the surrounding non-magnetic atomic environment, and the specific arrangement of the antiparallel magnetic dipolar ordering. The absence of time-reversal symmetry in an antiferromagnet signifies the presence of a ferroic ordering of higher-order magnetic multipoles, which can lead to NRSS within the spin-polarized bands, akin to the trivial NRSS in ferromagnets due to the conventional ferromagnetic (FM) dipolar ordering. Indeed, previous studies have demonstrated that in AFM materials exhibiting a d-wave pattern of NRSS, characterized by two nodal planes ($l = 2$) of degenerate spin-polarized bands, there exists a ferroic ordering of rank-3 inversion-symmetric and time-reversal-odd magnetic octupoles [199]. Identifying such higher-order ferroic magnetic multipoles provides insights into

the nature of NRSS and its tunability, and contributes to a broader understanding of the physical properties of these unconventional antiferromagnets [199].

Notably, the d-wave NRSS pattern is only one among several other patterns predicted and observed so far. For instance, the g-wave pattern, characterized by four nodal planes ($l = 4$), has recently garnered considerable attention [204–207]. However, the magnetic octupoles responsible for the d-wave spin splitting, can not explain g-wave spin splitting due to their quadratic spatial dependence. Identifying the corresponding ferroic magnetic multipole in g-wave spin-split antiferromagnets is the topic of this work.

Taking magnetic hematite (α-Fe_2O_3) as an g-wave altermagnetic material [16], we demonstrate that the magnetic ground state is a ferroic ordering of rank-5 magnetic triakontadipoles. These magnetic triakontadipoles exist without spin-orbit interaction, and they form the lowest-order ferroically ordered magnetic multipole in the absence of SOC. Our calculations reveal a correlation between the magnetic triakontadipoles on the Fe ions and their local coordination environment, characterized by charge hexadecapoles, suggesting the manipulation of the magnetic triakontadipole by controlling the positions of the oxygens surrounding the Fe ions. Such a manipulation offers in turn a means to regulate both the magnitude and sign of the spin splitting in hematite. Our study therefore provides both a multipolar description of the g-wave spin splitting and a framework for controlling it via the magnetic triakontadipole.

The remainder of this manuscript is structured as follows. In Section 5.2.4, we review the crystal structure and magnetic ground state of α-Fe_2O_3, and summarize the computational techniques used in this study. We present the results of our electronic structure calculations of the charge and magnetic multipoles and their relationship to the spin splitting in Section 5.2.5. In addition, we explore methods for tuning the magnetic triakontadipole and the spin splitting by modifying the magnetic ordering and structure, as well as changes in properties above the Morin transition temperature. Finally, we summarize our findings in Section 5.2.6.

5.2.4 Crystal and magnetic structure of α-Fe_2O_3 and computational methods

Hematite, α-Fe_2O_3, has the centrosymmetric corundum structure with crystallographic space group $R\bar{3}c$. The magnetic ground state has AFM-ordered spins, aligned along the z easy axis in a $+-{-}+$ pattern (Figure 5.2a). Between the Morin transition at 263 K and the Néel temperature of 960 K [125, 126], the spins lie in the plane perpendicular to $\hat{z}$ with the same $+-{-}+$ AFM order and a small canting within the plane, giving a weak net spin moment. This is called a canted AFM or weakly FM phase.

Below the Morin transition, the *magnetic* space group is R$\bar{3}$c, which in the absence of SOC gives the nontrivial spin Laue group ${}^1\bar{3}^2m = [E \parallel \bar{3}] + [C_2 \parallel \bar{3}m - \bar{3}]$. Here the operations on the left of the double bars act only in spin space and the operations on the right act only in real space. Furthermore, the group $\bar{3}$ is also called a halving subgroup, as it is formed with half of the elements of ${}^1\bar{3}^2m$. This halving subgroup $\bar{3}$ contains the six symmetry operations that leave the ordering of the spins unchanged, in this case, the identity operation, space inversion, the rotations about the z axis by $\frac{2\pi}{3}$ and $\frac{4\pi}{3}$, and the combinations of these rotations with space inversion. The coset $\bar{3}m - \bar{3}$ instead contains those operations that reverse the spins, which are the two-fold screw rotations about the axes $[1,0,0]$, $[-\frac{1}{2}, \frac{\sqrt{3}}{2}, 0]$ and $[-\frac{1}{2}, -\frac{\sqrt{3}}{2}, 0]$ with the corresponding translation of half a unit cell length along the z axis, and the combination of these screw rotations with space inversion, where the directions are indicated in Cartesian coordinates. This Laue group allows for g-wave spin splitting. Specifically, the $\frac{2\pi}{3}$ and $\frac{4\pi}{3}$ rotations about the z axis enforce a three-fold rotational symmetry in both real and reciprocal space.

Our first-principles calculations based on density functional theory (DFT) were performed in the plane-wave basis as implemented in the Vienna *ab initio* simulation package (VASP) [68, 69], within the collinear local spin density approximation (LSDA) [64] for the easy-axis magnetic phase below the Morin transition, and with non-collinear spins above the transition. In both cases a Hubbard U correction [1] was included, with U = 5.5 eV and J = 0.5 eV. As the NRSS occurs in the absence of SOC, this interaction was not included unless stated explicitly. The projector-augmented wave pseudopotentials [71] (valence electrons: Fe $3s^2 3p^6 3d^7 4s^1$, O $2s^2 2p^4$, datasets Fe_sv, O) were used, with a kinetic energy cut-off of 600 eV for the wavefunctions in the collinear phase and 800 eV in the canted magnetic phase. Brillouin zone (BZ) integrations were performed using a uniform Γ-centered $10 \times 10 \times 10$ k-point mesh. With these parameters, we obtained a spin moment on the Fe atoms of 4.01 μ_B and an electronic band gap of 2.16 eV, close to the experimentally observed values (4.1-4.2 μ_B [112, 113] and 2.14-2.2 eV [10, 11]). We used the DFT relaxed crystal structure for Fe_2O_3 that we obtained in [19], with rhombohedral lattice constants $a' = 5.35$ Å, $\alpha' = 55.25°$, deviating less than 1.5% from the experimental values [113]. Our lattice vectors in terms of Cartesian coordinates are

$$\boldsymbol{a}_1 = a' \left(-\sin\frac{\alpha'}{2}, \frac{1}{\sqrt{3}}\sin\frac{\alpha'}{2}, \sqrt{\frac{1}{3}(4\cos^2\frac{\alpha'}{2} - 1)} \right), \tag{5.1}$$

$$\boldsymbol{a}_2 = a' \left(0, -\frac{2}{\sqrt{3}}\sin\frac{\alpha'}{2}, \sqrt{\frac{1}{3}(4\cos^2\frac{\alpha'}{2} - 1)} \right), \tag{5.2}$$

$$\boldsymbol{a}_3 = a' \left(\sin\frac{\alpha'}{2}, \frac{1}{\sqrt{3}}\sin\frac{\alpha'}{2}, \sqrt{\frac{1}{3}(4\cos^2\frac{\alpha'}{2} - 1)} \right). \tag{5.3}$$

To describe the high-temperature weakly FM phase of Fe_2O_3, we constrained the direction of the spins on the Fe ions using the constrained moment routine implemented in VASP [208]. The angular components of the charge and magnetic multipoles were computed from a decomposition of the DFT-calculated charge and magnetic densities into spherical tensors [15, 85, 86]. We constrained multipoles by applying a shift in the local potential using the MULTIPYLES code [91], as described in Ref. [92].

5.2.5 Results and discussion

5.2.5.1 Multipole analysis

As stated earlier, the magnetically ordered phases of α-Fe_2O_3 break the global time-reversal symmetry. This implies that there must be a magnetic multipole with ferroic ordering, akin to the ferroic ordering of magnetic dipoles in ferromagnets. In the low-temperature collinear AFM phase, hematite has no net magnetic dipole so a higher-order ferroically ordered magnetic multipole must be present. The interaction energy $\mathcal{E}_{\text{int,mag}}$ of a system with a magnetic field $\vec{H}(\vec{r})$ applied to an arbitrary magnetization density $\vec{\mu}(\vec{r})$ is given by:

$$
\begin{aligned}
-\mathcal{E}_{\text{int,mag}} = & \underbrace{\left(\int \mu_i \, d\vec{r}\right)}_{\substack{\text{magnetic dipole}}} H_i|_{\vec{r}=\vec{0}} + \underbrace{\left(\int \mu_i r_j \, d\vec{r}\right)}_{\substack{\text{magnetoelectric} \\ \text{multipole}}} \partial_j H_i|_{\vec{r}=\vec{0}} + \underbrace{\left(\int \mu_i r_j r_k \, d\vec{r}\right)}_{\substack{\text{magnetic octupole}}} \partial_j \partial_k H_i|_{\vec{r}=\vec{0}} \\
& + \underbrace{\left(\int \mu_i r_j r_k r_l \, d\vec{r}\right)}_{\substack{\text{magnetic hexadecapole}}} \partial_j \partial_k \partial_l H_i|_{\vec{r}=\vec{0}} + \underbrace{\left(\int \mu_i r_j r_k r_l r_m \, d\vec{r}\right)}_{\substack{\text{magnetic triakontadipole}}} \partial_j \partial_k \partial_l \partial_m H_i|_{\vec{r}=\vec{0}} \\
& + \ldots \quad , \qquad (5.4)
\end{aligned}
$$

The terms within the parentheses indicate the magnetic multipoles of successive rank, that is the magnetic dipole (1), magnetoelectric (ME) multipole (2), magnetic octupole (3), magnetic hexadecapole (4), and magnetic triakontadipole (5) moments respectively (rank as indicated in the parentheses). Note that the second-order magnetic multipole is often called the ME multipole due to its association with the linear magnetoelectric effect [15]. As evidenced from Eq. 5.4, higher-order magnetic multipoles, characterizing the asymmetries and anisotropies in the magnetization density, can still have a ferroic ordering even in the absence of any net magnetic dipole.

To search for any such ferroically ordered magnetic multipole in hematite, we next perform explicit multipole calculations (see Section 5.2.4 for details). Focusing on the local multipoles centered on the Fe ions, our calculations show that in the absence of SOC, the lowest order magnetic multipole with ferroic ordering is the rank-5 magnetic

triakontadipole moment, specifically the w_3^{415}, w_{-3}^{414}, and w_3^{413} irreducible (IR) spherical tensor components (see Table 5.1, block a). Here, in the IR spherical tensor component w_t^{kpr}, k, p, r denote respectively the spatial index, spin index (i.e., $p = 0$ for charge and $p = 1$ for magnetic multipoles) and the rank ($r \in \{|k-p|, |k-p|+1, \ldots, k+p\}$) of the tensor, while $t \in \{-r, -r+1, \ldots, r\}$ labels the component of the tensor [84, 85, 209].

We note that the other components of the magnetic triakontadipole, as well as all lower-rank magnetic multipoles, if present, have antiferroic arrangements with opposite signs on different Fe ions and, hence, they can not break the global time-reversal symmetry. This suggests that the magnetic triakontadipole is likely responsible for the NRSS. Interestingly, the inclusion of spin-orbit interaction leads to a ferroic ordering of the rank-3 magnetic octupole components w_0^{212} and w_3^{213}. Since these magnetic octupoles are only induced by SOC, they are not relevant for the NRSS.

We point out the correlation between the magnetic triakontadipole and the rank-4 charge hexadecapole $\int r_i r_j r_k r_l \, d\vec{r}$, defined in the expansion of the interaction energy between an arbitrary charge density and an external electric field. By computing the charge multipoles, which quantify the angular distribution of the electronic charge density, we find that the charge hexadecapole component w_3^{404} has an antiferroic arrangement on the Fe ions with the same pattern as the z component of the Fe spin moment (see Table 5.1). This antiferroic pattern of the charge hexadecapoles in combination with the AFM spins gives rise to a ferroic ordering of magnetic triakontadipoles. Note that in the definition of w_t^{kpr}, p represents the spin, such that w_t^{011} gives the spin moments, which are opposite in sign to the magnetic dipole moments. The triakontadipole components w_t^{41r} are also given in terms of the spin, rather than the magnetic moments.

5.2.5.2 Spin splitting in the band structure of hematite

Next, we calculate the band structure of hematite in the absence of SOC. As expected from the nontrivial spin Laue group ${}^1\bar{3}^2m$, the spin splitting is zero at those points for which the little group contains elements of the coset $\bar{3}m - \bar{3}$ (the two-fold screw rotations). This includes the high symmetry points Γ, F, L, L_1, P, P_1, P_2, X, Z of the rhombohedral BZ, and the high symmetry paths between three sets of these points: [Γ, F, L_1, P_1, P_2, Z], [Γ, L, P, Z] and [Γ, X]. In other regions in k-space, we observe NRSS in all bands.

A representative low-symmetry path with large spin splitting is shown in Figure 5.2d. Here S and S^* are the points $(-\frac{1}{12}, \frac{1}{3}, -\frac{1}{4})$ and $(-0.241, 0.337, -0.096)$ in relative coordinates, with the reciprocal lattice vectors constructed from the real space vectors defined in Eqs. 5.1-5.3. S^* is obtained by rotating S by an angle of 30° about the k_z

TABLE 5.1: The computed spherical IR tensor components w_t^{kpr} of the relevant charge and magnetic multipoles in α-Fe_2O_3 without SOC and their ordering pattern on the Fe atoms, corresponding to the numbering indicated in Figure 5.2a. In w_t^{kpr}, p labels the spin. As a consequence w_t^{011} give the spin moments, which are opposite in sign to the magnetic dipole moments. The different blocks show multipole moments for both AFM domains (a,b), a different AFM order (the magnetic ground state of Cr_2O_3) (c), for a high symmetry crystal structure in its magnetic ground state (d) and with multipoles induced (e), the high-temperature phase without (f) and with spin canting (g).

	System	Multipole	w_t^{kpr}	Sign of multipoles on the Fe sites
a)	Hematite low-T magnetic structure	Spin moment	w_0^{011}	$+-\,-+$
		Charge Hexadecapole	w_3^{404}	$+-\,-+$
		Magnetic Triakontadipole	w_3^{415}	$----$
			w_{-3}^{414}	$----$
			w_3^{413}	$----$
b)	Hematite low-T magnetic structure AFM domain 2	Spin moment	w_0^{011}	$-+\,+-$
		Charge Hexadecapole	w_3^{404}	$+-\,-+$
		Magnetic Triakontadipole	w_3^{415}	$++\,++$
			w_{-3}^{414}	$++\,++$
			w_3^{413}	$++\,++$
c)	Hematite with Cr_2O_3 spin ordering	Spin moment	w_0^{011}	$+-\,+-$
		Charge Hexadecapole	w_3^{404}	$+-\,-+$
		Magnetic Triakontadipole	w_3^{415}	0 0 0 0
			w_{-3}^{414}	0 0 0 0
			w_3^{413}	0 0 0 0
d)	Hematite high symmetry crystal structure	Spin moment	w_0^{011}	$+-\,-+$
		Charge Hexadecapole	w_3^{404}	$----$
		Magnetic Triakontadipole	w_3^{415}	$-+\,+-$
			w_{-3}^{414}	$-+\,+-$
			w_3^{413}	$-+\,+-$
e)	Hematite high symmetry crystal structure induced hexadecapole	Spin moment	w_0^{011}	$+-\,-+$
		Charge Hexadecapole	w_{-3}^{404}	$-+\,+-$
		Magnetic Triakontadipole	w_3^{415}	$----$
			w_{-3}^{414}	$----$
			w_3^{413}	$----$
f)	Hematite high T magnetic structure (no canting)	Spin moment	w_{-1}^{011}	$+-\,-+$
		Charge Hexadecapole	w_3^{404}	$-+\,+-$
		Magnetic Triakontadipole	w_{-2}^{415}	$----$
			w_{-4}^{415}	$----$
			w_4^{414}	$----$
			w_2^{414}	$++\,++$
			w_{-2}^{413}	$++\,++$
g)	Hematite high T magnetic structure (with canting)	Spin moment	w_{-1}^{011}	$+-\,-+$
			w_1^{011}	$----$
		Charge Hexadecapole	w_3^{404}	$-+\,+-$
		Magnetic Triakontadipole	w_{-2}^{415}	$----$
			w_{-4}^{415}	$----$
			w_4^{414}	$----$
			w_2^{414}	$++\,++$
			w_{-2}^{413}	$++\,++$

axis. We point out that the NRSS is opposite in sign, but equal in magnitude at S and S^*. As expected, the spin splitting is zero at Γ. Note that, while there are additional

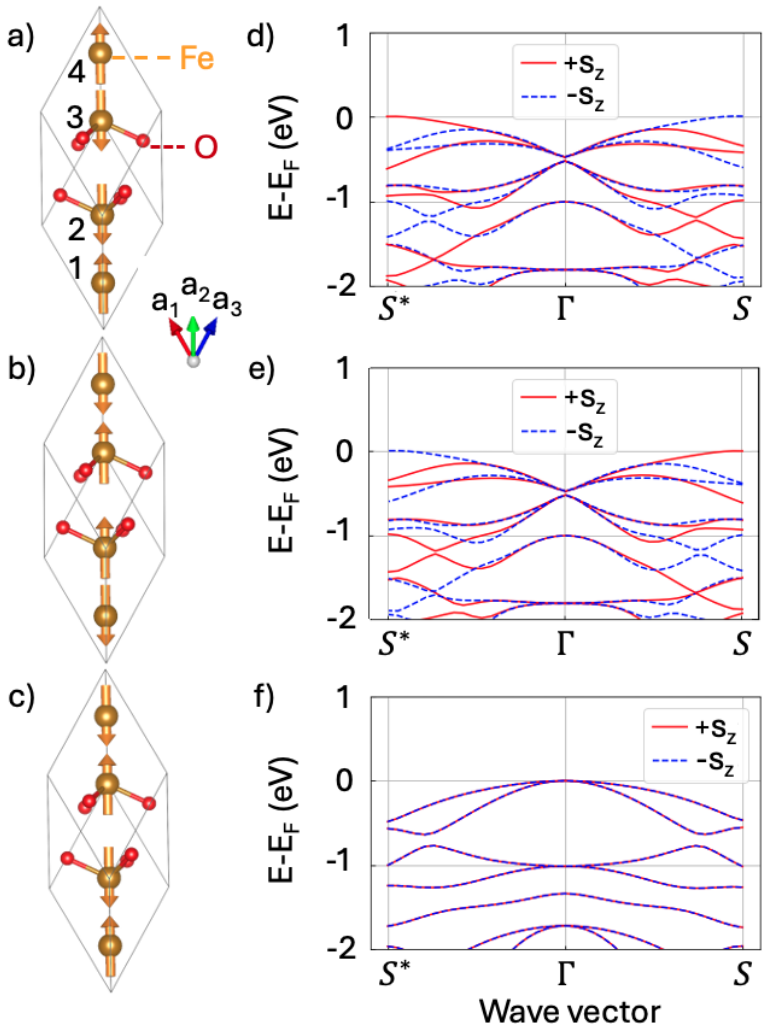

FIGURE 5.2: Different configurations of the spins on the Fe atoms and the corresponding spin splitting in α-Fe_2O_3. (a) The primitive unit cell of α-Fe_2O_3 and its ground state spin ordering $(+-+-)$. (b) The opposite domain with the opposite orientation of the spin moments at the Fe atoms $(-+-+)$. (c) A $(+-+-)$ spin ordering, the ground state spin ordering of isostructural antiferromagnet Cr_2O_3 (d)-(f) Band structures along the path S*-Γ-S for the spin ordering shown in (a), (b) and (c) respectively, with $S = (-\frac{1}{12}, \frac{1}{3}, -\frac{1}{4}), \Gamma = (0,0,0), S^* = (-0.241, 0.337, -0.096)$ in terms of the reciprocal lattice vectors.

band crossings along these paths, these crossing points are not dictated by symmetry.

5.2.5.3 Manipulation of magnetic triakontadipole and the resulting spin splitting

To establish the relation between the magnetic triakontadipoles and the NRSS, we next manipulate the size and sign of the magnetic triakontadipoles and compute the consequent changes in the spin splitting.

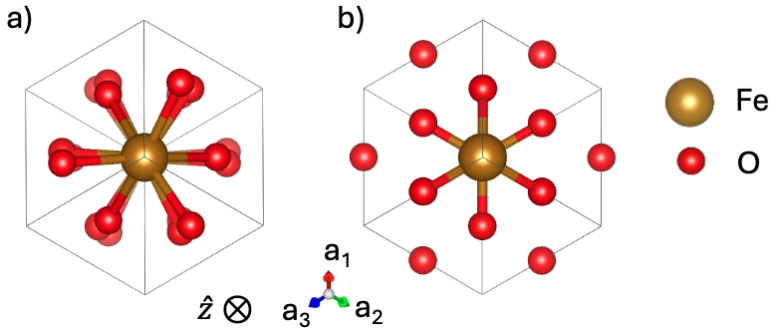

FIGURE 5.3: (a) Crystal structure of Fe_2O_3, and (b) modified high-symmetry crystal structure, both viewed along the z axis.

A: Change in magnetic ordering

Perhaps the most straightforward way to change the magnetic triakontadipoles is to change their sign by performing a time-reversal operation which can be achieved by flipping the orientation of the spins in our calculation (see Figure 5.2b). Physically, this corresponds to the opposite AFM domain. The computed multipoles for this magnetic configuration show that this operation indeed, changes the sign of all magnetic multipoles, while keeping the signs of charge multipoles, including the charge hexadecapole, unchanged (see Table 5.1, block b). We find, as expected, that the spin splitting changes sign as well. Specifically, the $+s_z$ and $-s_z$ bands are interchanged for the path $S^*-\Gamma-S$ (Figure 5.2e).

Next, we manipulate the spin ordering, by changing it to a $+-+-$ pattern (Figure 5.2c), the magnetic ground state of the isostructural antiferromagnet Cr_2O_3 [50, 51]. We find that this spin ordering leads to an antiferroic pattern of magnetic triakontadipoles, giving rise to a zero net magnetic triakontadipole in the unit cell (see Table 5.1, block c). The corresponding computed band structure has no spin splitting anywhere in the BZ (Figure 5.2f), again confirming the correlation between ferroic magnetic triakontadipoles and the NRSS.

B: Change in crystal structure

Next, we change the crystal symmetry by shifting the oxygen atoms from their original Wyckoff site symmetry 18e to 18d, while keeping the positions of the Fe atoms fixed (Figure 5.3a and b). In this higher-symmetry space group R$\bar{3}$m, ferroically ordered magnetic triakontadipoles are not allowed.

We perform DFT calculations with the R$\bar{3}$m structure and the original $+-+-$ ordering of the spin on the Fe atoms, and find antiferroically ordered magnetic triakontadipoles (see Table 5.1, block d). This is the result of ferroically ordered charge hexadecapoles combined with the antiferroic ordering of the spins. Consequently, we find no NRSS

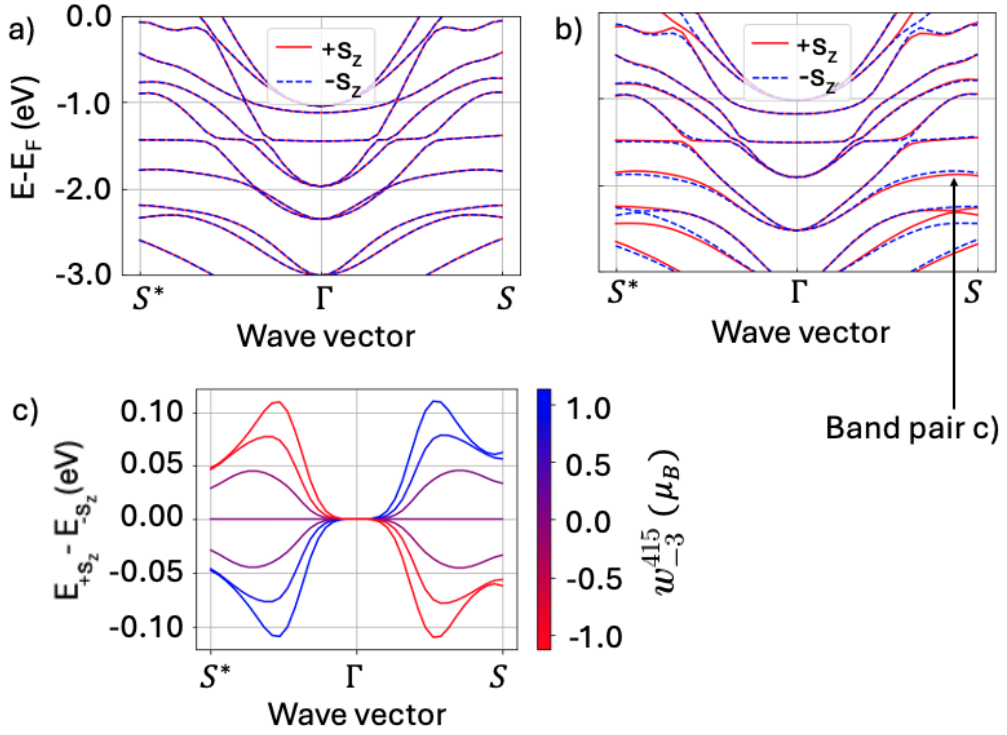

FIGURE 5.4: Band structures for the R$\bar{3}$m structure without induced ferroically magnetic triakontadipoles (a) and with induced magnetic triakontadipole component $w_{-3}^{415} = -0.087\,\mu_B$ (b). (c) shows the variation in the induced spin splitting between a specific pair of bands on manipulating the size of the angular component w_{-3}^{415} of the magnetic triakontadipole (color bar). The zero value of w_{-3}^{415} corresponds to the relaxed electronic structure with no constrained multipole moments. The pair of bands used in (c) is indicated with a black arrow in (b).

(Figure 5.4a). Our results highlight the importance of the surrounding nonmagnetic environment in establishing and manipulating both the magnetic triakontadipole and the g-wave NRSS in hematite. Similarly, the influence of the nonmagnetic environment on d-wave NRSS has also been emphasized [181, 199].

C: Constraining multipoles

We now use the constrained multipole method mentioned in Section 5.2.4 to manipulate the size of the ferroically ordered magnetic triakontadipoles in the actual $R\bar{3}c$ structure of hematite, and also to introduce them into the hypothetical $R\bar{3}m$ structure. We achieve this by manipulating the charge multipole of one order lower, i.e., the charge hexadecapoles.

We show the relation between the magnitude of the ferroically ordered triakontadipoles and the size of the constrained hexadecapoles in both structures in Figure 5.5. Note that w_t^{kpr} tensors capture only the angular part of the multipole, i.e., without performing the radial part of the integration in Eq. 5.4. Thus, the magnitude of the components is given is μ_B for the magnetic triakontadipoles and in terms of the electronic charge $|e|$

for the charge hexadecapoles. We see that in both structures the size of the magnetic triakontadipoles increases proportionally with the increase in the charge hexadecapole, with an approximate linear dependence, particularly over small ranges. However, there are some deviations from this trend in the hypothetical high-symmetry structure. We note that we induce a different antiferroically ordered charge hexadecapole component in the hypothetical high-symmetry structure compared to the actual α-Fe_2O_3 structure (since the same one already exists with ferroic ordering), so the introduced ferroically ordered magnetic triakontadipole components are also different.

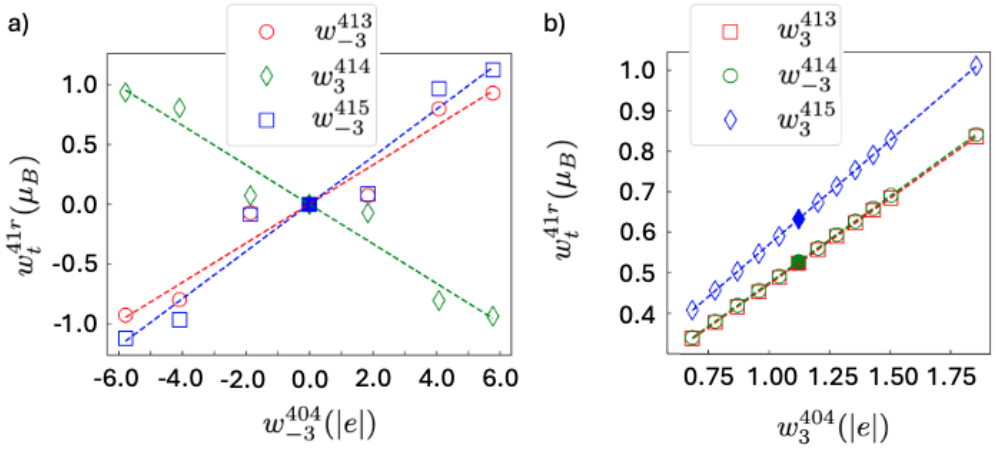

FIGURE 5.5: The magnitude of the angular component of the ferroically ordered magnetic triakontadipole components (in units of μ_B) as a function of the magnitude of the angular component of the constrained antiferroically ordered charge hexadecapole component (in units of $|e|$). a) the hypothetical R$\bar{3}$m structure, with the charge hexadecapole component w_{-3}^{404} constrained, and b) the actual α-Fe_2O_3 structure with the w_3^{404} hexadecapole component constrained. The dashed lines indicate the linear fit as a guide to the eye. The filled markers indicate the values of the multipoles without any constraints.

We now discuss the consequences of constraining these multipoles. First, by constraining the charge hexadecapole component w_{-3}^{404} to be non-zero and to have the same antiferroic ordering as the spins in the hypothetical $R\bar{3}m$ structure, we induce the ferroically ordered magnetic triakontadipoles w_3^{415}, w_{-3}^{414} and w_3^{413} (Table 5.1, block e). The computed bands show the presence of NRSS (Figure 5.4b), with equal and opposite splitting along $S^* - \Gamma$ and $\Gamma - S$, as expected.

Next, we vary the sign and magnitude of the induced charge hexadecapole while keeping the antiferroic ordering pattern the same. In Figure 5.4c, we see that with increasing magnitude of the magnetic triakontadipole w_{-3}^{415}, the magnitude of the NRSS increases, and when w_{-3}^{415} switches sign, so does the NRSS. This further confirms that the NRSS is driven by the magnetic triakontadipoles.

Furthermore, we show the effect of constraining the multipoles in the actual R$\bar{3}$c structure on the NRSS, analyzing the spin-split bands in the vicinity of the Γ point, where

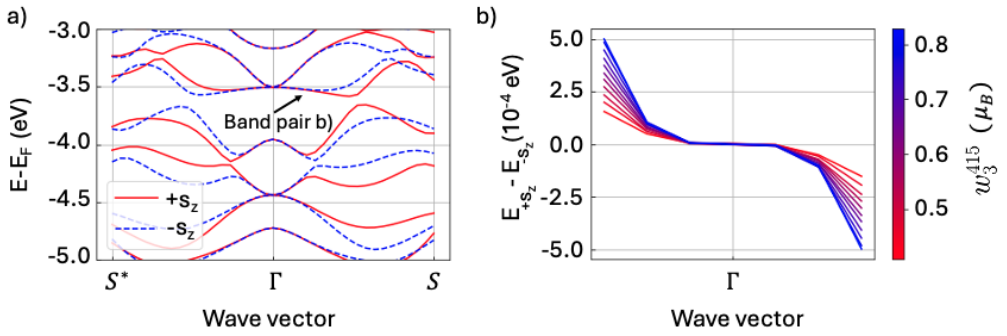

FIGURE 5.6: (a) Spin-polarized band structure of hematite, with an arrow indicating a pair of bands. (b) Spin splitting near Γ, for the bands indicated in (a) with a black arrow (approximately −3.5 eV below the Fermi energy at Γ), plotted as a function of the magnitude (in μ_B) of w_3^{415}, the angular component of one of the ferroically ordered magnetic triakontadipole components.

the bands, which have many crossings, can be easily distinguished. As expected, we see in Figure 5.6, that the NRSS increases with the increasing value of magnetic triakontadipole, further confirming the magnetic triakontadipole to be responsible for the spin splitting in hematite. We find the same behavior at smaller values of the Hubbard U, where the bands are less entangled and the change in NRSS is easier to distinguish.

5.2.5.4 Weakly ferromagnetic phase of α-Fe_2O_3

Finally, as discussed in Section 5.2.4, above the 263 K Morin transition, the spins in hematite lie in the xy plane, oriented in a $+--+$ AFM pattern along the y axis, with small ferroically ordered components along x [126]. This spin ordering has a lower symmetry than the ground state. We explore the multipoles and the corresponding NRSS in this high-temperature magnetic phase, in two steps. First, we orient the spins along the y axis and constrain them to be collinear and antiferromagnetically ordered. With this spin ordering, we find several ferroically ordered triakontadipoles (Table 5.1, block f), with different components than in the low-temperature ground state, and a NRSS with the bands now split in spin parallel or antiparallel to $\hat{y}$ (i.e., $+s_y$ and $-s_y$).

Next, we constrain the spins to allow for a small FM component along $\hat{x}$ of $\sim$0.1 μ_B per Fe atom. We note that this is larger than the experimentally observed 10^{-3} μ_B moment in hematite [210, 211]. The resulting multipoles are shown in Table 5.1, block g. In addition to the same ferroically ordered triakontadipole components as in the collinear AFM along $\hat{y}$ case. We now have a ferroic ordering of spins parallel to $\hat{x}$, and nine further small ferroically ordered triakontadipole components (not listed in Table 5.1). Now, we look at the NRSS in the weakly FM phase and compare it to the situation where the spins are collinear AFM along y. We observe that in the weak FM phase, there is a small additional splitting due to the ferroic ordering of the spins. This additional

splitting can best be seen along directions in which the NRSS due to the ferroic ordering of the triakontadipoles is absent, such as the $\Gamma - L$ direction. We see an absence of spin splitting for the collinear AFM arrangement, with moment along $\hat{y}$ (Figure 5.7a), and a small splitting upon canting (Figure 5.7b), induced by the weak ferromagnetism.

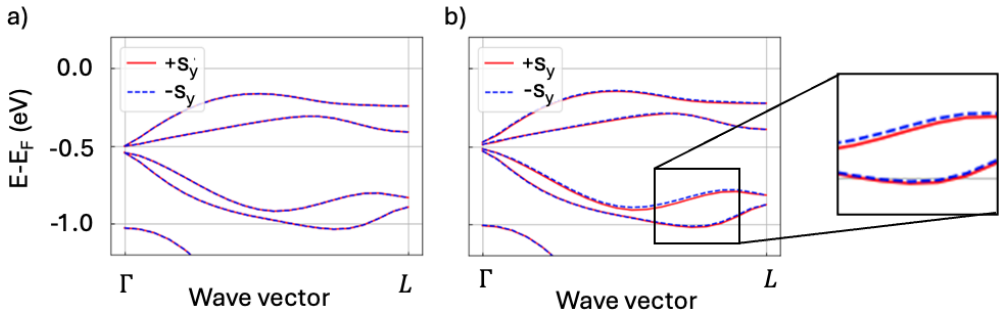

FIGURE 5.7: Band structure of α-Fe_2O_3 along a high symmetry path where splitting due to the ferroically ordered triakontadipoles is forbidden, (a) for an AFM ordering with the moments oriented along the $\hat{y}$ in a $+-{-}+$ pattern and (b) for the high-temperature magnetic phase with canted moment. The inset shows a zoomed-in view of the splitting between spin-polarized bands in (b). The bands are shown along the path $\Gamma \to L$, where $L \equiv (\frac{1}{2}, 0, 0)$ in relative coordinates.

5.2.6 Summary and Outlook

In summary, we have identified a ferroically ordered rank-5 magnetic triakontadipole in the low-temperature AFM phase of hematite. The ferroically ordered magnetic triakontadipole is present even in the absence of SOC, where it is the lowest-order time-reversal symmetry breaking multipole. As a result, it causes an NRSS with the same g-wave symmetry as the magnetic triakontadipoles. The ferroically ordered magnetic triakontadipoles persist in the weakly ferromagnetic phase above the Morin transition, where they dominate over the ferroically aligned spin components in their contribution to the spin splitting. Our findings indicate a method to manipulate both the sign and magnitude of the NRSS by altering the crystal structure and magnetic ordering. As such, they contribute to the recent efforts [204–207] aimed at harnessing g-wave spin splitting with specific implications for the unconventional transport properties observed in α-Fe_2O_3 [6, 212, 213]. The manifestation of the magnetic triakontadipole in the NRSS of hematite may be probed using spin-polarized angle-resolved photoemission spectroscopy, as has recently been reported to demonstrate the spin splitting in other AFM materials [205–207, 214]. The presence of the magnetic triakontadipoles and the NRSS may also be the source of some unexplained features in the spin-wave spectra of α-Fe_2O_3 [6].

We emphasize that the relevance of the ferroically ordered magnetic triakontadipoles goes beyond the NRSS. For example, they allow for a fourth-order ME effect, where the induced magnetization is quartic in the applied electric field. Furthermore, the

magnetic triakontadipoles give rise to a second-order piezomagnetic effect, where the induced magnetization scales quadratically with the applied strain [171, 215]. Similarly, the SOC-induced magnetic octupole in hematite, as discussed in the present work, gives rise to the second-order ME effect [19, 45] and piezomagnetic effect [199], which may also be probed experimentally.

Finally, our present understanding implies the rank-7 inversion symmetric magnetic multipole will be responsible for the i-wave spin splitting, which requires future investigation. We hope that our work will stimulate further theoretical and experimental work along these directions.

5.2.7 Acknowledgements

The authors thank Dr. Andrea Urru for useful discussions. NAS, XHV, and SB were supported by the ERC under the European Union's Horizon 2020 research and innovation programme grant No. 810451 and by the ETH Zürich. Computational resources were provided by ETH Zürich's Euler cluster.

5.3 Additional work

In this section, we show some additional results, extending the research discussed in the paper presented in the previous section. This includes the manipulation of the triakontadipoles and the spin splitting at lower values of U, a more detailed discussion of the Brillouin zone, and an explanation of the k-space representation of triakontadipoles and how this relates to the spin-splitting symmetry. I also discuss the difference in the multipole components between the hypothetical $R\bar{3}m$ structure and the real $R\bar{3}c$ structure, and how we can understand this from the difference in the oxygen coordination.

5.3.1 Triakontadipoles and non-relativistic spin splitting with smaller U

In Section 3.1.1, we discussed our choice for Hubbard U for Fe_2O_3, basing this choice on a comparison with experimental results on the band gap and the magnitude of the magnetic moment. This is not the only way to determine a value for U, and it is worth determining whether our results hold for different values of U. This simultaneously allows us to address a separate issue. As mentioned in Section 5.2.5.3C, the electronic bands in α-Fe_2O_3 in its real structure show many crossings. Thus, when we manipulate the magnitude of the magnetic triakontadipoles, it is difficult to observe the effect on the spin splitting anywhere other than close to a high symmetry point. Instead, when we lower the value of U, the bands become less hybridized, which makes it easier to follow the changes in NRSS. Calculating the multipoles at lower values of U, we find the same orderings, although the magnitudes vary. We also observe spin splitting with the same symmetry, regardless of the choice of U. Figure 5.8 shows the variation of the NRSS as a function of the magnetic triakontadipole component w_3^{415} for U = 1.0 eV and J = 0.5 eV.

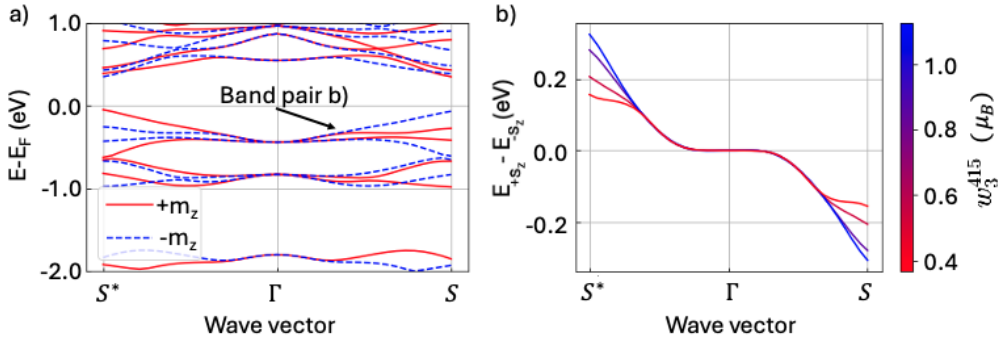

FIGURE 5.8: (a) Spin-polarized band structure and (b) the variation of the spin splitting as a function of the magnitude of the angular component of w_3^{415} (in μ_B) in Fe_2O_3 at $U = 1.0$ eV. The spin splitting in (b) corresponds to the band in (a) just below the Fermi energy.

As is clear from the plot, we obtain the same qualitative behavior, i.e., the larger the magnitude of the (induced) triakontadipoles, the larger the spin splitting. Thus we see that the relationship between the triakontadipoles and the NRSS is robust, and does not change in nature when we choose different DFT parameters.

5.3.2 The Brillouin zone of Fe_2O_3

As discussed previously there is a set of k-points in the Brillouin zone, where we find zero spin splitting. We also use a part with large spin splitting, along which to compare the effects of varying the magnetic triakontadipoles. We plot both the high-symmetry points with zero spin splitting and the low-symmetry path with large splitting in Figure 5.9. We note that the high symmetry points [Γ, L, P, Z] lie in the $kx = 0$ plane, and the spin splitting is zero for all the points on this plane. By employing the three-fold rotational symmetry about k_z, we can generate two more of these nodal planes. One of these contains the symmetry points [F, L_1, P_1, P_2], as well as Γ and Z, the line through which forms the intersection of the three planes. We also have the three nodal lines; the k_x axis, at its rotations by 120° and 240° about $\hat{k}_z$.

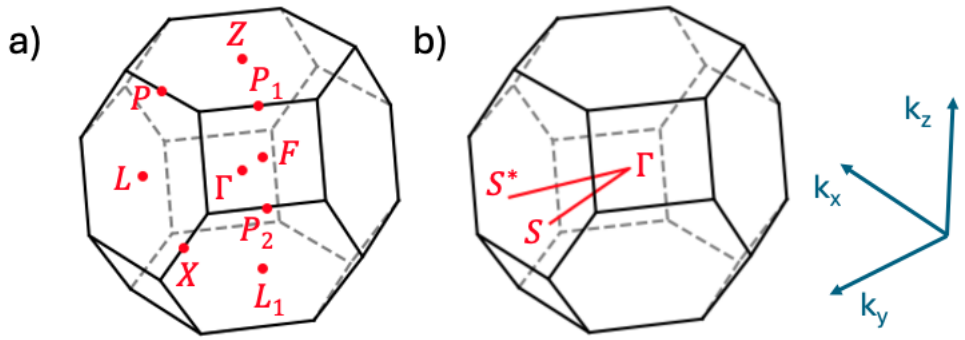

FIGURE 5.9: The Brillouin zone of α-Fe_2O_3, highlighting the high symmetry k-points (a), and the path used for the band structure plots (b).

5.3.3 The k-space representation of the triakontadipoles

We can also consider the k-space representations of the triakontadipoles, to further explore the relationship between them and the NRSS. As discussed in Section 5.2.5.1, the three ferroically ordered angular components of triakontadipoles in the low-temperature magnetic ground state of Fe_2O_3 are w_3^{415}, w_{-3}^{414} and w_3^{413}.

To describe the symmetry of these triakontadipole components, we need to find the corresponding irreducible representations (irreps) of SO(3). This is in principle a non-trivial task.

We can write the full rank-5 triakontadipole as a matrix product of 5 vectors, which each transform as three-dimensional irreps of SO(3), so that the full triakontadipole tensor transforms as a $\mathbf{3}\otimes\mathbf{3}\otimes\mathbf{3}\otimes\mathbf{3}\otimes\mathbf{3}$ reducible representation, which decomposes into irreps in the following way:

$$\mathbf{3}\otimes(\mathbf{3}\otimes\mathbf{3}\otimes\mathbf{3}\otimes\mathbf{3})_{\text{Symm}} = \mathbf{3}\otimes(\mathbf{9}\oplus\mathbf{5}\oplus\mathbf{1}) \tag{5.5}$$

$$= \underbrace{\mathbf{3}\otimes\mathbf{9}}_{\mathbf{11}\oplus\mathbf{9}\oplus\mathbf{7}} \oplus \underbrace{\mathbf{3}\otimes\mathbf{5}}_{\mathbf{7}\oplus\mathbf{5}\oplus\mathbf{3}} \oplus \underbrace{\mathbf{3}\otimes\mathbf{1}}_{\mathbf{3}} \tag{5.6}$$

$$= \mathbf{11}\oplus\mathbf{9}\oplus\mathbf{7}\oplus\mathbf{7}\oplus\mathbf{5}\oplus\mathbf{3}\oplus\mathbf{3}. \tag{5.7}$$

where we made use of the fact that the spatial components are equivalent, so the tensor must be symmetric under the exchange of them. Now, w_3^{415} belongs to the 11-dimensional irrep, w_{-3}^{414} to the 9-dimensional one, and w_3^{413} to a 7-dimensional irrep.

The 11-dimensional irrep is captured by the spherical harmonics with $L = 5$, such that w_3^{415}, transforms as the spherical harmonic $Y_{5,3}$. Transforming this to a k-space representation is trivial as inversion symmetry is preserved, e.g., x goes to k_x. Now we can check the symmetry of this triakontadipole component. In Sections 5.2.5.2 and 5.3.2 we mentioned a set of k-points, where we found the NRSS to be zero in all bands. We find that the k-space representation of w_3^{415} is zero in all these k-points as well. We note that it is also zero at some additional points, where we do find spin splitting. We hypothesize this is because the representations of *all* ferroically ordered triakontadipole components (w_3^{415}, w_{-3}^{414} and w_3^{413}) need to be zero, to cause the NRSS to be absent.

5.3.4 Multipole components in the high symmetry structure

In the hypothetical high-symmetry structure, there is no charge hexadecapole with the same antiferroic ordering as the magnetic dipoles, which leads to the absence of ferroically ordered triakontadipoles. Instead, in this structure, we induce the charge hexadecapoles with this antiferroic ordering. As mentioned in Section 5.2.5, both the induced hexadecapole and the corresponding triakontadipole components differ between the regular and hypothetical high-symmetry structure. This difference is due to the oxygen coordination. In both structures, the oxygens atoms form triangles in planes perpendicular to the z axis, and these triangles are rotated by 90° in the $R\bar{3}m$ structure, compared to the $R\bar{3}c$ structure (see Figure 5.4). Thus, the coordination environment is characterized by different hexadecapoles.

5.4 Comments

In this section, we discuss some of the open questions and discuss paths of further research. We begin by noting that, even though g-wave type spin splitting is classified by the presence of four nodal planes, we found only three. We understand these to be generated by the three glide mirrors, while the three nodal lines originate from the two-fold screw rotations. These six operations together form the coset $\bar{3}m - \bar{3}$, such that there is no generator for a fourth nodal plane, which we would have expected at $k_z = 0$. However, the spin splitting does appear to exhibit g-wave symmetry. It was suggested that in such cases, each band pair still crosses in the vicinity of $k_z = 0$, such that the spin splitting between the pair changes sign [216]. As the exact location is not dictated by symmetry, the points of these intra-pair crossings not coincide for the different band pairs. Due to the many inter band-pair crossings in Fe_2O_3, we were unable to isolate a pair of bands to show this particular behavior. Further investigation is needed to resolve this issue, possibly in the low U regime, where the bands are less hybridized.

Furthermore, as discussed in Section 5.3.3, we can compare the spin splitting symmetry to those of the triakontadipoles, but this is limited because we do not have the representations of w_{-3}^{414} and w_{3}^{413}. Showing that the joint symmetries of all three ferroically ordered magnetic triakontadipole components match the symmetry of the spin splitting would further establish the connection between them.

Finally, we remark that an oddity occurs in the sign of the spins and the charge hexadecapoles on the one hand, and the magnetic triakontadipoles on the other. As we understand the triakontadipole components to originate from a combination of the spins and the charge hexadecapoles, we would expect that the product of the signs of the latter two would give the sign of the former, but this is not the case. For example, if we look at Table 5.1, block a, we see that the spin moment w_0^{011} has ordering $+ - -+$, the same as the charge hexadecapole w_3^{404}. Multiplying these signs on each site would give $+ + ++$, but the magnetic triakontadipole components (w_3^{415}, w_{-3}^{414} and w_3^{413}) are all ordered as $- - --$. The origin of this sign discrepancy is unclear, but we note that it is not caused by the sign difference between the spin and the magnetic moment, as all (w_t^{k1r} components are given in terms of spin).

Chapter 6

Heterostructures

We can also examine the differences and similarities between Cr_2O_3 and Fe_2O_3 in the context of interfaces of the two materials. In this chapter, I will discuss how we studied the magnetism of Cr_2O_3/Fe_2O_3 interfaces by simulating supercells of these materials. As a consequence of such an interface, there is a transition in magnetic dipole order, allowing interfacial magnetization and magnetic frustration. We aim to understand the magnetic ordering of these supercells, both in the ground state and as a function of temperature. We begin by motivating the study of interfaces and reviewing examples of interesting behaviors that can occur at oxide interfaces. Next, I discuss how we chose the type of interfaces to study and previous work on these interfaces. I also describe our model Hamiltonians, the different magnetic interactions we considered, and explain how the interaction parameters were extracted from density functional theory (DFT) calculations. These parameters are then compared to literature values, from both computational and experimental sources. I evaluate the simulation results for the bulk compounds, comparing model Hamiltonians which include different magnetic interactions. I consider the temperature evolution, the Néel temperature, the Morin transition temperature, the ground state magnetic ordering and the orientation of the Néel vector. Next, I present the results for the Cr_2O_3/Fe_2O_3 interface, while comparing two models. One with only Heisenberg exchange and single-ion anisotropy, and a more complicated model, which includes tensorial exchange and dipole-dipole interactions. Finally, I discuss the convergence parameters and present some future research directions.

6.1 Oxide interfaces

In recent decades, oxide interfaces have emerged as a playground for new phenomena, many of which can be tuned using strain, doping, the choice of interface plane, etc. The

behavior of these interfaces is distinct from the bulk because the interface needs to compensate for the discontinuity between the compounds [217]. Depending on the type of discontinuity, we may see different types of reconstruction. For example, combining two compounds with different local ligand coordination can create a unique coordination at the interface. This effect has been shown for the γ-Al_2O_3/$SrTiO_3$ interface, where the combination of the tetrahedral and octahedral coordinated spinel structure of γ-Al_2O_3 combined with the octahedral coordination of $SrTiO_3$ leads to a square pyramid coordination for the Ti atoms at the interface. This change in local symmetry has significant consequences for the electronic band structure [18], as, for example, the crystal field splitting depends on the ligand coordination. New interface properties can also occur for combinations of materials with the same crystal structure, like when two materials with a 'so-called' polar mismatch are combined. When considering the formal charges on the atoms, the full unit cell should be neutral. However, depending on the crystal structure, we may define atomic layers within this unit cell, for which the former charge does not have to be zero. When two materials with different charges on these atomic layers are combined in an interface parallel to the layers, there is a discontinuity in the layer charges, which is called a polar mismatch. To ensure charge neutrality, the interface must compensate for this discontinuity. This polar mismatch is believed to be the origin of the two-dimensional electron gas which appears between some insulating non-polar transition metal oxides, like $LaAlO_3$ and $SrTiO_3$ [218]. Such a polar mismatch can also be used to tune the ferroelectric polarization in some materials [219], showing that interfacial discontinuities are also a potential pathway for controlling bulk properties. Magnetic interfaces have attracted attention because they sometimes allow for unique magnetic states, e.g., helical spin structures can arise from interfacing antiferromagnetic (AFM) and ferromagnetic (FM) materials [18]. Furthermore, the symmetry at the interface is lowered, allowing for couplings that are absent in bulk. For example, strong Dzyaloshinskii-Moriya interactions have been observed in interfaces between FM materials and paramagnetic heavy metals, originating from both the inversion symmetry breaking of the interface and the strong spin-orbit coupling in the heavy metal [220, 221].

In this chapter, we explore the magnetism of Cr_2O_3/Fe_2O_3 interfaces. As discussed in Chapters 2 and 3, Cr_2O_3 and Fe_2O_3 have the same crystal structure, but a different AFM ordering. The AFM ordering in Cr_2O_3 breaks inversion symmetry, while the Fe_2O_3 ordering preserves it, which has consequences for their magnetoelectric (ME) responses. When forming the interface, we thus have a discontinuity, which we expect to be compensated somehow.

6.2 Cr_2O_3/Fe_2O_3 interfaces

The discontinuity at the Cr_2O_3/Fe_2O_3 interface is complicated by the temperature dependence of the magnetic ordering in both compounds. As discussed previously, Cr_2O_3 is an easy-axis antiferromagnet below its Néel temperature of 307 K [49, 124], with two time-reversal distinct AFM domains (Figure 2.2). The Néel temperature of Fe_2O_3 is 960 K, below which adopts a weaklyFM phase, until the Morin transition at 263 K, when it switches to the easy-axis AFM phase [125, 126]. Both phases of Fe_2O_3 have two time-reversal distinct domains. The crystal structure and low-temperature easy-axis AFM ordering are shown in Figures 6.1a (Cr_2O_3) and 6.1b (Fe_2O_3), showing one of two allowed AFM domains for each and using the conventional unit cell of the corundum structure.[1]

We could construct many different interfaces between Cr_2O_3 and Fe_2O_3, depending on the choice of interface plane. The choice of interface plane is significant, both because of the orientation with the magnetic ordering, and because of strain. The bulk lattice parameters are different, but the exact strain may differ between interface planes. Here we focus on the (001) interface, i.e., the interface perpendicular to the z axis. The (001) interface is straightforward to construct from the conventional unit cell, and the growth of such an interface has been achieved experimentally [222]. Assuming an atomically sharp (001) interface, the corundum structure allows for two distinct possibilities with regards to the chemical ordering [120]. We call the first type 'oxygen-separated' (Figure 6.1c), as the interface has a layer of O atoms separating the Cr_2O_3 and Fe_2O_3 environment. The second type is called 'mixed-metal' (Figure 6.1d), because the interface is formed by a buckled layer of transition metal (TM) atoms (i.e., Cr and Fe).

The (001) interface between Cr_2O_3 and Fe_2O_3 has been previously examined in the context of transport, hinting at a surface chemistry dependent band offset [222, 223]. Specifically, it was suggested that growing Cr_2O_3 on Fe_2O_3 would favor a different interface environment than growing Fe_2O_3 on Cr_2O_3. It was shown that the mixed-metal and oxygen-separated interfaces indeed show different band offsets in DFT, with an offset difference similar in magnitude to the one observed in experiment. However, it was not confirmed that the experimental interfaces were indeed of the mixed-metal and oxygen-separated types.

Despite the potential for new phenomena due to the change in magnetic order, the magnetism of the Cr_2O_3/Fe_2O_3 interface has not been studied in detail. To the best of our knowledge, only one computational study has been undertaken, finding an enhanced spin correlation in Cr_2O_3 above its Néel temperature, using a simple Heisenberg Hamiltonian

[1] See Section 2.1.2 for a comparison between the two commonly used corundum unit cells.

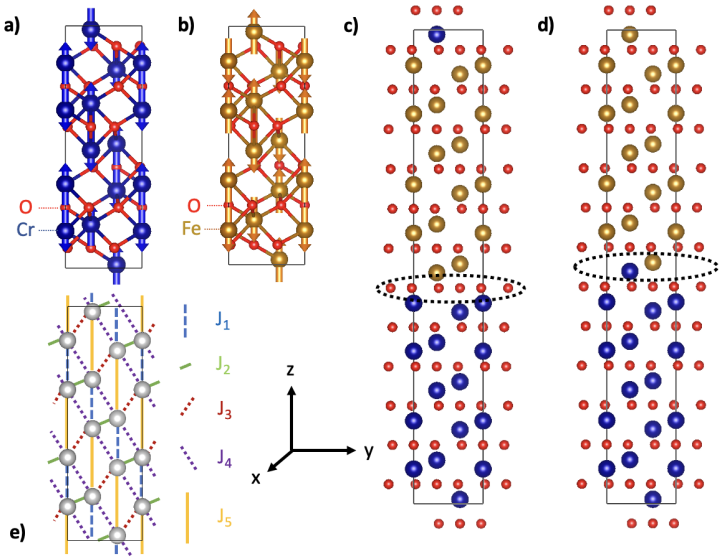

FIGURE 6.1: Unit cells and magnetic exchanges in Cr_2O_3, Fe_2O_3 and the heterostructures. The hexagonal 30-atom unit cell of Cr_2O_3 (a) and Fe_2O_3 (b). One antiferromagnetic (AFM) domain is shown for each compound, with magnetic moments on the Cr, Fe atoms are indicated with arrows of the same color as the atom. The two types of interfaces that were considered, the 'oxygen-separated' interface (c) and the 'mixed-metal' interface (d), with the interfacial regions, separating the Fe_2O_3 environment (top) from the Cr_2O_3 environment (bottom), indicated with dotted black ellipses. The symmetric exchanges J up to the 5^{th} shell for the transition metal ions in the corundum structure (e), in order of increasing interatomic distance. Due to the two-dimensional projection, some of the interatomic distances look shorter. Cartesian axes are chosen with $\hat{x}$ parallel to the hexagonal a axis and $\hat{z}$ parallel to the hexagonal c axis.

and simulating a single interface [120]. In this work, we investigate magnetic ordering and interfacial magnetism using different Hamiltonian models, and simulating supercells with multiple interfaces.

6.3 Magnetic interactions

To study the magnetism of the interfaces, we use model Hamiltonians, which capture the magnetic interactions between the magnetic moments on the TM ions. We can then simulate the magnetic moments using Monte Carlo (MC) or spin dynamics (SD). These methods were discussed in Section 2.4. We include different magnetic interactions in our model Hamiltonians, which we will discuss below. The most complex Hamiltonian, including all interactions we considered, looks as follows:

$$H = -\sum_{i\neq j} J_{ij}\ \hat{\boldsymbol{e}}_i \cdot \hat{\boldsymbol{e}}_j - \sum_{i\neq j} \boldsymbol{D}_{ij} \cdot\ \hat{\boldsymbol{e}}_i \times \hat{\boldsymbol{e}}_j - \sum_{i\neq j}\ \hat{\boldsymbol{e}}_i A_{ij} \hat{\boldsymbol{e}}_j - K_i \sum_i e_{i,z}^2$$
$$- K_i' \sum_i e_{i,z}^4 - \frac{\mu_0}{8\pi} \sum_{i\neq j} \mu_{s_i}\mu_{s_j} \left(\frac{3(\hat{\boldsymbol{e}}_i \cdot \boldsymbol{r}_{ij})(\boldsymbol{r}_{ij} \cdot \hat{\boldsymbol{e}}_j)}{|\boldsymbol{r}_{ij}^5|} - \frac{\hat{\boldsymbol{e}}_i \cdot \hat{\boldsymbol{e}}_j}{|\boldsymbol{r}_{ij}^3|}\right), \tag{6.1}$$

where i sums over the different sites, $\hat{\boldsymbol{e}}_i$ is the magnetic moment unit vector on lattice site i, $\boldsymbol{r}_{ij}$ is the vector connecting lattice sites i and j, J_{ij} is the symmetric (Heisenberg) exchange between the spins on sites i and j, $\boldsymbol{D}_{ij}$ is the Dzyaloshinskii-Moriya interaction (DMI) [126, 224, 225], and A_{ij} is the symmetric off-diagonal exchange. K_i and K_i' are the quadratic and quartic uniaxial single-ion anisotropy (SIA). The final term describes the dipole-dipole interaction, where μ_0 is the permeability of vacuum and μ_{s_i} is the magnitude of the magnetic moment on site i.

The symmetric exchange ($J_{ij} = J_{ji}$) is usually the leading term in energy and determines if it is favorable for moments to be aligned or anti-aligned. The DMI $\boldsymbol{D}_{ij}$ is also called antisymmetric exchange, as $\boldsymbol{D}_{ij} = -\boldsymbol{D}_{ji}$. The DMI has to obey strict symmetry rules [224], and is zero when there is an inversion center in the middle of the line connecting the sites i and j. The contribution of the DMI to the energy is zero when the spin on sites i and j are parallel (or antiparallel). This means it does not contribute for any collinear configuration of spins, which is the case for the low-temperature ground states of Cr_2O_3 and Fe_2O_3. However, in the heterostructure and at higher temperatures, it may become significant. In fact, it was first proposed to explain the weaklyFM phase in Fe_2O_3 [126, 224]. A_{ij} is the symmetric off-diagonal exchange, and is sometimes also called the two-site anisotropy, as it changes the effective anisotropy on each site. J_{ij}, $\boldsymbol{D}_{ij}$ and A_{ij} can be combined together into the matrix $\tilde{J}_{ij}$, which represent the tensorial exchange. I will refer to these terms together as the 'full' exchange. The single-ion anisotropies K_i and K_i' indicate the preferential orientation of the magnetic moments with respect to a single axis, e.g., the z axis. Note that the three-fold rotational symmetry of the corundum structure forbids more complex anisotropy terms, like cubic anisotropy. The dipole-dipole interactions indicate the favored alignment of the magnetic moments with respect to their connecting vector, and it also contributes to the effective anisotropy. It is the only term that explicitly depends on the atomic positions. We did not include more complex magnetic interactions, such as the bi-quadratic interaction, as these are unnecessary in the description of the bulk compounds [105, 226].

K_i, K_i' involve a single site only, and we will assume that they are the same for each site that contains the same element, i.e., all the Cr sites have the same K_i, which is different from the K_i of the Fe sites. J_{ij}, $\boldsymbol{D}_{ij}$, A_{ij} involve different sites, can be different

for different combinations of sites, and usually become smaller the further the distance between the sites. The cutoff radius for these interactions can be captured by the neighbors we consider for each site. We will label each set of neighbors by the shell, i.e., the nearest neighbors form the first shell, the next-nearest neighbors form the second shell, etc. We will consider including different amounts of neighbors for the magnetic interactions.

Now, to perform the simulation of the magnetic moments, we need to determine the values of each of the magnetic parameters in the Hamiltonian.

6.4 Determining the magnetic parameters

As mentioned in Chapter 2, we may extract magnetic interaction parameters from DFT. To describe the single compounds Cr_2O_3 and Fe_2O_3, we used the same parameters as discussed in Section 3.1. Using these settings we found the magnetic moment on the Fe and Cr atoms to be $4.01\,\mu_B$ and $2.6\,\mu_B$, respectively. Magnetism was considered collinearly when calculating the Heisenberg magnetic exchanges, and non-collinearly when calculating the magnetic anisotropy and DMI. We adapted the k-point grid to have a similar density in each unit cell and adopted an 800 eV energy cutoff for our plane wave basis. From the magnitude of the magnetic moments and the relaxed crystal structure, the dipole-dipole interactions may be calculated directly.

6.4.1 Determining the symmetric exchange

To extract the symmetric exchanges J_{ij}, we used the method pioneered by Xiang *et al.* [96]. Specifically, we compared the total energy of unit cells where the collinear magnetic moments were initialized in different configurations, generated by performing up to two spin flips in the ground-state configuration. We considered exchanges up to the 5^{th} shell, giving five different types of exchange to consider for each atom $J_1 - J_5$ (Figure 6.1e). Here J_1 labels the exchange between two TM ions with the shortest interatomic distance, J_2 with the second shortest, etc. To place the cutoff after the 5^{th} shell is in line with most previous studies on Cr_2O_3 and Fe_2O_3 [105–107, 120, 227, 228], but one study on Fe_2O_3 included interaction up to the 13^{th} shell [226]. We focus on the first five shells here for two reasons. First of all, the contribution of the J's between sites that lie far apart is not expected to contribute significantly to the energy, both because the magnitude of J generally decreases with interatomic distance and because this is not compensated by an increase in the number of neighbors (Table 6.1), e.g., the 13^{th} shell

Shell	1	2	3	4	5	6	7	8	9	10	11	12	13
Nr of neighbors	1	3	3	6	1	6	6	6	3	3	3	6	6

TABLE 6.1: The number of neighbors in each shell, up to the 13^{th} shell. Up to and including the 5^{th} shell the total number of neighbors is 14. Up to and including the 13^{th} shell the total number of neighbors is 53.

contains as many neighbors as the 4^{th} shell and J_{13} is expected to be much smaller than J_4.

The second reason to stick to the 5^{th} shell has to do with the extraction from DFT: we need a larger unit cell to capture an interaction at a larger interatomic distance, which is computationally more costly. Furthermore, small quantities are generally more difficult to determine accurately.

We extracted the symmetric exchanges up to and including the 5^{th} shell for Cr-Cr, Fe-Fe and Cr-Fe pairings. We compared the total DFT energy for different magnetic configurations in the 30-atom, conventional, corundum unit cell. Although computationally less expensive, the small, primitive, 10 atoms corundum unit cell cannot be used to extract these exchanges. This is a consequence of the periodic boundary conditions. When we flip one spin, we also flip the same spin in the next unit cell. In the small unit cell, each site and its copies are so close together, that we cannot entangle the different exchanges (e.g., we can only determine $J_1 + J_3$). The Cr-Cr and Fe-Fe exchanges are extracted from calculations of bulk Cr_2O_3 and Fe_2O_3 in the conventional, 30-atom, unit cell, while the Cr-Fe exchanges are determined from the average of the Cr-Fe exchanges in the 30-atom unit cell of bulk Cr_2O_3 with one Cr atom replaced by a Fe atom and the 30-atom unit cell of bulk Fe_2O_3 with one Fe atom replaced by a Cr atom, respectively.

We plot the five magnetic exchanges between Cr-Cr, Fe-Fe and Cr-Fe pairs in Figure 6.2. The Cr-Cr exchanges are dominated by J_1 and J_2, the Fe-Fe exchanges are dominated by J_3 and J_4, and the Cr-Fe exchanges are close to the average between the Cr-Cr and Fe-Fe exchanges. Furthermore, the Cr-Cr, Fe-Fe and Cr-Fe exchanges are of similar orders of magnitudes, so we can expect the Cr-Fe exchanges to play an important role at the interface.

We compare the values we calculated to values from previous calculations and experimental results (Tables 6.2 and 6.3). We note that several different conventions exist for defining J, which differ in sign, factors of two, and whether the size of the magnetic moments is absorbed into J. Hence, we opt to compare ratios of J's. We compare the ratio J_i/J_1 for Cr_2O_3 and J_i/J_3 for Fe_2O_3, because J_1 and J_3 are the largest exchange terms for Cr_2O_3 and Fe_2O_3, respectively.

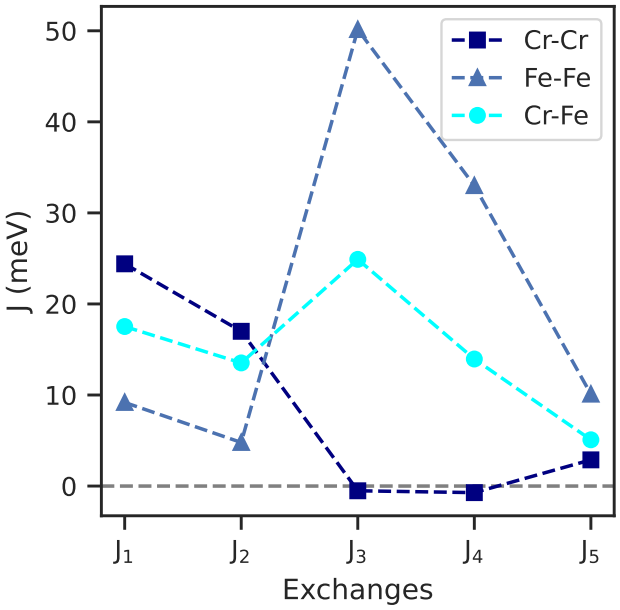

FIGURE 6.2: Magnetic exchanges J between Cr-Cr, Fe-Fe and Cr-Fe pairs for the first five nearest neighbors in the corundum structure.

	This work	Ref. [105]	Ref. [228] Ref. [120]	Ref. [106]	Ref. [107]	Ref. [229] (Exp.)	Ref. [50] (Exp.)
J_2/J_1	0.696	0.760	0.761	0.760	0.835	0.446	0.454
J_3/J_1	-0.0212	-0.145	-0.300	-0.144	-0.154	0.0676	0.0103
J_4/J_1	-0.0296	-0.203	-0.321	-0.204	-0.130	0.0270	-0.00229
J_5/J_1	0.118	0.148	0.188	0.145	0.165	-	0.0252

TABLE 6.2: A comparison between the symmetric (Heisenberg) magnetic change in Cr_2O_3 as calculated in this work and the literature. (Exp.) indicates parameters obtained from experiment by fitting a Heisenberg model to the magnon spectrum of Cr_2O_3 obtained with neutron scattering.

As expected, there is some spread in the J's obtained from DFT, because of different methods and parameters. For Cr_2O_3, we see a clear consensus on the relative signs of J_{1-5}, which we also find in our calculations. The values we find for J_2 and J_5 match well, and J_3 and J_4 are relatively small compared to the previous computations. For Fe_2O_3 our calculations match well with most of the computational literature, with our J_5 a bit larger than those found previously. For both compounds, there are discrepancies between the experimental and computational results. We note that, in neither of the two compounds, all J_{1-5} all help to lower the energy in the ground state. For example, in Fe_2O_3, all J_{1-5} have the same sign, preferring an antiferroic arrangement. Looking at Figure 6.1b however, we see that in the ground state, the neighbors in the second (J_2) and fourth shell (J_4) are arranged ferroically instead.

Even though the Heisenberg exchange term in the Hamiltonian does not explicitly depend on the atomic positions, J_{ij} can change when we strain the material. It has been

	This work	Ref. [227]	Ref. [228] Ref. [120]	Ref. [230]	Ref. [226]	Ref. [52] (Exp.)
J_1/J_3	0.183	0.340	0.150	0.252	0.123	-0.202
J_2/J_3	0.0955	-0.289	0.0270	0.230	0.147	-0.0539
J_4/J_3	0.658	0.694	0.692	0.705	0.602	0.781
J_5/J_3	0.201	-0.00278	0.0339		0.00651	0.0337

TABLE 6.3: A comparison between the symmetric (Heisenberg) magnetic change in Fe_2O_3 as calculated in this work and the literature. (Exp.) indicates parameters obtained from experiment by fitting a Heisenberg model to the magnon spectrum of Fe_2O_3 obtained with neutron scattering.

shown previously that the Fe-Fe J_{ij} in Fe_2O_3 are relatively independent of strain, while the Cr-Cr J_{ij} are more sensitive to strain [120]. Yet, to determine the effect of strain, we need to know what the strain would be in Cr_2O_3/Fe_2O_3 heterostructures or supercells, which is unclear. When we relax the unit cells of Figure 6.1c and d in DFT, we obtain lattice parameters that are close to the average between the Cr_2O_3 and Fe_2O_3 lattice parameters. However, it is also possible Cr_2O_3 adopts the Fe_2O_3 in-plane lattice parameters [222]. We opt to use the bulk Cr_2O_3 and Fe_2O_3 J's in our simulations of the heterostructures, assuming that the potential change due to the strain would not qualitatively alter the results. The validity of this approach is supported by our other computations, where we extracted Cr-Cr, Fe-Fe and Cr-Fe exchanges in the heterostructure strained to the Al_2O_3 in-plane lattice parameters.[2] Although these J's differ from those presented in Figure 6.2, the general trends remain the same. We will compare the results for the magnetic ordering in the heterostructure using the strained and bulk J's.

6.4.2 Determining the single-ion anisotropy

The magnetic anisotropy was calculated using non-collinear moments in the bulk materials, using the small primitive unit cell. We define the anisotropy energy as the difference between the energy when the magnetization (and thus the Néel vector $\boldsymbol{L}$) is parallel to the z axis, which is the ground state configuration, and the energy when the magnetization axis lies in the xy plane. Starting from the ground state configuration, where all the spins are collinearly aligned along the z axis, we slowly rotated the magnetization axis into the xy plane, while constraining the moments along the new axis. In other words, we rotate the magnetic moments in phase, such that they all remain aligned along a singular axis, but the orientation of this axis changes. These rotated configurations do not represent the ground state, so we constrain the magnetic moments, for which we used the constrained moment subroutine as implemented in the Vienna *ab initio* simulation package (VASP).[208].

[2] Al_2O_3 is a common choice of substrate for Cr_2O_3 and Fe_2O_3 thin films, as it shares the corundum structure.

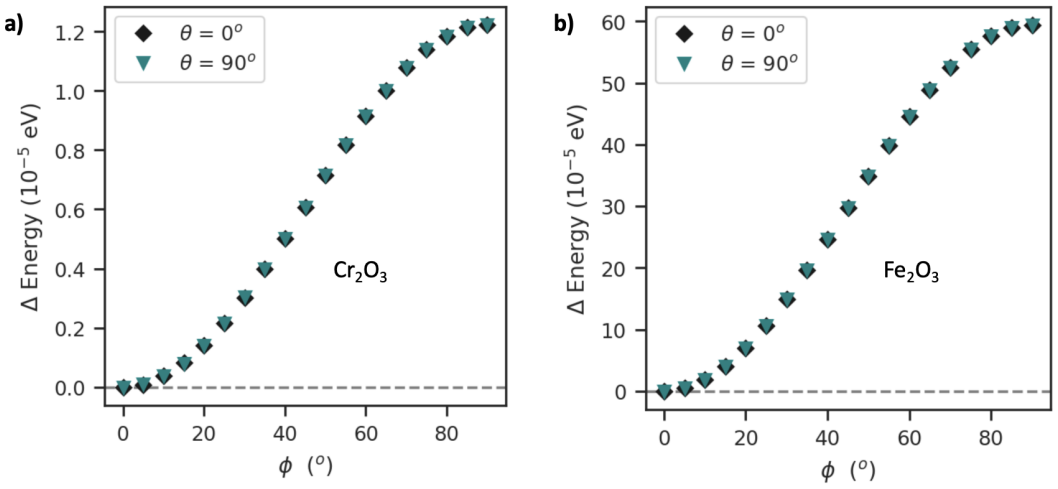

FIGURE 6.3: Difference in DFT energy per unit cell with respect to the ground state as a function of the orientation of the magnetization axis in Cr_2O_3 (a) and Fe_2O_3 (b), where ϕ denotes the angle of the magnetization axis with the z axis and θ the angle with the x axis within the xy plane.

In Figure 6.3, we plot the change in DFT energy as a function ϕ, the angle between the magnetization axis and the z axis, for Cr_2O_3 (Figure 6.3a) and Fe_2O_3 (Figure 6.3b). We consider two different in-plane angles θ, i.e., we compare on the one hand rotating the magnetization axis from $\parallel \hat{z}$ to $\parallel \hat{x}$ ($\theta = 0°$), and on the other rotating the magnetization axis from $\parallel \hat{z}$ to $\parallel \hat{y}$ ($\theta = 90°$).

We see the energy is independent of the orientation in the xy plane, as there is no θ dependence. We subsequently fit the energy difference $\Delta E = E(\phi) - E(\phi = 0)$ with the following function to determine K and K':

$$\Delta E = 4\big(K \sin^2(\phi) + K' \sin^4(\phi)\big). \tag{6.2}$$

The factor of four comes from the fact that the energy is per unit cell, and there are four magnetic moments per unit cell. For Cr_2O_3, we find an energy difference $\Delta E = E_{\boldsymbol{L}\perp\hat{z}} - E_{\boldsymbol{L}\parallel\hat{z}} = 12.2\,\mu$eV per unit cell (6.1 μeV per formula unit) for Cr_2O_3, in good agreement with experiment [124, 150, 231]. This results in the single-ion anisotropy K = 3.020(2) μeV and for K' = 0.032(2) μeV. We note here that K' is so small that it is unlikely to play a significant role.

For Fe_2O_3, we find an anisotropy energy $\Delta E = E_{\boldsymbol{L}\perp\hat{z}} - E_{\boldsymbol{L}\parallel\hat{z}} = 593.9\,\mu$eV per unit cell (296.95 μeV per formula unit), giving K = 149.00(2) μeV and K' = -0.525(12) μeV. These values are of a similar order of magnitude as the previous calculations by Dannegger *et al.* [226], with our value for K being about 30% larger, and our value for K'

being a factor two smaller. Our value for K' also has opposite sign, but again K' is very small. We will come back to the role of K' in the next section.

We assume that the anisotropy will not change significantly between the bulk and the supercells, as the materials are not strongly strained. Thus, we will use the values for K and K' we calculated for the bulk materials for our simulations of the interfaces as well. This is a valid approximation, as the anisotropy is several orders of magnitude smaller than the exchanges, and, unless it changes sign, deviations in its value are unlikely to change the ground state. Because the anisotropy of Cr_2O_3 is quite small, small deviations in its value could quickly lead to a sign change. However, an interface with Fe_2O_3 places Cr_2O_3 under tensile strain. The anisotropy energy was shown to increase in magnitude under tensile strain (while maintaining the same sign), due to the change in the crystal field [232, 233].

6.4.3 Finding the Dzyaloshinskii-Moriya interactions and the two-site anisotropy

To obtain the DMI $\boldsymbol{D}_{ij}$, we attempted to use a similar energy difference method as for the symmetric exchanges, now comparing the energies of four different *non-collinear* magnetic configurations [96]. This total energy technique has been successful for calculating the DMI in other compounds [221]. We performed these calculations while constraining the moments, but found these calculations challenging to converge properly. They would either fail to converge, 'converge' with large penalty energies away from the constraint, or converge with large fluctuations in the size of the magnetic moments. It seems that these configurations are so energy-unfavorable that it is difficult to enforce them. Perhaps, because the DMI does not contribute to the energy in the low-temperature collinear ground states of Cr_2O_3 and Fe_2O_3 they are difficult to determine with this method. Furthermore, the DMI are expected to be relatively small, on the order of μeV, so three orders of magnitude smaller than the symmetric exchanges.

Many different methods for extracting the DMI from first principles exist [221], but these methods would not necessarily give DMI consistent with the J, K, and K' we extracted. Rather than redoing all our calculations using a different method, we note that a consistent set of magnetic exchange parameters was previously determined for Fe_2O_3 [226]. This parameter set includes both the DMI $\boldsymbol{D}_{ij}$ and two-site anisotropy A_{ij}, which we were also unable to calculate.

We obtain the $\boldsymbol{D}_{ij}$ and two-site anisotropy A_{ij} in Fe_2O_3 by adopting those found by Dannegger *et al.* [226] and carefully checking the magnetic simulation of the bulk compound. For Cr_2O_3, we make an assumption based on the ratio of the single-ion anisotropy K. Both the SIA, the DMI, and the two-site anisotropy are relativistic effects, which depend on spin-orbit coupling. Thus we assume that the ratio between K in Cr_2O_3 and Fe_2O_3, and the ratio between the DMI in Cr_2O_3 and Fe_2O_3, is similar [3]. We make the same assumption for the two-site anisotropy. For the Cr-Fe interactions (DMI and two-site anisotropy), we take averages of the values for Cr_2O_3 and Fe_2O_3, similar to what we saw from our calculated J's. We also vary our variables when we simulate the bulk compounds, to establish which parameters are responsible for which component of the observed behavior.

6.5 Simulating the bulk materials

Using the magnetic interaction parameters, we can now use MC or SD to study the magnetism of the bulk materials. As the materials' bulk behavior is well-known experimentally, this will serve as a check that we have found appropriate values for the magnetic interaction parameters. Moreover, it will allow us to discern which magnetic interactions are responsible for which magnetic behavior. For the bulk materials, we use unit cells that contain approximately 100000 magnetic moments. These unit cells were constructed from the unit cells of the bulk compound. For example, starting from the conventional corundum unit cell, we can create a unit cell for our magnetic simulation of $30 \times 30 \times 10$ of these conventional cells. Here the number of cells is counted along the conventional unit cell axes. We performed simulations using both the primitive and conventional unit cells as a base, and found no significant differences, as long as the total number of spins was similar. In both cases, periodic boundary conditions were applied. We note that the oxygen atoms are not simulated, because they carry little to no magnetic moment and their role in facilitating the exchange interactions is captured by the parameters that we extracted from first principles. To obtain the ground state, we performed simulations cooling down from 1500 K to 10 K, using 300000 relaxation steps at each temperature to ensure proper convergence of the Néel vector. A discussion on how we arrived at these settings can be found in Section 6.7.

To judge the accuracy of the model Hamiltonian, we can consider the evolution of the Néel vector in each compound. The AFM ordering in both compounds is different, so we must define a different Néel vector for each, $\boldsymbol{L}_{Cr}$ for Cr_2O_3 and $\boldsymbol{L}_{Fe}$ for Fe_2O_3.

[3] The shape of the DMI vector is set by the crystal symmetry, which is the same for Cr_2O_3 and Fe_2O_3, so this assumption automatically leads to DMI which are consistent with the Cr_2O_3 symmetry.

Following the numbering of the TM according to the Wyckoff positions (Eq. 3.10 and Figure 3.7, the Néel vectors are (in the small unit cell):

$$\boldsymbol{L}_{Cr} = \frac{1}{4}\left(-\boldsymbol{m}_{\mathrm{Cr}_1} + \boldsymbol{m}_{\mathrm{Cr}_2} - \boldsymbol{m}_{\mathrm{Cr}_3} + \boldsymbol{m}_{\mathrm{Cr}_4}\right) \tag{6.3}$$

$$\boldsymbol{L}_{Fe} = \frac{1}{4}\left(-\boldsymbol{m}_{\mathrm{Fe}_1} + \boldsymbol{m}_{\mathrm{Fe}_2} + \boldsymbol{m}_{\mathrm{Fe}_3} - \boldsymbol{m}_{\mathrm{Fe}_4}\right) \tag{6.4}$$

where the magnetic moments $\boldsymbol{m}$ are unit vectors in our magnetic simulations, such that $\boldsymbol{L}$ is a unit vector as well. For larger unit cells, the definition is equivalent: the moments are summed with signs depending on their positions, and then divided by the total number of moments. In any unit cell we can describe each of the atoms as being symmetry equivalent to one of the four Wyckoff sites, thus allowing us to determine with which sign they enter the summation.

6.5.1 Cr_2O_3

For Cr_2O_3 we expect the Néel vector $\boldsymbol{L}_C$ to be zero as long as the material is paramagnetic, i.e., as long as the temperature is above the Néel temperature (T_N). Below T_N we expect $\boldsymbol{L}_{Cr}$ to increase until the material reaches its AFM ground state. We furthermore expect $\boldsymbol{L}_{Cr} \parallel \hat{z}$, for all $T < T_N$. In Figure 6.4, we show the evolution of the different components of $\boldsymbol{L}_{Cr}$ as a function of temperature in our simulations, where we split $\boldsymbol{L}_{Cr}$ into the component parallel to $\hat{z}$ ($L_\parallel = |L_z|$) and the component in the xy plane ($L_\perp = \sqrt{(L_x)^2 + (L_y)^2}$). We compare a simulation where we only took the symmetric exchanges J and the quartic single-ion anisotropy K into account (Figure 6.4a) and one where we used the full Hamiltonian of Eq. 6.1 (Figure 6.4b).

We find a the ground state with the expected AFM ordering ($|\boldsymbol{L}_{Cr}| = 1$) and orientation of the moments ($\boldsymbol{L}_{Cr} \parallel \hat{z}$). Also, the magnetic transition occurs around 300 K, close to the experimental Néel temperature of 307 K. This behavior is completely captured by the simple Hamiltonian, showing that including only J and K is sufficient as a minimal model for Cr_2O_3. Furthermore, we observe only a small difference between the two models, indicating that the values for the DMI and two-site anisotropy we estimated are sufficiently small. Note that, if they would be too larger, we would see a 'Morin transition' in Cr_2O_3.

6.5.2 Fe_2O_3

We can make the same comparison for Fe_2O_3. We plot the temperature evolution of $\boldsymbol{L}_{Fe}$ and in Figure 6.5, again comparing a model with only the symmetric exchanges J and the quartic anisotropy K, and a model with the full exchange, uniaxial anisotropy, and dipole-dipole interactions.

We see that, with either model, we capture the same T_N and ground state, slightly overestimating the Néel temperature in both cases. However, we only capture the Morin transition in the second model, showing that we need more interactions than just J and K to capture this transitions correctly. Next, we explore which of the additional interactions (K', $\boldsymbol{D}_{ij}$, A_{ij} and the dipole-dipole interactions) are important to stabilize the Morin transition, and give an accurate description of the full temperature dependent magnetic behavior of Fe_2O_3. First, we try using only J, K and $\boldsymbol{D}_{ij}$, and see that the DMI do not suffice to stabilize the transition. By comparing different combinations of interactions, we find that both the dipole-dipole interactions and the two-site anisotropy play important roles, because they lower the effective anisotropy. To model the Morin transition accurately we need the DMI, the two-site anisotropy *and* the dipole-dipole interactions.

Furthermore, we explore the number of neighbors that are necessary to accurately model the magnetic behavior of Fe_2O_3. As previously mentioned, Ref. [226] extracted parameters up to the 13$^{\text{th}}$ shell, but we expect that including interactions up to the 5$^{\text{th}}$ shell would be sufficient. We test this hypothesis by comparing two models, one including interactions up to the 5$^{\text{th}}$ and one including interactions up to the 13$^{\text{th}}$ shell (Figure 6.6). We find that placing the cutoff at the 5$^{\text{th}}$ shell, does not lead to a Morin transition.

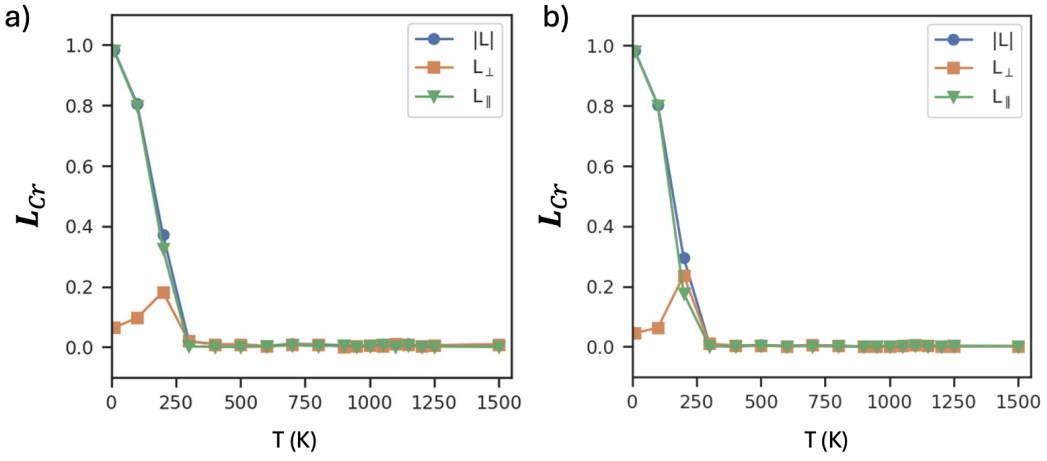

FIGURE 6.4: Temperature dependence of the Néel vector for simulations of Cr_2O_3 when only taking the symmetric exchanges J and single-ion anisotropy K into account (a), and when including all the interactions of Eq. 6.1 (b).

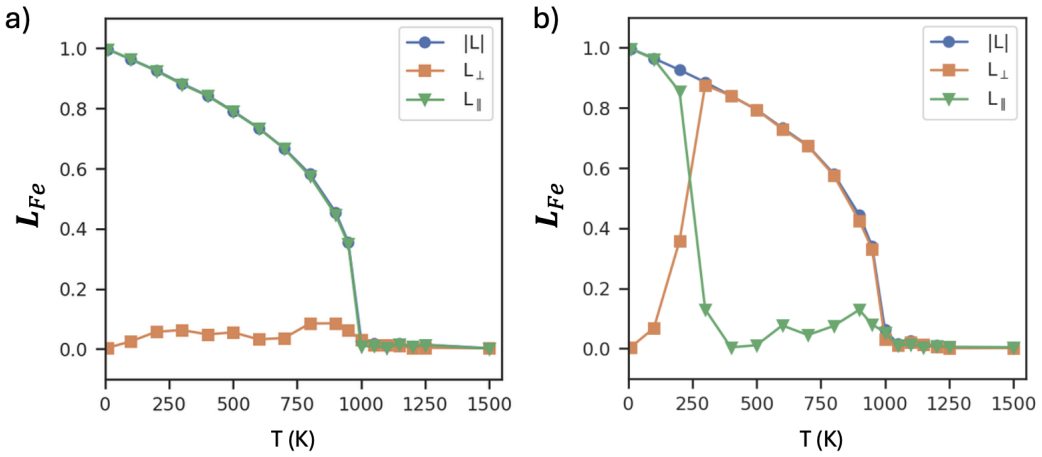

FIGURE 6.5: Temperature dependence of the Néel vector for simulations of Fe_2O_3 when only taking the symmetric exchanges J and single-ion anisotropy K into account (a), and when including all the interactions of Eq. 6.1 (b).

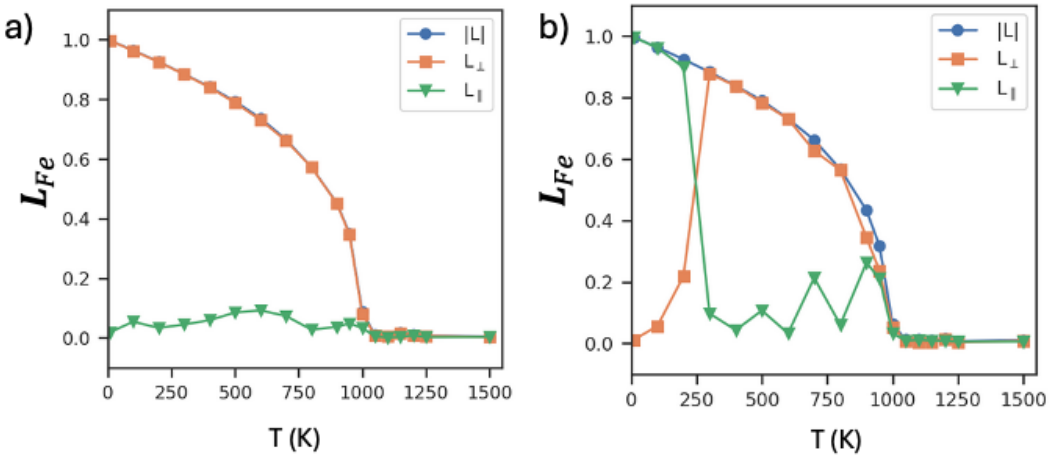

FIGURE 6.6: Temperature dependence of the Néel vector for simulations of Fe_2O_3 when only taking the magnetic interactions up to the 5^{th} shell into account (a), and when including all the interactions up to the 13^{th} shell 6.1 (b).

Instead, the Néel vector remains perpendicular to $\hat{z}$ for all $T<T_N$, and the ground state is not capture correctly. Only when we keep the interactions up to the 13^{th} shell, do we capture the Morin transition. Further testing showed that the inclusion of neighbors beyond the 5^{th} shell is only significant for the dipole-dipole interactions. When we including the 'full' exchange up to the 5^{th} shell, but the dipole-dipole interactions up the the 13^{th} shell, we simulate both the Morin transition and the ground state accurately. In fact, Figure 6.5b shows the evolution of the Néel vector with all the exchange interactions cutoff at the 5^{th} shell, but keeping the dipole-dipole interactions up to the 13^{th} shell. Comparing Figures 6.6b and 6.5b, we see that these show very similar behavior, confirming that the symmetric exchange, the DMI, and two-site anisotropy beyond the 5^{th} shell do not contribute significantly to the magnetic behavior.

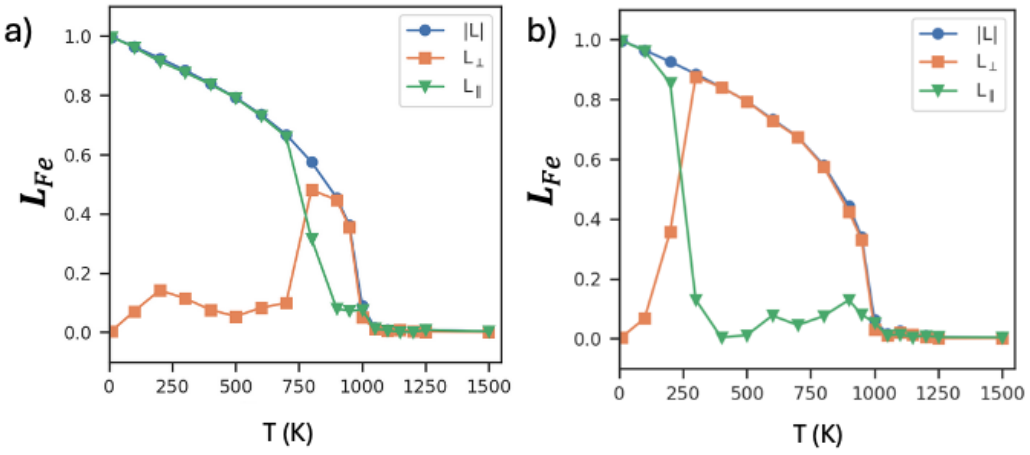

FIGURE 6.7: Temperature dependence of the Néel vector for simulations of Fe_2O_3 when using our calculated J, K, and K' (a), and using the parameters from Ref. [226] (b). In both cases, the full exchanges were considered up to the 5^{th} shell, and the dipole-dipole interactions up to the 13^{th} shell.

As discussed in Section 6.4, we extracted J's, K, and K' from DFT. Of course, the parameter set from Ref. [226] also contains values for J, K, and K', which are similar but not the same. We can compare simulations of the magnetism of bulk Fe_2O_3, using the values we extracted for J, K, and K' or those from Ref. [226] (Figure 6.7). In both cases, we used the $\boldsymbol{D}_{ij}$ and A_{ij} from Ref. [226].

We see that both sets of parameters capture the Néel temperature correctly, show a Morin transition, and capture the same ground state. However, using the J, K and K' we extracted, the transition temperature T_M is overestimated. Although this does not qualitatively change the physics, we decided to use the J, K, and K' from Ref. [226] for the simulations of the heterostructures.

Finally, as discussed previously, for both Cr_2O_3 and Fe_2O_3, the values of K' are very small. We tested setting K' to zero and did not observe any changes. However, it was reported that K' is necessary to describe the spin-flop transition, which occurs under the application of a magnetic field. We did not simulate this transition, but keep the K' of Ref. [226] for the Fe sites, and use the K' we calculated for the Cr sites, in the simulation of the heterostructures.

6.5.3 Dipole-dipole interactions

Next, we look more closely at the dipole-dipole interactions and why they are so important in Fe_2O_3. The primary contribution of the dipole-dipole interactions is changing the anisotropy, but this anisotropy also depends on the orientation of the two dipoles with one another. This orientation is set mostly by the symmetric exchange. If the connecting

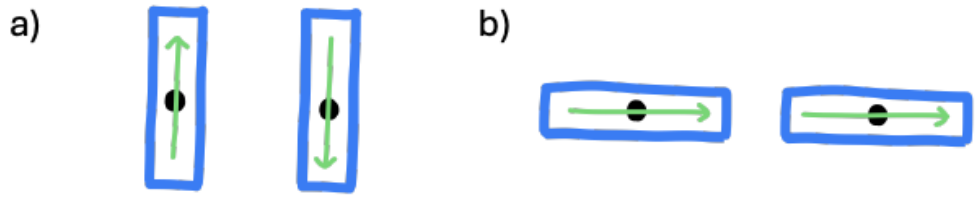

FIGURE 6.8: The arrangement of two dipoles that minimize the energy of the dipole-dipole interaction for two dipoles oriented perpendicular to their connecting vector (a) and parallel to their connecting vector (b).

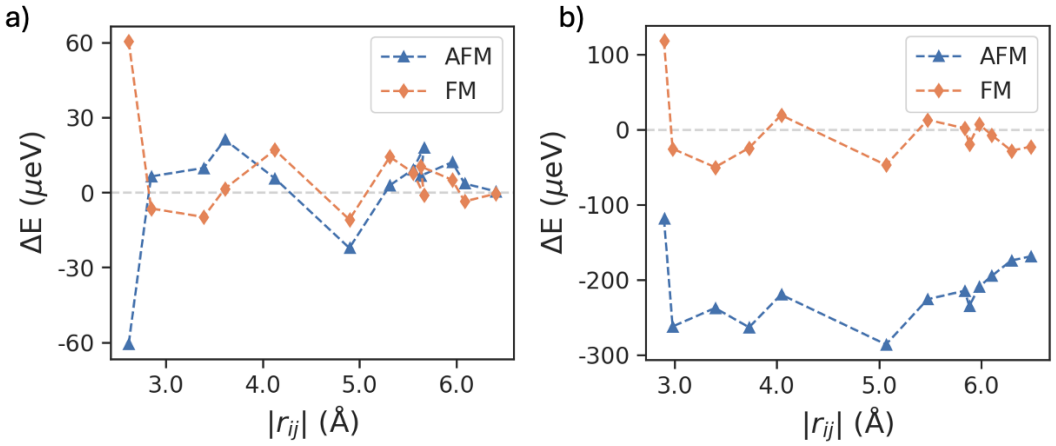

FIGURE 6.9: The magnitude of the dipole-dipole interaction per unit cell, for Cr_2O_3 (a) and Fe_2O_3 (b), comparing ferromagnetic (FM) and antiferromagnetic (AFM) arrangements of the magnetic dipoles. Note that we used the ground state AFM orderings for each compound, $+-+-$ for Cr_2O_3 and $+--+$ for Fe_2O_3.

vector is perpendicular to the two dipoles, the dipole-dipole interaction prefers them to be arranged antiferroically (Figure 6.8a). If the connecting vector is parallel, the dipole-dipole interaction energy is minimized when the dipoles are ordered ferroically (Figure 6.8b). In our materials, this means that when two dipoles are ordered antiferroically, due to other magnetic interactions, the dipole-dipole interaction energy is lowered when they are oriented perpendicular to their connecting vector. Vice-versa, when they are ordered ferroically, an orientation parallel to the connecting vector is favored by the dipole-dipole interaction

The contribution to the effective anisotropy is captured by $\Delta E = E_{dd}(\boldsymbol{m} \perp z) - E_{dd}(\boldsymbol{m} \perp z)$, with $E_{dd} = -\frac{\mu_0}{8\pi} \sum_{i \neq j} \mu_{s_i} \mu_{s_j} \left(\frac{3(\hat{\boldsymbol{e}}_i \cdot \boldsymbol{r}_{ij})(\boldsymbol{r}_{ij} \cdot \hat{\boldsymbol{e}}_j)}{|\boldsymbol{r}_{ij}^5|} - \frac{\hat{\boldsymbol{e}}_i \cdot \hat{\boldsymbol{e}}_j}{|\boldsymbol{r}_{ij}^3|} \right)$. In Figure 6.9, we plot the cumulative ΔE as a function of atomic distance and compare the respective ground state AFM ordering and FM ordering in Cr_2O_3 and Fe_2O_3.

We see that for Cr_2O_3 the total contribution of the dipole-dipole interaction to the anisotropy converges to comparable small values of opposite sign for the FM and AFM

arrangement. For Fe_2O_3 ΔE remains significant for both FM and AFM arrangement at large distances. We can explain the difference in ΔE for the FM ordering in the two compounds from the difference in the bulk lattice parameters and the difference in the magnitude of the magnetic moments. Note that the dipole-dipole interaction scales with the square of this magnitude, so the difference between $2.6\,\mu_B$ (Cr_2O_3) and $4.1\,\mu_B$ (Fe_2O_3) is significant. The remaining difference between ΔE for AFM orderings in the two compounds originates from the difference in these orderings. If we check the ΔE contribution in Fe_2O_3 for the AFM ordering that is the ground state of Cr_2O_3 ($+-+-$), we find ΔE to have a compatible value to ΔE for FM arrangement, but of opposite sign, the exact same behavior we saw in Cr_2O_3.

Even though we see that the role of the dipole-dipole interaction is very small in Cr_2O_3, it is significant in Fe_2O_3 and may play an important role in the magnetism of the heterostructures as well. Also, it is desirable to keep a consistent set of interactions. So for the simulations of the heterostructure, we set the cutoff for the full exchange at the 5^{th} shell, and for the dipole-dipole interactions at the 13^{th} shell.

6.6 Simulating the heterostructures

To simulate the magnetic behavior of the heterostructures, we need to establish the atomic positions, as the dipole-dipole interactions depend on these.

We can do this in DFT, but there is a caveat; the atomic positions are not independent of the magnetic ordering. We proceed as follows. We relax the mixed-metal and oxygen-separated interfaces with different collinear AFM orderings, letting the unit-cell volume *and* the atomic positions relax. We see that the unit cell size is very similar for each of these, so we take the average. With this unit cell size, we then relax the atomic positions again. We find these positions to be fairly similar for different magnetic arrangements with the same interface, but to differ for the two interface types. We average over the magnetic arrangements but keep two sets of atomic positions, one for the mixed-metal interface and one for the oxygen-separated interface. We note that these positions only change the dipole-dipole interactions, as all the other magnetic interactions were calculated in the bulk, and do not explicitly depend on the positions.

6.6.1 Electronic properties of the interface

We confirm in DFT that the heterostructure remains insulating by looking at the density of states (DOS). In the full DOS, a band gap is present, although it is reduced compared

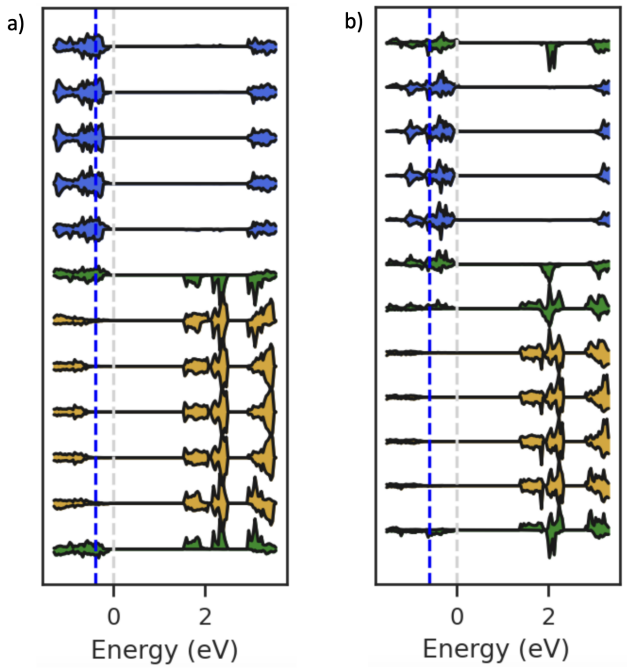

FIGURE 6.10: Layered density of states (DOS) for the oxygen-separated interface (a) and the mixed-metal interface (b). Layers are formed by three oxygens at the same z-position and the two metal ions above and below along the z axis. Layers containing Cr and O contributions are colored blue, layers with Fe and O contributions are colored yellow, and layers with Cr, Fe and O are colored green. The grey dotted line indicates the global Fermi level, and the blue dotted line indicates the lowest the top valence band goes in the layers. The difference between the blue and grey dotted lines indicates the band offset.

to the bulk compounds. This band gap changes size, but never vanishes for any collinear AFM ordering we sampled. We can also look at the DOS in different layers of the unit cell. We plot the density of states layer by layer in Figure 6.10, and see that the reduction of the band gap is caused by a band offset. Although the aim of this study was not to accurately determine the band gaps and offsets in the heterostructure, the band offsets we find differ for the two interface types (-0.4 eV for the oxygen-separated interface and -0.6 eV for the mixed-metal interface), and are similar to those found in previous computational studies [223].

6.6.2 Simple model

Now, we will derive the ground state of our heterostructures for two scenarios, starting with a minimal Hamiltonian, which includes only the symmetric exchange J, included up to the 5^{th} shell, and the leading term of the SIA, the quadratic term K:

$$H = -\sum_{i \neq j} J_{ij}\ \hat{\boldsymbol{e}}_i \cdot \hat{\boldsymbol{e}}_j - K_i \sum_i e_{i,z}^2 \tag{6.5}$$

As established in the previous section, with just these terms we capture both the Néel temperatures of Cr_2O_3 and Fe_2O_3 and find the correct ground states. This works because the magnetic ordering transition is dominated by the terms that have the largest contribution to the energy, which are the J's. Furthermore, we can capture the ground states of both compounds correctly, as the final orientation of the Néel vector is determined by the anisotropy term. Yet, this model cannot capture the Morin transition, which requires the addition of the DMI, the two-site anisotropy and the dipole-dipole interactions.

We constructed unit cells of $20 \times 20 \times 12$ unit cells of the oxygen-separated or mixed-metal interface type (Figures 6.1c and d). As these unit cells contain one layer of each compound, stacking them along z results in multiple layers forming; a supercell. For the $20 \times 20 \times 12$ unit cell, there are 24 layers, 12 layers of each compound. We tried different unit cell sizes, for example $25 \times 25 \times 8$, but found no significant differences, so we focus on the results for the $20 \times 20 \times 12$ unit cell here. We can derive the ground state of both interface types from the set of exchanges and anisotropies described above. We again cool down from 1500 K to 10 K, and find the expected signatures of ordering at the Néel temperatures for Cr_2O_3 and Fe_2O_3. For both interface types, we see a slightly reduced Néel temperature for Fe_2O_3, which we understand in the following way. In the heterostructure, the Fe moments order first. Because of the supercell structure, the order Fe moments in each layer order independently, as they by layers of unordered Cr moments. When we look at Fe_2O_3 in a slab geometry, we see a similar reduction in Néel temperature, and this trend has also been observed experimentally in thin films of Fe_2O_3 [234].

Now to classify the type of ordering in the heterostructures, we first looked at the individual magnetic moments, and noticed that, at 10 K they were oriented mostly parallel to $\hat{z}$. Furthermore, the Cr moments in the Cr_2O_3 layers and the Fe moments in Fe_2O_3 seemed to stick to the bulk AFM orderings. Thus, we can use the Néel vector of each layer, to classify the order of the heterostructure. Here the assumption is that each layer will be a single domain, meaning that the Néel vector is the same for every unit cell in the layer.

Starting with the oxygen-separated interface, we show the Néel vectors $\boldsymbol{L}_{Cr}$ in the Cr_2O_3 layers and in the $\boldsymbol{L}_{Fe}$ in the Fe_2O_3 layers, where we averaged over all the unit cells in

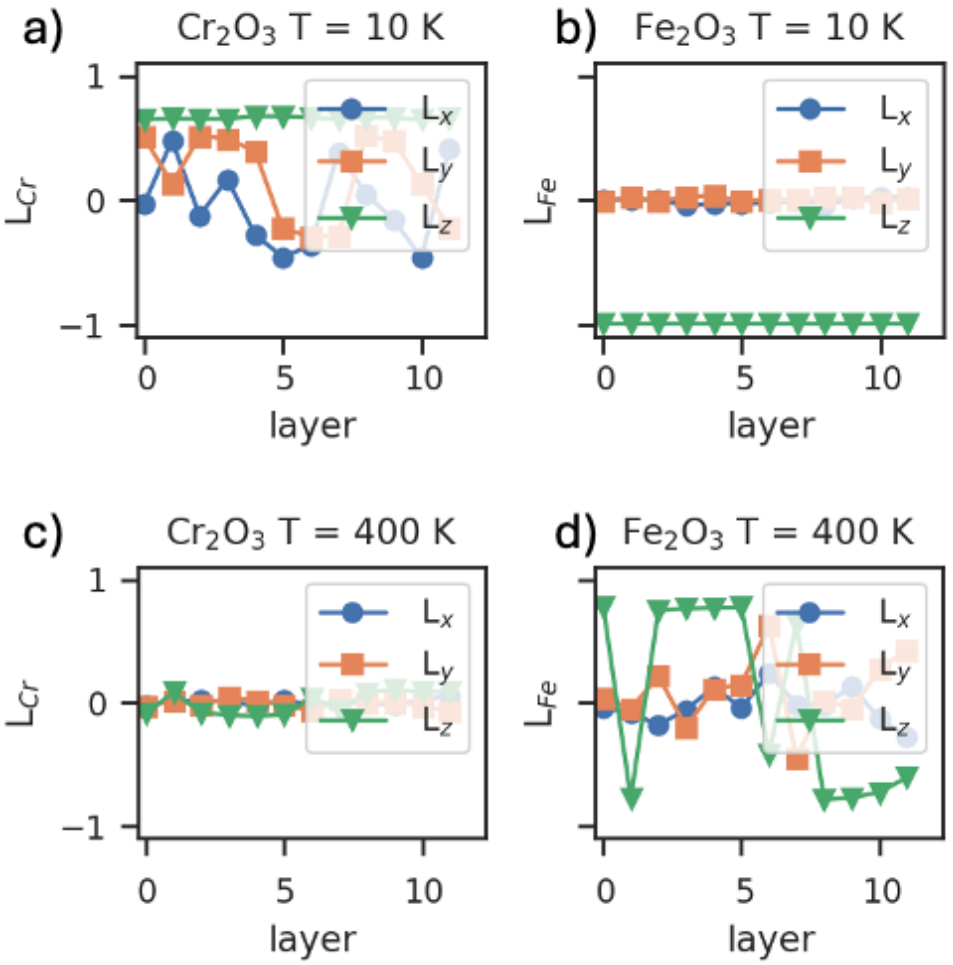

FIGURE 6.11: Néel vector per layer in the oxygen-separated interface, for the Cr_2O_3 layers (a, c) and the Fe_2O_3 layers (b,d) at 10 K (a,b) and at 400 K (c,d). The $20\times20\times12$ unit cell results in twelve layers of each compound. The Néel vectors $\boldsymbol{L}_{Cr}$ and $\boldsymbol{L}_{Fe}$ are as defined in Eqs. 6.3 and 6.4.

each layer (Figure 6.11). Note that we show the components of the vector along each Cartesian axis, rather than the components parallel and perpendicular to $\hat{z}$.

At 10 K both the Cr_2O_3 and Fe_2O_3 layers are ordered, with the Néel vectors parallel to z. Furthermore, all the layers of the same compound have the same sign of L, which means that we have a specific combination of AFM domains, domain 1 of Cr_2O_3 and domain 2 of Fe_2O_3, as defined in Figure 2.2. At 400 K, the Cr_2O_3 layers are completely unordered, as we would expect as $T_{N,Cr} < 400$ K. The Fe_2O_3 layers are ordered, but the ordering of the layers is independent; some are in AFM domain 1 and some in AFM domain 2. Then, when the Cr_2O_3 layers order, the Fe_2O_3 layers adapt to all have the same domain and match the Cr_2O_3 layers. Thus, it seems that for the oxygen-separated interface, the ground state involves layers of Cr_2O_3 domain 1 and Fe_2O_3 domain 2 (or equivalently Cr_2O_3 domain 2 and Fe_2O_3 domain 1 are combined), because ferroically aligning the magnetic moments of the interfacial Cr-Fe pair with the shortest interatomic distance

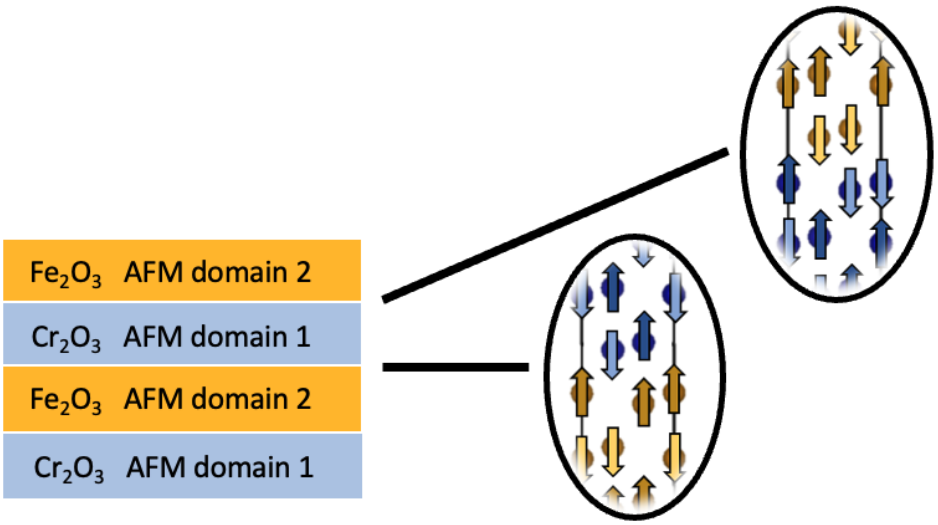

FIGURE 6.12: The ground state for the oxygen-separated interface supercell, showing a single antiferromagnetic (AFM) domain for each Cr_2O_3 layer and single AFM domain for each Fe_2O_3 layer. The Cr_2O_3 layers are displayed in blue and Fe_2O_3 layers in orange, with the AFM domains as defined in Figure 2.2. Insets show the local magnetic environment at each interface, with the Cr and Fe atoms displayed in blue and gold, respectively. Magnetic moments on Cr are displayed in blue, with the moments pointing down in a lighter shade for contrast. Similarly, magnetic moments on Fe are displayed in gold, with the moments pointing down in a lighter shade for contrast.

(J_1) is favored. We visualize this ground state and the local ordering of the moments at the interface in Figure 6.12. We perform DFT simulations, where we compare the energy of the oxygen-separated interface which combines Cr_2O_3 domain 1 and Fe_2O_3 domain 1, and the interface with Cr_2O_3 domain 1 and Fe_2O_3 domain 2, and find that the latter is indeed lower in energy. This also follows from analytically comparing the different arrangements using the given exchanges, further establishing that the magnetic ground state of the oxygen-separated interface is this combination of domains.

In comparison, the mixed-metal interface shows a very different ground state. Here the Néel vector switches sign every other layer, combining both AFM domains of both compounds (Figure 6.13). Similarly to the oxygen-separated interface, the Fe_2O_3 layers are already quite ordered at 400 K, with each layer independent. This ordering adapts completely once the Cr_2O_3 layers also start to order. We perform DFT calculations and an analytic analysis, this time comparing the switching domains with other domain patterns, and indeed find the switching domains to be the lowest energy arrangement.

This mixed-metal ground state corresponds to a magnetic ordering with the interfacial Cr-Fe pair with a J_2 interaction aligned ferromagnetically. Interestingly, the switching AFM domains ensure that the FM J_2 pair at the interface is maintained (Figure 6.14). The smallest magnetic unit cell for supercells with this interface type thus contains 120 atoms, instead of 60, as it includes both AFM domains of each compound. This complex

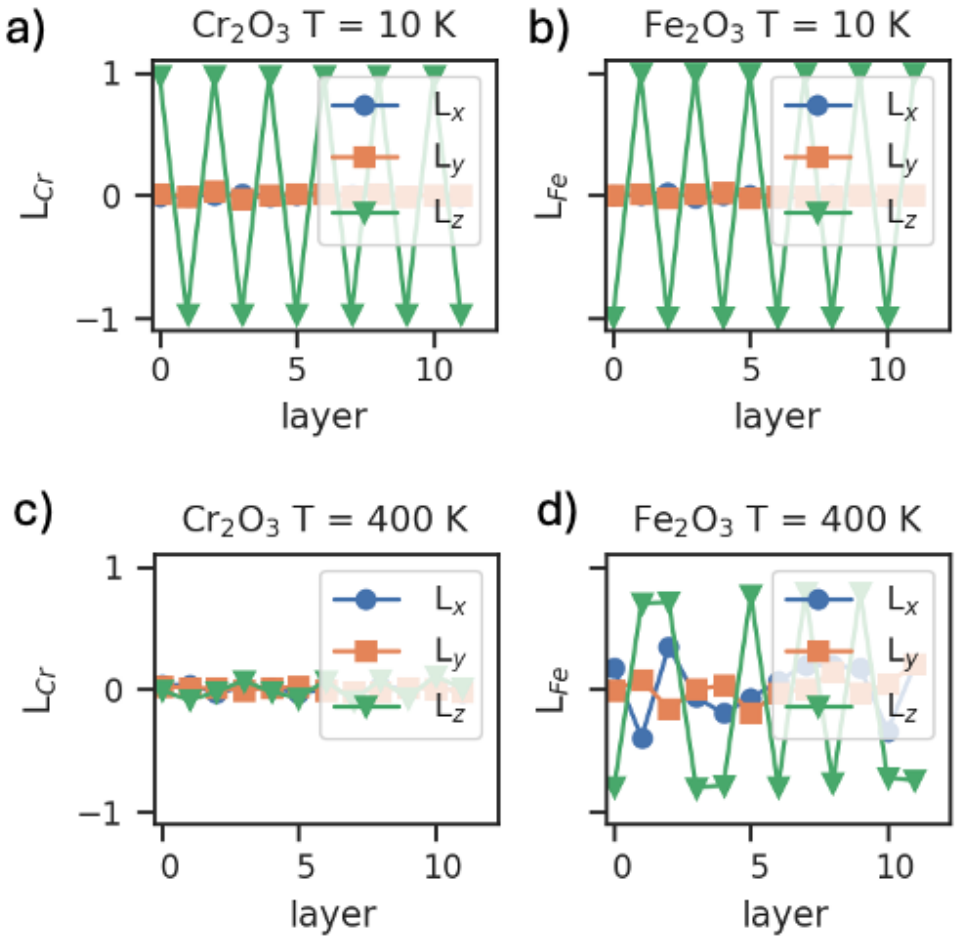

FIGURE 6.13: Néel vector per layer in the mixed-metal interface, for the Cr_2O_3 layers (a, c) and the Fe_2O_3 layers (b,d) at 10 K (a,b) and at 400 K (c,d). The $20 \times 20 \times 12$ unit cell results in twelve layers of each compound. The Néel vectors $\boldsymbol{L}_{Cr}$ and $\boldsymbol{L}_{Fe}$ are as defined in Eqs. 6.3 and 6.4.

magnetic order results purely from the physical interface engineering. We note that in our DFT calculations, the oxygen-separated interface with its favored magnetic ordering was slightly lower in energy than the mixed-metal interface with its favored magnetic ordering.

We point out that we find the same ground states for both the oxygen-separated interface and the mixed-metal interface using the Js we extracted for heterostructure constrained to the Al_2O_3 in-plane lattice parameters, showing that the ground states are robust against the degree of changes in the exchange that is caused by strain.

Finally, we see that in both ground states there is a change in the layer magnetization. In bulk Fe_2O_3 we have buckled layers that are ordered ferroically, with each layer having opposite magnetization to the next. In contrast, each buckled layer in Cr_2O_3 has compensated moments. Looking at Figure 6.14, the interface layer has ferroically aligned Fe

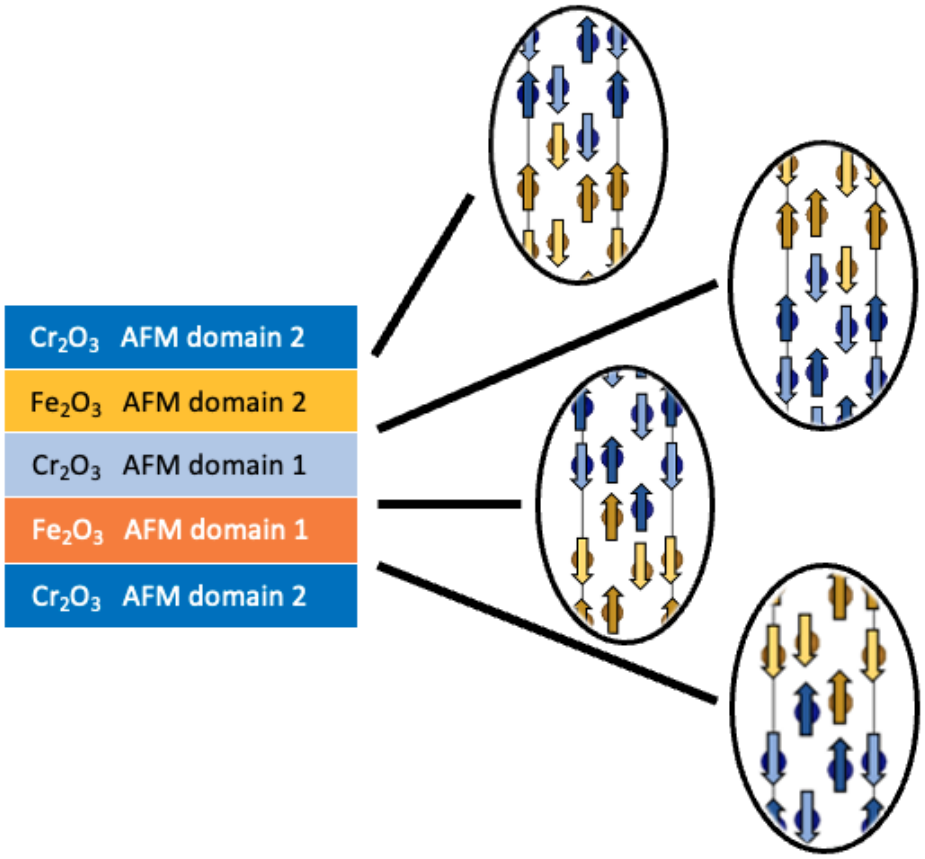

FIGURE 6.14: The ground state for the mixed-metal interface supercell, showing alternating antiferromagnetic (AFM) domains for Cr_2O_3 and Fe_2O_3. Cr_2O_3 layers are displayed in shades of blue and Fe_2O_3 layers in shades of orange, with the AFM domains as defined in Figure 2.2. Insets show the local magnetic environment at each interface, with the Cr and Fe atoms displayed in blue and gold, respectively. Magnetic moments on Cr are displayed in blue, with the moments pointing down in a lighter shade for contrast. Similarly, magnetic moments on Fe are displayed in gold, with the moments pointing down in a lighter shade for contrast.

and Cr magnetic moments. The magnetization of this layer is less than that of the Fe layers, as the magnitude of the Cr moment is smaller. This 'interfacial magnetization' is the same for two consecutive interfaces, and then switches sign. In the oxygen-separated interface, the transition is abrupt, changing directly from a compensated Cr layer to a ferroically ordered Fe layer. Of course, for both interfaces, each Cr_2O_3 and Fe_2O_3 layer still contains an even number of 'up' and 'down' magnetic moments, so the full stack is always AFM.

6.6.3 Full set of magnetic interactions

Now we simulate the supercells with all the magnetic interactions, so with the DMI, the two-site anisotropy, the quartic SIA, and the dipole-dipole interactions included (Eq. 6.1). Of course, the magnetic simulation will attempt to find the ground state

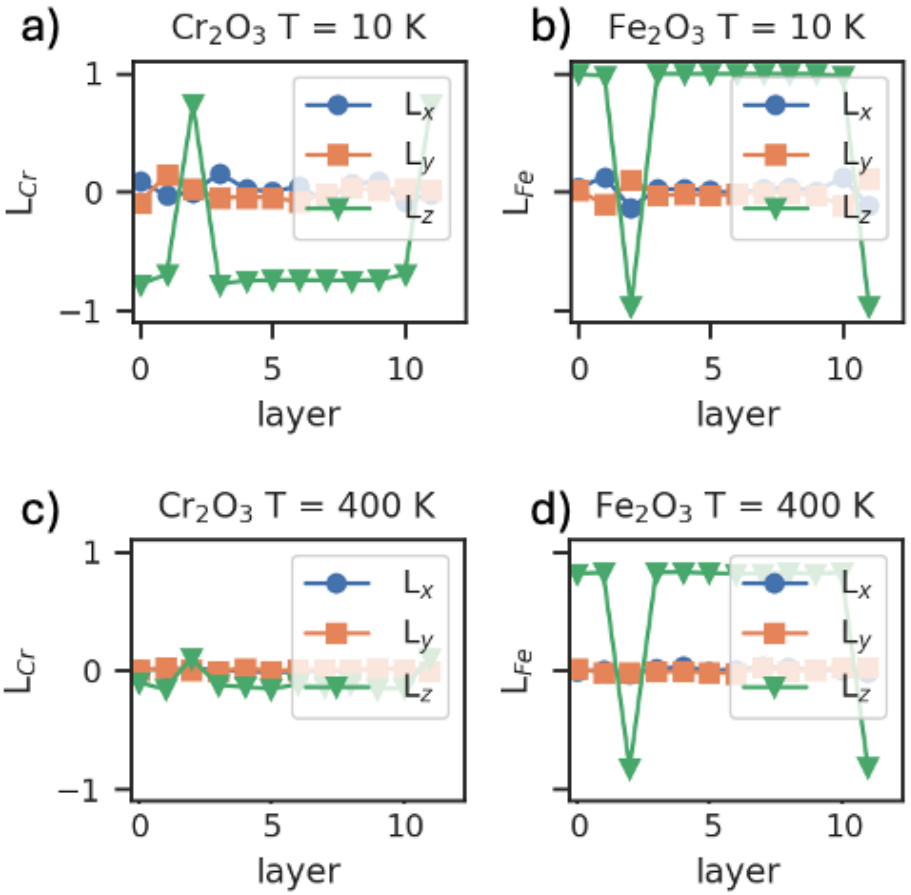

FIGURE 6.15: Néel vector per layer in the oxygen-separated interface, for the Cr_2O_3 layers (a, c) and the Fe_2O_3 layers (b,d) at 10 K (a,b) and 400 K (c,d). The $20 \times 20 \times 12$ unit cell results in twelve layers of each compound. The Néel vectors $\boldsymbol{L}_{Cr}$ and $\boldsymbol{L}_{Fe}$ are as defined in Eqs. 6.3 and 6.4.

corresponding to the Hamiltonian we supplied it with. How accurately this describes our system depends on how well the physics of the real system is captured by this Hamiltonian. In the previous model, it was perhaps expected to find a ground state in which the spins were aligned collinearly, as the only possible driver of canting was competition between the J's. Now, including the DMI, the two-site anisotropy, and the dipole-dipole interactions, there is a possibility of finding more complex magnetic behavior, and probably giving a more accurate description of the real interfacial system. We plot the Néel vector per layer at 10 K and 400 K for simulations cooling down from 1500 K to 10 K for the oxygen-separated interface (Figure 6.15) and the mixed-metal interface (Figure 6.16) using the full Hamiltonian.

We see that in both cases, we no longer find the ground states we had in the simple Hamiltonian model. In both cases, the Fe_2O_3 layers order first and maintain that order even when the Cr_2O_3 starts to order, rather than adjust. However, we still find a state that has a collinear AFM ordering in both cases.

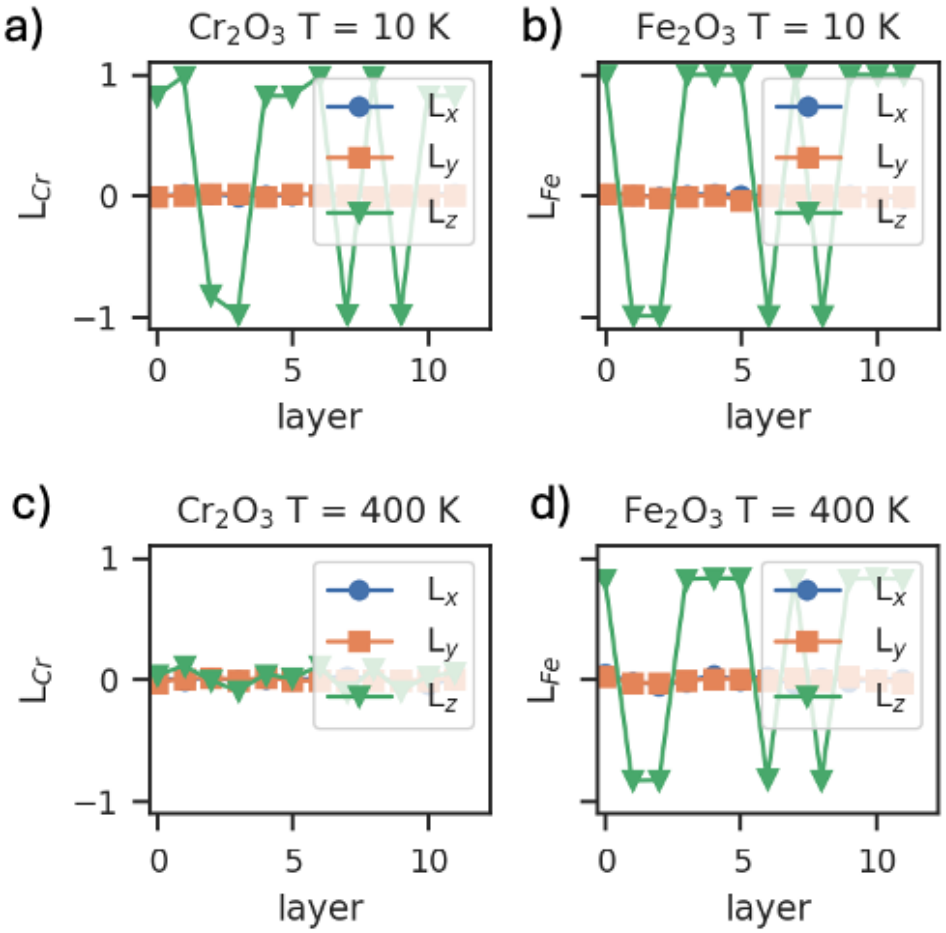

FIGURE 6.16: Néel vector per layer in the mixed-metal interface, for the Cr_2O_3 layers (a, c) and the Fe_2O_3 layers (b,d) at 10 K (a,b) and at 400 K (c,d). The $20 \times 20 \times 12$ unit cell results in twelve layers of each compound. The Néel vectors $\boldsymbol{L}_{Cr}$ and $\boldsymbol{L}_{Fe}$ are as defined in Eqs. 6.3 and 6.4.

The question is whether the states we find at 10 K are truly the ground states, or whether the simulations get stuck in a local minimum. We test this by looking at the energy of the previous ground states we found in the model using just J and K. We start with the mixed-metal interface, for which we found a ground state with a switching AFM domain pattern in the model with just J and K. We find that switching AFM domain arrangement still has a low energy, lower than the state we found by cooling the system with the full Hamiltonian (Figure 6.16). Furthermore, when we start from the switching AFM domain pattern arrangement, the system remains in that state when we heat it, until the Cr_2O_3 and Fe_2O_3 layers disorder when the respective Néel temperatures are reached. We see very similar behavior for the oxygen-separated interface, where the single AFM domain of each ground state is also lower in energy than the state we found by cooling (Figure 6.15). This suggests that including the DMI, the two-site anisotropy, and the dipole-dipole interactions, does not change the ground state, but the system is more likely to get stuck in a local minimum. We point out that this could be

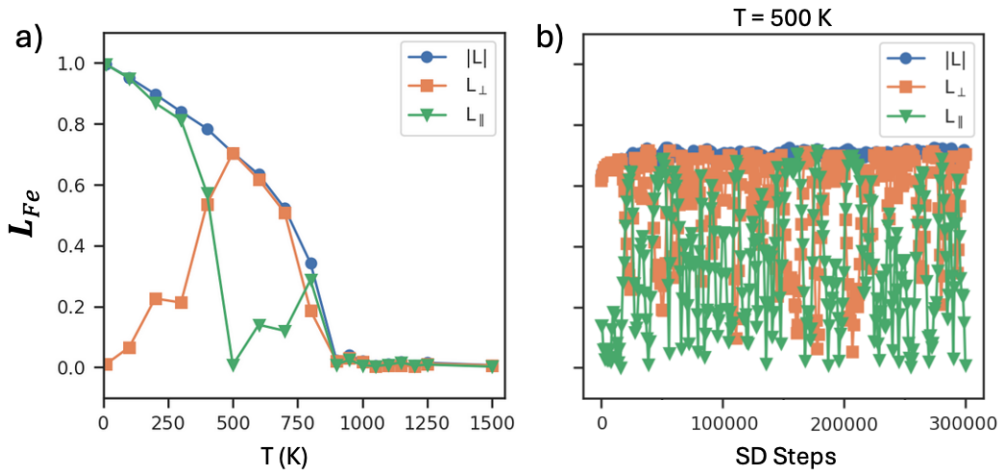

FIGURE 6.17: Temperature dependence (a) and convergence at 500 K (b) of the Néel vector for simulations of Fe_2O_3 in a slab geometry with $65 \times 65 \times 1$ conventional unit cells of Fe_2O_3 (50700 spins).

representative of the real system, and we may see something similar in experiment; the Fe_2O_3 layers would also order first, and may not be able to overcome the energy barrier to change the AFM domain state when the Cr_2O_3 layers start to order.

Finally, we mention that we do not see a strong signature of the Morin transition in the simulations of the heterostructure. Like the lowering of the Néel temperature, this is a consequence of the slab geometry. Compared to the bulk, the Morin transition temperature is raised for simulations of Fe_2O_3 in a slab, (Figure 6.17a). This has also been observed in experiments: in thin films the Morin temperature is enhanced [234, 235]. We furthermore see that the slab geometry raises issues with convergence. As mentioned previously, and as will be discussed in detail in Section 6.7, we need a large amount of spins to reach proper convergence. This is an issue in the heterostructure because our Fe_2O_3 layers are separated, lowering the effective amount of spins. Although the magnitude of the Néel vector is well converged, its direction varies. As we capture the Morin transition through the reorientation of the Néel vector, this convergence issue impacts our ability to simulate that transition.

This suggest that we need much larger unit cells, and possibly more convergence steps to properly capture the Morin transition and its effect on the magnetism of the heterostructure. Furthermore, it shows that there is fine balance between the different magnetic parameters, and finding the global minimum is not straightforward.

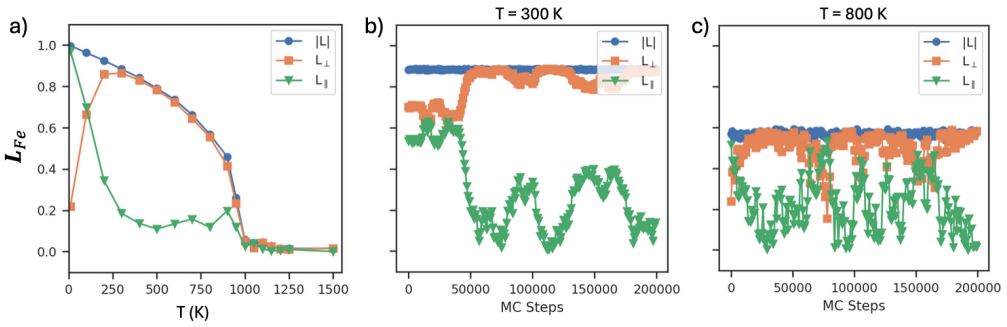

FIGURE 6.18: Temperature dependence (a) and convergence at 300 K (b) and 800 K (c) of the Néel vector for a Monte Carlo (MC) simulation of Fe_2O_3 with 16384 spins, and 200000 MC steps per temperature.

6.7 Convergence

In this section, we discuss some of the convergence parameters, such as the number of simulation steps and the number of simulated spins. We also compare the differences and similarities between MC and SD simulations.

We will compare different calculations of bulk Fe_2O_3, all with the same, full interaction Hamiltonian of Eq. 6.1.

We start by looking at the convergence of a MC simulation of approximately 16000 spins, cooling down from 1500 K to 10 K, with 200000 steps at each temperature (Figure 6.18). We see that the proper ground state is found; at 10 K the length of the Néel vector is 1 and it is oriented parallel to z. We also find an appropriate Néel temperature. However, if we look at the Néel vector as a function of the number of MC steps at a specific temperature, we see that there are issues with the convergence of the direction of the Néel vector (Figure 6.18a,b). The length $|\boldsymbol{L}|$ is well converged, but the direction seems to change during the 200000 MC steps, without looking like it is converging to a steady value, suggesting that adding more MC steps does not resolve the problem. This effect seems to be more prominent at higher temperatures (until the Néel temperature is reached, and all component of $\boldsymbol{L}$ are zero).

Performing the same calculations with SD, now with 200000 timesteps at each temperature (and the timestep set to the standard value of 10_{-16}s), we see very similar behavior to the MC simulation of the same system (Figure 6.19). The correct ground state is found at 10 K, but the orientation of the Néel vector does not converge well at higher temperatures. We point out that the Néel temperature is slightly larger than in the MC simulation. We observe the same comparing simulations of Cr_2O_3; with exactly the same Hamiltonian, the MC simulation always gives a slightly lower ordering temperature than the SD simulation. The origin of the discrepancy is unclear.

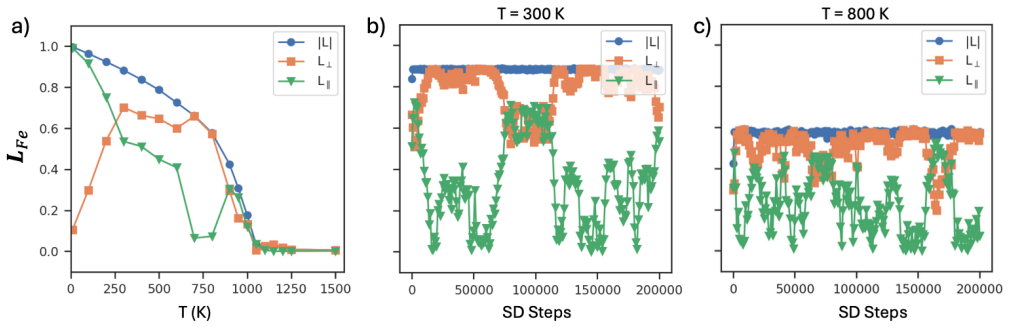

FIGURE 6.19: Temperature dependence (a) and convergence at 300 K (b) and 800 K (c) of the Néel vector for a spin dynamics (SD) simulation of Fe_2O_3 with 16384 spins, and 200000 SD timesteps per temperature.

The issue with converging the orientation of the Néel vector stems from the fine balance between the different magnetic interaction parameters. We could potentially resolve it by artificially enlarging the SIA. This works well for Cr_2O_3, which is a collinear easy-axis AFM below its Néel temperature, but it completely suppresses the Morin transition in Fe_2O_3. We can resolve the issue with the convergence instead by including more spins in the simulation, i.e., by choosing a larger unit cell. We show the results of an SD simulation with approximately 100000 spins in Figure 6.20. Here the convergence is much better, and we can distinguish the Morin transition clearly. We also see that using 500000 timesteps is not necessary, as very little changes after the first 100000 steps. To be sure, we used 300000 steps in the calculation shown previously.

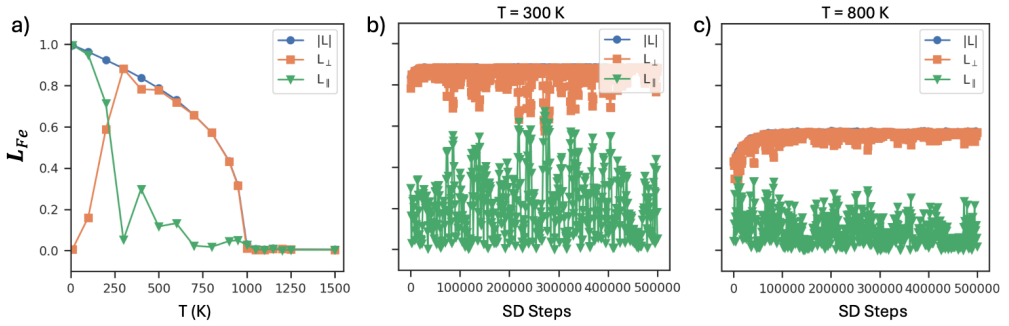

FIGURE 6.20: Temperature dependence (a) and convergence at 300 K (b) and 800 K (c) of the Néel vector for spin dynamics (SD) simulation of Fe_2O_3 with 108000 spins, and 500000 SD timesteps per temperature.

6.8 Conclusion

We explore the interface between Cr_2O_3 and Fe_2O_3, which shows a discontinuity, changing between two types of AFM order. We extract magnetic interaction parameters from DFT, obtaining reasonable parameters for the symmetric exchanges J, and the quadratic single-ion anisotropy K. With our method, we are unable to extract the DMI and the

two-site anisotropy, and base them instead on previous computational work from Ref. [226]. We test the role of the different magnetic interactions in the bulk materials and find the Cr_2O_3 behavior to be dominated by the symmetric exchanges J and the single-ion anisotropy K. In Fe_2O_3, J and K are sufficient to capture the Néel temperature and the ground state correctly, but the DMI, two-site anisotropy, and the dipole-dipole interactions are necessary to describe the reorientation of the Néel vector that occurs with the Morin transition. We also test including different numbers of nearest neighbors, and conclude that up to the 5^{th} shell (14 neighbors in total per atom) is sufficient for the full exchange (J, $\boldsymbol{D}$ and A), but the dipole-dipole interactions need to be included up to the 13^{th} shell (53 neighbors in total per atom). We compare the dipole-dipole interactions in Cr_2O_3 and Fe_2O_3 and show that they contribute more significantly in Fe_2O_3, which we attribute mostly to the difference in the AFM ordering in the two compounds. The remaining difference can be explained by the unit cell volume and size of the magnetic moments, which are also distinct. We model the magnetism of the (001) interface and consider two atomically sharp interface types: oxygen-separated and mixed-metal. We compare two models for the magnetism of the interfaces, one with only J and K, and one with the full set of magnetic interactions. For the first model, we find a ground state for the oxygen-separated interface which consists of a combination of one AFM domain of each material. Instead, the mixed-metal interface shows switching AFM domains for both compounds. We confirm that these are the ground states with a combination of DFT calculations and analytical analysis. Additionally, even though the Fe_2O_3 layers order first, they readjust their ordering once the Cr_2O_3 layer order as well. In the second model, the fine balance between the different magnetic interactions makes it more difficult to find the ground state in for both interface types. Here the Fe_2O_3 layers order first, and then the system is stuck with that ordering, i.e., the ordering of the Cr_2O_3 layers is unable to adjust the Fe_2O_3 ordering. We find that the ground states are likely the same as in the model with just J and K, but that the system cannot reach these ground states as easily. We note that the inability to find the ground state may be representative of the real system; it can be difficult to switch the Fe_2O_3 domains so far below its Néel temperature. Regardless of the model, we find distinct ground states for the oxygen-separated and mixed-metal interfaces. Finally, we see that the layer geometry changes the behavior of Fe_2O_3. In the thin layers, the Néel temperature is suppressed and the Morin temperature enhanced, such that thin layers mostly the low-temperature collinear AFM ordering. Furthermore, the simulation struggles to converge the orientation of the Néel vector, which may be resolved by simulating more spins, or choosing a different unit cell geometry, e.g., thicker layers.

6.9 Outlook

This work can be extended in several ways, for example by studying different interface planes or more rough interfaces. In principle, there are many possibilities to simulate. Take for example the interface environment of the (001) interface. First of all, it is known that the electrostatically favorable surface termination for the corundum structure is the one with a dangling metal ion at the top, i.e., the one that would result in the mixed-metal interface when a different material is grown on top. However, Fe_2O_3 may show an oxygen layer at the top, when grown under sufficient oxygen pressure [222]. The top layer can host vacancies as well, and the (001) surface of Cr_2O_3 shows several surface reconstructions at different temperatures [236]. Furthermore, thin film growth, using methods like pulsed laser deposition or molecular beam epitaxy, occurs at very high temperatures, and metal ions may diffuse into the layer of the other compound. Taking all these factors together, it is unlikely that the (001) Cr_2O_3/Fe_2O_3 interface would be atomically sharp, as we simulated here. Other than chemical disorder, there is the additional option of dislocations due to the strain, as in known to occur for Cr_2O_3 and Fe_2O_3 grown on Al_2O_3 [237, 238]. It would be useful to have experimental results, for example from transmission electron microscopy, to confirm what such an interface would look like, or at least reduce the number of possibilities.

Besides changing the interface plane and roughness, we can explore various unit cell geometries. For example, we may consider the role of the layer thickness, study the effect of a single interface, rather than supercells, or examine supercells with both interface types. The dependence of the ground state on the chemistry of the interface is intriguing, and it would be interesting to see if this persists when there is a single interface. Moreover, we could use the chemistry of the interface as a pathway to control the domain state of one compound, by controlling the domain state of the other. For example, the oxygen-separated interface prefers a combination of a single domain of each compound. As we saw in Chapter 4, we can use ME annealing to control the domain state of Cr_2O_3. Controlling the Fe_2O_3 order this way, does require that the Fe_2O_3 layers are able to reorder when the Cr_2O_3 layers order. If the coupling across the interface is sufficiently strong, in a thin layer of Fe_2O_3 on top of a think layer of Cr_2O_3 or bulk Cr_2O_3, the Fe moments may be able to overcome the reordering barrier. Furthermore, we could purposefully create an excited magnetic state, for example by enforcing all the Cr_2O_3 layers in the mixed-metal supercell to have the same AFM domain, using ME annealing.

Another possibility, which would be strengthened by collaboration with experiment, would be to model dynamics, rather than equilibrium states. For example, the propagation of spin waves has recently attracted attention in Fe_2O_3 [6, 53], and it would be interesting to observe such propagation across Cr_2O_3/Fe_2O_3 interfaces.

Finally, there is the somewhat intriguing question of the inversion symmetry across the slab. In bulk, the inversion symmetry in Cr_2O_3 is broken, while the inversion symmetry in Fe_2O_3 is preserved. The presence of a single interface breaks the inversion symmetry by definition, although this does not have to be the case for multiple interfaces. Yet, both the oxygen-separated and mixed-metal ground states break inversion symmetry. It would be interesting to explore the effects of this symmetry breaking on the multipoles, ME effects, and spin-splitting.

Chapter 7

Conclusion and Outlook

During my PhD, I have studied the interplay of symmetry, magnetic multipoles, magnetoelectric (ME) effects, and magnetic ordering in the corundum structure transition metal oxides Cr_2O_3 and Fe_2O_3, as well as heterostructures of the two materials. Despite sharing a crystal structure and both being insulating antiferromagnets, the magnetic ordering in Cr_2O_3 breaks the inversion symmetry, while the magnetic ordering of Fe_2O_3 preserves it. The similarities of their local symmetries mean that the same magnetic multipoles are allowed on the atomic sites in both compounds. Still, the difference in global symmetry gives rise to different ordering of these local magnetic multipoles, resulting in distinct properties. Another consequence of the difference in magnetic ordering is a discontinuity at Cr_2O_3/Fe_2O_3 interfaces. To deepen the understanding of the magnetic multipoles and the effects they give rise to, I used a combination of symmetry analysis and density functional theory (DFT). These methods gave me access to the signs and magnitude of the multipoles, the local ME effects, and the non-relativistic spin splitting, allowing me to address vital questions regarding their relationship. Furthermore, I used a combination of DFT and spin dynamics techniques to address the problem of the magnetic ordering of the Cr_2O_3/Fe_2O_3 interface, allowing the simulation of temperature-dependent magnetism in large unit cells.

In this thesis, I presented my research divided into four topics: Magnetic multipoles and local ME effects in Cr_2O_3 and Fe_2O_3, the sign of the linear ME effect in Cr_2O_3, non-relativistic spin splitting (NRSS) and magnetic triakontadipoles in Fe_2O_3, and the magnetism of Cr_2O_3/Fe_2O_3 heterostructures, each of which I summarize here:
In Chapter 3, I established a relation between the local magnetic quadrupolar order and the local atomic linear ME response, discussing both Cr_2O_3 and Fe_2O_3 as examples. Using a combination of symmetry and multipole analysis, we predicted an off-diagonal linear anti-ME in Cr_2O_3, beyond the well-established diagonal linear ME effect. In

Fe_2O_3, we predicted both diagonal and off-diagonal linear anti-ME effects. We confirmed our predictions using *ab initio* calculations of the induced moments. In both materials, we additionally found non-negligible local second-order ME responses, which we rationalized with the presence of magnetic octupoles. In Fe_2O_3, the local second-order ME responses sum up to net response along some directions, revealing Fe_2O_3 to be a net second-order ME material. Thus, we showed the strong connection between the different (local) ME effects and the underlying ordering of magnetic quadrupoles and octupoles. In particular, we identified an antiferroic order of magnetic quadrupoles that constitutes a new type of hidden order, adding another example to the growing list of hidden orders in condensed matter physics and highlighting their importance in determining material responses. Furthermore, the concept of ME response in ordered materials can be broadened using our results; a local ME response does not require global symmetry breaking, so even in materials that preserve both time reversal (with a fractional translation) and inversion a non-zero local ME tensor is allowed.

I subsequently discussed the relation between the sign of the net linear ME effect and the antiferromagnetic (AFM) domains of Cr_2O_3 in Chapter 4. This relationship was well established, but which sign belonged with which domain had been a point of contention in the literature, which we resolved by combining a literature review, new *ab initio* results, and a careful reanalysis of spherical neutron polarimetry data. The discussion regarding this domain-dependent sign of the ME coefficient α, was complicated by the temperature dependence of the two independent components of α, $\alpha_\perp$ and $\alpha_\parallel$, and ambiguous terminology related to the usage of spin and magnetic moment. We showed that all *ab initio* results, those from the literature and our own, consistently assigned the same sign of the low-temperature α to the same domain across multiple codes and methods. Furthermore, we established that the room-temperature spherical neutron polarimetry *data* are consistent with the low-temperature *ab initio* findings given that the room-temperature sign of $\alpha_\parallel$ is opposite to its low-temperature sign. Thus, this work demonstrates the previously questioned agreement between computational and experimental findings regarding the sign of the ME coefficient in the two AFM domains of Cr_2O_3, and highlights the importance of treating signs and nomenclature carefully.

Next, in Chapter 5 we demonstrated the connection between the ferroic ordering of magnetic multipoles and the non-relativistic spin splitting (NRSS) in Fe_2O_3. First, we identified ferroically ordered rank-5 magnetic triakontadipoles in the low-temperature AFM phase of Fe_2O_3 and showed they are present even in the absence of spin-orbit coupling, where they are the lowest-order time-reversal symmetry breaking multipole. This ferroic ordering of the magnetic triakontadipoles is the likely cause for the NRSS in Fe_2O_3, which has the same g-wave symmetry as the magnetic triakontadipoles. We established this relation by varying the sign, ordering, and magnitude of these magnetic triakontadipoles, showing that the spin splitting alters as a consequence. We further

demonstrated that the ferroic ordering of the magnetic triakontadipoles persists in the weakly ferromagnetic (FM) phase above the Morin transition. Here the spin splitting is dominated by the magnetic triakontadipole contribution compared to the magnetic dipoles, which also have a ferroically ordered component in this phase.
Finally, I examined the magnetism of Cr_2O_3/Fe_2O_3 heterostructures in Chapter 6, focusing on two atomically sharp arrangements of the (001) interface, which we called oxygen-separated and mixed-metal. We showed that with Heisenberg exchanges and the single ion anisotropy extracted from DFT, we capture the Néel temperatures and magnetic ground states of both compounds correctly, but need to include the Dzyaloshinskii-Moriya interaction, two-site anisotropy, and dipole-dipole interaction to described the Morin transition and the high-temperature weakly FM phase of Fe_2O_3. Specifically, we find the dipole-dipole interactions to give a much larger contribution to the effective anisotropy in Fe_2O_3, than Cr_2O_3, which we attribute to the different AFM ordering, atomic positions and size of the magnetic moment. For the heterostructure, we compared two magnetic models, one with only the Heisenberg exchanges and the single ion anisotropy, and one with the Dzyaloshinskii-Moriya interaction, two-site anisotropy, and dipole-dipole interaction included as well. For both models, we find different magnetic ground states for the two interface types: the oxygen-separated interface shows a combination of one domain of each compound, while the mixed interface has layers with switching AFM domains. In the simple model, the Fe_2O_3 layers, which order at higher temperatures, adjust their ordering when the Cr_2O_3 layers order. The additional interactions in the complex model make the Fe_2O_3 ordering more robust, and this readjustment does not take place, such that the system adopts a low-temperature state which is not the ground state.

Throughout this thesis, I have mentioned several prospects for future research, some of which I highlight here. For the magnetic multipoles and the local ME effect, it would be illuminating to resolve questions regarding the sign of the multipoles in different materials, and the corresponding signs of the ME effects. Furthermore, research into possible observables resulting from local ME effects would guide experimental observation.
Regarding the sign of the ME coefficient in Cr_2O_3, this may guide further exploration of the surface magnetism of Cr_2O_3, as well as inspire similar studies on other ME materials.
In the context of the magnetic triakontadipoles and the non-relativistic spin splitting, finding the representation of the rank-4 and rank-3 triakontadipole components would allow the comparison of the k-space representations and further our understanding of the nodal points. Also, our present understanding of the relation between d-wave and g-wave spin splitting with magnetic multipoles of rank 3 and rank 5, implies that rank-7 magnetic multipole will be responsible for the i-wave spin splitting, which requires future investigation. Finally, the heterostructures could be explored further with many

different geometries, varying the interfacial planes and roughness, the thickness of the Cr_2O_3 and Fe_2O_3 layers, and the number of interfaces. Together with experiment, future research has the potential to resolve the questions on the common interfacial geometries, the band offset, and the likelihood of the Fe_2O_3 layer reordering.

Appendix A

Overview of acronyms used in this thesis

Acronym	Meaning
AFM	Antiferromagnetic
APW	Augmented plane wave
BZ	Brillouin Zone
Cr	Chromium
DFT	Density functional theory
DMI	Dzyaloshinskii-Moriya interaction
DOS	Density of states
Fe	Iron
FM	Ferromagnetic
GGA	Generalized gradient approximations
LDA	Local density approximation
LSDA	Local spin density approximation
NRSS	Non-relativistic spin splitting
MC	Monte Carlo
ME	Magnetoelectric
O	Oxygen
PBE	Perdew-Burke-Ernzerhof
PAW	Projector-augmented wave
SCF	Self-consistent field
SD	Spin dynamics
SIA	Single-ion anisotropy
SNP	Spherical neutron polarimetry
SOC	Spin-orbit coupling
TM	Transition metal
VASP	Vienna *ab initio* simulation package
XC	Exchange-correlation

Appendix B

List of publications

1. X. H. Verbeek, A. Urru, and N. A. Spaldin. "Hidden orders and (anti-)magnetoelectric effects in Cr_2O_3 and α-Fe_2O_3". *Phys. Rev. Res.* 5 (2023), p. L042018. DOI: 10.1103/PhysRevResearch.5.L042018. URL: https://link.aps.org/doi/10.1103/PhysRevResearch.5.L042018 (Chapter 3)

2. E. Bousquet, E. Lelièvre-Berna, N. Qureshi, J.-R. Soh, N. A. Spaldin, A. Urru, X. H. Verbeek, and S. F. Weber. "On the sign of the linear magnetoelectric coefficient in Cr_2O_3*". *J. Phys.: Condens. Matter* 36.15 (2024), p. 155701. DOI: 10.1088/1361-648X/ad1a59 * Authors in alphabetical order (Chapter 4)

3. X. H. Verbeek, D. Voderholzer, S. Schären, Y. Gachnang, N. A. Spaldin, and S. Bhowal. "Non-relativistic ferromagnetotriakontadipolar order and spin splitting in hematite" (2024). https://arxiv.org/abs/2405.10675 (Chapter 5)

4. X. H. Verbeek, M. Si, and N. A. Spaldin. *In preparation* (Chapter 6)

Appendix C

Curriculum Vitae

Education			
2019-2024	Doctorate in Materials Science	ETH Zürich	Switzerland
2016-2019	Master of Science in Physics and Astronomy	University of Amsterdam	The Netherlands
2013-2016	Bachelor of Science in Physics and Astronomy	University of Amsterdam	The Netherlands

Talks		
2023	Materials Research Society Fall Meeting	Boston, Massachusetts, USA
2023	Swiss & Austrian Physics Societies Meeting	Basel, Switzerland
2020	Joint European Magnetic Symposia (JEMS)	*online*
2020	Magnetism and Magnetic Materials (MMM)	*online*

Bibliography

[1] A. I. Liechtenstein, V. I. Anisimov, and J. Zaanen. "Density-functional theory and strong interactions: Orbital ordering in Mott-Hubbard insulators". *Phys. Rev. B* 52.8 (1995), R5467. DOI: 10.1103/PhysRevB.52.R5467.

[2] S. Emin, M. de Respinis, T. Mavrič, B. Dam, M. Valant, and W. A. Smith. "Photoelectrochemical water splitting with porous α-Fe_2O_3 thin films prepared from Fe/Fe-oxide nanoparticles". *Appl. Catal. A: General* 523 (2016), pp. 130–138. DOI: 10.1016/j.apcata.2016.06.007.

[3] T. C. Kaspar, D. K. Schreiber, S. R. Spurgeon, M. E. McBriarty, G. M. Carroll, D. R. Gamelin, and S. A. Chambers. "Built-in potential in Fe_2O_3-Cr_2O_3 superlattices for improved photoexcited carrier separation". *Adv. Mater.* 28.8 (2016), pp. 1616–1622. DOI: 10.1002/adma.201504545.

[4] M. Isacfranklin, F. Ameen, G. Ravi, R. Yuvakkumar, S. I. Hong, D. Velauthapillai, M. Thambidurai, and C. Dang. "Single-phase Cr_2O_3 nanoparticles for biomedical applications". *Ceram. Int.* 46.12 (2020), pp. 19890–19895. DOI: 10.1016/j.ceramint.2020.05.050.

[5] J. Li, C. B. Wilson, R. Cheng, M. Lohmann, M. Kavand, W. Yuan, M. Aldosary, N. Agladze, P. Wei, M. S. Sherwin, and J. Shi. "Spin current from sub-terahertz-generated antiferromagnetic magnons". *Nature* 578.7793 (2020), pp. 70–74. DOI: 10.1038/s41586-020-1950-4.

[6] A. E. Kanj, O. Gomonay, I. Boventer, P. Bortolotti, V. Cros, A. Anane, and R. Lebrun. "Antiferromagnetic magnon spintronic based on nonreciprocal and nondegenerated ultra-fast spin-waves in the canted antiferromagnet α-Fe_2O_3". *Sci. Adv.* 9.32 (2023), eadh1601. DOI: 10.1126/sciadv.adh1601.

[7] J. A. Crawford and R. W. Vest. "Electrical conductivity of single-crystal Cr_2O_3". *J. Appl. Phys.* 35.8 (1964), pp. 2413–2418. DOI: 10.1063/1.1702871.

[8] C.-S. Cheng, H. Gomi, and H. Sakata. "Electrical and optical properties of Cr_2O_3 films prepared by chemical vapour deposition". *Phys. Status Solidi (a)* 155.2 (1996), pp. 417–425. DOI: 10.1002/pssa.2211550215.

[9] M. M. Abdullah, F. M. Rajab, and S. M. Al-Abbas. "Structural and optical characterization of Cr_2O_3 nanostructures: Evaluation of its dielectric properties". *AIP Adv.* 4.2 (2014), p. 027121. DOI: 10.1063/1.4867012.

[10] S. Mochizuki. "Electrical conductivity of α-Fe_2O_3". *Phys. Status Solidi (a)* 41.2 (1977), pp. 591–594. DOI: 10.1002/pssa.2210410232.

[11] B. Gilbert, C. Frandsen, E. R. Maxey, and D. M. Sherman. "Band-gap measurements of bulk and nanoscale hematite by soft x-ray spectroscopy". *Phys. Rev. B* 79.3 (2009), p. 035108. DOI: 10.1103/PhysRevB.79.035108.

[12] Y.-Y. Li. "Superexchange interactions and magnetic lattices of the rhombohedral sesquioxides of the transition elements and their solid solutions". *Phys. Rev.* 102.4 (1956), pp. 1015–1020. DOI: 10.1103/PhysRev.102.1015.

[13] I. E. Dzyaloshinskii. "On the magneto-electrical effect in antiferromagnet". *Zh. Eksp. Teor. Fiz* 37.3 (1959), pp. 881–882. [*Sov. Phys. JETP* 10.3 (1960), pp. 628-629].

[14] D. N. Astrov. "Magnetoelectric effect in chromium oxide". *Zh. Eksp. Teor. Fiz.* 40.4 (1961), pp. 1035–1041. [*Sov. Phys. JETP* 13.4 (1961), pp. 729-733].

[15] N. A. Spaldin, E. Bousquet, A. Balatsky, and L. Nordström. "Monopole-based formalism for the diagonal magnetoelectric response". *Phys. Rev. B* 88.9 (2013), p. 094429. DOI: 10.1103/PhysRevB.88.094429.

[16] L. Šmejkal, J. Sinova, and T. Jungwirth. "Beyond conventional ferromagnetism and antiferromagnetism: A phase with nonrelativistic spin and crystal rotation symmetry". *Phys. Rev. X* 12.3 (2022), p. 031042. DOI: 10.1103/PhysRevX.12.031042.

[17] L. Šmejkal, J. Sinova, and T. Jungwirth. "Emerging research landscape of altermagnetism". *Phys. Rev. X* 12 (2022), p. 040501. DOI: 10.1103/PhysRevX.12.040501.

[18] J. Chakhalian. *Strong correlations at oxide interfaces: What is hidden in a plane view?* 2024. DOI: 10.48550/arXiv.2403.00015.

[19] X. H. Verbeek, A. Urru, and N. A. Spaldin. "Hidden orders and (anti-)magnetoelectric effects in Cr_2O_3 and α-Fe_2O_3". *Phys. Rev. Res.* 5 (2023), p. L042018. DOI: 10.1103/PhysRevResearch.5.L042018.

[20] E. Bousquet, E. Lelièvre-Berna, N. Qureshi, J.-R. Soh, N. A. Spaldin, A. Urru, X. H. Verbeek, and S. F. Weber. "On the sign of the linear magnetoelectric coefficient in Cr_2O_3*". *J. Phys.: Condens. Matter* 36.15 (2024), p. 155701. DOI: 10.1088/1361-648X/ad1a59.

[21] W. C. Röntgen. "Ueber die durch Bewegung eines im homogenen electrischen Felde befindlichen Dielectricums hervorgerufene electrodynamische Kraft". *Ann. Phys.* 271.10 (1888), pp. 264–270. DOI: 10.1002/andp.18882711003.

[22] P. Curie. "Sur la symétrie dans les phénomènes physiques, symétrie d'un champ électrique et d'un champ magnétique". *J. Phys. Theor. Appl.* 3.1 (1894), pp. 393–415. DOI: 10.1051/jphystap:018940030039300.

[23] P. Debye. "Bemerkung zu einigen neuen Versuchen über einen magneto-elektrischen Richteffekt". *Z. Physik* 36.4 (1926), pp. 300–301. DOI: 10.1007/BF01557844.

[24] Y. Shiratsuchi, T. V. A. Nguyen, and R. Nakatani. "Magnetoelectric control of antiferromagnetic domain of Cr_2O_3 thin film toward spintronic application". *J. Magn. Soc. Jpn.* 42.6 (2018), pp. 119–126. DOI: 10.3379/msjmag.1811R001.

[25] M. M. Vopson. "Fundamentals of multiferroic materials and their possible applications". *Critical Reviews in Solid State and Materials Sciences* 40.4 (2015), pp. 223–250. DOI: 10.1080/10408436.2014.992584.

[26] W. Eerenstein, N. D. Mathur, and J. F. Scott. "Multiferroic and magnetoelectric materials". *Nature* 442.7104 (2006), pp. 759–765. DOI: 10.1038/nature05023.

[27] M. Bibes and A. Barthélémy. "Towards a magnetoelectric memory". *Nat. Mater.* 7.6 (2008), pp. 425–426. DOI: 10.1038/nmat2189.

[28] D. Halley, N. Najjari, H. Majjad, L. Joly, P. Ohresser, F. Scheurer, C. Ulhaq-Bouillet, S. Berciaud, B. Doudin, and Y. Henry. "Size-induced enhanced magnetoelectric effect and multiferroicity in chromium oxide nanoclusters". *Nat. Commun.* 5.1 (2014), p. 3167. DOI: 10.1038/ncomms4167.

[29] M. Fiebig. "Revival of the magnetoelectric effect". *J. Phys. D: Appl. Phys.* 38.8 (2005), R123–R152. DOI: 10.1088/0022-3727/38/8/R01.

[30] G. A. Gehring. "On the microscopic theory of the magnetoelectric effect". *Ferroelectrics* 161.1 (1994), pp. 275–285. DOI: 10.1080/00150199408213376.

[31] R. Hornreich and S. Shtrikman. "Statistical mechanics and origin of the magnetoelectric effect in Cr_2O_3". *Phys. Rev.* 161.2 (1967), pp. 506–512. DOI: 10.1103/PhysRev.161.506.

[32] P. J. Brown, J. B. Forsyth, and F. Tasset. "A study of magnetoelectric domain formation in Cr_2O_3". *J. Phys.: Condens. Matter* 10.3 (1998), pp. 663–672. DOI: 10.1088/0953-8984/10/3/017.

[33] M. Mostovoy, A. Scaramucci, N. A. Spaldin, and K. T. Delaney. "Temperature-dependent magnetoelectric effect from first principles". *Phys. Rev. Lett.* 105.8 (2010), p. 087202. DOI: 10.1103/PhysRevLett.105.087202.

[34] L. Néel. "Propriétés magnétiques de l'état métallique et énergie d'interaction entre atomes magnétiques". *Ann. Phys.* 11.5 (1936), pp. 232–279. DOI: 10.1051/anphys/193611050232.

[35] J. Mydosh and P. Oppeneer. "Hidden order behaviour in URu_2Si_2 (A critical review of the status of hidden order in 2014)". *Philos. Mag.* 94.32-33 (2014), pp. 3642–3662. DOI: 10.1080/14786435.2014.916428.

[36] E. Herrera, V. Barrena, I. Guillamón, J. A. Galvis, W. J. Herrera, J. Castilla, D. Aoki, J. Flouquet, and H. Suderow. "1D charge density wave in the hidden order state of URu_2Si_2". *Commun. Phys.* 4.1 (2021), pp. 1–6. DOI: 10.1038/s42005-021-00598-0.

[37] M. Kimata, N. Sasabe, K. Kurita, Y. Yamasaki, C. Tabata, Y. Yokoyama, Y. Kotani, M. Ikhlas, T. Tomita, K. Amemiya, H. Nojiri, S. Nakatsuji, T. Koretsune, H. Nakao, T. Arima, and T. Nakamura. "X-ray study of ferroic octupole order producing anomalous Hall effect". *Nat. Commun.* 12.1 (2021), p. 5582. DOI: 10.1038/s41467-021-25834-7.

[38] I. B. Zel'dovich. "Electromagnetic interaction with parity violation". *Zh. Eksp. Teor. Fiz* 33 (1957), pp. 1531–1533. [*Sov. Phys. JETP* 6 (1958), pp. 1184-1186].

[39] A. A. Gorbatsevich, Y. V. Kopaev, and V. V. Tugushev. "Anomalous nonlinear effects at phase transitions to ferroelectric and magnetoelectric states". *Zh. Eksp. Teor. Fiz.* 85 (1983), pp. 1107–1121. [*Sov. Phys. JETP* 58 (1983), pp. 643-651].

[40] P. F. de Chatel and A. K. Buin. "Toroid dipole moments and hybridization in uranium compounds". *Physica B* 319 (2002), pp. 193–198. DOI: 10.1016/S0921-4526(02)01120-1.

[41] C. Ederer and N. A. Spaldin. "Towards a microscopic theory of toroidal moments in bulk periodic crystals". *Phys. Rev. B* 76.21 (2007), p. 214404. DOI: 10.1103/PhysRevB.76.214404.

[42] J. J. Sakurai and J. Napolitano. *Modern quantum mechanics*. Third edition. Cambridge: Cambridge University Press, 2020. ISBN: 978-1-108-64592-8.

[43] N. A. Spaldin, M. Fiebig, and M. Mostovoy. "The toroidal moment in condensed-matter physics and its relation to the magnetoelectric effect". *J. Phys.: Condens. Matter* 20.43 (2008), p. 434203. DOI: 10.1088/0953-8984/20/43/434203.

[44] F. Thöle, A. Keliri, and N. A. Spaldin. "Concepts from the linear magnetoelectric effect that might be useful for antiferromagnetic spintronics". *J. Appl. Phys.* 127.21 (2020), p. 213905. DOI: 10.1063/5.0006071.

[45] A. Urru and N. A. Spaldin. "Magnetic octupole tensor decomposition and second-order magnetoelectric effect". *Ann. Phys.* 447 (2022), p. 168964. DOI: 10.1016/j.aop.2022.168964.

[46] B. B. Van Aken, J.-P. Rivera, H. Schmid, and M. Fiebig. "Observation of ferrotoroidic domains". *Nature* 449.7163 (2007), pp. 702–705. DOI: 10.1038/nature06139.

[47] Z. Latacz. "Magnetoelectric effect of Cr_2O_3". *Acta Phys. Pol. A* 97.5 (2000), pp. 733–735. DOI: 10.12693/APhysPolA.97.733.

[48] C. Liu, Y. Luo, D. Hong, S. S.-L. Zhang, H. Saglam, Y. Li, Y. Lin, B. Fisher, J. E. Pearson, J. S. Jiang, H. Zhou, J. Wen, A. Hoffmann, and A. Bhattacharya. "Electric field control of magnon spin currents in an antiferromagnetic insulator". *Sci. Adv.* 7.40 (2021), eabg1669. DOI: 10.1126/sciadv.abg1669.

[49] S. Mu, A. L. Wysocki, and K. D. Belashchenko. "Effect of substitutional doping on the Néel temperature of Cr_2O_3". *Phys. Rev. B* 87.5 (2013), p. 054435. DOI: 10.1103/PhysRevB.87.054435.

[50] E. J. Samuelsen, M. T. Hutchings, and G. Shirane. "Inelastic neutron scattering investigation of spin waves and magnetic interactions in Cr_2O_3". *Physica* 48.1 (1970), pp. 13–42. DOI: 10.1016/0031-8914(70)90158-8.

[51] P. J. Brown, J. B. Forsyth, E. Lelièvre-Berna, and F. Tasset. "Determination of the magnetization distribution in Cr_2O_3 spherical neutron polarimetry". *J. Phys.: Condens. Matter* 14.8 (2002). DOI: 10.1088/0953-8984/14/8/323.

[52] E. J. Samuelsen and G. Shirane. "Inelastic neutron scattering investigation of spin waves and magnetic interactions in α-Fe_2O_3". *Phys. Status Solidi (b)* 42.1 (1970), pp. 241–256. DOI: 10.1002/pssb.19700420125.

[53] A. Ross, R. Lebrun, O. Gomonay, D. A. Grave, A. Kay, L. Baldrati, S. Becker, A. Qaiumzadeh, C. Ulloa, G. Jakob, F. Kronast, J. Sinova, R. Duine, A. Brataas, A. Rothschild, and M. Kläui. "Propagation length of antiferromagnetic magnons governed by domain configurations". *Nano Lett.* 20.1 (2020), pp. 306–313. DOI: 10.1021/acs.nanolett.9b03837.

[54] R. A. Lunt, A. J. Jackson, and A. Walsh. "Dielectric response of Fe_2O_3 crystals and thin films". *Chem. Phys. Let.* 586 (2013), pp. 67–69. DOI: 10.1016/j.cplett.2013.09.023.

[55] W. Koch and M. C. Holthausen. *A chemist's guide to density functional theory*. Wiley-VCH, 2000. ISBN: 3-527-60004-3.

[56] K. Capelle. "A bird's-eye view of density-functional theory". *Braz. J. Phys.* 36 (2006), pp. 1318–1343. DOI: 10.1590/S0103-97332006000700035.

[57] K. Burke. *The ABC of DFT*. 2007.

[58] R. M. Martin. *Electronic structure: Basic theory and practical methods*. Cambridge: Cambridge University Press, 2004. ISBN: 978-0-521-53440-6. DOI: 10.1017/CBO9780511805769.

[59] R. O. Jones. "Density functional theory: Its origins, rise to prominence, and future". *Rev. Mod. Phys.* 87.3 (2015), pp. 897–923. DOI: 10.1103/RevModPhys.87.897.

[60] A. Pribram-Jones, D. A. Gross, and K. Burke. "DFT: A theory full of holes?" *Annu. Rev. Phys. Chem.* 66 (2015), pp. 283–304. DOI: 10.1146/annurev-physchem-040214-121420.

[61] M. Born and R. Oppenheimer. "Zur Quantentheorie der Molekeln". *Ann. Phys.* 389.20 (1927), pp. 457–484. DOI: 10.1002/andp.19273892002.

[62] P. Hohenberg and W. Kohn. "Inhomogeneous electron gas". *Phys. Rev.* 136.3B (1964), B864–B871. DOI: 10.1103/PhysRev.136.B864.

[63] W. Kohn and L. J. Sham. "Self-consistent equations including exchange and correlation effects". *Phys. Rev.* 140.4A (1965), A1133–A1138. DOI: 10.1103/PhysRev.140.A1133.

[64] J. P. Perdew and A. Zunger. "Self-interaction correction to density-functional approximations for many-electron systems". *Phys. Rev. B* 23.10 (1981), pp. 5048–5079. DOI: 10.1103/PhysRevB.23.5048.

[65] J. P. Perdew, K. Burke, and M. Ernzerhof. "Generalized gradient approximation made simple". *Phys. Rev. Lett.* 77.18 (1996), pp. 3865–3868. DOI: 10.1103/PhysRevLett.77.3865.

[66] J. P. Perdew, A. Ruzsinszky, G. I. Csonka, O. A. Vydrov, G. E. Scuseria, L. A. Constantin, X. Zhou, and K. Burke. "Restoring the density-gradient expansion for exchange in solids and surfaces". *Phys. Rev. Lett.* 100.13 (2008), p. 136406. DOI: 10.1103/PhysRevLett.100.136406.

[67] D. J. Singh and L. Nordström. *Planewaves, pseudopotentials, and the LAPW method*. 2nd ed. Springer New York, 2006. DOI: https://doi.org/10.1007/978-0-387-29684-5.

[68] G. Kresse and J. Furthmüller. "Efficiency of ab-initio total energy calculations for metals and semiconductors using a plane-wave basis set". *Comput. Mater. Sci.* 6 (1996), pp. 15–50. DOI: 10.1016/0927-0256(96)00008-0.

[69] G. Kresse and J. Furthmüller. "Efficient iterative schemes for ab initio total-energy calculations using a plane-wave basis set". *Phys. Rev. B* 54.16 (1996), pp. 11169–11186. DOI: 10.1103/PhysRevB.54.11169.

[70] J. K. Dewhurst *et al. The Elk code : An all-electron full-potential linearised augmented-plane wave (LAPW) code*. https://elk.sourceforge.io/. 2020.

[71] P. E. Blöchl. "Projector augmented-wave method". *Phys. Rev. B* 50.24 (15, 1994), pp. 17953–17979. DOI: 10.1103/PhysRevB.50.17953.

[72] G. Kresse and D. Joubert. "From ultrasoft pseudopotentials to the projector augmented-wave method". *Phys. Rev. B* 59.3 (1999), pp. 1758–1775. DOI: 10.1103/PhysRevB.59.1758.

[73] M. Cococcioni. "Chapter 4 - The LDA+U approach: A simple Hubbard correction for correlated ground states". In: *Correlated electrons: From models to materials*. Ed. by E. Pavarini, E. Koch, F. Anders, and M. Jarrell. Jülich: Forschungszentrum Jülich GmbH, 2012. ISBN: 978-3-89336-796-2.

[74] V. I. Anisimov, J. Zaanen, and O. K. Andersen. "Band theory and Mott insulators: Hubbard U instead of Stoner I". *Phys. Rev. B* 44.3 (1991), pp. 943–954. DOI: 10.1103/PhysRevB.44.943.

[75] J. Hubbard and B. H. Flowers. "Electron correlations in narrow energy bands". *Proc. Math. Phys. Eng. Sci. A* 276.1365 (1963), pp. 238–257. DOI: 10.1098/rspa.1963.0204.

[76] J. Hubbard and B. H. Flowers. "Electron correlations in narrow energy bands. II. The degenerate band case". *Proc. Math. Phys. Eng. Sci. A* 277.1369 (1964), pp. 237–259. DOI: 10.1098/rspa.1964.0019.

[77] J. Hubbard. "Electron correlations in narrow energy bands III. An improved solution". *Proc. Math. Phys. Eng. Sci. A* 281.1386 (1964), pp. 401–419. DOI: 10.1098/rspa.1964.0190.

[78] J. Hubbard and B. H. Flowers. "Electron correlations in narrow energy bands - IV. The atomic representation". *Proc. Math. Phys. Eng. Sci. A* 285.1403 (1965), pp. 542–560. DOI: 10.1098/rspa.1965.0124.

[79] J. Hubbard and B. H. Flowers. "Electron correlations in narrow energy bands V. A perturbation expansion about the atomic limit". *Proc. Math. Phys. Eng. Sci. A* 296.1444 (1967), pp. 82–99. DOI: 10.1098/rspa.1967.0007.

[80] J. Hubbard and B. H. Flowers. "Electron correlations in narrow energy bands VI. The connexion with many-body perturbation theory". *Proc. Math. Phys. Eng. Sci. A* 296.1444 (1967), pp. 100–112. DOI: 10.1098/rspa.1967.0008.

[81] J. Íñiguez. "First-principles approach to lattice-mediated magnetoelectric effects". *Phys. Rev. Lett.* 101.11 (2008), p. 117201. DOI: 10.1103/PhysRevLett.101.117201.

[82] E. Bousquet, N. A. Spaldin, and K. T. Delaney. "Unexpectedly large electronic contribution to linear magnetoelectricity". *Phys. Rev. Lett.* 106.10 (2011), p. 107202. DOI: 10.1103/PhysRevLett.106.107202.

[83] A. Malashevich, S. Coh, I. Souza, and D. Vanderbilt. "Full magnetoelectric response of Cr_2O_3 from first principles". *Phys. Rev. B* 86.9 (2012), p. 094430. DOI: 10.1103/PhysRevB.86.094430.

[84] F. Bultmark, F. Cricchio, O. Grånäs, and L. Nordström. "Multipole decomposition of LDA+U energy and its application to actinide compounds". *Phys. Rev. B* 80.3 (2009), p. 035121. DOI: 10.1103/PhysRevB.80.035121.

[85] F. Cricchio. "Multipoles in correlated electron materials". PhD thesis. Uppsala: Acta Universitatis Upsaliensis, 2010.

[86] O. Grånäs. "Theoretical studies of magnetism and electron correlation in solids". PhD thesis. Acta Universitatis Upsaliensis, 2012.

[87] G. van der Laan. "Angular momentum sum rules for X-Ray absorption". *Phys. Rev. B* 57.1 (1998), pp. 112–115. DOI: 10.1103/PhysRevB.57.112.

[88] O. R. Cruzan. "Translational addition theorems for spherical vector wave functions". *Quart. Appl. Math.* 20.1 (1962), pp. 33–40. DOI: 10.1090/qam/132851.

[89] A. R. Edmonds. *Angular Momentum in Quantum Mechanics*. Princeton University Press, 2016. ISBN: 978-1-4008-8418-6. DOI: 10.1515/9781400884186.

[90] F. Thöle and N. A. Spaldin. "Magnetoelectric multipoles in metals". *Phil. Trans. R. Soc. A* 376.2134 (2018), p. 20170450. DOI: 10.1098/rsta.2017.0450.

[91] M. E. Merkel. *multipyles v1.1.0*. 2023. DOI: 10.5281/zenodo.8199391.

[92] L. Schaufelberger, M. E. Merkel, A. M. Tehrani, N. A. Spaldin, and C. Ederer. "Exploring energy landscapes of charge multipoles using constrained density functional theory". *Phys. Rev. Res.* 5.3 (2023), p. 033172. DOI: 10.1103/PhysRevResearch.5.033172.

[93] W. Kohn. "Density functional and density matrix method scaling linearly with the number of atoms". *Phys. Rev. Lett.* 76.17 (1996), pp. 3168–3171. DOI: 10.1103/PhysRevLett.76.3168.

[94] U. Nowak. "Classical spin models". In: *Handbook of magnetism and advanced magnetic materials*. John Wiley & Sons, Ltd, 2007, pp. 859–876. DOI: 10.1002/9780470022184.hmm205.

[95] O. N. Mryasov, U. Nowak, K. Y. Guslienko, and R. W. Chantrell. "Temperature-dependent magnetic properties of FePt: Effective spin Hamiltonian model". *EPL* 69.5 (2005), p. 805. DOI: 10.1209/epl/i2004-10404-2.

[96] H. J. Xiang, E. J. Kan, S.-H. Wei, M.-H. Whangbo, and X. G. Gong. "Predicting the spin-lattice order of frustrated systems from first principles". *Phys. Rev. B* 84.22 (2011), p. 224429. DOI: 10.1103/PhysRevB.84.224429.

[97] B. Skubic, J. Hellsvik, L. Nordström, and O. Eriksson. "A method for atomistic spin dynamics simulations: implementation and examples". *J. Phys.: Condens. Matter* 20.31 (2008), p. 315203. DOI: 10.1088/0953-8984/20/31/315203.

[98] D. W. H. Kurt Binder. *Monte Carlo simulation in statistical physics:An Introduction*. Berlin: Springer-Verlag, 1997. ISBN: 978-3-540-63265-8.

[99] D. P. Landau and K. Binder. *A guide to Monte Carlo simulations in statistical physics*. 3rd ed. Cambridge University Press, 2009.

[100] L. Landau and E. Lifshitz. "On the theory of the dispersion of magnetic permeability in ferromagnetic bodies". In: *Perspectives in theoretical physics*. Ed. by L. P. Pitaevski. Amsterdam: Pergamon, 1992, pp. 51–65. ISBN: 978-0-08-036364-6. DOI: 10.1016/B978-0-08-036364-6.50008-9.

[101] T. Gilbert and J. Kelly. "Anomalous rotational damping in ferromagnetic sheets". *Conf. Magnetism and Magnetic Materials* (1955).

[102] T. Gilbert. "A Lagrangian formulation of the gyromagnetic equation of the magnetization field". *Phys. Rev.* 100.4 (1955), p. 1243.

[103] T. Gilbert. "A phenomenological theory of damping in ferromagnetic materials". *IEEE Transactions on Magnetics* 40.6 (2004), pp. 3443–3449. DOI: 10.1109/TMAG.2004.836740.

[104] A. Lyberatos, D. V. Berkov, and R. W. Chantrell. "A method for the numerical simulation of the thermal magnetization fluctuations in micromagnetics". *J. Phys.: Condens. Matter* 5.47 (1993), p. 8911. DOI: 10.1088/0953-8984/5/47/016.

[105] S. Shi, A. L. Wysocki, and K. D. Belashchenko. "Magnetism of chromia from first-principles calculations". *Phys. Rev. B* 79.10 (2009), p. 104404. DOI: 10.1103/PhysRevB.79.104404.

[106] S. Mu, A. L. Wysocki, and K. D. Belashchenko. "First-principles microscopic model of exchange-driven magnetoelectric response with application to Cr_2O_3". *Phys. Rev. B* 89.17 (2014), p. 174413. DOI: 10.1103/PhysRevB.89.174413.

[107] M. Fechner, A. Sukhov, L. Chotorlishvili, C. Kenel, J. Berakdar, and N. A. Spaldin. "Magnetophononics: Ultrafast spin control through the lattice". *Phys. Rev. Materials* 2.6 (2018), p. 064401. DOI: 10.1103/PhysRevMaterials.2.064401.

[108] M. Ye and D. Vanderbilt. "Dynamical magnetic charges and linear magnetoelectricity". *Phys. Rev. B* 89.6 (5, 2014), p. 064301. DOI: 10.1103/PhysRevB.89.064301.

[109] A. H. Hill, A. Harrison, C. Dickinson, W. Zhou, and W. Kockelmann. "Crystallographic and magnetic studies of mesoporous eskolaite, Cr_2O_3". *Microporous Mesoporous Mater.* 130.1 (2010), p. 280. DOI: 10.1016/j.micromeso.2009.11.021.

[110] Z. Zhou, J. Shi, and L. Guo. "A comparative study on structural and electronic properties and formation energy of bulk α-Fe_2O_3 using first-principles calculations with different density functionals". *Comput. Mater. Sci.* 113 (2016), pp. 117–122. DOI: 10.1016/j.commatsci.2015.11.030.

[111] Y. Si, M. Li, Z. Zhou, M. Liu, and O. Prezhdo. "Improved description of hematite surfaces by the SCAN functional". *J. Chem. Phys.* 152.2 (2020), p. 024706. DOI: 10.1063/1.5134951.

[112] V. Baron, J. Gutzmer, H. Rundlöf, and R. Tellgren. "Neutron powder diffraction study of Mn-bearing hematite, α-Fe_{2-x}-Mn_xO_3, in the range $0 \leq x \leq 0.176$". *Solid State Sci.* 7.6 (2005), pp. 753–759. DOI: 10.1016/j.solidstatesciences.2004.11.021.

[113] A. H. Hill, F. Jiao, P. G. Bruce, A. Harrison, W. Kockelmann, and C. Ritter. "Neutron diffraction study of mesoporous and bulk Hematite, α-Fe_2O_3". *Chem. Mater.* 20.15 (2008), pp. 4891–4899. DOI: 10.1021/cm800009s.

[114] E. Krén, P. Szabó, and G. Konczos. "Neutron diffraction studies on the (1-x)Fe_2O_3 - xRh_2O_3 system". *Phys. Lett.* 19.2 (1965), pp. 103–104. DOI: 10.1016/0031-9163(65)90731-6.

[115] R. W. G. Wyckoff. *The Analytical Expression of the Results of the Theory of Space Groups*. Carnegie Institution of Washington, 1922.

[116] L. Kantorovich. *Quantum Theory of the Solid State: An Introduction*. Kluwer academic publishers, Springer, 2004. ISBN: 978-1-4020-2153-4.

[117] D. Sands. "Chapter 3 - Crystal Systems and Geometry". In: *Introduction to Crystallography*. Dover Publications, 1975. ISBN: 0-486-67839-3.

[118] D. F. McMorrow, K. A. McEwen, U. Steigenberger, H. M. Rønnow, and F. Yakhou. "X-ray resonant scattering study of the quadrupolar order in UPd_3". *Phys. Rev. Lett.* 87.5 (2001), p. 057201. DOI: 10.1103/PhysRevLett.87.057201.

[119] N. A. Spaldin and M. Fiebig. "The renaissance of magnetoelectric multiferroics". *Science* 309.5733 (2005), pp. 391–392. DOI: 10.1126/science.1113357.

[120] Y. Kota, H. Imamura, and M. Sasaki. "Enhancement of spin correlation in Cr_2O_3 film Above Néel temperature induced by forming a junction with Fe_2O_3 layer: First-principles and Monte-Carlo Study". *IEEE Trans. Magn.* 50.11 (2014), pp. 1–4. DOI: 10.1109/TMAG.2014.2324014.

[121] L. D. Landau and E. M. Lifshitz. *Electrodynamics of continuous media*. Pergamon press, 1960.

[122] X. Zhang, Q. Liu, J.-W. Luo, A. J. Freeman, and A. Zunger. "Hidden spin polarization in inversion-symmetric bulk crystals". *Nat. Phys.* 10.5 (2014), pp. 387–393. DOI: 10.1038/nphys2933.

[123] L. Yuan, Q. Liu, X. Zhang, J.-W. Luo, S.-S. Li, and A. Zunger. "Uncovering and tailoring hidden Rashba spin–orbit splitting in centrosymmetric crystals". *Nat. Commun.* 10.1 (2019), p. 906. DOI: 10.1038/s41467-019-08836-4.

[124] S. Foner. "High-field antiferromagnetic resonance in Cr_2O_3". *Phys. Rev.* 130.1 (1963), pp. 183–197. DOI: 10.1103/PhysRev.130.183.

[125] F. J. Morin. "Electrical properties of α-Fe_2O_3 and α-Fe_2O_3 containing titanium". *Phys. Rev.* 83.5 (1, 1951), pp. 1005–1010. DOI: 10.1103/PhysRev.83.1005.

[126] I. Dzyaloshinsky. "A thermodynamic theory of "weak" ferromagnetism of antiferromagnetics". *J. Phys. Chem. Solids* 4.4 (1958), pp. 241–255. DOI: 10.1016/0022-3697(58)90076-3.

[127] T. Kosub, M. Kopte, R. Hühne, P. Appel, B. Shields, P. Maletinsky, R. Hübner, M. O. Liedke, J. Fassbender, O. G. Schmidt, and D. Makarov. "Purely antiferromagnetic magnetoelectric random access memory". *Nat. Commun.* 8.1 (2017), p. 13985. DOI: 10.1038/ncomms13985.

[128] L.-D. Yuan, Z. Wang, J.-W. Luo, and A. Zunger. "Prediction of low-Z collinear and noncollinear antiferromagnetic compounds having momentum-dependent spin splitting even without spin-orbit coupling". *Phys. Rev. Mater.* 5.1 (2021), p. 014409. DOI: 10.1103/PhysRevMaterials.5.014409.

[129] "Hidden orders and (anti-)magnetoelectric effects in Cr_2O_3 and α-Fe_2O_3". *Materials Cloud Archive* 2023.152 (2023). DOI: 10.24435/materialscloud:x7-6w.

[130] *See Supplemental Material at http://link.aps.org/supplemental/10.1103/PhysRevResearch.5.L042018 for the details regarding the symmetry analysis, the method used to calculate the magnetoelectric response and the parameters that were used for our density functional theory calculations, as well as convergence tests of the canted moment calculations.*

[131] A. Togo and I. Tanaka. "First principles phonon calculations in materials science". *Scr. Mater.* 108 (2015), pp. 1–5. DOI: 10.1016/j.scriptamat.2015.07.021.

[132] A. Togo. "First-principles phonon calculations with Phonopy and Phono3py". *J. Phys. Soc. Jpn.* 92.1 (2023), p. 012001. DOI: 10.7566/JPSJ.92.012001.

[133] C. R. Woods, P. Ares, H. Nevison-Andrews, M. J. Holwill, R. Fabregas, F. Guinea, A. K. Geim, K. S. Novoselov, N. R. Walet, and L. Fumagalli. "Charge-polarized interfacial superlattices in marginally twisted hexagonal boron nitride". *Nat. Commun.* 12.1 (2021), p. 347. DOI: 10.1038/s41467-020-20667-2.

[134] H. J. Monkhorst and J. D. Pack. "Special points for Brillouin-zone integrations". *Phys. Rev. B* 13.12 (1976), p. 5188. DOI: 10.1103/PhysRevB.13.5188.

[135] F. Thöle. "Magnetoelectric multipoles in condensed-matter systems". Doctoral Thesis. Zurich: ETH Zurich, 2018. DOI: 10.3929/ethz-b-000302691.

[136] D. N. Astrov and N. B. Ermakov. "Quadrupole magnetic-Field of magnetoelectric Cr_2O_3". *Pis'ma Zh. Eksp. Teor. Fiz.* 59.4 (1994), pp. 274–277. [*Sov. Phys. JETP Lett.* 59.4 (1994), pp. 297-300].

[137] D. N. Astrov, N. B. Ermakov, A. S. Borovik-Romanov, E. G. Kolevatov, and V. I. Nizhankovskii. "External quadrupole magnetic field of antiferromagnetic Cr_2O_3". *Pis'ma Zh. Eksp. Teor. Fiz.* 63.9 (1996), pp. 713–718. DOI: 10.1134/1.566976. [*Sov. Phys. JETP Lett.* 63.9 (1996), pp. 745-751].

[138] E. Lelièvre-Berna, P. J. Brown, F. Tasset, K. Kakurai, M. Takeda, and L.-P. Regnault. "Precision manipulation of the neutron polarisation vector". *Phys. B: Condens. Matter* 397.1-2 (2007), pp. 120–124. DOI: 10.1016/j.physb.2007.02.076.

[139] P. J. Brown. "Chapter 5 - Spherical neutron polarimetry". In: *Neutron scattering from magnetic materials*. Ed. by T. Chatterji. Amsterdam: Elsevier Science, 2006, pp. 215–244. ISBN: 978-0-444-51050-1. DOI: 10.1016/B978-044451050-1/50006-9.

[140] M. Blume. "Polarization effects in the magnetic elastic scattering of slow neutrons". *Phys. Rev.* 130.5 (1963), pp. 1670–1676. DOI: 10.1103/PhysRev.130.1670.

[141] S. V. Maleev, V. G. Bar'yakhtar, and R. A. Suris. "The scattering of slow neutrons by complex magnetic structures". *Sov. Phys.-Solid State* 4 (1963).

[142] S. Shtrikman and D. Treves. "Observation of the magnetoelectric effect in Cr_2O_3 powders". *Phys. Rev.* 130.3 (1963), pp. 986–988. DOI: 10.1103/PhysRev.130.986.

[143] T. Martin and J. Anderson. "Antiferromagnetic domain switching in Cr_2O_3". *IEEE Trans. Magn.* 2.3 (1966), pp. 446–449. DOI: 10.1109/TMAG.1966.1065857.

[144] C. Brown and T. O'Dell. "Domain switching measurements in an antiferromagnet". *IEEE Trans. Magn.* 5.4 (1969), pp. 964–967. DOI: 10.1109/TMAG.1969.1066657.

[145] J.-P. Rivera. "The linear magnetoelectric effect in $LiCoPO_4$ revisited". *Ferroelectrics* 161.1 (1994), pp. 147–164. DOI: 10.1080/00150199408213364.

[146] P. Borisov, A. Hochstrat, V. V. Shvartsman, W. Kleemann, and P. M. Hauck. "Magnetoelectric Cr_2O_3 for spintronic applications". *Integr. Ferroelectr.* 99 (2008), pp. 69–76. DOI: 10.1080/10584580802107700.

[147] D. N. Astrov. "The magnetoelectric effect in antiferromagnetics". *Zh. Eksp. Teor. Fiz.* 38 (1960), pp. 984–985. [*Sov. Phys. JETP* 11.3 (1960), pp. 708-708].

[148] B. N. Brockhouse. "Antiferromagnetic structure in Cr_2O_3". *J. Chem. Phys.* 21 (1953), pp. 961–962. DOI: 10.1063/1.1699098.

[149] K. L. Dudko, V. V. Eremenko, and L. M. Semenenko. "Magnetostriction of antiferromagnetic Cr_2O_3 in strong magnetic fields". *Phys. Status Solidi (b)* 43 (1971), pp. 471–477. DOI: 10.1002/pssb.2220430203.

[150] D. Tobia, E. De Biasi, M. Granada, H. E. Troiani, G. Zampieri, E. Winkler, and R. D. Zysler. "Evolution of the magnetic anisotropy with particle size in antiferromagnetic Cr_2O_3 nanoparticles". *J. Appl. Phys.* 108 (2010), p. 104303. DOI: 10.1063/1.3506535.

[151] P. J. Brown, J. B. Forsyth, and F. Tasset. "Precision determination of antiferromagnetic form factors". *Physica B* 267-268 (1999), pp. 215–220. DOI: 10.1016/S0921-4526(99)00018-6.

[152] F. Tasset, P. J. Brown, and J. B. Forsyth. "Determination of the absolute magnetic moment direction in Cr_2O_3 using generalized polarization analysis". *J. Appl. Phys.* 63.8 (1988), pp. 3606–3608. DOI: 10.1063/1.340709.

[153] X. Gonze, B. Amadon, G. Antonius, F. Arnardi, L. Baguet, J.-M. Beuken, J. Bieder, F. Bottin, J. Bouchet, E. Bousquet, N. Brouwer, F. Bruneval, G. Brunin, T. Cavignac, C. J.-B., W. Chen, M. Côté, S. Cottenier, J. Denier, G. Geneste, P. Ghosez, M. Giantomassi, Y. Gillet, O. Gingras, D. R. Hamann, G. Hautier, X. He, N. Helbig, N. Holzwarth, Y. Jia, F. Jollet, W. Lafargue-Dit-Hauret, K. Lejaeghere, M. A. L. Marques, A. Martin, C. Martins, H. P. C. Miranda, F. Naccarato, K. Persson, G. Petretto, V. Planes, Y. Pouillon, S. Prokhorenko, F. Ricci, G.-M. Rignanese, A. H. Romero, M. M. Schmitt, M. Torrent, M. J. van Setten, B. Van Troeye, M. J. Verstraete, G. Zérah, and J. W. Zwanziger. "The Abinit project: Impact, environment and recent developments". *Comput. Phys. Commun.* 248 (2020), p. 107042. DOI: 10.1016/j.cpc.2019.107042.

[154] A. H. Romero, D. C. Allan, B. Amadon, G. Antonius, T. Applencourt, B. L., J. Bieder, F. Bottin, J. Bouchet, E. Bousquet, F. Bruneval, G. Brunin, D. Caliste, M. Côté, J. Denier, C. Dreyer, P. Ghosez, M. Giantomassi, Y. Gillet, O. Gingras, D. R. Hamann, G. Hautier, F. Jollet, G. Jomard, A. Martin, H. P. C. Miranda, F. Naccarato, G. Petretto, N. A. Pike, V. Planes, S. Prokhorenko, T. Rangel, F. Ricci, G.-M. Rignanese, M. Royo, M. Stengel, M. Torrent, M. J. van Setten, B. Van Troeye, M. J. Verstraete, J. Wiktor, J. W. Zwanziger, and X. Gonze. "ABINIT: Overview, and focus on selected capabilities". *J. Chem. Phys.* 152 (2020), p. 124102. DOI: 10.1063/1.5144261.

[155] P. Giannozzi, S. Baroni, N. Bonini, M. Calandra, R. Car, C. Cavazzoni, D. Ceresoli, G. L. Chiarotti, M. Cococcioni, I. Dabo, A. Dal Corso, S. de Gironcoli, S. Fabris, G. Fratesi, R. Gebauer, U. Gerstmann, C. Gougoussis, A. Kokalj, M. Lazzeri, L. Martin-Samos, N. Marzari, F. Mauri, R. Mazzarello, S. Paolini, A. Pasquarello, L. Paulatto, C. Sbraccia, S. Scandolo, G. Sclauzero, A. P. Seitsonen, A. Smogunov, P. Umari, and R. M. Wentzcovitch. "QUANTUM ESPRESSO: a modular and open-source software project for quantum simulations of materials". *J. Phys. Condens. Matter* 21 (2009), p. 395502. DOI: 10.1088/0953-8984/21/39/395502.

[156] P. Giannozzi, O. Andreussi, T. Brumme, O. Bunau, M. Buongiorno Nardelli, M. Calandra, R. Car, C. Cavazzoni, D. Ceresoli, M. Cococcioni, N. Colonna, I. Carnimeo, A. Dal Corso, S. de Gironcoli, P. Delugas, R. A. DiStasio, A. Ferretti, A. Floris, G. Fratesi, G. Fugallo, R. Gebauer, U. Gerstmann, F. Giustino, T. Gorni, J. Jia, M. Kawamura, H.-Y. Ko, A. Kokalj, E. Küçükbenli, M. Lazzeri, M. Marsili, N. Marzari, F. Mauri, N. L. Nguyen, H.-V. Nguyen, A. Otero-de-la-Roza, L. Paulatto, S. Poncé, D. Rocca, R. Sabatini, B. Santra, M. Schlipf, A. P. Seitsonen, A. Smogunov, I. Timrov, T. Thonhauser, P. Umari, N. Vast, X. Wu, and S. Baroni. "Advanced capabilities for materials modelling with Quantum ESPRESSO". *J. Phys.:Condens. Matter* 29.46 (2017), p. 465901. DOI: 10.1088/1361-648X/aa8f79.

[157] K. T. Delaney. *Private communication*. 2023.

[158] "On the sign of the linear magnetoelectric coefficient in Cr_2O_3". *Materials Cloud Archive* 2023.171 (2023). DOI: 10.24435/materialscloud:ek-fp.

[159] F. Tasset, P. J. Brown, E. Lelièvre-Berna, T. W. Roberts, S. Pujol, J. Allibon, and E. Bourgeat-Lami. "Spherical neutron polarimetry with Cryopad-II". *Physica B* 267-268 (1999), pp. 69–74. DOI: 10.1016/S0921-4526(99)00029-0.

[160] E. Lelièvre-Berna, E. Bourgeat-Lami, P. Fouilloux, B. Geffray, Y. Gibert, K. Kakurai, N. Kernavanois, B. Longuet, F. Mantegazza, M. Nakamura, S. Pujol, L.-P. Regnault, F. Tasset, M. Takeda, M. Thomas, and X. Tonon. "Advances in spherical neutron polarimetry with Cryopad". *Phys. B: Condens. Matter* 356.1-4 (2005), pp. 131–135. DOI: 10.1016/j.physb.2004.10.063.

[161] N. Qureshi. "*Mag2Pol*: a program for the analysis of spherical neutron polarimetry, flipping ratio and integrated intensity data". *J. Appl. Crystallogr.* 52.1 (2019), pp. 175–185. DOI: 10.1107/S1600576718016084.

[162] X. He, Y. Wang, N. Wu, A. N. Caruso, E. Vescovo, K. D. Belashchenko, P. A. Dowben, and C. Binek. "Robust isothermal electric control of exchange bias at room temperature". *Nat. Mater.* 9.7 (2010), pp. 579–585. DOI: 10.1038/nmat2785.

[163] P. Borisov, T. Ashida, T. Nozaki, M. Sahashi, and D. Lederman. "Magnetoelectric properties of 500-nm Cr_2O_3 films". *Phys. Rev. B* 93 (2016), p. 174415. DOI: 10.1103/PhysRevB.93.174415.

[164] S. F. Weber and N. A. Spaldin. "Characterizing and overcoming surface paramagnetism in magnetoelectric antiferromagnets". *Phys. Rev. Lett.* 130 (2023), p. 146701. DOI: 10.1103/PhysRevLett.130.146701.

[165] *thermo_pw is an extension of the Quantum ESPRESSO (QE) package which provides an alternative organization of the QE workflow for the most common tasks. For more information see https://dalcorso.github.io/thermo_pw/.*

[166] D. Vanderbilt. "Soft self-consistent pseudopotentials in a generalized eigenvalue formalism". *Phys. Rev. B* 41.11 (1990), p. 7892. DOI: 10.1103/PhysRevB.41.7892.

[167] A. Dal Corso. "Pseudopotentials periodic table: From H to Pu". *Comp. Mater. Sci.* 95 (2014), p. 337. DOI: 10.1016/j.commatsci.2014.07.043.

[168] *See https://dalcorso.github.io/pslibrary/.*

[169] S. Baroni, S. de Gironcoli, A. Dal Corso, and P. Giannozzi. "Phonons and related crystal properties from density-functional perturbation theory". *Rev. Mod. Phys.* 73 (2001), pp. 515–562. DOI: 10.1103/RevModPhys.73.515.

[170] M.-J. Van Setten, M. Giantomassi, E. Bousquet, M. J. Verstraete, D. R. Hamann, X. Gonze, and G.-M. Rignanese. "The PseudoDojo: Training and grading a 85 element optimized norm-conserving pseudopotential table". *Comput. Phys. Commun.* 226 (2018), p. 39. DOI: 10.1016/j.cpc.2018.01.012.

[171] P. A. McClarty and J. G. Rau. "Landau theory of altermagnetism". *Phys. Rev. Lett.* 132.17 (2024), p. 176702. DOI: 10.1103/PhysRevLett.132.176702.

[172] X. H. Verbeek, D. Voderholzer, S. Schären, Y. Gachnang, N. A. Spaldin, and S. Bhowal. "Non-relativistic ferromagnetotriakontadipolar order and spin splitting in hematite" (2024). https://arxiv.org/abs/2405.10675.

[173] H. A. Kramers. "Théorie générale de la rotation paramagnétique dans les cristaux". *Proc. Amsterdam Acad.* 33 (1930), pp. 959–972.

[174] E. Wigner. "Ueber die Operation der Zeitumkehr in der Quantenmechanik". *Nachr. Akad. Ges. Wiss. Göttingen* 1932 (1932), pp. 546–559.

[175] S. Pekar and É. I. Rashba. "Combined resonance in crystals in inhomogeneous magnetic fields". *Zh. Eksp. Teor. Fiz.* 47 (1964), pp. 1927–1932. [*Sov. Phys. JETP* 20.5 (1965), pp. 1295-1298].

[176] E. Rashba. "Properties of semiconductors with an extremum loop. I. Cyclotron and combinational resonance in a magnetic field perpendicular to the plane of the loop". *Sov. Phys.-Solid State* 2 (1960), p. 1109.

[177] Y. A. Bychkov and E. I. Rashba. "Oscillatory effects and the magnetic susceptibility of carriers in inversion layers". *J. Solid State Phys.* 17.33 (1984), p. 6039. DOI: 10.1088/0022-3719/17/33/015.

[178] M. Naka, S. Hayami, H. Kusunose, Y. Yanagi, Y. Motome, and H. Seo. "Spin current generation in organic antiferromagnets". *Nat. Commun.* 10.1 (2019), p. 4305. DOI: 10.1038/s41467-019-12229-y.

[179] K.-H. Ahn, A. Hariki, K.-W. Lee, and J. Kuneš. "Antiferromagnetism in RuO_2 as d-wave Pomeranchuk instability". *Phys. Rev. B* 99 (2019), p. 184432. DOI: 10.1103/PhysRevB.99.184432.

[180] S. Hayami, Y. Yanagi, and H. Kusunose. "Momentum-Dependent Spin Splitting by Collinear Antiferromagnetic Ordering". *J. Phys. Soc. Jpn.* 88.12 (2019), p. 123702. DOI: 10.7566/JPSJ.88.123702.

[181] L. Šmejkal, R. González-Hernández, T. Jungwirth, and J. Sinova. "Crystal time-reversal symmetry breaking and spontaneous Hall effect in collinear antiferromagnets". *Sci. Adv.* 6.23 (2020), eaaz8809. DOI: 10.1126/sciadv.aaz8809.

[182] L.-D. Yuan, Z. Wang, J.-W. Luo, E. I. Rashba, and A. Zunger. "Giant momentum-dependent spin splitting in centrosymmetric low-Z antiferromagnets". *Phys. Rev. B* 102 (2020), p. 014422. DOI: 10.1103/PhysRevB.102.014422.

[183] S. Hayami, Y. Yanagi, and H. Kusunose. "Bottom-up design of spin-split and reshaped electronic band structures in antiferromagnets without spin-orbit coupling: Procedure on the basis of augmented multipoles". *Phys. Rev. B* 102 (2020), p. 144441. DOI: 10.1103/PhysRevB.102.144441.

[184] I. I. Mazin, K. Koepernik, M. D. Johannes, R. González-Hernández, and L. Šmejkal. "Prediction of unconventional magnetism in doped $FeSb_2$". *PNAS* 118.42 (2021), e2108924118. DOI: 10.1073/pnas.2108924118.

[185] H.-Y. Ma, M. Hu, N. Li, J. Liu, W. Yao, J.-F. Jia, and J. Liu. "Multifunctional antiferromagnetic materials with giant piezomagnetism and noncollinear spin current". *Nat. Commun.* 12.1 (2021), p. 2846. DOI: 10.1038/s41467-021-23127-7.

[186] M. Naka, Y. Motome, and H. Seo. "Perovskite as a spin current generator". *Phys. Rev. B* 103 (2021), p. 125114. DOI: 10.1103/PhysRevB.103.125114.

[187] L.-D. Yuan and A. Zunger. "Degeneracy removal of spin bands in collinear antiferromagnets with non-interconvertible spin-structure motif pair". *Adv Mater* 35.31 (2023), e2211966. DOI: 10.1002/adma.202211966.

[188] L.-D. Yuan, X. Zhang, C. M. Acosta, and A. Zunger. "Uncovering spin-orbit coupling-independent hidden spin polarization of energy bands in antiferromagnets". *Nat. Commun.* 14.1 (2023), p. 5301. DOI: 10.1038/s41467-023-40877-8.

[189] R. González-Hernández, L. Šmejkal, K. Výborný, Y. Yahagi, J. Sinova, T. Jungwirth, and J. Železný. "Efficient electrical spin splitter based on nonrelativistic collinear antiferromagnetism". *Phys. Rev. Lett.* 126 (2021), p. 127701. DOI: 10.1103/PhysRevLett.126.127701.

[190] D.-F. Shao, S.-H. Zhang, M. Li, C.-B. Eom, and E. Y. Tsymbal. "Spin-neutral currents for spintronics". *Nat. Commun.* 12.1 (2021), p. 7061. DOI: 10.1038/s41467-021-26915-3.

[191] A. Bose, N. J. Schreiber, R. Jain, D.-F. Shao, H. P. Nair, J. Sun, X. S. Zhang, D. A. Muller, E. Y. Tsymbal, D. G. Schlom, and D. C. Ralph. "Tilted spin current generated by the collinear antiferromagnet ruthenium dioxide". *Nat. Electron.* 5.5 (2022), pp. 267–274. DOI: 10.1038/s41928-022-00744-8.

[192] H. Bai, L. Han, X. Y. Feng, Y. J. Zhou, R. X. Su, Q. Wang, L. Y. Liao, W. X. Zhu, X. Z. Chen, F. Pan, X. L. Fan, and C. Song. "Observation of spin splitting torque in a collinear antiferromagnet RuO_2". *Phys. Rev. Lett.* 128 (2022), p. 197202. DOI: 10.1103/PhysRevLett.128.197202.

[193] S. Karube, T. Tanaka, D. Sugawara, N. Kadoguchi, M. Kohda, and J. Nitta. "Observation of spin-splitter torque in collinear antiferromagnetic RuO_2". *Phys. Rev. Lett.* 129 (2022), p. 137201. DOI: 10.1103/PhysRevLett.129.137201.

[194] H. Reichlová, R. L. Seeger, R. González-Hernández, I. Kounta, R. Schlitz, D. Kriegner, P. Ritzinger, M. Lammel, M. Leiviskä, V. Petříček, P. Doležal, E. Schmoranzerová, A. Bad'ura, A. Thomas, V. Baltz, L. Michez, J. Sinova, S. T. B. Goennenwein, T. Jungwirth, and L. Šmejkal. "Macroscopic time reversal symmetry breaking by staggered spin-momentum interaction". *arXiv 2012.15651* (2020). DOI: 10.48550/ARXIV.2012.15651.

[195] Z. Feng, X. Zhou, L. Šmejkal, L. Wu, Z. Zhu, H. Guo, R. González-Hernández, X. Wang, H. Yan, P. Qin, X. Zhang, H. Wu, H. Chen, Z. Meng, L. Liu, Z. Xia, J. Sinova, T. Jungwirth, and Z. Liu. "An anomalous Hall effect in altermagnetic ruthenium dioxide". *Nat. Electron.* 5.11 (2022), pp. 735–743. DOI: 10.1038/s41928-022-00866-z.

[196] R. D. Gonzalez Betancourt, J. Zubáč, R. Gonzalez-Hernandez, K. Geishendorf, Z. Šobáň, G. Springholz, K. Olejník, L. Šmejkal, J. Sinova, T. Jungwirth, S. T. B. Goennenwein, A. Thomas, H. Reichlová, J. Železný, and D. Kriegner. "Spontaneous anomalous Hall effect arising from an unconventional compensated magnetic phase in a semiconductor". *Phys. Rev. Lett.* 130 (2023), p. 036702. DOI: 10.1103/PhysRevLett.130.036702.

[197] L. Šmejkal, A. H. MacDonald, J. Sinova, S. Nakatsuji, and T. Jungwirth. "Anomalous Hall antiferromagnets". *Nat. Rev. Mater.* 7.6 (2022), pp. 482–496. DOI: 10.1038/s41578-022-00430-3.

[198] L. Šmejkal, A. Marmodoro, K.-H. Ahn, R. González-Hernández, I. Turek, S. Mankovsky, H. Ebert, S. W. D'Souza, O. Šipr, J. Sinova, and T. Jungwirth. "Chiral magnons in altermagnetic RuO_2". *Phys. Rev. Lett.* 131 (2023), p. 256703. DOI: 10.1103/PhysRevLett.131.256703.

[199] S. Bhowal and N. A. Spaldin. "Ferroically ordered magnetic octupoles in *d*-wave altermagnets". *Phys. Rev. X* 14 (2024), p. 011019. DOI: 10.1103/PhysRevX.14.011019.

[200] L. Šmejkal, A. B. Hellenes, R. González-Hernández, J. Sinova, and T. Jungwirth. "Giant and tunneling magnetoresistance in unconventional collinear antiferromagnets with nonrelativistic spin-momentum coupling". *Phys. Rev. X* 12 (2022), p. 011028. DOI: 10.1103/PhysRevX.12.011028.

[201] I. I. Mazin. "Notes on altermagnetism and superconductivity". *arXiv 2203.05000* (2022). DOI: 10.48550/ARXIV.2203.05000.

[202] D. Zhu, Z.-Y. Zhuang, Z. Wu, and Z. Yan. "Topological superconductivity in two-dimensional altermagnetic metals". *Phys. Rev. B* 108 (2023), p. 184505. DOI: 10.1103/PhysRevB.108.184505.

[203] S.-B. Zhang, L.-H. Hu, and T. Neupert. "Finite-momentum Cooper pairing in proximitized altermagnets". *Nat. Commun.* 15.1 (2024), p. 1801. DOI: 10.1038/s41467-024-45951-3.

[204] S. W. Lovesey, D. D. Khalyavin, and G. van der Laan. "Templates for magnetic symmetry and altermagnetism in hexagonal MnTe". *Phys. Rev. B* 108 (2023), p. 174437. DOI: 10.1103/PhysRevB.108.174437.

[205] S. Lee, S. Lee, S. Jung, J. Jung, D. Kim, Y. Lee, B. Seok, J. Kim, B. G. Park, L. Šmejkal, C.-J. Kang, and C. Kim. "Broken Kramers degeneracy in altermagnetic MnTe". *Phys. Rev. Lett.* 132 (2024), p. 036702. DOI: 10.1103/PhysRevLett.132.036702.

[206] J. Krempaský, L. Šmejkal, S. W. D'Souza, M. Hajlaoui, G. Springholz, K. Uhlířová, F. Alarab, P. C. Constantinou, V. Strocov, D. Usanov, W. R. Pudelko, R. González-Hernández, A. Birk Hellenes, Z. Jansa, H. Reichlová, Z. Šobáň, R. D. Gonzalez Betancourt, P. Wadley, J. Sinova, D. Kriegner, J. Minár, J. H. Dil, and T. Jungwirth. "Altermagnetic lifting of Kramers spin degeneracy". *Nature* 626.7999 (2024), pp. 517–522. DOI: 10.1038/s41586-023-06907-7.

[207] S. Reimers, L. Odenbreit, L. Šmejkal, V. N. Strocov, P. Constantinou, A. B. Hellenes, R. Jaeschke Ubiergo, W. H. Campos, V. K. Bharadwaj, A. Chakraborty, T. Denneulin, W. Shi, R. E. Dunin-Borkowski, S. Das, M. Kläui, J. Sinova, and M. Jourdan. "Direct observation of altermagnetic band splitting in CrSb thin films". *Nat. Commun.* 15.1 (2024), p. 2116. DOI: 10.1038/s41467-024-46476-5.

[208] P.-W. Ma and S. L. Dudarev. "Constrained density functional for noncollinear magnetism". *Phys. Rev. B* 91.5 (2015), p. 054420. DOI: 10.1103/PhysRevB.91.054420.

[209] F. Cricchio, F. Bultmark, O. Grånäs, and L. Nordström. "Itinerant Magnetic Multipole Moments of Rank Five as the Hidden Order in URu_2Si_2". *Phys. Rev. Lett.* 103.10 (2009), p. 107202. DOI: 10.1103/PhysRevLett.103.107202.

[210] P. J. Flanders and J. P. Remeika. "Magnetic properties of hematite single crystals". *Phil. Mag: J. Theor. Exp. Appl. Phys.* 11.114 (1965), pp. 1271–1288. DOI: 10.1080/14786436508224935.

[211] F. Bødker, M. F. Hansen, C. B. Koch, K. Lefmann, and S. Mørup. "Magnetic properties of hematite nanoparticles". *Phys. Rev. B* 61.10 (2000), pp. 6826–6838. DOI: 10.1103/PhysRevB.61.6826.

[212] J. Fischer, M. Althammer, N. Vlietstra, H. Huebl, S. T. Goennenwein, R. Gross, S. Geprägs, and M. Opel. "Large spin Hall magnetoresistance in antiferromagnetic α-Fe_2O_3/Pt heterostructures". *Phys. Rev. Appl.* 13 (2020), p. 014019. DOI: 10.1103/PhysRevApplied.13.014019.

[213] R. Lebrun, A. Ross, O. Gomonay, V. Baltz, U. Ebels, A.-L. Barra, A. Qaiumzadeh, A. Brataas, J. Sinova, and M. Kläui. "Long-distance spin-transport across the Morin phase transition up to room temperature in ultra-low damping single crystals of the antiferromagnet α-Fe_2O_3". *Nat. Commun.* 11.1 (2020), p. 6332. DOI: 10.1038/s41467-020-20155-7.

[214] Z. Lin, D. Chen, W. Lu, X. Liang, S. Feng, K. Yamagami, J. Osiecki, M. Leandersson, B. Thiagarajan, J. Liu, C. Felser, and J. Ma. *Observation of giant spin splitting and d-wave spin texture in room temperature altermagnet RuO_2*. 2024. DOI: 10.48550/arXiv.2402.04995.

[215] T. Aoyama and K. Ohgushi. *Piezomagnetic properties in altermagnetic MnTe*. 2023. DOI: 10.48550/arXiv.2305.14786.

[216] L. Šmejkal. *Private communication*. 2023.

[217] R. D. King-Smith and D. Vanderbilt. "Theory of polarization of crystalline solids". *Phys. Rev. B* 47.3 (1993), pp. 1651–1654. DOI: 10.1103/PhysRevB.47.1651.

[218] A. Ohtomo and H. Y. Hwang. "A high-mobility electron gas at the $LaAlO_3/SrTiO_3$ heterointerface". *Nature* 427.6973 (2004), pp. 423–426. DOI: 10.1038/nature02308.

[219] P. Yu, W. Luo, D. Yi, J. X. Zhang, M. D. Rossell, C.-H. Yang, L. You, G. Singh-Bhalla, S. Y. Yang, Q. He, Q. M. Ramasse, R. Erni, L. W. Martin, Y. H. Chu, S. T. Pantelides, S. J. Pennycook, and R. Ramesh. "Interface control of bulk ferroelectric polarization". *Proc. Natl. Acad. Sci. USA* 109.25 (2012), pp. 9710–9715. DOI: 10.1073/pnas.1117990109.

[220] S. Heinze, K. von Bergmann, M. Menzel, J. Brede, A. Kubetzka, R. Wiesendanger, G. Bihlmayer, and S. Blügel. "Spontaneous atomic-scale magnetic skyrmion lattice in two dimensions". *Nature Phys.* 7.9 (2011), pp. 713–718. DOI: 10.1038/nphys2045.

[221] H. Yang, J. Liang, and Q. Cui. "First-principles calculations for Dzyaloshinskii–Moriya interaction". *Nat. Rev. Phys.* 5.1 (2023), pp. 43–61. DOI: 10.1038/s42254-022-00529-0.

[222] S. A. Chambers, Y. Liang, and Y. Gao. "Noncummutative band offset at α-Cr_2O_3/α-Fe_2O_3 (0001) heterojunctions". *Phys. Rev. B* 61.19 (2000), pp. 13223–13229. DOI: 10.1103/PhysRevB.61.13223.

[223] J. E. Jaffe, M. Dupuis, and M. Gutowski. "First-principles study of noncommutative band offsets at α-Cr_2O_3/α-Fe_2O_3 (0001) interfaces". *Phys. Rev. B* 69.20 (2004), p. 205106. DOI: 10.1103/PhysRevB.69.205106.

[224] T. Moriya. "Anisotropic superexchange interaction and weak ferromagnetism". *Phys. Rev.* 120.1 (1960), pp. 91–98. DOI: 10.1103/PhysRev.120.91.

[225] T. Moriya. "New mechanism of anisotropic superexchange interaction". *Phys. Rev. Lett.* 4.5 (1960), pp. 228–230. DOI: 10.1103/PhysRevLett.4.228.

[226] T. Dannegger, A. Deák, L. Rózsa, E. Galindez-Ruales, S. Das, E. Baek, M. Kläui, L. Szunyogh, and U. Nowak. "Magnetic properties of hematite revealed by an ab initio parameterized spin model". *Phys. Rev. B* 107 (2023), p. 184426. DOI: 10.1103/PhysRevB.107.184426.

[227] V. V. Mazurenko and V. I. Anisimov. "Weak ferromagnetism in antiferromagnets: α-Fe_2O_3 and La_2CuO_4". *Phys. Rev. B* 71.18 (2005), p. 184434. DOI: 10.1103/PhysRevB.71.184434.

[228] Y. Kota, H. Imamura, and M. Sasaki. "Strain-induced Néel temperature enhancement in corundum-type Cr_2O_3 and Fe_2O_3". *Appl. Phys. Express* 6.11 (2013), p. 113007. DOI: 10.7567/APEX.6.113007.

[229] R. A. Alikhanov, Ž. Dimitrijević, A. Kowalska, S. Kraśnicki, H. Rżany, J. Todorović, and A. Wanic. "Neutron investigation of the Spin System Dynamics in α-Cr_2O_3". *Phys. Status Solidi (b)* 32.1 (1969), pp. 41–48. DOI: 10.1002/pssb.19690320105.

[230] R. Logemann, A. N. Rudenko, M. I. Katsnelson, and A. Kirilyuk. "Exchange interactions in transition metal oxides: the role of oxygen spin polarization". *J. Phys.: Condens. Matter* 29.33 (2017), p. 335801. DOI: 10.1088/1361-648X/aa7b00.

[231] M. Tachiki and T. Nagamiya. "Origin of the magnetic anisotropy energy of antiferromagnetic Cr_2O_3". *J. Phys. Soc. Jpn.* 13.5 (1958). DOI: 10.1143/JPSJ.13.452.

[232] S. Mu and K. D. Belashchenko. "Influence of strain and chemical substitution on the magnetic anisotropy of antiferromagnetic Cr_2O_3: An ab-initio study". *Phys. Rev. Mater.* 3.3 (2019), p. 034405. DOI: 10.1103/PhysRevMaterials.3.034405.

[233] P. V. B. Pinho, A. Chartier, F. Miserque, D. Menut, and J.-B. Moussy. "Impact of epitaxial strain on crystal field splitting of α-Cr_2O_3 (0001) thin films quantified by X-ray photoemission spectroscopy". *Mat. Res. Lett.* 9.4 (), pp. 163–168. DOI: 10.1080/21663831.2020.1863877.

[234] S. Park, H. Jang, J.-Y. Kim, B.-G. Park, T.-Y. Koo, and J.-H. Park. "Strain control of Morin temperature in epitaxial α-Fe_2O_3 (0001) film". *EPL* 103.2 (2013), p. 27007. DOI: 10.1209/0295-5075/103/27007.

[235] N. Shimomura, S. P. Pati, Y. Sato, T. Nozaki, T. Shibata, K. Mibu, and M. Sahashi. "Morin transition temperature in (0001)-oriented α-Fe_2O_3 thin film and effect of Ir doping". *J. Appl. Phys.* 117.17 (2015), p. 17C736. DOI: 10.1063/1.4916304.

[236] A. L. Wysocki, S. Shi, and K. D. Belashchenko. "Microscopic origin of the structural phase transitions at the Cr_2O_3 (0001) surface". *Phys. Rev. B* 86.16 (2012), p. 165443. DOI: 10.1103/PhysRevB.86.165443.

[237] Y. Wang, X. P. Liu, and G. W. Qin. "Strain analysis of misfit dislocations in α-Fe_2O_3/α-Al_2O_3 heterostructure interface by geometric p0hase analysis". *Micron* 69 (2015), pp. 21–24. DOI: 10.1016/j.micron.2014.11.001.

[238] P. Appel, B. J. Shields, T. Kosub, N. Hedrich, R. Hübner, J. Faßbender, D. Makarov, and P. Maletinsky. "Nanomagnetism of magnetoelectric granular thin-film antiferromagnets". *Nano Lett.* 19.3 (2019), pp. 1682–1687. DOI: 10.1021/acs.nanolett.8b04681.

[239] X. H. Verbeek, M. Si, and N. A. Spaldin. *In preparation.*